Computational Investigation of Electrical Conductivities and Magnetism of Phosphonate Metal-Organic Frameworks and Frontier Orbital Gaps, Structure, and Proton Transfer Mechanisms in Phosphonate Hydrogen-Bonded Organic Frameworks

by

Craig Allan Peeples

A thesis submitted in partial fulfillment of the requirements for the degree of

Doctor of Philosophy

Department of Chemistry
University of Alberta

Abstract

The study of metal-organic frameworks (MOFs) and hydrogen-bonded organic frameworks (HOFs) has gained much interest over the last decade. MOFs and HOFs are constructed through the self-assembly of organic building units and metals (in the case of MOFs), giving rise to a diverse range of framework materials with varying properties. Herein, we focus on an emerging class of MOFs/HOFs known as phosphonate MOFs/HOFs, which are generally known to be highly thermally and chemically stable. We computationally study the electronic structures of several recently synthesized phosphonate MOFs/HOFs and the mechanisms of proton conduction in two phosphonate HOFs, to gain a deeper understanding of the microscopic origins of their macroscopic properties. We use density functional theory (DFT) to study the structures and electronic factors contributing to their electrical conductivity and magnetic behaviour and Born-Oppenheimer molecular dynamics (BOMD) to study the proton conduction mechanisms in the HOFs.

In the DFT studies, we considered three copper phosphonate MOFs, namely, TUB75, TUB40, and TUB1. Our work on TUB75 revealed a low frontier orbital gap, which paved the way for our further study of electrically conductive phosphonate MOFs. Our DFT calculations of the highest occupied crystal orbital (HOCO) to lowest unoccupied crystal orbital (LUCO) gaps agree well with the experiment results. An analysis of the orbitals revealed that the HOCOs lie on the organic linkers, while the location of the LUCOs is system-dependent. We also confirmed that the magnetic behaviour of these MOFs is due to the unpaired electrons on the copper atoms. In addition to the DFT studies on MOFs, we considered five porphyrin-based phosphonate HOFs, namely GTUB-5, Cu-, Ni-, Pd-, and Zn-GTUB-5, investigating their structures, HOCO-LUCO gaps, and relative hydrogen bond strengths. From the experimental structure, Ni-GTUB-5 is twisted compared to the other GTUB-5 systems. Our DFT results suggest that this twisting is due

the d-orbital composition of the Ni HOCO, short Ni-N bonds in the porphyrin, and sharing of the electron density between the Ni and N atoms in the porphyrin. We found that the HOCOs and LUCOs for GTUB-5, (α-spin) Cu-, Pd-, and Zn-GTUB-5 all lie on the porphyrin, while the LUCO for (β-spin) Cu-GTUB-5 is localized on the copper d-orbitals, its HOCO lies on the porphyrin, and the HOCO and LUCO for Ni-GTUB-5 are localized on the nickel d-orbitals. A DFT-based vibrational analysis on Zn-GTUB-5 revealed that the O-H bond stretch gives rise to a similar peak structure/width for all the HOFs, suggesting that all four metalated HOFs have similar hydrogen bond strengths.

In the BOMD study, we examined the proton transport mechanisms in two HOFs, namely GTUB-5 and UPC-H5a, under humid conditions. These two HOFs have similar porphyrin-based building blocks, but UPC-H5a has a metal in its porphyrin core (while GTUB-5 does not) and GTUB-5 has an extra phenylphosphonate linker in its unit cell. Furthermore, the experimental activation energies suggest a Grotthuss mechanism for proton transport in both cases. However, despite their similarities, UPC-H5a has a much higher experimental proton conductivity than GTUB-5. To study the proton transport mechanisms and gain insight into this difference, we inserted water molecules and excess protons into the pores of each HOF and simulated their dynamics using a combination of BOMD and metadynamics (MTD). Radial distribution functions (calculated from unbiased BOMD trajectories) show that, on average, the O-O bond lengths in GTUB-5 are shorter than in UPC-H5a, whereas the O-H bond lengths are shorter in UPC-H5a than in GTUB-5, suggesting that GTUB-5 has stronger hydrogen bonds than UPC-H5a. Based on the unbiased trajectories, we identified three proton transport pathways, which were used to define the MTD simulations: water-to-water (WtW), water-to-framework (WtF), and framework-to-framework (FtF). The MTD results reveal that, for both GTUB-5 and UPC-H5a, the free energy

barriers associated with proton transfers between hydrogen bonded oxygen atoms increase in going from WtF to WtW to FtF, and all pathways in UPC-H5a have lower barriers compared to their respective ones in GTUB-5. Lastly, we observed three proton transport mechanisms in the pathways, viz., single-proton, stepwise, and concerted transport.

Preface

This thesis is an original contribution by Craig Peeples and collaborators. This thesis is a partial collection of the research I completed at the University of Alberta during my PhD tenure from September 2018 – April 2023. The work presented here is part of an international collaboration led by Prof. Dr. Gündoğ Yücesan based initially out of the Technische Universität Berlin (TUB) and currently based out of the Heinrich Heine Universität Düsseldorf, with Prof. Dr. Gabriel Hanna being the lead at the University of Alberta.

The studies in Chapter 3 are presented in semi-monograph format, this includes only relevant experimental data in which the computational studies examine directly. This chapter includes the study of three phosphonate metal-organic frameworks, namely: TUB75, TUB40, and TUB1. With TUB75, TUB40 and TUB1 having experimentally determined x-ray diffraction structures, and UV-vis. Where TUB75 and TUB40 also have experimentally determined magnetic susceptibility, and electrical conductivity. We make use of computational modeling to determine electrical conductivity and magnetic mechanisms, as well as study of the frontier orbital gaps. This chapter is based on three peer-reviewed publications: 1) is published by Konrad Siemensmeyer, Craig A. Peeples, Patrik Tholen, Franz-Josef Schmitt, Bünyemin Çoşut, Gabriel Hanna, and Gündoğ Yücesan "Phosphonate Metal-Organic Frameworks: A Novel Family of Semiconductors" *Adv. Mater.* 2020, 32, 24, and I am co-first author. 2) is published by Craig A. Peeples, Delf Kober, Franz-Josef Schmitt, Patrik Tholen, Konrad Siemensmeyer, Quinn Halldorson, Bünyemin Çoşut, Aleksander Gurlo, Ahmet Ozgur Yazaydin, Gabriel Hanna, and Gündoğ Yücesan. "A 3D Cu-Naphthalene-Phosphonate Metal-Organic Framework with Ultra-High Electrical Conductivity" *Adv. Funct. Mater.* 2021, 31, 3. 3) is published by Craig A. Peeples, Ahmet Çetinkaya, Patrik Tholen, Franz-Josef Schmitt, Yunus Zorlu, Kai Bin Yu, Ozgur Yazaydin, Jens Beckmann, Gabriel Hanna, and Gündoğ Yücesan "Coordination-induced Band Gap Reduction in a metal-Organic Framework" *Chem. Eur. J.* 2022, 28, 8. Dr. Gündoğ Yücesan supervised the whole process, and wrote the introductions. Dr. Gündoğ Yücesan with help from Prof. Gabriel Hanna formulated the project. Dr. Gündoğ Yücesan organized and edited the manuscripts. Prof. Gabriel Hanna organized/edited the manuscripts, helped guide the DFT calculations/analysis, helped with experimental analysis, added discussion points, and edited the DFT analysis. Craig A. Peeples performed the DFT calculations, wrote initial drafts of the DFT analysis, made all the figures/tables associated with the DFT analysis, helped organize/edit the manuscripts, added discussion points, and helped with experimental analysis. Quinn Halldorson did initial DFT optimizations of TUB40, helped with writing the computational details and initial analysis of the DFT results. The experimental results presented in Chapter 3 include x-ray diffraction, band gap measurements conducted by Patrik Tholen under the supervision of Gündoğ Yücesan, magnetic measurements conducted by Dr. Konrad Siemensmeyer, and conductivity measurements by Dr. Franz-Josef Schmitt (TUB75 & TUB40), and Prof. Ahmet Ozgur Yazaydin (TUB40).

The studies in Chapter 4 are presented in semi-monograph format, this includes only relevant experimental data in which the computational studies support directly. This chapter includes the study of five phosphonate hydrogen-bonded organic frameworks, namely: GTUB-5, Cu-GTUB-5, Ni-GTUB-5, Zn-GTUB-5, and Pd-GTUB-5. Where, experimental x-ray diffraction, UV-vis, and proton conductivities were performed. Our work focused on analysis of the frontier orbital gaps through computational study; the results also include computational analysis of the structural influence of metalation on GTUB-5. This chapter is based on two peer-reviewed publications: 1) is published by Patrik Tholen, Craig A. Peeples, Raoul Schaper, Ceyda Bayraktar, Turan Selman Erkal, Mehmet Menaf Ayhan, Bünyemin Çoşut, Jens Beckmann, Ahmet Ozgur Yazaydin, Michael Wark, Gabriel Hanna, Yunus Zorlu, and Gündoğ Yücesan "Semiconductive microporous hydrogen-bonded organophosphonic acid framework" *Nat. Commun.* 2020, 11, 1. 2) Patrik Tholen, Craig A. Peeples, Mehmet Menaf Ayhan, Lukas Wagner, Heidi Thomas, Paulius Imbrasas, Yunus Zorlu, Clemens Baretzky, Sebation Reineke, Gabriel Hanna, and Gündoğ Yücesan "Tuning structural and optical properties of porphyrin-based hydrogen-bonded organic frameworks by metal insertion" *Small*, 2022, 18, 49, and I am co-first author. Dr. Gündoğ Yücesan supervised the whole process, and wrote the introductions. Dr. Gündoğ Yücesan with help from Prof. Gabriel Hanna formulated the project. Dr. Gündoğ Yücesan organized and edited the manuscripts. Prof. Gabriel Hanna organized/edited the manuscripts, helped guide the experimental and DFT calculations/analysis, added discussion points, and edited the DFT analysis. Craig A. Peeples performed all the DFT calculations, wrote initial drafts of the DFT analysis, made all the figures/tables associated with the DFT analysis, helped organize/edit the manuscripts, added discussion points, and helped with experimental analysis. The experimental results presented in

Chapter 4 include x-ray diffraction, band gap, and attenuated total reflectance infrared, and surface area measurements conducted by Patrik Tholen under the supervision of Dr. Gündoğ Yücesan, and proton conductivity measurements performed by Prof. Michael Wark.

The study in Chapter 5 is composed in manuscript format. The research elucidates the proton conductivity mechanisms of two phosphonate hydrogen-bonded organic frameworks, namely: GTUB-5 and UPC-H5a, using Born-Oppenheimer molecular dynamics and metadynamics. This is to be submitted for peer-review as Craig. A Peeples, Suni Guo, Gündoğ Yücesan, and Gabriel Hanna "Mechanistic insights into the proton transport in phosphonate hydrogen-bonded organic frameworks: an Born-Oppenheimer molecular dynamics and metadynamical study". Dr. Gündoğ Yücesan supplied the initial GTUB-5 structure. Both Craig A. Peeples and Prof. Gabriel Hanna formulated the project. Both Craig A. Peeples and Suni Guo are responsible for running the Born-Oppenheimer molecular dynamics simulations. Craig A. Peeples was responsible for the metadynamic simulation setup. Craig A. Peeples was responsible for collecting the data and analysis. Craig A. Peeples and Prof. Gabriel Hanna are both responsible for the interpretation of the data. Craig A. Peeples was responsible for writing the manuscript, and Prof. Gabriel Hanna edited and gave feedback on the writing process and editing of the manuscript.

To my mother and grandmother, for their infinite support

"Creativity is a combination of stimulus and teamwork."

-Lyn Heward, Cirque du Soleil

Acknowledgements

I would like to express my overwhelming gratitude to my supervisor Prof. Gabriel Hanna, for his support, knowledge, patience, and guidance throughout my PhD studies, for without him, I would have never made it this far. I would also like to thank members of the examination committee: Prof. Gilles Peslherbe, Prof. Arthur Mar, Prof. Yunji Xu, and Prof. Mariusz Klobukowski for taking the time to read my thesis and provide valuable feedback. I am also appreciative of the funding from the University of Alberta, The Department of Chemistry through the Gunning RA Award and travel awards, the Faculty of Graduate Studies and Research through the Alberta Graduate Excellence Scholarship and the J. Gordin Kaplan Graduate Student Award, Alberta Innovates through the Alberta Innovates Graduate Student Scholarship, the Resource Allocation Competition Award from Compute Canada/The Digital Research Alliance of Canada, the National Research Council of Canada, and Prof. Gabriel Hanna are gratefully acknowledged. I would also like to thank Dr. Farid Bensebaa and Dr. Sergey Gusarov for giving me the opportunity to internship at the National Research Council of Canada. I would like to thank my family for the support as well, my Mother, Corrine Peeples, Father, William Peeples, my Grandmother, Annie Fulton, Aunt and Uncle, Rick & Candice Sherbo, In-laws, Vera & Richard Szczepanski, and of course my loving Wife, Vanessa Szczepanski, for without her I would never have been able to accomplish my dreams.

Table of Contents

List of Tables

List of Figures

List of Schemes

List of Symbols

C	Capacitance
ε	Electrolyte permittivity
SA	Surface area
d	Distance
σ	Conductivity
e	Elementary charge unit
h^+	Hole concentration
e^-	Electron concentration
μ_h	Hole mobility
μ_e	Electron mobility
D_{H^+}	Proton diffusion
C_{H^+}	Proton concentration
R	Ideal gas constant
T	Temperature
$\widehat{H}$	Hamiltonian operator
E	Energy
Ψ	Wavefunction
F	Force
m	Mass
a	Acceleration
V	Potential energy
F_{araday}	Faraday constant
∇^2	Laplacian
$\hbar$	Planck's constant divided by 2 π
Z	Atomic number
$\rho(\vec{r})$	Electron density
$P(1)$	Probability of electron 1
T	Kinetic Energy

E_{Ne}	Electron-nuclear interaction
F_{HK}	Hohenberg-Kohn functional
V_{ext}	External potential
E_{ee}	Electron-electron energy
$\hat{V}_{ee}$	Electron-electron repulsion operator
T_S	Kinetic energy of non-interacting system
J	Coulomb integral
E_{XC}	Exchange-correlation energy
T_C	True kinetic energy not incorporated from non-interacting system
E_{ncl}	Non-classical contribution to electron-electron interaction
V_{XC}	Exchange-correlation potential
φ	Single electron orbital
E_X^{LDA}	Exchange energy for the local density approximation
E_C^{LDA}	Correlation energy for the local density approximation
E_X^{GGA}	Exchange energy for the generalized gradient approximation
E_C^{GGA}	Correlation energy for the generalized gradient approximation
ρ_α	Alpha-spin density
ρ_β	Beta-spin density
ω	Switching parameter for HSE06
E_{DFT-D3}	Energy for DFT and D3 dispersion
C_6^{AB}	Pair parameter for dispersion
f_6	Damping function for dispersion
t	Time
a	Hartree-Fock percentage
V_{LJ}	Lennard-Jones potential
ε_{ij}	Potential well between atoms i and j
σ_{ij}	Distance at which the potential between i and j goes to zero
ε_0	Electric constant
q	Atomic charge
H_e	Electronic Hamiltonian

∇	Gradient
L	Lattice-length
k	K-point
$Y_l^m(\theta, \phi)$	Spherical harmonics
n	Principal quantum number
l	Azimuthal quantum number
m	Magnetic quantum number
$k_B T$	Boltzmann constant
E_{ex}	Magnetic exchange energy
E_{AFM}	Antiferromagnetic energy
E_{FM}	Ferromagnetic energy
$J_{chain}\ and\ J'$	Magnetic coupling constants
χ	Magnetic susceptibility
μ_B	Bohr magneton
$\|Z\|$	Magnitude of impedance
Ω	Ohm, electrical resistance
eV	Electronvolt
meV	Milielectronvolt
l	Length
χ_B	Ferromagnetic background
χ_{dia}	Diamagnetic background
E_a	Activation energy
E^0	Chemical potential
S	Siemens
s_{ij}	Coordination number between i and j
r_{ij}	Distance between i and j
d_0, r_0, n, m	Switching parameters for coordination number cut-off in MTD
ΔG_{PT}	Free energy of proton transfer
E_g	Frontier orbital gap

List of Abbreviations

%r.h.	Percent relative humidity
AFM	Antiferromagnetic
AIMD	Ab-initio molecular dynamics
ASPC	Always stable predictor-corrector
ATR	Attenuated total reflectance
BJ	Becke-Johnson
BO	Born-Oppenheimer
bpy	Bipyridine
CIF	Crystallographic information file
CM5	Charge model 5
CMD	Classical molecular dynamics
CN	Coordination number
CSVR	Canonical sampling through velocity rescaling
CV	Collective variables
DFT	Density functional theory
DMA	Dimethyl-ammonia ion
DMF	Dimethylformamide
DMSO	Dimethyl sulfoxide
DOF	Degrees of freedom
DOS	Density of states
DRS	Diffuse reflectance spectroscopy
DZP	Double zeta polarized
DZVP	Double zeta valence polarized
EOM	Equations of motion
erfc	Complementary error function
erf	Error function
ES	Electronic structure
FF	force field
FIRE	Fast inertial relaxation engine

FM	Ferromagnetic
FtF	Framework-to-framework
GGA	Generalized-gradient approximation
GPW	Gaussian-plane waves
GTH	Goedecker-Teter-Hutter
GTO	Gaussian-type orbital
GTUB	Gebze-Technische Universität Berlin
HF	Hartree-Fock
HOCO	Highest occupied crystal orbital
HOF	Hydrogen-bonded organic framework
HOMO	Highest occupied molecular orbital
HSE06	Heyd-Scuseria-Ernzerhof 06
IBU	Inorganic building unit
IR	Infrared
IUPAC	International Union of Pure and Applied Chemistry
LCAO	Linear combination of atomic orbitals
LDA	Local density approximation
LJ	Lennard-Jones
LR	Long-range
LUCO	Lowest unoccupied crystal orbital
LUMO	Lowest unoccupied molecular orbital
MD	Molecular dynamics
MO	Molecular orbital
MOF	Metal-organic framework
MOF	Molecular orbitals
MTD	Metadynamics
NAO	Numerical atomic orbital
NDPA	Naphthalenediphosphonic acid
NPT	Constant number of particles, pressure, and temperature
NVE	Constant number of particles, volume, and energy
NVT	Constant number of particles, volume, and temperature

OT	Orbital transformation
PBC	Periodic boundary conditions
PBE	Perdew-Burke-Ernzerhof
PDB	Protein data base
pDOS	Partial density of states
PEM	Proton-exchange membrane
PES	Potential energy surface
PPA	Phenylphosphonic acid
RDF	Radial distribution function
REPEAT	Repeating electrostatic potential extracted atomic
RESP	Restrained electrostatic potential
SBU	Secondary building unit
SCF	Self-consistent field
SQUID	Superconducting quantum interference device
SR	Short-range
STO	Slater-type orbital
TISE	Time-independent Schrodinger equation
TPPA	5,10,15,20-tetrakis [*p*-phenylphosphonic acid] porphyrin
TUB	Technische Universität Berlin
TZP	Triple zeta polarized
UFF	Universal force field
UV-Vis	Ultraviolet - visual spectrum
VMD	Visual molecular dynamics
WtF	Water-to-framework
WtW	Water-to-water
XRD	X-ray diffraction

Chapter 1

INTRODUCTION

1.1 MOTIVATION: ENERGY STORAGE

Energy storage is a key area of research in the material sciences.[1,2,3] Lithium-ion batteries have been the go-to in terms of long-term energy storage,[4,5] however, they have a limited number charge/discharge cycles.[6] This cycle deficiency can be mitigated by augmenting the batteries with supercapacitors, which have high cycling efficiencies and quick charge/discharge cycles, but less charge density than their Li^+ counterparts. A supercapacitor working in conjunction with a Li^+ battery can lead to reduction in the battery-powered load for initialization of a device and ultimately extend the battery's lifetime.[7] Capacitance, C, is defined as

$$C = \varepsilon \frac{SA}{d} \tag{1.1}$$

where d is the distance between the electrode and the electrolyte, ε is the permittivity of the electrolyte, and SA is the surface area of the electrode.[8] Therefore, a porous electrode material with high surface area is desirable for increasing capacitance.[9] Metal-organic frameworks (MOFs) are ideal candidates for these electrodes, as they are highly porous structures and can be electrically conductive.[9]

Another aspect of energy storage we are interested in is the improvement of solid-state electrolytes for hydrogen fuel-cells.[10] These fuel-cells take in H_2 and O_2 to produce energy with heat and water as byproducts, giving a non-carbon alternative to traditional fossil-fuel-based harvesting of energy. A typical hydrogen fuel-cell consists of an anode at which H_2 is split into H^+ and e^-, a cathode which reacts O_2 and H^+, and a proton-conducting electrolyte which separates the anode and cathode.[10] Electrolytes in these cells require high proton conductivity, along with high thermal and chemical stability.[11] Hydrogen-bonded organic frameworks (HOFs) have been proposed as a good candidate for the electrolyte in a fuel-cell,[12] as they can be highly proton conductive[13] and have similar pores to their MOF counterparts, allowing the inclusion of guests molecules which can help increase conductivity.[12,14]

1.2 METAL-ORGANIC FARMEWORKS AND HYDROGEN-BONDED ORGANIC FRAMEWORKS

Metal-organic frameworks (MOFs) are two- or three-dimensional solid-state materials comprised of inorganic building units (IBUs) and secondary building units (SBUs) called organic linkers, held together by covalent/ionic bonding between the SBUs and IBUs **Figure 1.1**.[15,16,17,18] Under a given set of experimental conditions, a particular combination of IBUs and SBUs will undergo self-assembly and form nano-sized porous materials.[19] As described by IUPAC, MOFs are considered a subgroup of coordinated polymers.[20] The first MOF was synthesized by Yaghi, *et al.*, named MOF-5, in which an IBU zinc oxide is connected through carboxylate SBU linkers.[21] This study led to a new field of synthesis known as reticular chemistry, in which Yaghi and other groups have made use of similar carboxylate building blocks to make an extensive library of MOFs for different potential applications.[22,23,24] In particular, the original goal of reticular MOF chemistry was to maximize the surface area of the pores, e.g., MOF-5 has a surface area of 2900 m^2/g and other groups synthesized MOFs with surface areas as high as 10500 m^2/g.[15,25] Such high surface areas are beneficial for various applications and allow for guest-in-pore interactions. One can functionalize a MOF by changing the SBUs to target specific meso-characteristics, allowing for high versatility and structural tunability.[9,15,26,27] In particular, MOFs can be used in many different applications such as gas sequestration,[26,28] gas separation,[29,30] drug delivery,[31,32] electrical conductivity,[9,33] and magnetism,[34,35] etc.

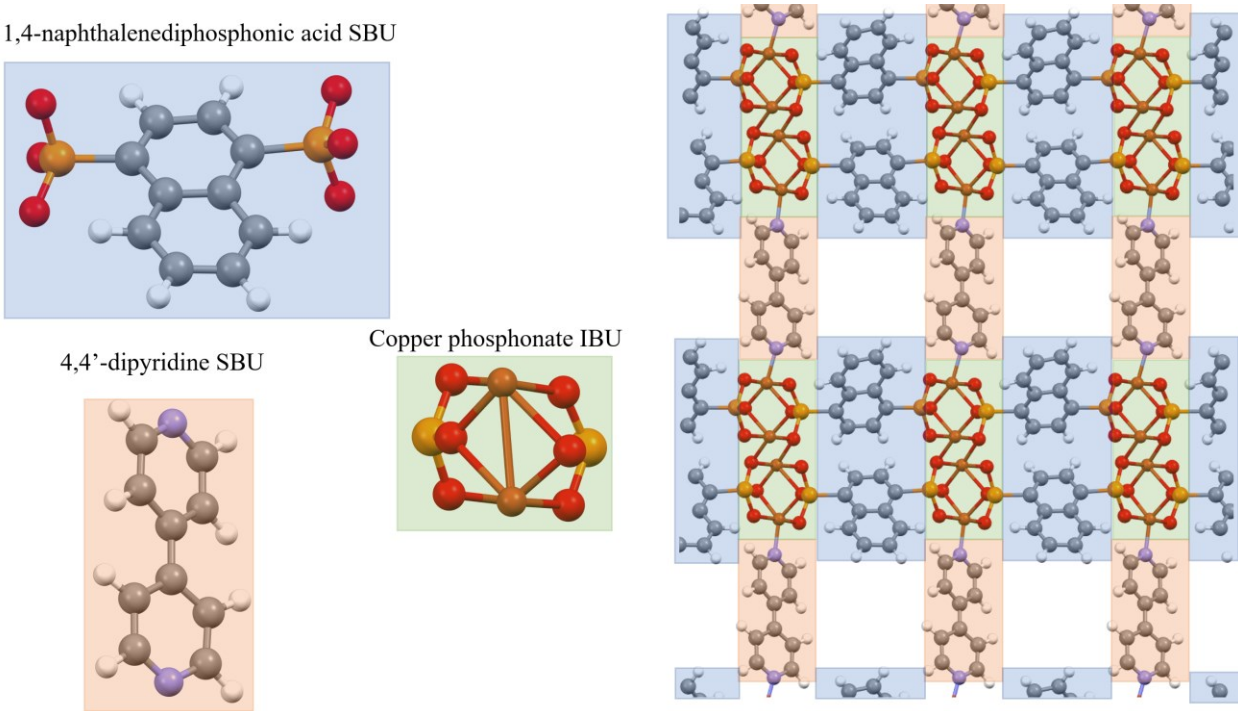

1,4-naphthalenediphosphonic acid SBU

4,4'-dipyridine SBU

Copper phosphonate IBU

Figure 1.1. *Building blocks for the TUB75 copper phosphonate-MOF. The first SBU highlighted in blue on the left forms an interconnected phosphonate network with the copper atoms. The second SBU highlighted in orange on the left donates electrons to the copper atoms. The IBU highlighted in green and shown on the left forms copper-dimer structures. The right is the superstructure of the two SBUs holding the IBU together to create a MOF, where the white space in between linkers indicates the pores. Colour scheme – blue nitrogen, grey – carbon, orange – copper, white – hydrogen, and yellow – phosphorous.*

Hydrogen-bonded organic frameworks (HOFs) are similar to MOFs because they are also framework structures that are held together by linkers.[19] However, in HOFs the linkers are connected by hydrogen bonding, as opposed to by ionic/covalent bonding as in MOFs.[19,36] Also, there is no metal-linking unit holding HOFs together as in MOFs, but HOFs can have metals in their SBUs, just not participating in holding the structure together. There have been early reports of HOF-like materials in the literature,[36,37] but the HOF nomenclature is more recent.[38,39,40] Since hydrogen bonds are relatively weak bonding interactions, reticular chemistry can be more difficult than with MOFs, as covalent, ionic, and pi-bonding interactions now hinder the self-assembly process.[19,41,42] On the other hand, due to the weak bonding interactions, HOFs can be used for an application, then post-processed, recycled, and regenerated for repeated use.[42] While HOFs lack the surface area that is seen in some MOFs, they can still have significantly large pores, allowing for molecule capture and guest interactions as well.[14] Proposed applications of HOF materials include gas capture,[38] semi-conductivity,[43] and proton conductivity.[12,44]

The vast majority of MOFs and HOFs in the literature are composed of carboxylate-based SBU linkers.[18,45] This is due to the availability of carboxylate building blocks for SBUs, with dozens of functionalized structures readily available.[45] Additionally, the ease with which carbon chain lengths can be increased allows for the creation of large pore sizes.[22,25,46] Also, the conjugated benzene-based backbones create rigid building blocks, reducing the risk of pore collapse upon removal of guests in the pores.[47] There is also great versatility in the coordination modes between the O^- groups and the metals.[45,48] However, there are some major issues that plague carboxylate MOFs. Carboxylates are susceptible to hydrolysis, as the negative O^- groups readily react with H_2O, causing instability in highly humid conditions.[46,49] Furthermore, carboxylate MOFs are susceptible to heat and can become unstable under highly basic or acidic conditions.[50,51] Thus, the field of MOF synthesis has been striving for improved stability, and more robust MOF construction.[45]

1.3 PHOSPHONATE-ORGANIC FRAMEWORKS

Phosphonate-based MOFs are constructed of organophosphonic acid SBUs, where the linker is defined by a PO_3H_2 building block.[52,53] While the diversity of organophosphonic acids is less than carboxylates, similar building blocks can be used to synthesize phosphonate MOF materials.[52,53,54] Phosphonates are known for their high structural diversity due to the multiple metal-binding modes; phosphonates can coordinate up to nine metal atoms[52] giving high versatility in the structural composition of their IBUs.[55,56] Moreover, the pyramidal structure formed by the PO_3H_2 group allows for 3D frameworks.[57,58] Phosphonate groups are strongly metal-binding, producing high chemical and thermal stability.[59,60] This stability allows for resistance to corrosion, degradation, and resistance to water-based effects; reducing the likelihood of hydrolysis occurring within the framework.[52,61] The high stability also affords pre- and post-functionalization under harsh experimental conditions. [62] The robust properties of phosphonates in MOFs are why they have attracted the attention of the MOF community and have been proposed for applications in which conditions are more extreme compared to the carboxylate-based MOFs.[53,54] However, there are several issues with phosphonate materials, viz., the high number of coordination modes makes *a priori* synthesis difficult,[52,62] they tend to have low porosity,[63] and metal-phosphonates are poorly crystalline with a high tendency to be amorphous.[52,60,62,64]

Phosphonates are also well-known for their ability to hydrogen bond to other phosphonates.[52,65] This allows for highly inter-connected hydrogen bonding interactions which, in combination with their stability, makes phosphonates ideal starting structures for HOF materials.[44] Furthermore, the phosphonate group is an intrinsic proton carrier (P-OH), which makes it a good candidate for the development of proton-conductive HOF materials.[52] The stability and resistance to hydrolysis makes phosphonate HOFs attractive for use in fuel-cells, as these devices function under high temperature and in highly humid environments.[10] On the other hand, carboxylate-based HOFs are typically unstable and highly susceptible to hydrolysis.[49,66]

1.4 ELECTRICAL AND PROTON CONDUCTIVITIES

In the study of electrically conductive MOFs, most of the focus has been on creating materials using carboxylate SBU linkers; however, this methodology leads to a more ionic interaction between the metal and linkers and low conductivity.[18] Electrical conductivity in MOFs is believed to occur via two mechanisms, namely "through-bond" and "through-space" mechanisms.[18] The through-bond mechanism occurs when there is significant overlap between the ligand and metal frontier orbitals, leading to significant charge delocalization over the bond. This mechanism has been shown to improve by increased covalency in metal-to-linker bonding, as some groups have shown improved conductivity by substituting the oxalate ligands with sulfur or nitrogen-based SBUs.[33,67] The through-space mechanism involves non-covalent charge delocalization, where strong pi-conjugation between two-dimensional sheets increases charge delocalization and in turn the conductivity.[68] The through-space mechanism is mediated by frontier orbitals localized on spatially separated SBUs. Overall, due to the poor orbital overlap of traditional SBUs, and the search for large pores, progress in the design of electrically conductive MOFs has been difficult.

In the area of proton-conductive materials, Nafion®[69] is the most widely used solid-state material, as its proton conductivity[69] is quite high and it has high chemical and mechanical stability.[70,71] For a MOF to be proton-conductive, one must incorporate hydrogen bonding into its structure and increase the mobility of its charge carriers.[72] Intrinsic proton carriers, such as O-H and N-H groups, may be used to mediate the proton transport.[72,73] While MOFs possess a lot of internal space for the charge transport, their pores typically lack the intrinsic proton carriers. On the other hand, HOFs are constructed of proton carriers, and thus are good candidates for use as proton electrolytic materials.[44] As mentioned previously, carboxylate HOFs are typically unstable under ambient conditions, and suffer from the aforementioned hydrolysis issue, while phosphonate HOFs are both stable and resistant to hydrolysis.

Conductivity, σ (S/m), itself can be defined, in simplistic terms, as the concentration of charge carriers and the mobility of said carriers. For electrical conductivity in semiconductors the requirement is that an electron is promoted from the valence band to the conduction band, creating an electron-hole pair. Where the elementary charge unit, e (C), holes, h^+ (number/L), electrons, e^- (number/L), and their respective mobilities, μ_h [cm^2/(V*s)], μ_e [cm^2/(V*s)] **Eqn. 1.2**, are required for a conductivity approximation. Within most theoretical publications the concentrations and mobilities are only alluded to, in referencing exact energies of low highest-occupied orbital to lowest-unoccupied orbital transitions, and the energy differences of the bands along reciprocal space in the band structure. Theoretically obtaining these values, and thus the overall electrical conductivity, requires a more-exhaustive approach: including multiple strain calculations and accurate calculations of either the highest-occupied or the lowest-unoccupied orbitals.[74] For most practical purposes, and this thesis, the concentration of holes and electrons are alluded based on how narrow the gap is between the valence and conduction band, one way to approximated mobility is through energy changes of bands in the band structure of the material, which will be explored in Chapters 3, and 4.

$$\sigma = e(e^-\mu_e + h^+\mu_h) \qquad 1.2$$

where e is the elementary charge unit, $h^+$is the concentration of holes (number/L), e^- is the concentration of electrons (number/L), and μ_h [cm^2/(V*s)] and μ_e [cm^2/(V*s)] are their respective mobilities.[74] For practical purposes in this thesis, the concentrations of the holes and electrons are approximately inversely proportional to the gap between the valence and conduction bands. As for the mobilities, one can approximate them from the energy changes of the bands in the band structure of the material, which will be explored in Chapters 3 and 4.

The proton conductivity is given by the Nernst-Einstein relation, i.e.,[75,76]

$$\sigma_{H^+} = \frac{{F_{araday}}^2}{RT} D_{H^+} C_{H^+} \tag{1.3}$$

where D_{H^+} (m^2/s) is the diffusion coefficient of the protons within the material, C_{H^+} (mol/L) is the concentration of the protons, and F (S*m) is the Faraday constant. D_{H^+} can in principle be calculated from a molecular dynamics simulation and the charge concentration is dependent on the initial conditions of a simulation.

1.5 MOF MAGNETISM

Magnetic MOFs have recently attracted attention due to the possibility of creating tunable magnetic materials by varying the host-guest interactions in the pores or the metals within the IBUs.[77] In order to produce magnetism in a MOF, the material requires closely packed metals with unpaired electrons and repeating units of these metals to yield cooperatively aligned spins.[77] The key to design is incorporating short linkers because, if a linker is too large, long-range cooperativity is not possible.[77] Thus, pore size inhibits magnetic cooperation between metals. In order to address this disparity, linkers such as cyanide or a combination of short and long linkers are used to ensure that the metals are close enough to each other.[78] Furthermore, the magnetism itself is dependent on the metals used in the framework. Varying the metals can produce different magnetic responses, such as ferromagnetism (FM) due to Co[79] and antiferromagnetic responses due to Cu.[80] Magnetic carboxylate-based MOFs have been produced in the past, with one of the most well-known MOFs, M-MOF-74, showing an interesting meso-scale FM response in the Co-substituted version.[79]

Magnetism in MOFs is influenced by the building blocks of the SBU.[81] Particularly, in this thesis, the focus and interest is in pairing magnetism with conductivity, as the vast majority of MOFs are not magnetic and are considered insulating.[82] Phosphonate MOFs are also ideal for creating magnetic MOFs, as they typically have short or medium sized linkers allowing for more metal-metal interactions. Also, since the PO_3 group allows for many metal-binding sites, it allows metals to be closer to one another. In Chapter 3, we discuss two magnetic and electrically conducting phosphonate MOFs.

1.6 THEORETICAL APPROACH TO STUDY STRUCTURED FRAMEWORKS

The work done on the MOFs/HOFs studied in this thesis begins with the experimentally determined x-ray diffraction (XRD) structures. The crystallographic information file (CIF) obtained from XRD is converted and imported to the code of choice and the xyz components of the unit cell and experimental lattice are used as an input structure. The density functional theory (DFT) formalism was used for all electronic structure calculations throughout this thesis; the basics of the DFT formalism are presented in Chapter 2, but for a extensive overview one may refer to Teale *et al*.[83] for a perspective of the current experts in the DFT field. From the xyz coordinates a geometry optimization is performed using DFT, for which the minimum of the atomic positions with respect to energy is obtained within a certain numerical precision. The local minimum structure is compared to the experimental input to ensure the unit cell and heavier atoms have not changed the pristine structure significantly. Hydrogen atoms have low electron density and thus are not easily amenable to XRD refinement,[84] so the obtained CIFs only provide estimates of the hydrogen positions.[85] DFT gives reasonable results for atomic positions, including hydrogens.[86] Thus, geometry optimizations are done as a first step as slight changes in geometries could have profound effects on the solutions to the electronic structure (ES).[87] Following the geometry optimization, a single-point energy calculation is performed to see how the energy gap of the frontier orbitals compares to the experimental UV-vis results. If the DFT results are poor, a single-point calculation at an elevated DFT '*level-of-theory*' that includes Hartree-Fock exchange is performed to improve the results, as this methodology has been used to great success in studying MOFs.[88,89] Once an acceptable gap is obtained, several properties are calculated to obtain further insight into the system, including the frontier orbital gap, magnetic exchange energy, density of states (DOS), band structure, and partial atomic charges; all of which will be discussed in more detail in Chapter 2.

In order to study the dynamics of a system, one needs to accurately describe the forces of each atom as they move in time. This requires a knowledge of the potential energy surface (PES) as a function of all degrees of freedom (DOF) in the system. For a large number of DOF, obtaining an entire PES is computationally inaccessible. To circumvent this issue, one can calculate the forces at each step in a trajectory by making approximations to the solution of the electronic problem. In Chapter 5 of this thesis, we use Born-Oppenheimer molecular dynamics (BOMD)[90,90] to propagate the system in time using forces obtained from DFT calculations of the electronic structure (within the BO approximation) at each time step. However, the computational cost of using DFT limits the length of BOMD simulations to tens of picoseconds at a time, versus the microsecond timescales accessible in classical molecular dynamics (CMD). The dynamical methodologies used in this thesis will be described in more detail in Chapter 2.

The codes of choice for the work in this thesis are ADF-BAND[91] and CP2K.[92] ADF-BAND has the advantage of localized atom-centered basis sets, while CP2K has the advantages of efficient calculations and the ability to perform BOMD and metadynamics (MTD) simulations. The basis sets used by each program will be described in Chapter 2.

1.7 OBJECTIVES AND OUTLINE OF THIS THESIS

The main objectives of this thesis are as follows:

- First and foremost, to elucidate the microscopic origins of various experimentally observed properties of phosphonate-organic frameworks.
- To determine which components of the frameworks are involved in the frontier orbital gaps of the phosphonate-organic frameworks.
- To elucidate the atomic contributions to the magnetic response observed in several phosphonate MOFs.
- To investigate how compositional changes will affect the overall structure and frontier orbital gaps.
- To elucidate the proton conductivity mechanisms in phosphonate HOFs.

An outline of the topics covered in each chapter of this thesis is presented below:

1. In Chapter 2, we introduce the theoretical background for DFT, classical dynamics, BOMD, and metadynamics (MTD). Furthermore, we describe the use of periodic boundary conditions (PBCs) for studying solid state systems and the various basis sets used in our work, and discuss properties such as magnetism, DOS, band structures, and charge analysis.

2. In Chapter 3, we study three phosphonate MOFs, their frontier orbitals, and the atoms that participate in their magnetic responses. We analyze the atomic contributions to the energy gap of each MOF, elucidate which atoms participate in the magnetic response, the charges associated with the phosphonates, and comment on similarities between the three materials.

3. In Chapter 4, we study five porphyrin-based phosphonate HOFs, their frontier orbitals, and structural consequences of metal insertion into the porphyrin cores. We analyze the changes in the energy gaps, overall structure, and partial charges associated with the metallation.

4. In Chapter 5, we study the proton conductivity mechanisms of two HOFs. We simulate the unbiased dynamics of these systems, focusing on hydrogen bonding and proton transport dynamics. We then explore three pathways for proton transport throughout the HOFs, estimate their free energy barriers, and propose three hopping mechanisms based on MTD simulations.

5. In Chapter 6, we present the concluding remarks and future studies.

Chapter 2

THEORETICAL AND COMPUTATIONAL BACKGROUND

2.1 INTRODUCTION

In the study of MOFs and HOFs, research is mainly focused on understanding their structural characteristics and structure-property relationships and developing new materials with useful functions. Computational chemistry has been an extremely valuable tool in this research for providing atomic-level details, which could in turn explain the macroscopic properties of these materials. For example, molecular dynamics (MD) simulations could be used to show how molecules move through the pores of MOFs and HOFs, as well as to calculate bulk properties of these materials. Given the large number of atoms required to model these materials, approximations are needed to make electronic structure and ab initio MD simulations computationally feasible. Here, we present an overview of the fundamental theories and approximations that are used throughout the rest of the thesis.

2.2 DENSITY FUNCTIONAL THEORY

2.2.1 DFT foundations

All the calculations in this thesis rely on the density functional theory (DFT) approach. Ignoring electron spin, DFT simplifies the electronic problem by replacing the *N*-electron wave function of a system with a density that depends only on the three spatial coordinates of Euclidean space. For an electron residing in one dimension, the probability of finding the electron between a distance *r* and r+dr can be represented by the wave function probability $|\Psi(r)|^2 dr$, where the electron density is expressed as $\rho(r) = |\Psi(r)|^2$. For an *N*-electron system residing in three dimensions, one may arrive at the electron density by integrating the wave function of all electrons over all but one of the spatial variables,[93] i.e.,

$$\rho(\overrightarrow{r_1}) = N\int |\Psi(\overrightarrow{r_1},\overrightarrow{r_2},\dots,\overrightarrow{r_N})|^2 d\overrightarrow{r_2}\dots d\overrightarrow{r_N} \tag{2.3}$$

In terms of the electron density, the probability of finding electron *1* at position $\overrightarrow{r_1}$ and within $d\overrightarrow{r_1}$, while the other electrons are situated elsewhere, can be expressed as:

$$P(1) = \left[\int |\Psi(\overrightarrow{r_1},\overrightarrow{r_2},\dots,\overrightarrow{r_N})|^2\, d\vec{r}_2\dots d\vec{r}_N\right] d\vec{r}_1 = \rho(\overrightarrow{r_1})d\vec{r}_1 \tag{2.4}$$

where this can be generalized to any electron (ie. $P(2) = \rho(\overrightarrow{r_2})d\vec{r}_2$), as the electrons are indistinguishable from each other. Therefore, the probability of finding an electron at *r* within *dr* and the other *N*-1 electrons elsewhere is *N*P(1)*, thus one can express the probability density of finding one electron as

$$\rho(\vec{r}) = N\rho(\vec{r}_1) \tag{2.5}$$

When electron spin is taken into consideration, a secondary integral over the spin coordinates of the first electron, *s*, is performed,

$$\rho(\overrightarrow{r_1}) = N\int\dots\int |\Psi(\overrightarrow{r_1},\overrightarrow{r_2},\dots,\overrightarrow{r_N})|^2 ds_1 d\overrightarrow{r_2}\dots d\overrightarrow{r_N} \tag{2.6}$$

Integration of this density over the entire space must equal the total number of electrons in the system, i.e., $N = \int \rho(\vec{r})d\,\vec{r}_1$, and the density at infinity must be zero, i.e., $\rho(\vec{r}\to\infty) = 0$.

To obtain the energy of a system from the density, a mapping between the two is required. Such a mapping was originally proposed by Thomas and Fermi, who realized that the ground-state of a homogeneous electron gas depends on the density, from which one may map to the kinetic energy.[93,94] Hohenberg and Kohn extended the original idea to incorporate inhomogeneous systems, with two theorems that initiated DFT, namely 1) the existence theorem and 2) the second Hohenberg-Kohn theorem, an exact formal variational principle for the ground-state energy.[94] The existence theorem states that the ground state energy of a many-particle system can be described by a functional of the density of that system, i.e.,[94]

$$E_0[\rho_0] = T[\rho_0] + E_{ee}[\rho_0] \; + E_{Ne}[\rho_0] \qquad 2.7$$

where E_0 is the ground state energy of the ground state density ρ_0, E_{Ne} is the electron-nuclear interaction energy, and E_{ee} is the electron-electron interaction energy, and T is the kinetic energy. The ground state energy can be separated into two components: (i) a part that depends on the nuclear positions and is system-dependent due to electron-nuclear interactions, and (ii) a part which is valid for any system, $F_{HK}[\rho_0]$, i.e.,

$$E_0[\rho_0] = \int \rho_0(r) V_{ext} dr + \; F_{HK}[\rho_0] \qquad 2.8$$

where V_{ext} is the external potential for a fixed set of nuclear coordinates (owing to the Born-Oppenheimer approximation), which incorporates the electron-nuclear Coulombic interaction, and F_{HK} is the Hohenberg-Kohn functional. The external potential is a unique functional of the density since the nuclear positions define the positions of the electrons.[94] For an arbitrary density, the Hohenberg-Kohn functional gives the expectation value of the sum of the kinetic energy, $\hat{T}$, and electron-electron repulsion operators, $\hat{V}_{ee}$, over the ground state wave function, Ψ_0[94], i.e.,

$$F_{HK}[\rho_0] = \; T[\rho_0] + E_{ee}[\rho_0] = \; \langle \Psi_0 | \hat{T} + \hat{V}_{ee} | \Psi_0 \rangle \qquad 2.9$$

This functional, if known, contains all the information about electron exchange and correlation.[93,94] That is, the theory behind the Hohenberg-Kohn functional is exact in the case of nearly constant density and slowly varying density.[94] The second component to the Hohenberg-Kohn theorems makes use of the variational principle: if any trial density satisfies the conditions that $\rho(\vec{r}) \; \geq 0$, and $N = \int \rho(\vec{r}) d\vec{r}$, and is linked with an external potential, V_{ext}, the energy produced by **Eqn. 2.8**, will give an upper-bound to the ground state energy, E_0.[93]

In order to approach potential universal functionals that represent the Hohenberg-Kohn functional, Kohn-Sham suggested that direct density functionals, like the Thomas-Fermi methodology, are connected to the kinetic energy.[93,95] They also realized that orbital-based methods, like the Hartree-Fock approximation perform fairly well. Thus, the idea behind Kohn-Sham DFT is to assume that there exists a virtual system of non-interacting electrons that generates the same density as the interacting system, and one can calculate the non-interacting kinetic energy, T_S, by[93]

$$T_S = -\frac{1}{2}\sum_{i}^{N}\langle\varphi_i|\nabla^2|\varphi_i\rangle \tag{2.10}$$

where φ_i a single-electron orbital. This kinetic energy is different from the actual kinetic energy of the interacting system; the difference between them is dealt with by introducing the separation of the electronic portion as follows,

$$F[\rho(\vec{r})] = T_S[\rho(\vec{r})] + J[\rho(\vec{r})] + E_{XC}[\rho(\vec{r})] \tag{2.11}$$

where

$$E_{XC}[\rho] = (T[\rho] - T_S[\rho]) + (E_{ee}[\rho] - J[\rho]) = T_C[\rho] + E_{ncl}[\rho], \tag{2.12}$$

J is the Coulombic integral, E_{XC} is the exchange-correlation energy (which is unknown), T_C is the part of the true kinetic energy that is not incorporated in T_S, and E_{ncl} is the non-classical contribution to the electron-electron interaction. Since the electrons in the virtual system are non-interacting fermions, the equations can be formulated in terms of a single Slater determinant constructed of single-electron orbitals. In this approach, the total energy functional is given by,

$$\begin{aligned} E[\rho] &= T_S[\rho] + J[\rho] + E_{XC}[\rho] + E_{Ne}[\rho] \\ &= T_S[\rho] + \frac{1}{2}\iint \frac{\rho(\vec{r}_1)\rho(\vec{r}_2)}{r_{12}} d\vec{r}_1 d\vec{r}_2 + E_{XC}[\rho] + \int V_{ext}\rho(\vec{r})d\vec{r} \end{aligned} \tag{2.13}$$

As can be seen, E_{XC} accounts for the remaining effects in the system such as the remainder of the kinetic energy and electron correlation. Applying the variational principle using single-electron orbitals, φ_i, with the orthonormal constraint, $\langle\varphi_i|\varphi_j\rangle = \delta_{ij}$, yields the following equation:

$$\left(-\frac{1}{2}\nabla^2 + \left[\int \frac{\rho(\vec{r}_2)}{r_{12}} d\vec{r}_2 + V_{XC}(r_1) - \sum_{A}^{M} \frac{Z_A}{r_{1A}}\right]\right)\varphi_i = \varepsilon_i\varphi_i \tag{2.14}$$

$$V_{XC} \equiv \frac{\delta E_{XC}}{\delta\rho} \tag{2.15}$$

where $\int \rho(\vec{r}_2)/r_{12}$ is the electronic Coulombic energy, V_{XC} (defined as the functional derivative of E_{XC} with respect to the density) is the exchange-correlation potential, A is the nuclear index, M is the total number of nuclei interacting with electron *1*, r_{1A} is the nuclear-electron distance, Z_A is the nuclear charge, φ_i is the one-electron orbital, and ε_i is the energy. If the exact solution to E_{XC}

exists, the resulting energy will be an exact solution, and one will have the exact ground state energy for any system, since the solution is unknown, approximations must be made. For the purposes of this thesis, we will discuss only a few approximations to the exchange-correlation potential, including the local density approximation (LDA), generalized-gradient approximation (GGA), and hybridization with Hartree-Fock (HF) exact exchange, and the addition of dispersion to incorporate long-range dispersion.

2.2.2 Local density approximation

The local density approximation (LDA) is the basis of most approximate exchange-correlation functionals. In the LDA, the energy is calculated by approximating the density as a uniform electron gas sitting on a positive background charge. This methodology resembles that of a perfect metal surface where the nuclei are smeared to obtain a positive uniform charge.[93] The LDA functional has the following form,

$$E_{XC}^{LDA}[\rho] = \int \rho(\vec{r})\varepsilon_{XC}(\rho(\vec{r}))d\vec{r} \tag{2.16}$$

where ε_{XC} is the exchange-correlation energy of a uniform gas of density $\rho(\vec{r})$. The probability, $\rho(\vec{r})$, is a weighting of the energy per particle at a specified point in space, *r*.[93] Furthermore, the exchange energy, E_X, and correlation energy, E_C, contributions can be approximated separately, i.e.,

$$E_{XC}^{LDA}\big(\rho(\vec{r})\big) = E_X^{LDA}\big(\rho(\vec{r})\big) + E_C^{LDA}(\rho(\vec{r})) \tag{2.17}$$

The exchange is taken from the exchange energy of the aforementioned uniform electron gas. One such approximation was formulated by Dirac,[93,96,97]

$$E_X^{LDA}[\rho] = -\frac{3}{4}\sqrt[3]{\frac{3}{\pi}}\int \rho(\vec{r})^{4/3}\,dr \tag{2.18}$$

where the electron correlation is either represented in a functional form or it can be fitted using stochastic quantum Monte-Carlo simulations, for example, of a system of charged bosons and fermions.[98,99,100] The LDA approach can perform well for equilibrium structures, compared to HF; however, it does not capture energies accurately.[93]

2.2.3 Generalized gradient approximation

The LDA approach can be improved by incorporating the change in density, i.e., gradient of the charge density around a local point, into the exchange-correlation term. The LDA approach treats an electron as a specific point in a uniform electron gas, while the incorporation of the gradient tells us how the electron density is changing around that point, thereby introducing the inhomogeneity one would expect from electronic density in a diverse molecule.[93] This is the basis of the GGA. In general, the energies associated with the exchange and correlation can be separated as

$$E_{XC}^{GGA} = E_X^{GGA} + E_C^{GGA} \tag{2.19}$$

In the Perdew-Burke-Ernzerhof (PBE) GGA functional, the correlation term incorporates a uniform electron gas correlation ϵ_C^{unif}, with a simplified version of the correlation expressed as,

$$E_C^{GGA}[\rho_\alpha, \rho_\beta] \approx \int \rho[\epsilon_C^{unif}(\zeta) + H(\zeta, \nabla\zeta)]d^3r \tag{2.20}$$

where ρ_α is the α-spin denisty, ρ_β is the β-spin density, $\zeta = (\rho_\alpha - \rho_\beta)/\rho$ is the relative spin polarization, and *H* is the gradient contribution. The exchange term may be expressed in terms of the LDA exchange ϵ_X^{unif} and density gradient as

$$E_X^{GGA} = \int \epsilon_X^{unif}(\rho)F_X(s)d^3r \tag{2.21}$$

In the above equation,

$$F_X(s) = 1 + \kappa - \frac{\kappa}{1 + \mu s^2/\kappa} \tag{2.22}$$

$$s \approx \frac{|\nabla\rho|}{\rho^{4/3}}$$

where *s* is called an inhomogeneity parameter.[93] When κ = 0.804 and μ = 0.21951, **Eqn. 2.22** yields **Eqn. 2.21**. Finally, putting **Eqn. 2.21**, **Eq. 2.20**, together with **Eqn. 2.19** yields a simplified version of the Perdew-Burke-Ernzerhof (PBE) GGA functional, which is used extensively in this thesis.[101]

2.2.4 Hybridization with HF exchange

While GGAs have been used to great success,[83] the inability to treat long-range interactions reduces their applicability. A proposed solution to this issue is to incorporate HF exact exchange into the DFT functional, which accounts for the exact exchange of two electrons.[102] Such a hybrid approach achieves accurate electron correlation from DFT, as well as more accurate exact exchange from HF. Many hybrid functionals exist, but in this thesis we will only present the Heyd-Scuseria-Ernzerhof (HSE06)[103] hybrid functional, which is the *gold-standard* functional for calculating energy gaps in solid-state materials and is used in the work described in Chapter 3 of this thesis.[88] First, when considering potentials over an infinite solid, the DFT approach is only formulated with a positional density and how that density changes locally. The potential from the density in the central cell converges with respect to the surrounding cells when they reach the 6th nearest neighbouring cell.[103] With HF the exchange is a sum over all electron-electron integrals within the unit cell and surrounding cells, which leads to extremely slow convergence (with no convergence by the 15th nearest neighbouring cell).[103] This slow convergence problem is a well-known issue in solid-state theory when dealing with potentials while invoking periodic boundary conditions, which can be solved by screening the potential. The HSE06 functional makes use of screening, and is a so-called 'range-separated' hybrid functional because a switching parameter, ω, is used to turn off the HF exchange at a distance weighted by the parameter, i.e.,

$$\frac{1}{r} = \frac{\mathrm{erfc}(\omega r)}{r} + \frac{\mathrm{erf}(\omega r)}{r};\ \mathrm{erfc}(\omega r) = 1 - \mathrm{erf}(\omega r) \qquad 2.23$$

where erf is the error function, erfc is the complementary error function, and ω is a parameter set by HSE06 (ω = 0.11 in ADF-BAND), and r is the electron-electron distance. At short ranges (SR), the exchange will have a typical hybrid-DFT contribution, while at long ranges (LR) the non-convergent exact HF exchange is smoothed out and the convergent PBE exchange becomes dominant. Since the GGA density is local, the energy at LR drops off and the overall energy will be convergent. This is a typical approach used when incorporating exact exchange into periodic hybrid-DFT. The HSE06 functional takes the form,

$$E_{xc}^{\omega PBE0}(\omega r) = aE_x^{HF,SR}(\omega r) + (1-a)E_x^{PBE,SR}(\omega r) + E_x^{PBE,LR}(\omega r) + E_c^{PBE}(r) \qquad 2.24$$

where a is the percentage of HF exchange, ω is the switching parameter, $E_x^{HF,SR}$ is the exact HF exchange at SR, $E_x^{PBE,SR}$ is the PBE exchange at SR, $E_x^{PBE,LR}$ is the PBE exchange at LR, and E_c^{PBE} is the PBE correlation energy over all distances. When $\omega = 0$, the result is equal to the PBE0 hybrid functional,[104] and when $\omega = \infty$, the result is equal to the pure PBE GGA.

2.2.5 Dispersion corrections

DFT based on semi-local density functionals has benefits, particularly when dealing with periodic boundary conditions. However, again, it leaves out important long-range interactions as the *1/r* behavior of the electrons is not fully captured. One such interaction is the dipole-induced dipole interaction, which can be described as a dispersion effect.[105] Dispersion effects are of particular importance when there are non-bonded interactions, such as in hydrogen bonding or between guest molecules in the pores of frameworks. The DFT error can be improved by including an analytical parameterized function to correct for the missing dispersion through modification of the energy,[106]

$$E_{DFT-D3} = E_{DFT} - E_{disp} \tag{2.25}$$

where E_{DFT-D3} is the overall energy, E_{DFT} is the energy from DFT, and E_{disp} is the energetic correction from dispersion. The design of the methodology excludes the need for the wave function altogether, considering only nuclear positions and atomic numbers and exploiting parameterized dipole-dipole pair interactions between elements. In this thesis, we employ the D3BJ dispersion correction, with the D3 dispersion energy given by the following equations,[106]

$$E_{disp} = E^{(2)} + E^{(3)} \tag{2.26}$$

$$E^{(2)} = \sum_{AB} \frac{C_6^{AB}}{r_{AB}^6} f_6(r_{AB}) \tag{2.27}$$

$$E^{(3)} = \sum_{ABC} f_6(\overline{r}_{ABC}) E_{ABC} \tag{2.28}$$

$$E_{ABC} = \frac{C_9^{ABC} 3 \cos\theta_a \cos\theta_b \cos\theta_c + 1}{(r_{AB} r_{BC} r_{CA})^3} \tag{2.29}$$

$$f_6(r_{AB}) = \frac{1}{1+6\left(\frac{r_{AB}}{s_{r,6}R_0^{AB}}\right)^{-\alpha}} \tag{2.30}$$

Where $E^{(2)}$ is the dispersion energy due to a two-body interaction, $E^{(3)}$ is the dispersion due to a three-body interaction, r_{AB}^6 is a two particle (A-B) distance to the power of 6, $\overline{r}$ is the average of all distances between three bodies (ABC), θ_a is the angle between vector $\overrightarrow{AB}$ and $\overrightarrow{AC}$, θ_b is the angle between vectors $\overrightarrow{BA}$ and $\overrightarrow{BC}$, θ_C is the angle between vectors $\overrightarrow{CA}$ and $\overrightarrow{CB}$, R_0^{AB} is a pair cut-off radius parameter between atoms A and B, $s_{r,6}$ is a screening parameter based on the functional of choice ($s_{r,6}$ = 1.217 for PBE), α = 12/16 for $E^{(2)}/E^{(3)}$, C_6^{AB} is a pair-wise dispersion coefficient parameterized for atom pairs (i.e., C-C), and C_9^{ABC} is a parameterized dispersion coefficient for three-bodies (i.e., C-C-H).[106] The Becke-Johnson (BJ) damping[107] is a damping function that corrects for the over-compensation of energies by D3 at short ranges; this is done by adding a constant to the r in the denominator of 2.31 and adding an 8th order term, i.e.,

$$\begin{gathered} E_{disp}^{D3(BJ)} = \sum_{A\neq B}\left(s_6\frac{C_6^{AB}}{r_{AB}^6+[f(R_{AB}^0)]^6} + s_8\frac{C_8^{AB}}{r_{AB}^8+[f(R_{AB}^0)]^8}\right) \\ f(R_0^{AB}) = a_1R_{AB}^0 + a_2 \\ R_{AB}^0 = \sqrt{\frac{C_8^{AB}}{C_6^{AB}}} \end{gathered} \tag{2.31}$$

where for the PBE functional a_1 = 0.4289, a_2 = 4.4407, s_8 = 0.7875. The effect is that the dispersion diminishes similarly to the non-damped version at extended distances, while at short ranges the energy is damped by the $[f(R_{AB}^0)]^6$ increase to the $1/r^6$ term from dispersion.

All in all, DFT is particularly good at obtaining better geometries than HF, and the calculations require less computational time as DFT scales as N^3, where N is number of basis functions and the 3 arises from the three spatial coordinates. However, DFT has some general shortcomings in yielding accurate energies for systems, as the energy calculated by any one functional is dependent upon that functional. Thus, in switching between any two functionals the calculations could give different energetic results.[108] A typical approach to improve the DFT energy issue is to utilize the accurate geometries calculated by DFT, then escalate the level-of-theory for single point calculations using the resulting geometry. In non-periodic works one makes use of post-HF methods,[109,110] while within this thesis, this is done through GGA optimizations followed by hybrid-DFT analysis.

2.3 MOLECULAR DYNAMICS

2.3.1 Basics

Simulating the dynamics of a molecular system under a given set of external conditions allows one to calculate observables that can be used to study and understand experimental results. Within the Born-Oppenheimer (BO) approximation, the motion of the nuclei in a system can often be well-described using classical mechanics or Newton's equations of motion (EOM), i.e.,

$$F(R) = ma(R) = m\ddot{R} = -\frac{\partial E(R)}{\partial R} = m\frac{d^2R}{dt^2} \qquad 2.32$$

where F is the force, R is the nuclear position, m is the mass of the nucleus, t is time, $\ddot{R}$ is the second derivative with respect to time, and $E(R)$ is the BO potential energy surface (PES).[111] Thus, to simulate the dynamics of a system of N nuclei, one requires an accurate description of its 3N-dimensional PES, $E(R)$. There are several common ways of obtaining a PES. For small systems ($N < \sim 10$ atoms), it is possible to thoroughly sample the PES and solve the electronic TISE to obtain the potential energy at each sampling point; however, when N is large, this strategy is not computationally feasible. One of the most popular approaches is to construct an empirical model of the PES or force field (FF) prior to performing the MD simulation. This approach requires parameterized descriptions of two types of atom-atom interactions: (i) bonded interactions such as bond stretching, bond bending, bond torsions, and (ii) non-bonded interactions such as dispersion (described through a Lennard-Jones potential) and electrostatic interactions (described through a Coulombic potential). The FF approach requires input either from experiment, or high-level quantum calculations for an accurate description. Some examples are the SPC[112] FF for water and the GROMOS[113] FF for a general set of organic molecules. When using such FFs, however, chemical reactions cannot be modeled and their transferability is limited (since FFs are parameterized for specific atom-atom interactions). The third approach is to calculate the potential 'on-the-fly' at each time step of the MD simulation (for example, using DFT), which is known generally as ab initio molecular dynamics (AIMD).[114,115,116] The results presented in Chapter 5 of this thesis were generated using an AIMD method known as Born-Oppenheimer MD (BOMD), which will be described in the following subsection.

After deciding on an approach for tackling the PES, the EOM, **Eqn. 2.35**, must be integrated subject to an appropriate set of initial conditions, i.e., atomic positions and velocities. The initial positions could be obtained from a model, experiment, or energy minimization of pre-determined configuration, while the velocities could be obtained by running an initial equilibration simulation (starting with velocities randomly sampled from a Boltzmann distribution at temperature *T*) in the appropriate statistical mechanical ensemble, e.g., an ensemble that is consistent with the conditions under which an experiment is carried out.[111] Two popular integration algorithms are the velocity-Verlet[117] and leapfrog[118] algorithms. The main difference between them is that Verlet-type algorithms calculate positions, velocities, and forces at each timestep, requiring the information to be stored in memory, while the leapfrog approach staggers the updating of the positions and velocities at different times, essentially "leapfrogging" from a position at t=1 to t=3, and a velocity at t=2 to t=4. Ideally, integrators should be time-reversible, numerically stable, and fast.

As mentioned above, the MD simulations should be carried out in an appropriate statistical mechanical ensemble. Some popular ensembles include the microcanonical (or NVE), canonical (or NVT), and isobaric isothermal (or NPT) ensembles. The NVE ensemble is composed of trajectories in which the number of particles, volume, and energy of the system remain constant, and is used when calculating dynamical properties of the system. The NVT ensemble is composed of trajectories in which the number of particles, volume, and temperature of the system remain constant, and is used when equilibrating a system or calculating equilibrium properties of a system under constant temperature conditions. The NPT ensemble is composed of trajectories in which the number of particles, pressure, and temperature of the system remain constant, and is used when equilibrating a system or calculating equilibrium properties of a system under constant temperature and pressure conditions.

To perform the NVT simulations in Chapter 5, a thermostat was used, which effectively couples the system to a thermal reservoir at a desired temperature. A thermostat modifies the atomic velocities over the course of a trajectory in such a way that generates a canonical distribution of velocities at the desired temperature. For our simulations, the canonical sampling through velocity rescaling (CSVR) thermostat was used, which is similar to the Berendsen thermostat (mimicking weak coupling to a heat bath).[119] However, CSVR adds noise (sampled from a Gaussian distribution) to the thermostat to rescale the velocities in such a way that samples the canonical ensemble.[120]

2.3.2 Born-Oppenheimer molecular dynamics

Most FFs used in classical MD simulations do not account for electronic polarization or chemical reactivity.[121] Accounting for these effects can be achieved by solving the electronic problem for the potential at a fixed nuclear geometry, R, and integrating the following EOM to propagate the system to the next time step,[114]

$$m\ddot{R} = -\nabla \min_{\Psi_0}[\langle\Psi|H_e|\Psi\rangle] \tag{2.33}$$

where ∇ is the gradient with respect to nuclear position, Ψ is the wave function, H_e is the electronic Hamiltonian under the BO approximation, m is the mass of the nucleus, $\ddot{R}$ is the second time derivative of nuclear position, and $\min_{\Psi_0}$ represents a minimization of the energy with respect to the ground state wave function. Because solving the electronic problem on-the-fly is computationally demanding, one is limited to much smaller systems and shorter timescales than those achievable with FF-based classical MD. The self-consistency of the electronic calculation must be satisfied at every time-step, so any error that propagates through the iterative self-consistent field (SCF) calculation will affect the dynamics of the system. Therefore, a stricter numerical criterion is required for the iterative process, further increasing the computational demand. CP2K-Quickstep[92] has addressed this issue by making use of a predictor-corrector approach known as the always stable predictor-corrector (ASPC) method.[122] The ASPC method uses previous solutions to the wave function to predict new approximations, and corrects them with a damping procedure.[122] The EOM are solved using integrators that are commonly used in FF-based classical MD. In this thesis, BOMD is used in Chapter 5, with the on-the-fly solution of the electronic problem performed at the DFT-D3(BJ) level. In this approach DFT is utilized as a replacement of the wavefunction in **Eqn. 2.33**. As a result, the potential comes from the energy associated with the combination of DFT and dispersion, **Eqn. 2.25**, and **Eqn. 2.19**, and ultimately **Eqn. 2.16**. Here, DFT-based BOMD seeks the density which produces the lowest energy at every step via. the variational principle, **Eqn. 2.17**.

2.3.3 Metadynamics

To explore the high energy regions of a PES and sample rare events, one could in principle run very long simulations and, if need be, run the simulations at elevated temperatures and/or pressures. However, this approach raises two problems: how long must these simulations be run to adequately explore the phase space, and how does an increase in temperature and/or pressure affect the other variables of the system? To circumvent these problems, several methods which introduce biases along certain degrees of freedom have been proposed. Of particular relevance to the work in Chapter 5 of this thesis is the metadynamics (MTD) technique.[123] In MTD, a history-dependent biasing potential, which depends on carefully selected collective variables (CVs), is added to the natural potential of the system to accelerate the dynamics of the system along the CVs.[124] These biasing potentials take the form of Gaussian functions added along a particular CV,[125] i.e.,

$$V(S(x),t) = \sum_{\substack{t'=\tau_G,2\tau_G \\ t'< t}} \omega\ exp\left(-\frac{\left(S(x) - s(t')\right)^2}{2\delta s^2}\right) \qquad 2.34$$

where x is the coordinates, $s(t')$ is the CV value at time t', $S(x)$ the bias potential as a function of the coordinate, ω is the height of the Gaussian, δs is the width of the Gaussian, and τ_G is the frequency at which the potential is applied.[123] Some examples of CVs are torsion angles, atomic distances, atomic angles, gyration radius, etc. In Chapter 5 of this thesis, we use the coordination number (CN) CV to monitor the coordination around oxygen atoms. Adding energy along a given CV will push the system along that direction and eventually the system will have enough energy to overcome the local barrier and explore the region of interest. In fact, the energy that is added to reach the barrier top provides an estimate of the free energy along the CV.[126,75] Well-tempered MTD is an extension that adds a temperature-dependent biasing potential, where the Gaussian height, ω, decreases over time, and thus the magnitude of the applied bias also reduces,[125] i.e.,

$$\omega = \omega(t') = \omega_0 exp\left(-\frac{V(s(t'),t')}{k_B \Delta T}\right) \qquad 2.35$$

$$\gamma = \frac{T + \Delta T}{T}$$

where k_B is the Botlzmann constant, V is the potential from the previous applied Gaussian, s is the CV, ω_0 is the initial Gaussian height, and ΔT is a user-inputted 'bias factor', which is a ratio between the CV's temperature and the system temperature T. An advantage of the well-tempered approach is that the trajectory is allowed to explore the phase-space more thoroughly, as a lot of energy is initially put in but then tempered over time, allowing the CVs to relax to minimums. Well-tempered MTD was implemented using the PLUMED[127] plugin for CP2K in Chapter 5 of this thesis.

2.4 PERIODIC BOUNDARY CONDITIONS

Simulation of periodic structures requires one of two approaches, either the crystal structure is truncated and studied as a large molecule in a vacuum, or periodic boundary conditions (PBCs) are invoked.[128] The molecular approach requires cutting out a portion of the repeating crystal structure and then capping the edges of the system.[89] There are many advantages to treating the system as a molecule, as the methods available in molecular computational chemistry codes are vast, allowing ease of calculation of various properties, e.g., transition states,[129] spectroscopic quantities,[130] etc. However, the main advantage to molecular calculations is the availability of exact exchange, where the exact exchange integrals leads to extremely slow convergence in reciprocal space and requires approximations.[131] The disadvantage comes when attempting to accurately describe the electronic structure of a periodic system, which possess '*band-like*' energy levels that can only be reproduced through continuous overlap of adjacent orbitals. Moreover, the truncation produces edge effects due to the inclusion of new atoms that are not physically present in the actual structure and the neglect of long-range interactions. In this thesis, PBCs are applied to all electronic structure and dynamics calculations performed, allowing for a more complete understanding of the full repeating structure while sacrificing exact exchange.

In order to implement PBCs, one must write the Schrödinger equation in a repeating way, which can be achieved by re-expressing the wave function according to Bloch's formalism,[132]

$$\psi(R + L) = e^{-i\vec{k}L}\psi(R) \qquad 2.36$$

where R is a position in the incident cell, L is a position in an adjacent cell, and $e^{-i\vec{k}L}$ is a phase factor with wave vector k. Bloch's theorem states that the wave function can be represented as a traveling wave solution, where in k-space (or momentum space) the wave function repeats with a phase-factor based on the symmetry of the lattice. By expressing the wave function in this way, all edge effects disappear from the solutions, and since the solutions at a position R+L are equivalent to the solutions at R, the adjacent cell will be treated as a mirror of the incident cell. The energy of a system in reciprocal space may be evaluated at individual k-points, using a specific number of points in each of the k-space directions.[133] The more dense the k-grid is populated the better description of the space.[128] Since the invocation of PBCs requires the transformation from the real lattice to a reciprocal lattice, the density of the k-grid is inversely proportional to the size of real unit cell. If the unit cell has a large volume, then the first Brillouin zone will be small (the first Brillouin zone describes the primitive cell in reciprocal space). The inverse relation allows for the use of less k-points when dealing with MOF/HOF systems, as these systems often have large pores and large unit cell volumes. The origin of the first Brillouin zone is denoted by Γ, and thus in k-space the origin is called the Γ-point; therefore, when a single point is used for populating the k-grid, the calculation is referred to as a Γ-point calculation. The consequence of using a single Γ-point is that the molecular orbitals are projected onto the first Brillouin zone, yielding less information about surrounding cells; to more accurately model cell-to-cell interactions, more k-points should be used.[89] In this thesis, the k-space grids used for the ADF-BAND calculations are all done with varying numbers of k-points, while the CP2K-based calculations all make use of a Γ-point description.

2.5 BASIS SETS

In this thesis, we make use of two types of basis sets. For the ADF-BAND[134] calculations, the basis sets are composed of numerical atomic orbitals (NAOs) to describe the core electrons and Slater-type orbitals (STOs)[135] to allow for versatility in describing the valence electrons. For the

CP2K calculations, the basis sets are composed of Gaussian-type orbitals (GTOs)[136] combined with plane waves for a Gaussian plane wave (GPW) hybrid approach.[137] While STOs give accurate energies and are the 'natural' solutions to a hydrogen-like atom, there are no analytical solutions to integration of two-electron STO integrals, and when used to describe orbitals they require numerical solutions.[98,135] Thus, solutions of the TISE using a STO basis are computationally expensive, but they produce more accurate energies than other approaches. The computational cost associated with using STOs is the reason why Gaussian basis sets were introduced[136]; integration of Gaussians functions is analytically solvable, leading to quick solutions.[136] The approach does come with the caveat that Gaussians do not have the cusp that is expected at the nucleus, and fall off too quickly at long ranges, giving a worse description of atomic orbitals and energies. The inaccuracies at the nuclei and long-distances can be improved by introducing additional Gaussians, allowing the shape of the radial portion of the orbitals to closely resemble that of the hydrogen atom-like solutions. Furthermore, the Fourier transform of a Gaussian is another Gaussian, which makes it convenient to use these orbitals in the PBC formalism.

When invoking PBCs it is common to use plane waves because they are not atom-centered, but rather span all periodic space. That being said, plane waves will occupy any void spaces in a system and, as a result, have energy associated with these spaces, a particular difficulty when trying to model MOFs and HOFs.[128] Plane wave basis sets also require the use of pseudopotentials to map out regions close to nuclei; due to the rapidly varying nature of the orbitals in this region, an enormous number of plane waves are required to describe it.[114,138] To get a chemical sense of what plane waves physically mean with respect to atomic orbitals, a projection of the plane waves unto localized basis sets is required. Along these lines, Lippert *et al.*[137] devised the Gaussian and plane waves (GPW) method, which incorporates GTOs in real space and a combination of GTOs and an auxiliary plane wave basis in reciprocal space.

In general, improving the energies of a system requires the addition of more basis functions. Expanding the basis set can be done by adding more STOs or GTOs (which gives rise to the double-ζ and triple-ζ nomenclature). There can also be further improvement through the addition of higher-order angular momentum functions known as polarization functions.[139] Also, adding diffuse functions accounts for longer distances and non-neutral charges accurately.[140] With regards to plane waves, increasing the cut-off in reciprocal space will add more plane waves.[114] In practice, the addition of more basis functions comes with an increased computational cost, where HF scales as N^4 and DFT scales as N^3, where N is the number of basis functions used.

2.6 PROPERTIES OF INTEREST

The last section of this Chapter discusses the properties that are calculated for the MOFs and HOFs studied in this thesis.

2.6.1 Magnetism

Magnetism depends on the alignment of spins of unpaired electrons in a system, i.e., when unpaired electrons from different atoms are in proximity their spins can align and create a magnetic ordering.[77] Unpaired electrons on atoms can either be spin up (α) or spin down (β). When invoking PBCs one repeats the spins on atoms in a unit cell across all adjacent cells. Thus, one can approximate mesoscale magnetism by considering the microscale unpaired electron configurations. Magnetism in MOFs originates from closely layered metal nodes with unpaired electrons which are aligned in a column/row, where the unpaired spin on each metal in the column/row is the same.[77] This ordering gives rise to several potential configurations, where each has a mesoscale consequence on the magnetism of the material. An antiferromagnetic (AFM) configuration occurs if two different columns/rows of metal atoms are aligned but have opposite spins, while if two different columns/rows of metal atoms are aligned but have the same spins, it is called a ferromagnetic (FM) configuration (see **Figure 2.1**).[34]

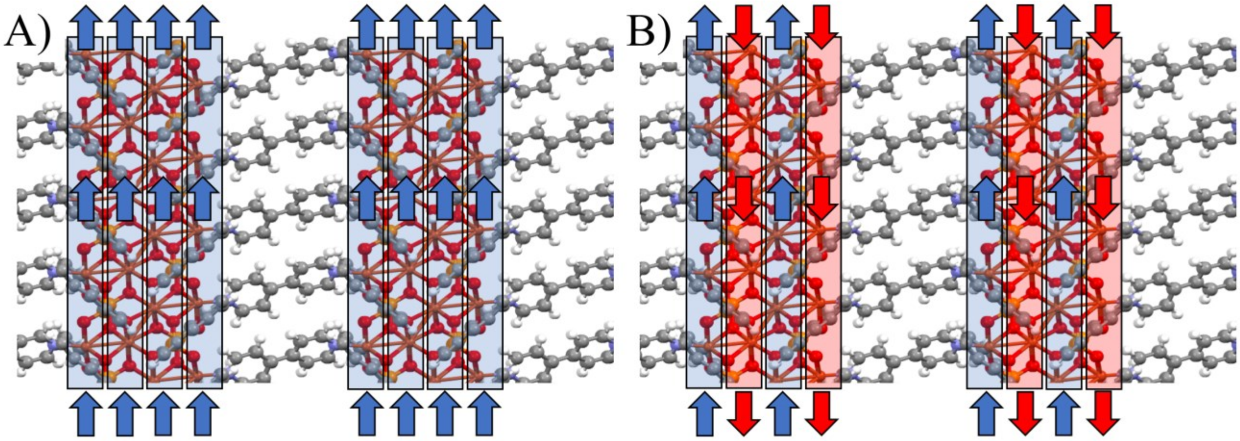

Figure 2.1. *Highlights of magnetic domains in TUB75.*[58] *A) FM configuration, in which all unpaired spins are in the same direction. B) AFM configuration, in which the spin domains are staggard between up and down. Colour scheme: blue - β-spin, red - α-spin. Atomic scheme: grey – carbon, white – hydrogen, yellow – phosphorous, red – oxygen, brown – copper.*

The magnetic exchange energy is defined as[34]

$$E_{ex} = E_{AFM} - E_{FM} \qquad 2.41$$

where E_{AFM} is the energy of the AFM configuration and E_{FM} is the energy of the FM configuration. To calculate E_{ex} for a MOF, the structure is first optimized with all unpaired electrons in a parallel configuration.[128] For example, if there are six Cu^{2+} atoms, each with an unpaired α-electron, the calculation would be done with a multiplicity of 7,

$$Multiplicity = 2S + 1 \qquad 2.37$$

where S is the total spin of the system (e.g., 1 unpaired electron $S = ½$ and multiplicity = 1; 6 unpaired electrons of the same spin, $S = 6/2$ and multiplicity = 7). Afterwards, further optimizations are performed with one column/row of aligned metals having the unpaired electrons in the spin-up configuration (α) and a parallel column of metals in the spin-down configuration (β). Lastly, a single-point energy calculation at either the GGA and/or hybrid level of theory is done, and the total energies of the two systems are used to calculate the magnetic exchange energy. If the magnetic exchange energy is negative/positive, the AFM/FM alignment is the ground-state configuration. To gain further insight into which atoms contribute to the magnetic character of the system, one may plot spin-density iso-surfaces, which show the difference between the α-spin and β-spin densities.[34] Spin-density plots highlight the parts of the system that contribute to the magnetism and confirm that the spins are localized on the metals.

2.6.2 Density of states

Density of states (DOS) is the number of states at a given energy per unit volume, i.e., the number of allowed electron/hole states per unit energy per unit volume. Of particular interest, the DOS gives insight into the highest occupied molecular orbital (HOMO) and lowest unoccupied molecular orbital (LUMO), which are involved in the excitation of an electron to create an electron-hole pair. While the HOMO-LUMO nomenclature is commonly used in reference to the frontier orbitals in solid-state systems, we have moved away from this nomenclature as these systems are periodic in nature and not molecules. Rather, we use the highest occupied crystal orbital (HOCO) and lowest unoccupied crystal orbital (LUCO) nomenclature.[141,142] As will be seen in Chapters 3 and 4, bands do not describe the energy level structure in MOFs/HOFs particularly well. Where many closely packed atoms over long distances will create continuous bands of energy levels, if atoms are separated by large voids as in MOFs, the band thins out resulting in "spaced-out" levels. Therefore, the terms valence band, conduction band, and band gap are not well-suited for describing MOFs. Rather, we refer to the energy gap between the HOCO and LUCO simply as the HOCO-LUCO gap.

From the projected density of states (pDOS), one can determine which atoms are contributing to the HOCO and LUCO, and which orbitals from these atoms have the largest contributions to them.[34] Knowledge of the atomic orbitals which contribute to the HOCO/LUCO can be used to propose a conduction mechanism, viz., the orbitals on atoms in the HOCO/LUCO describe the location of the holes/excited electron. Based on the structures of the HOCO and LUCO, one may infer a through-bond or through-space electrical conduction mechanism.[18]

2.6.3 Band structure

The band structure refers to the plot of orbital energy vs. wavevector *k* and can give insight into where in reciprocal space the largest contributions to the HOCO and LUCO are in the crystal lattice, which in turn gives us information about these contributions in direct space. Furthermore, larger changes in energy along a particular path in momentum space correlate with higher electron mobility in moving from one point in *k*-space to another, described as electron dispersion. The electron dispersion can also be used to describe the directionality of the electron/hole movement in *k*-space.[18,33] In band structure calculations, the energy is calculated along the first Brillouin zone *k*-space vectors.[143] For example, if a lattice has an orthogonal unit cell, going from the (0,0,0) point to the (1,0,0) point in *k*-space space will correspond to the x-axis in real space. The energy may be calculated along many different vectors in reciprocal space; if sufficiently explored or smart choices are made for the vectors, the paths will yield a great deal of information about the HOCO-LUCO gap and the electron dispersion within the unit cell.[33,82] Identification of the nature of the gap, i.e., direct vs. indirect, in this thesis is done in two ways, viz., from dispersions in the band structure and Tauc plotting of the UV-vis spectrum. If the highest occupied band energy is located at one point in reciprocal space and the lowest unoccupied band energy at another, the transition requires the energy difference plus movement of the electron in *k*-space and is called an indirect gap. If the highest occupied and lowest unoccupied band energy both occur at the same *k*-point in reciprocal space, the transition involves a direct gap and excitation requires the exact energy difference between the bands.

2.6.4 Partial atomic charges

The many-body electronic wave function, which describes the probability density associated with finding electrons, may be used to calculate charges on atoms. By defining local regions around each atom, one could use the electronic populations of electrons from the wave function to calculate the partial atomic charges from the difference between the number of electrons in a given region and the nuclear charge of the atom.[98] These charges are a purely theoretical construct, which cannot be directly probed experimentally;[98] in general, the only experimental validation of charge models comes from measurements of dipole moments. The disparity between experimental and calculated values has resulted in the development of different charge models based on different spatial partitioning of the electrons. In modeling the charges of atoms in our systems, we use the following rule, viz., if all the charge models agree in sign, then the negative or positive charges are describing the atoms qualitatively accurately. For the localized NAO/STO basis sets in ADF-BAND, the charge models that are used are Mulliken,[144] Hirshfeld,[145] Voronoi,[146] and Charge Model 5 (CM5) charges.[147,148] Mulliken partitions the population based on the density of the orbital and the overlap of orbitals with surrounding atoms. Hirshfeld is an integral over space of the initial atomic density of an atom multiplied by the optimized density from the SCF procedure and divides it by the total sum of the initial atomic densities of all the individual atoms. Voronoi is based on atomic partitions of each atom and a deformation density, and CM5 uses Hirshfeld charges corrected by empirically determined values for the periodic table. On the other hand, for the non-localized basis sets used by the GPW approach in CP2K, Mulliken and Hirshfeld charges are typically unrealistic. The poor description provided by localized charge models is a well-known issue and was solved through the development of RESP-REPEAT charges.[149,150] In RESP-REPEAT, the potential is calculated and then fitted (restrained) to the electrostatic potential, where the fitting is done by least-squares absolute difference between the two. The repeating electrostatic potential atomic charges further correct this in the periodic case by fitting to the variance of the potentials, as opposed to the absolute difference.[92]

Chapter 3

Phosphonate Metal-Organic Frameworks Insights from DFT[R1]

3.1 INTRODUCTION

Metal organic frameworks (MOFs) emerged as a new family of microporous materials at the beginning of the 21st century.[15,17,151,152,153] They are composed of inorganic building units (IBUs) and organic linkers, which combine to create microporous frameworks.[15,17,154,155] Owing to the vast range of organic linker geometries and functional groups, and the option of post-synthetic modification of pore surfaces,[156,157,158] many diverse applications of MOF chemistry have emerged, including small molecule storage,[159] greenhouse gas sequestration,[160] drug delivery,[161,31] and detoxifying agents[162]; and the presence of IBUs has led to applications in heterogeneous catalysis,[163,164] magnetism,[165,77,166,35] and conductivity.[35,167] Among these applications, magnetic MOFs have recently attracted a great deal of attention due to the possibility of creating tunable magnetic materials by varying the host-guest interactions at pore sites or exploiting structural changes induced by MOF breathing; and conductive MOFs are expected to serve as next-generation porous electrode materials with higher and customizable surface areas compared to active carbon electrodes.[35,167,9]

[R1] This chapter contains research copied and/or adapted from 3 separate publications: **1)** Siemensmeyer, K.; Peeples, C. A.; Tholen, P.; Schmitt, F. J.; Çoşut, B.; Hanna, G.; Yücesan, G. Phosphonate Metal–Organic Frameworks: A Novel Family of Semiconductors. *Adv. Mater.* **2020**, *32* (24), 2000474. **2)** Peeples, C. A.; Kober, D.; Schmitt, F. J.; Tholen, P.; Siemensmeyer, K.; Halldorson, Q.; Çoşut, B.; Gurlo, A.; Yazaydin, A. O.; Hanna, G.; Yücesan, G. A 3D Cu-Naphthalene-Phosphonate Metal–Organic Framework with Ultra-High Electrical Conductivity. *Adv. Funct. Mater.* **2021**, *31* (3), 2007294. **3)** Peeples, C. A.; Çetinkaya, A.; Tholen, P.; Schmitt, F. J.; Zorlu, Y.; Bin Yu, K.; Yazaydin, O.; Beckmann, J.; Hanna, G.; Yücesan, G. Coordination-Induced Band Gap Reduction in a Metal–Organic Framework. *Chem. - A Eur. J.* **2022**, *28* (8), e202104041. The supporting information for this chapter can be found in Appendix A: Figures A1-A7 and Tables A1 & A2.

Traditional MOFs have primarily relied on molecular IBUs known widely as paddle wheel patterns.[15,151,17] To synthesize magnetic MOFs based on molecular IBUs, the IBUs must be close enough to each other to generate the desired magnetic interactions. The design patterns for such magnetic MOFs have been summarized in two recent review articles.[165,77] Typically, shorter linkers such as CN or azolate linkers make magnetic interactions possible between the inorganic components.[168,169] Also, linkers that can generate free radicals may be used to create magnetically significant MOFs.[170,171] However, because MOF chemistry has evolved towards the use of longer organic linkers for larger surface areas, the distances between the molecular IBUs has increased and thereby diminished the possibility of constructing magnetic MOFs with molecular IBUs.[172] Thus, new architectural strategies for synthesizing magnetic MOFs are in need. Along these lines, one-dimensional (1D) and two-dimensional (2D) IBUs can provide a more suitable platform for magnetic interactions as the metal centres may come into close proximity to each other in such geometries.[173,174,175] MOFs, which are synthesized at high temperatures and under hydrothermal reaction conditions, usually form 1D chain IBUs.[64,176,53] In contrast, conventional MOFs, which are synthesized at low temperatures in the presence of organic solvents,[15,151,17,152,153,154] usually form molecular IBUs. One-dimensional magnetic chains are well known,[173] but relatively few porous magnetic MOFs with 1D IBUs have been reported in the literature.[165,77,169,175,177]

The construction of conductive MOFs requires more subtle design elements. For example, highly conjugated linkers such as phthalocyanine or porphyrins with ortho-diimine, ortho-dihydroxy, and azolate metal-binding units connected via molecular IBUs composed of a single metal ion, are known to give rise to conductivity.[35,167,9] However, due to the limited number of metal-binding modes for the single nitrogen and oxygen donating linkers and the highly conservative nature of metal binding in these systems, progress in the design of conductive MOFs has been limited. Alternative metal binding units capable of yielding both rich structural diversity and conductivity are needed for constructing next-generation conductive MOFs.[53,178]

To this end, presented herein is the study of two magnetic low band gap MOF's, namely TUB75[58] and TUB40,[80] and a low band gap MOF with unpaired spin configurations, TUB1.[57]

3.2 METHODOLOGICAL APPROACH

All three MOFs were investigated in a similar fashion, what follows is a general procedure applied to each MOF, followed by the specifics of the individual calculations.

3.2.1 General Density Functional Theory Approach for Phosphonate MOFs

The DFT calculations were performed with the Amsterdam Density Functional BAND package.[179,180] Since these MOFs are bulk materials, periodic boundary conditions have been applied to all three MOFs, making use of Bloch's theorem to approximate the infinite material.[132] All wave functions were expanded using atomic Slater-type orbital (STO) basis sets, which are all-electron basis sets and are more similar to "real" atomic orbitals than plane-wave basis sets (avoiding the use of pseudo-potentials and effective core potentials). Atomic geometry optimizations of the experimental crystal structures were performed using static experimental lattice vectors. The optimizations were done using spin-polarized, unrestricted Kohn-Sham[181,182] DFT (as each Cu^{2+} has an unpaired electron in all MOFs studied here) at the PBE[101]-D3-BJ-damping[106,107] level of theory. This is followed up by single-point calculations performed on each of the optimized structures using the range-separated hybrid HSE06[103,183,184,185] functional to obtain the band gap, exchange energy, spin densities, partial charges, band structure, and projected density of states (pDOS).

3.2.2 DFT methodology for TUB75

All the DFT calculations on TUB75 were performed with the ADF2018 package.[179,134] Periodic boundary conditions were applied to a 1x3x1 supercell with cell lattice parameters of a=17.907 Å, b=13.931 Å, c=10.086 Å, α=90.0°, β=90.4°, γ=90.0°, containing six copper dimers and the associated organic linkers (see **Figure 3.1**). The optimization was done using PBE-D3-BJ and the fast inertial relaxation engine (FIRE)[186] algorithm with a triple-ζ polarized (TZP) STO basis set for the copper(II) atoms and a double-ζ polarized (DZP) STO basis set for the main group atoms, Γ-point sampling, and good numerical quality. Single-point calculations were then performed on the optimized structure using the range-separated hybrid HSE06[103,183,184,185] functional with basic numerical quality.

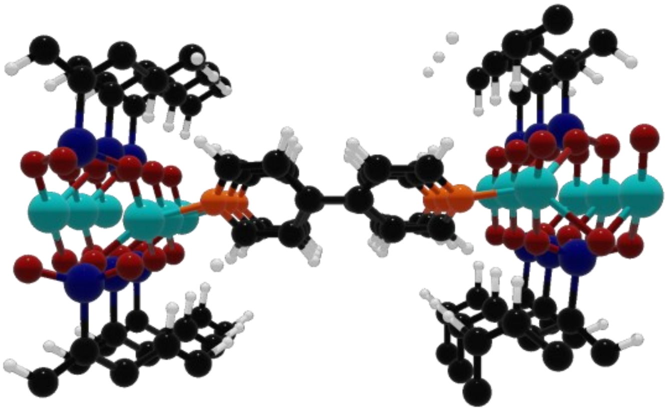

Figure 3.1. *Top-down view of optimized AFM structure of the 1x3x1 supercell obtained at the PBE-D3-BJ level of theory.*

The energy of the ferromagnetic (FM) configuration was calculated by enforcing all 12 unpaired electrons on the 12 copper atoms to have α-spins, and the energy of the antiferromagnetic (AFM) configuration was calculated by enforcing 6 α-spins and 6 β-spins.

3.2.3 DFT methodology for TUB40

All the DFT calculations on TUB40 were performed with the ADF2019.301 package.[179,180] Periodic boundary conditions were applied to a 1x1x1 unit cell (a=11.656 Å, b=7.575 Å, c=7.549 Å, α=90.0°, β=103.1°, γ=90.0°). The geometry optimization of the TUB40 crystal structure was performed using the quasi-Newton method[187] with a triple-ζ polarized (TZP) basis set with no frozen cores for the copper(II) atoms, and a double-ζ polarized (DZP) basis set with no frozen cores for the remaining atoms. This was done with the PBE-D3-BJ[101,106,107] functional and good numerical quality (sampling 24 symmetry unique k-points in the Brillouin zone). The HSE06[103,183,184,185] calculations were perfromed with TZP for the coppers and DZP for the remaining atoms, good numerical quality (sampling 24 symmetry unique k-points in the Brillouin zone), and unrestricted DFT. The optimizations and subsequent calculations, as described above, were done for both the ferromagnetic (FM) and antiferromagnetic (AFM) configurations, where all unpaired electrons on the coppers are all spin-up for FM and alternate for AFM.

3.2.4 DFT methodology for TUB1

All of the DFT calculations on TUB1 were performed using ADF2019.301.[179,180] Periodic boundary conditions were applied to the 1x1x1 unit cell (a=23.966 Å, b=25.394 Å, c=26.281 Å, α=118.4°, β=106.2°, γ=97.0°), which contains three copper(II) atoms and their organic building units.

Geometry optimizations were performed using the Quasi-Newton algorithm.[187] This was accomplished at the PBE-D3-BJ[101,106,107] level of theory, with Γ-point sampling in k-space. The first optimization was done using a triple-ζ polarized (TZP) STO basis set for the copper atoms and a double-ζ polarized (DZP) STO basis set for all the main group elements, with an enforced spin polarization of three alpha electrons. The optimized structure was then used as the input for a second optimization with all the atoms' orbitals described by a triple-ζ polarized (TZP) STO basis set with good numerical quality, 14 k-points with default ADF-BAND spacing, and an enforced spin polarization of three alpha electrons. After this optimization, a HSE06[103,183,184,185] single-point calculation was performed with different numerical qualities, and from here it was determined that the square planar copper(II) atom has an excess beta electron, while the other two trigonal bipyramidal copper(II) atoms each have an excess alpha electron. This motivated us to carry out a third geometry optimization at the PBE-D3-BJ TZP level of theory with an enforced spin polarization of one alpha electron (to allow the two trigonal bipyramidal copper(II) atoms to each have an excess alpha electron and the square planar copper(II) atom to have an excess beta electron). This calculation was done with good numerical quality and a k-space sampling of 14 k-points (**Table A1**). The resulting structure produced electronic Mulliken populations[144] (**Table A2**), which revealed that the square planar copper atom conforms to the +1-oxidation state. To gain confidence that this was not an artifact of the PBE functional, we also optimized the structure with the BLYP[188,189]-D3-BJ-damping exchange-correlation functional and found the same oxidation state.

From the calculations, the oxidation state of the square planar copper atom is unclear. Therefore, four geometry optimizations with the following enforced spin polarizations were performed using PBE-D3-BJ TZP to identify the lowest energy structure (**Table 3.1**):

1. Three alpha electrons with all three copper atoms being Copper(II) (3-α)
2. Two alpha electrons and one beta electron with all three copper atoms being Copper(II) (2-α, 1-β)

3. No excess alpha or beta electrons on the square planar copper atom, and one excess alpha electron and one excess beta electron for the two trigonal bipyramidal Copper(II) atoms (1-α, 1-β)
4. No excess alpha or beta electrons on the square planar copper atom, and two excess alpha electrons for the two trigonal bipyramidal Copper(II) atoms (2-α)

The resulting structures were then analyzed with the HSE06 hybrid functional (**Table 3.1**) using the same initial spin polarizations. From these calculations it was determined that an enforced spin polarization of three alpha electrons led to the lowest-energy configuration (for both PBE and HSE06) by 5.44 meV and 32.65 meV for PBE and HSE06, respectively (**Table 3.1**). Given these results, in section 3.3.3, we performed our analysis based on the PBE-D3-BJ TZP geometry optimization (with good numerical quality, 14 k-points, and 3-α electron spin polarization) and the single-point HSE06 calculation (with normal numerical quality, Γ-point sampling, and 3-α electron spin polarization).

Table 3.1. *Results from various single-point calculations using HSE06 functional. The HOCO-LUCO energy gaps are all reported in eV, while the total bonding energy is reported in atomic units.*

Enforced spin polarization	**α HOCO-LUCO gap**	**β HOCO-LUCO gap**	**Total bonding energy**
(3-α)	2.62	0.48	-874.760
(2-α, 1-β)	2.63	0.10	-874.754
(1-α, 1-β)[a]	0.36	0.36	-874.758
(2-α)[a]	2.28	0.36	-874.759

[a] *The α and β HOCOs each have an electronic occupation of 0.5.*

Based on the results in **Table A2**, it is difficult to unambiguously determine the oxidation state of the square planar copper atom. Thus, one must analyze the orbital populations through the scope of the underlying chemistry. Copper(II) has an electronic configuration of [Ar]$3d^9 4s^0$, which means that there should be more population of one spin than the other. However, for all the PBE-D3-BJ- and BLYP-D3-BJ- optimized structures, the Mulliken populations reveal that the square planar copper atom conforms to the +1 state, [Ar]$3d^{10} 4s^0$, as there is a negligible excess population of one spin over the other (**Table A2**). On the other hand, all of the HSE06 calculations show that the square planar copper atom conforms to the +2 oxidation state (having excess beta spin population) and the two trigonal bipyramidal copper atoms conform to the +2 oxidation state (having excess alpha or beta spin, depending on the initial enforced spin configuration). It is known that GGAs (e.g., PBE, BLYP) tend to favor low-spin configurations, while hybrid functionals (e.g., HSE06) tend to favor high-spin configurations.[190] [Here, low-spin refers to roughly equal alpha and beta spin populations, while high-spin refers to unequal alpha and beta spin populations.] To have a more definitive answer on which is the correct square planar copper oxidation state, one would have to use post-Hartree-Fock methods.[190] That being said, based on its structure, the square planar copper atom should be Copper(II) (as tetrahedrally coordinated copper atoms usually have a +1 oxidation state). Therefore, in the main text, we present the results from the HSE06 (3-α) calculations, as the corresponding structure has the lowest energy and the expected electronic configuration.

3.3 RESULTS AND DISCUSSION

3.3.1 Phosphonate Metal-Organic Frameworks a Novel Family of Semiconductors: TUB75

Phosphonate MOFs are known for their high structural diversity due to the multiple metal-binding modes and protonation states of the phosphonic acid group.[191] They are known to contain complex molecular clusters and 1D/2D IBUs.[174,176,53,177,178] Recently, Yücesan *et al.* synthesized the phosphonate MOF TUB75 (where TUB stands for Technische Universität Berlin) at temperatures above 180°C and under hydrothermal reaction conditions.[192] The crystal structure revealed that this MOF contains 1D copper dimer chains linked by polyaromatic 1,4-naphthalenediphosphonic acid (1,4-NDPA) and 4,4'-bipyridines (4,4'-bpy) linkers (see **Figure 3.2**). This chain structure is unique compared to that of previously reported 1D IBUs in the literature with respect to the presence of three different (and relatively short) characteristic Cu-Cu distances along the 1D IBU (see **Figure 3.2B**).[174,176,53,177,178] As seen in **Figure 3.2B**, TUB75 is composed of zigzag copper dimer chains (one of which is portrayed in **Figure 3.2B**; the experimental and calculated Cu–Cu distances are given in **Figure 3.3** and **Table 3.2**). MOFs in this family have a general tendency to be thermally stable up to ~375 °C, after which thermal decomposition begins. In our previous work with 2,6-naphthalendiphosphonic acid, we found that removing the 4,4'-bipyridines to obtain pure metal phosphonates increases the thermal stability to ~400 °C.[191]

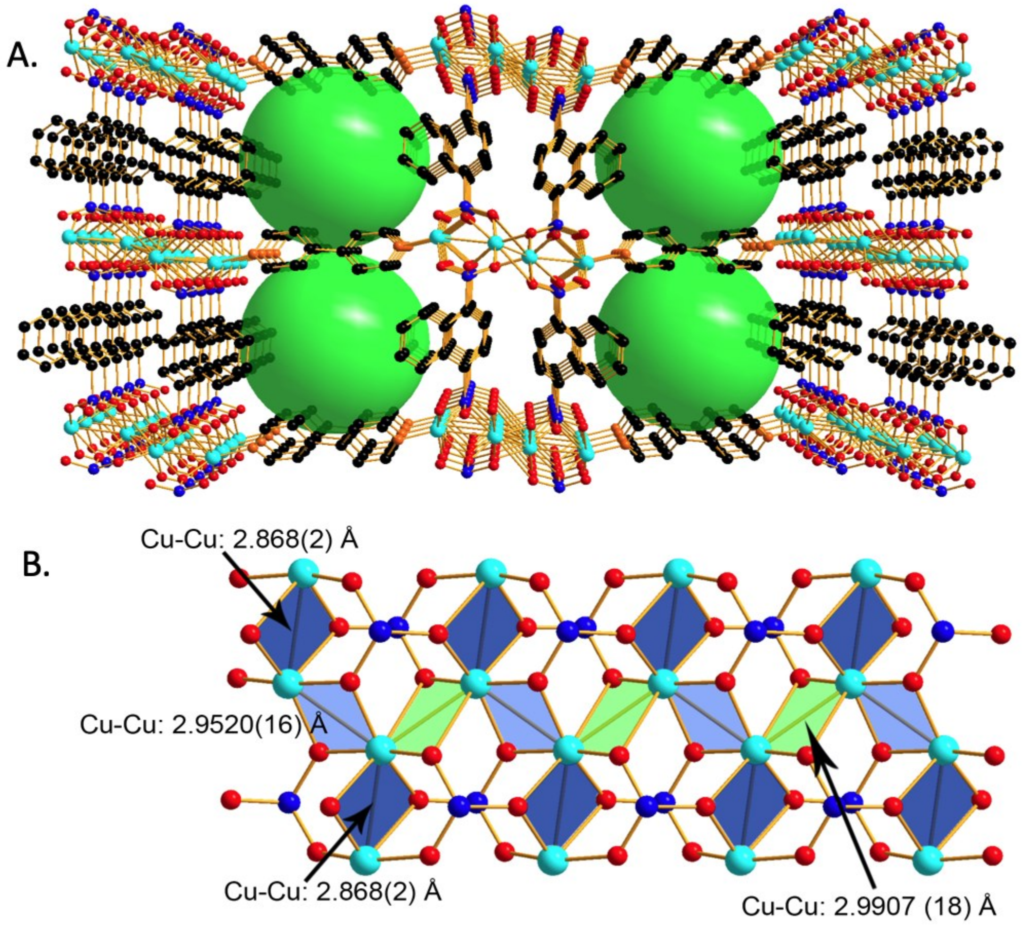

Figure 3.2. ***A)*** *One layer of the* $[\{Cu_2(4,4'\text{-bpy})_{0.5}\}(1,4\text{-NDPA})]$ *(TUB-75) MOF, showing nine 1D copper dimer IBUs and four void channels (which extend into and out of plane).* ***B)*** *Side view of the 1D IBU consisting of a zigzag chain of corner-sharing copper dimers, with Cu-Cu distances of less than 3 Å. Dimers are colored based on their Cu-Cu bond distances. Color definitions: (O – red; N – orange; Cu – cyan; C – black; P – blue).*

In light of the above, in this study, we revisit our phosphonate MOF TUB75 to explore its conductive and magnetic properties. As we will discuss below, we find that TUB75 has an indirect band gap of 1.4 eV (based on a Tauc plot of the UV-Vis spectrum), making it a semiconductor. In addition, we find that TUB75 possesses an antiferromagnetic chain-type IBU. Our density functional theory (DFT) calculations of TUB75's band gap, band structure (**Figure A2**), partial density of states, and relative energies of the ferromagnetic (FM) and antiferromagnetic (AFM) configurations, provide detailed insight into its electronic structure. The experimental and calculated Cu-Cu distances are given in **Figure 3.3** and **Table 3.2**, respectively, and agree reasonably well.

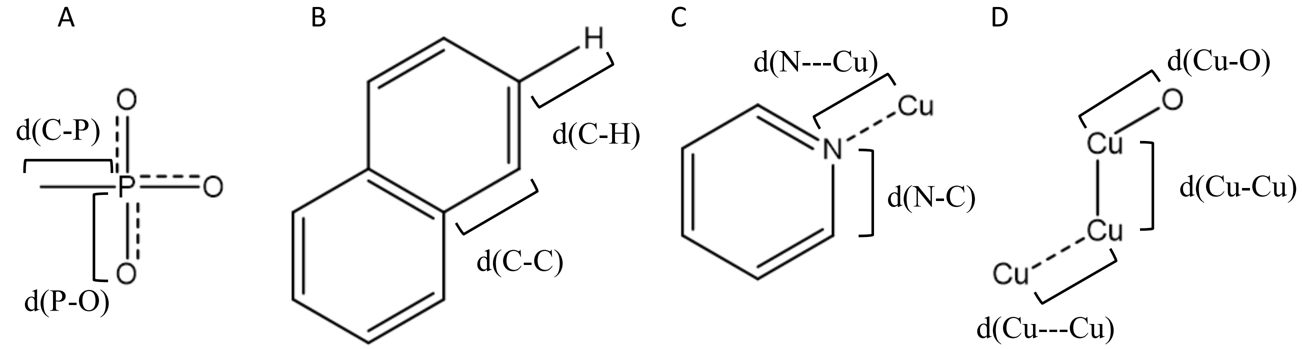

Figure 3.3. *Schematic depicting key inter-atomic separations (distances given in Table S1) in* ***A)*** *phosphonic acid group,* ***B)*** *naphthalene group,* ***C)*** *bipyridine group, and* ***D)*** *copper chain.*

Table 3.2. *Comparison of experimental and calculated average inter-atomic distances (in Å) in TUB75. Standard deviations in distances are given in brackets. The calculated structure was obtained from a geometry optimization of the experimental crystal structure at the PBE-D3-BJ TZP/DZP level of theory.*

Atom Pair	Experimental	Calculated
	Figure 3.2A	
C-P	1.81 (0.001)	1.83 (0.006)
P-O	1.53 (0.01)	1.56 (0.013)
	Figure 3.2B	
C-C	1.40 (0.051)	1.41 (0.024)
C-H	0.93 (0.001)	1.09 (0.007)
	Figure 3.2C	
Cu-N	2.02 (0.001)	2.03 (0.007)
N-C	1.33 (0.027)	1.35 (0.001)
	Figure 3.2D	

Cu-O	2.06 (0.148)	1.97 (0.03)
Cu-Cu	2.74 (0.000)	2.78 (0.002)
Cu --- Cu	2.97 (0.020)	2.84 (0.108)

In **Figure 3.5–B**, we present a Tauc plot derived from the UV-Vis spectrum (shown in **Appendix Figure A1**) of a sample of pure handpicked (under a microscope) crystals – thin green needles with an average length of 0.5 mm. An optical band gap of 1.4 eV, typical of a semiconductor, was determined by linear extrapolation of an indirect Tauc plot[193,194] yields an estimate of the optical bandgap of 1.4 eV, indicative of a semiconductor. To shed light on the origin of the semiconductivity, we performed DFT calculations. The density of states calculation yielded a HOCO-LUCO gap of $E_g = 1.77$ eV, which is in good agreement with the experimental band gap of 1.4 eV. Based on the projected density of states (pDOS) in **Figure 3.4**, we see that the HOCO-LUCO gap is predominantly due to atomic orbitals associated with the carbon atoms in the π-conjugated 1,4-naphthalenediphosphonic acid (1,4-NDPA) and 4,4'-bipyridine (4,4'-bpy) auxiliary linker groups. It also appears that there is some contribution from the nitrogen orbitals to the LUCO and a very small contribution from the oxygen orbitals to the HOCO. As for copper, there is effectively no contribution from the copper orbitals to the HOCO and LUCO. There is indication of spin dependence in the higher energy virtual orbitals, primarily associated with the copper atoms and smaller contributions coming from carbon, nitrogen, phosphorous, and oxygen. We further projected the carbon pDOS into the individual contributions from the 1,4-NDPA and the 4,4'-bpy carbons (**Figure 3.5**). This projection reveals that the HOCO and LUCO are spatially separated, with the HOCO localized on the 1,4-NDPA carbons and the LUCO localized on the 4,4'-bpy carbons. In such a case, a photo-excited electron (in the LUCO) would be spatially separated from its hole (in the HOCO).

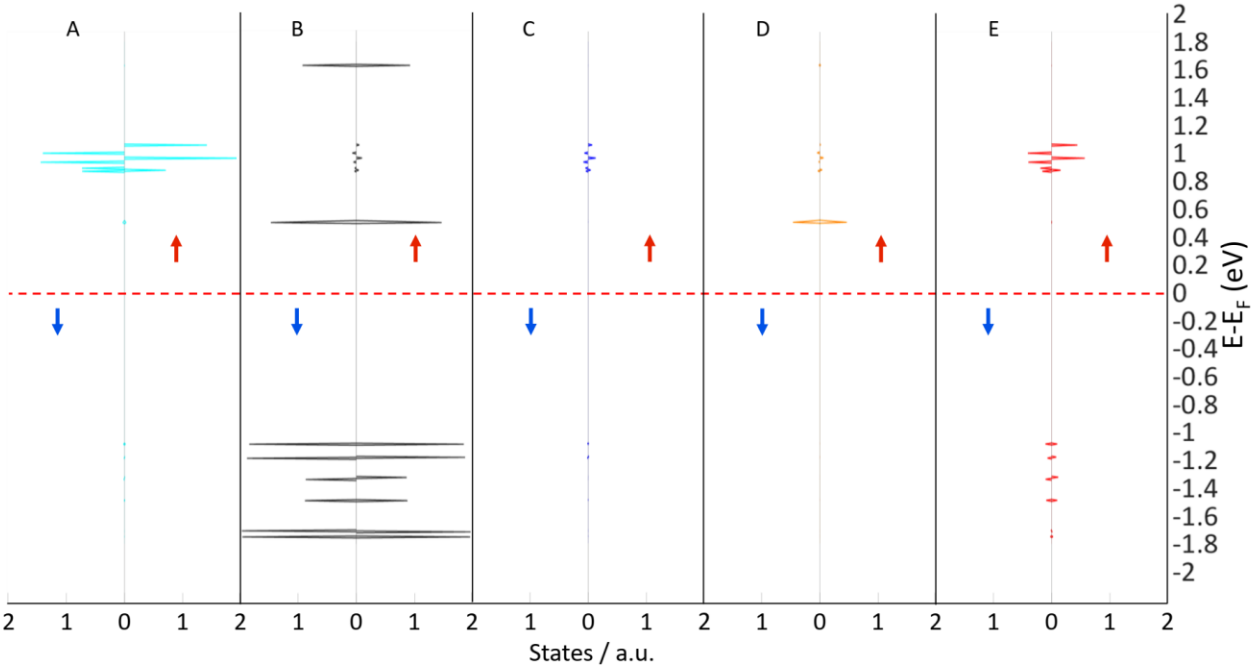

Figure 3.4. *Spin-up and spin-down projected density of states for TUB75 in the AFM configuration. (A) Copper, (B) Carbon, (C) Phosphorous, (D) Nitrogen, (E) Oxygen.*

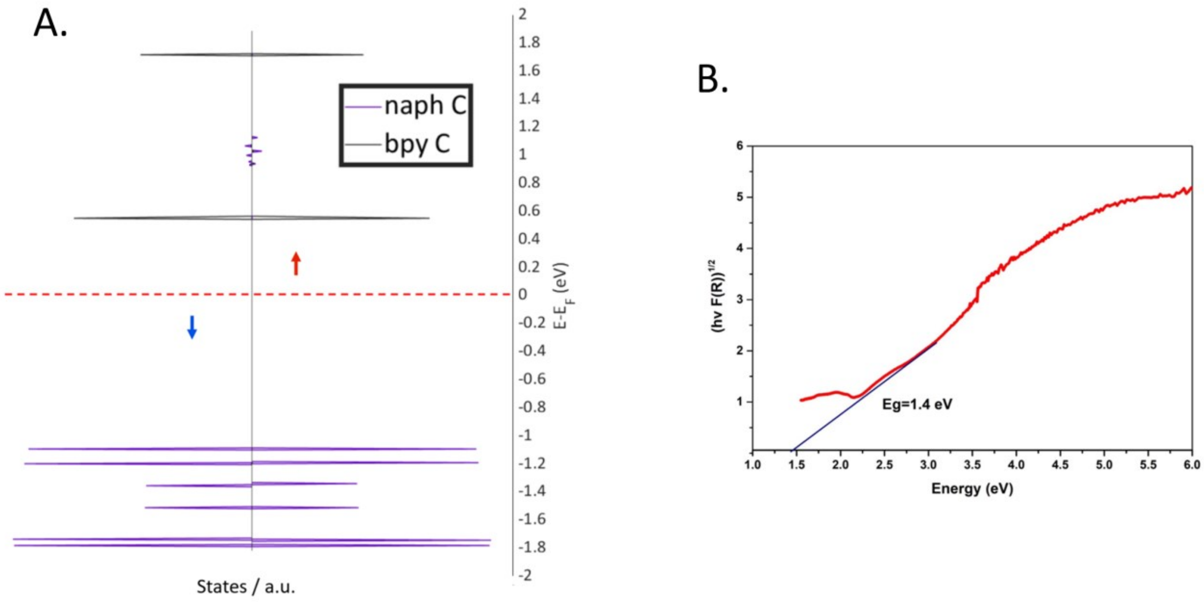

Figure 3.5. *A) Spin-up and spin-down projected density of states of the 1,4-NDPA and 4,4'-bpy carbons for TUB75 in the AFM configuration. B) Indirect Tauc plot of TUB75 indicating a typical semiconductor pattern, which reveals a band gap, E_g, of 1.4 eV (See* ***Figure A1*** *for UV-Vis spectrum).*

Electrical conductivity measurements on MOFs have been mainly based on polycrystalline pellets. However, such measurements may greatly underestimate the conductance of the MOF due to contact/grain boundary resistances and anisotropic electrical conduction. On the other hand, single-crystal measurements can provide much more accurate conductance values, provided that the crystals are large enough. In light of this, we carried out a number of single-crystal measurements on TUB75 by clamping the individual crystals between two gold surfaces of a relay. From room-temperature measurements, we obtained a range of resistances from 10 Ω to 10 MΩ, depending on the orientation of the crystal with respect to the gold surfaces. Assuming that the TUB75 crystal makes perfect contact with the gold surfaces, these resistances yield a maximum conductance of $\approx 10^3$ S m^{-1} and a minimum conductance of $\approx 10^{-3}$ S m^{-1} (see Supporting Information for the details of the calculations). However, since the TUB75 crystals do not make perfect contacts with the gold surfaces, the actual conductances could even be higher than our reported values. Nevertheless, our results show that TUB75 is a semiconductor and provide strong evidence of the directional nature of the electrical conductivity of TUB75. We are currently working on growing larger crystals to maximize the contact surface area in order to better understand TUB75's directional conductivity.

Next, we report the results of our magnetization measurements on TUB75 in **Figure 3.6–A** (see Appendix A, section A.1, for the details of the measurements). The magnetization data exhibits a Néel temperature of $T \cong 30$ K (i.e., the temperature corresponding to the maximum magnetization) that increases with increasing field strength, a behavior that is characteristic of a material with AFM correlations (see **Figure 3.7** for a depiction of the AFM correlations of spins in the geometry-optimized structure). This is corroborated by our DFT-calculated exchange energy (i.e., the energy difference between the AFM and FM configurations) of $E_{ex} = E_{AFM} - E_{FM} = -37.3$ meV, indicating that the AFM configuration is more stable than the FM one. Moreover, the position of the maximum does not vary with temperature, which is characteristic of the presence of short-range order in the 1D spin chains and is consistent with the zigzag chains observed in the crystal structure (**Figure 3.2–B**). At 2 K, we observe a non-zero magnetization that increases with increasing field strength and appears to plateau at higher fields; for the lower field strengths, the magnetization initially decreases and then increases with increasing temperature (up to 10 K), while for the higher field strengths the magnetization simply increases with increasing temperature (up to 10 K). The upturn of the magnetization below 10 K (known as a Curie tail) observed for the lower field strengths is suggestive of the presence of a small amount of paramagnetic impurity, e.g., Cu ions that are not embedded in the TUB75 crystal structure.[64] At high temperatures, the magnetization decreases to zero with increasing temperature, as expected (see **Figure 3.6–A**).

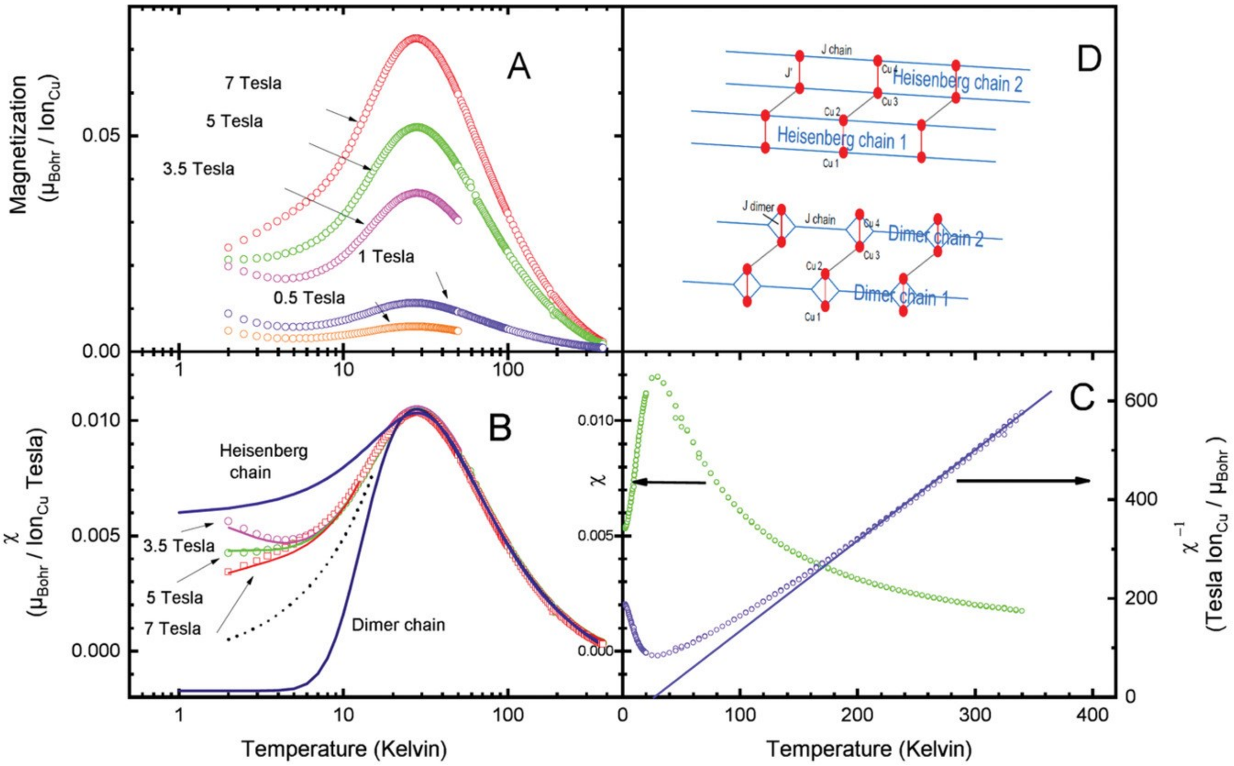

Figure 3.6. *Magnetic response data for TUB75. (A) Magnetization vs. temperature data for TUB75 in different applied magnetic fields. (B) Magnetic susceptibility, χ, (coloured circles) obtained from the magnetization data along with fits (solid blue lines) to the Heisenberg chain and dimer chain models. The upturn in the low-temperature signal (< 10 K), which is suggestive of the presence of paramagnetic impurities, is fit by Brillouin functions (solid coloured lines) with a baseline signal (dotted black line). (C) Magnetic susceptibility (green circles) obtained in a 5 T*

magnetic field, corrected for the diamagnetic background, and the inverse susceptibility (blue circles) on which a Curie-Weiss high-temperature linear fit is shown (solid blue line). (D) Schematic pictures of Heisenberg chains and dimer chains, the models used to fit the magnetic susceptibility data. See Appendix A for details.

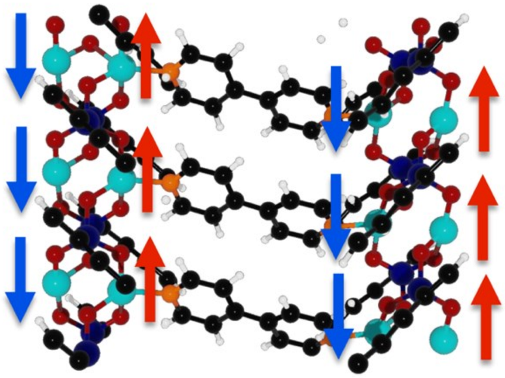

Figure 3.7. *Minimum energy structure of the 1x3x1 supercell depicting the antiferromagnetic configuration of the electrons on each copper (α-spin: red, β-spin: blue). (O – red; N – orange; Cu – cyan; C – black; P – blue; H – white).*

Given the underlying 1D chain geometry, we fit our high-temperature (> 30 K) magnetic susceptibility data (**Figure 3.6–B**) to Heisenberg chain and dimer chain models (depicted in **Figure 3.6–D**). As shown in **Figure 3.6–B**, close fits to the data were obtained with coupling constants of J_{chain} = 16.8 K and J' = -22 K for the Heisenberg chain model,[195,196] and coupling constants of J_{dimer} = 54 K and J_{chain} = -2.6 K for the dimer chain model.[197,198,199] The signs and magnitudes of the coupling constants reveal, consistent with those observed in antiferromagnetically coupled 1D chain models. The diamagnetic contribution is small in both cases. As the temperature is lowered to 1K from 30K, the magnetic susceptibility predicted by the dimer chain model drops rapidly (ultimately to negative values), in contrast with the experimental susceptibility which drops less rapidly and remains positive. On the other hand, the magnetic susceptibility predicted by the Heisenberg chain model drops less rapidly than the experimental susceptibility and remains positive. As mentioned earlier, these deviations may be due to the presence of impurity spins; thus, we fit the low-temperature (< 10 K) magnetic susceptibility data to a field-dependent Brillouin function plus a baseline signal (dotted black line) that is due to the 1D chains. From **Figure 3.6–B**, we see that this combination of functions (with an impurity content of ~8 %, S = 1⁄2 and g = 2) closely fits the low-temperature data. Given that the magnetic susceptibilities of TUB75, the Heisenberg chain, and the dimer chain are positive, positive, and negative, respectively, at very low temperatures (see **Figure 3.6–B**), it appears that its IBU is best described in terms of Heisenberg chains. A Curie–Weiss fit to the high temperature portion of the inverse magnetic susceptibility is shown in **Figure 3.6–C**. All details of the data fitting are given in Appendix A, section A.1.

Finally, in **Figure 3.8**, we present the DFT-calculated spin density isosurface, focusing on a portion of the IBU in the AFM configuration. The antiparallel spin density along the copper dimer chain is clearly seen and it is delocalized onto the coppers and their nearest-neighbor oxygen and nitrogen atoms. This result suggests that the magnetic behavior of TUB75 is likely dependent on the shared spin density of these three atoms.

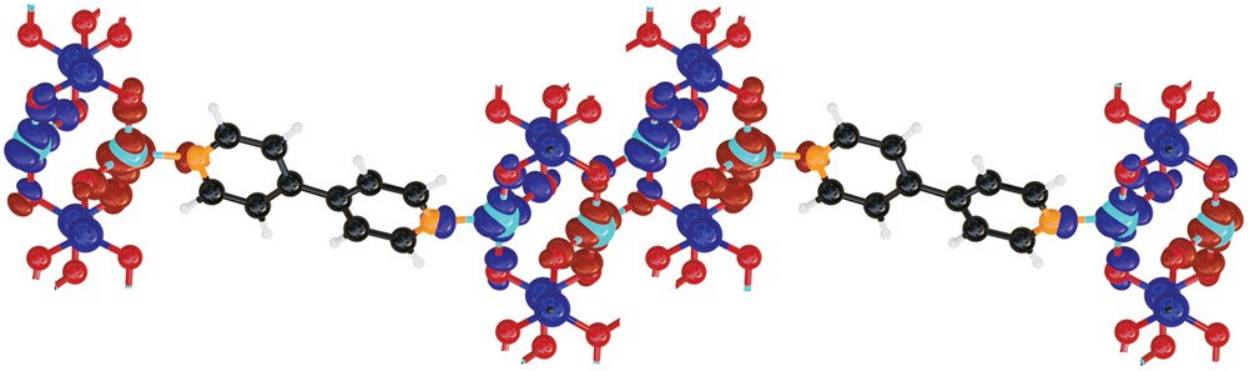

Figure 3.8. *Spin density isosurface of a portion of the IBU. β/α spin density is shown in blue/red and corresponds to a difference between the spin-up and spin-down density of 0.005 electrons per Å3. (O – red; N – orange; Cu – cyan; C – black; P – blue; H – white).*

As seen in **Figure 3.2–B**, all the 1,4-naphthalenediphosphonic acids in TUB75 are fully deprotonated, which leads to substantial electron delocalization within the 1D IBU. Electronic population analyses of the HSE06-calculated density were performed using the Hirshfeld,[145] Voronoi,[146] CM5,[147,148] and Mulliken[144] methods. As seen in **Table 3.3**, each O has, on average, less than -0.3 elementary charge units for a total of less than -0.9 elementary charge units on the three terminating oxygens in 1,4-NDPA. While the partial charges obtained from the various methods differ considerably in magnitude in some cases, the signs are all the same. Together, the results suggest that Cu, P, and H have slightly positive charges, while N, O, and C have slightly negative charges.

Table 3.3. *Average partial charges obtained using several electronic population analysis techniques.*

Atom	**Hirshfeld**[145]	**Voronoi**[146]	**CM5**[147,148]	**Mulliken**[144]
Cu	0.536	0.561	0.867	0.921
N	-0.090	-0.126	-0.369	-0.626
O	-0.331	-0.376	-0.434	-0.836
P	0.456	0.484	0.393	1.858
C	-0.022	-0.030	-0.043	-0.083
H	0.039	0.073	0.105	0.131

3.3.2 A 3D Cu-Naphthalene-Phosphonate Metal-Organic Framework with Ultra-High Electrical Conductivity: TUB40

In the current study, we revisit our previously published MOF TUB40,[200] which is composed of 2D sheets of corner-sharing copper and phosphorus polyhedral with 2,6-naphthalenediphosphonic acid (2,6-NDPA) linkers (see **Figure 3.9** for a depiction of the 2D sheets and crystal structure of TUB40) and explore its conductive and magnetic properties. In particular, we perform pellet conductivity, single-crystal conductivity, solid-state diffuse reflectance (to estimate the band gap via Tauc plotting), temperature-dependent magnetization measurements, and density functional theory (DFT) calculations.

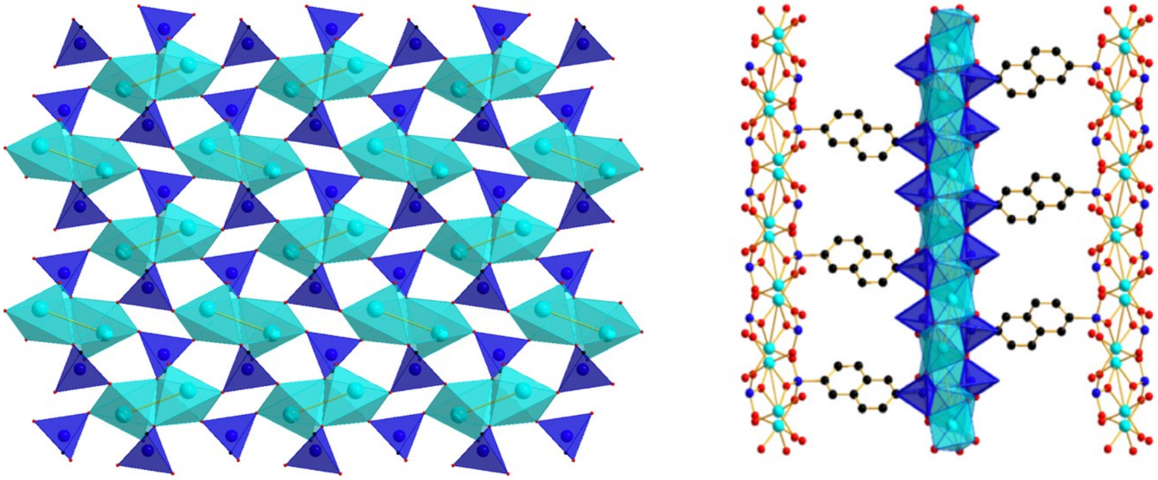

Figure 3.9. *Superstructure overview of TUB40.* ***a)*** *View of [{Cu(H_2O)}(2,6-NDPA)$_{0.5}$] TUB40's 2D copper phosphonate IBU composed of edge-sharing Cu-O-P-O-Cu-O-P-O polyhedra (see* **Scheme 3.1** *for the Lewis structure of 2,6-NDPA).* ***b)*** *Crystal structure of the three-dimensional pillared-layered network of TUB40.*

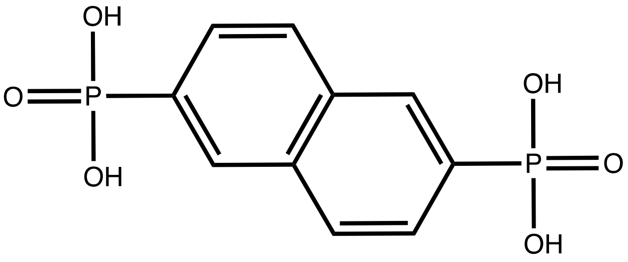

Scheme 3.1. *Lewis structure of 2,6-naphthalenediphosphonic acid (2,6-NDPA).*

CuO is known to be a good semiconductor with a band gap of 1.2 eV.[201] In addition, the rich metal-binding modes found in phosphonate MOFs allows for optimizable surface areas, which could expand the range of semiconductor applications. Therefore, we sought to estimate the band gap of TUB40 from the UV-Vis diffuse reflectance spectrum of handpicked crystals of TUB40. As seen in **Figure 3.10A**, indirect Tauc plotting of the reflectance data reveals a band gap of 1.42 eV, which lies in the semiconductive range.[194,202]

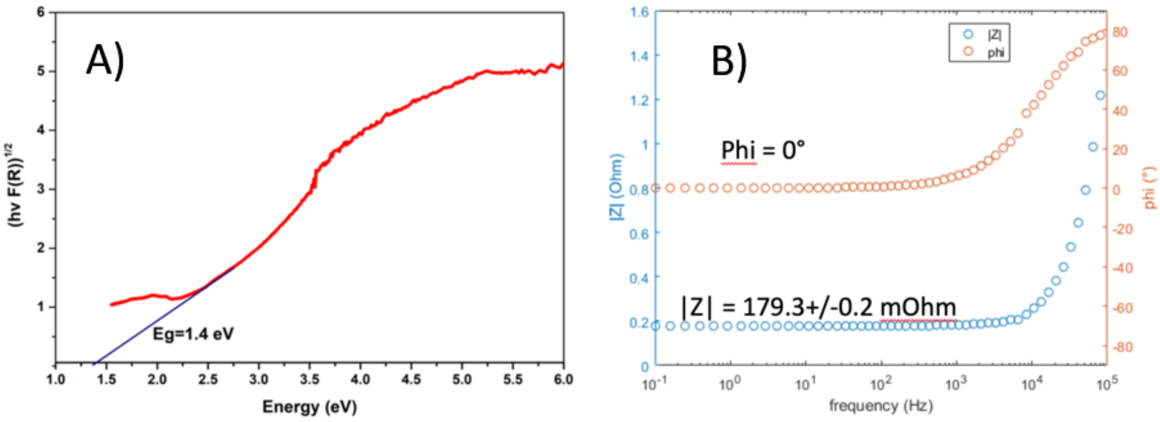

Figure 3.10. *Experimental band gap and conductivity measurements.* ***A)*** *Tauc plot of UV-Vis diffuse reflectance spectrum for TUB40, showing the indirect band gap of 1.4 eV.* ***B)*** *Impedance spectrum of TUB40 revealing purely Ohmic behavior with |Z|=179.3±0.2 mΩ between 0.1 Hz and ~500 Hz. Above ~500 Hz, |Z| and ϕ increase due to the increasing parasitic contributions from the connectors and cables in the setup.*

Given the narrow bandgap, we then used impedance spectroscopy to measure the resistance of a 5 mm (diameter) x 0.5 mm (thickness) TUB40 pellet at room temperature and calculated the resulting electrical conductivity σ. This was done using a Zahner ZENNIUM impedance measurement unit in the potentiostatic mode (with 20 mV amplitude between 100 mHz and 100 kHz). To reduce the influence of contact resistance between the pellet surface and electrodes (stainless steel cylinders), the impedance measurement was done under a mechanical load of 1 MPa. In **Figure 3.10B**, the complex-valued impedance is displayed in the Bode representation in terms of the magnitude of the impedance, |Z|, and the phase shift, ϕ, between the input potential wave and measured current wave (NB: ϕ=0 for ohmic resistors and ϕ≠0 for serial or parallel combinations of capacitive, inductive, and resistive elements). From 0.1 Hz to ~500 Hz, we see that |Z| and ϕ remain constant at 179.3±0.2 mΩ and 0°, respectively. This frequency independence is characteristic of pure ohmic resistors. Above ~500 Hz, the plot exhibits a common feature of an impedance measurement setup, namely ϕ increases with increasing frequency towards 90° (here, 80° at 100 kHz). This artifact is caused by parasitic contributions from the connectors and cables, which lead to measurable inductances due to mutual induction or object- and wiring-inductance. Thus, frequencies with ϕ values higher than 1° were not considered in the calculation of the resistance, R, i.e., R was calculated from the mean |Z| between 0.1 Hz and 200 Hz. Finally, the conductivity, σ **Eqn. 3.1**, was calculated to be 142 S m^{-1},

$$\sigma = \frac{l}{RA} = \frac{5 \cdot 10^{-4} m}{0.1793\Omega \cdot (0.25 \cdot \pi \cdot (5 \cdot 10^{-3} m)^2)} \tag{3.1}$$

As measurements on polycrystalline pellets may underestimate the conductance of the MOF due to contact/grain boundary resistances and anisotropic electrical conduction, we also performed single-crystal measurements according to the setup described in Ref [58]. The TUB40 crystals were handpicked under a microscope (see **Appendix Figure A–3**) and a number of measurements were performed by clamping the individual crystals in a flat alignment between two gold surfaces of a relay (see Appendix A for more details). Assuming that the TUB40 crystal made perfect contact with the gold surfaces, the measured resistances yielded a maximum conductance of ~10^3 S m^{-1} with an average of ~200 S m^{-1}. Since the main crystal body is surrounded by smaller rectangular plates of TUB40 crystals (see **Appendix Figure A–3**), perfect contact with the gold surfaces is probably not made and thus the reported average conductance may underestimate the actual average.

Temperature-dependent magnetization measurements of a 20 mg sample of TUB40 were conducted using a Squid-based vibrating sample magnetometer (MPMS by Quantum Design) in direct current mode. The magnetization data was obtained in a temperature range between 2 K and 380 K for applied magnetic fields between 0.1 and 7 Tesla and the corresponding susceptibilities [calculated from the magnetization (M) and applied magnetic field (B)] are shown in **Figure 3.11–A**. For low applied fields up to 2 Tesla, the magnetic susceptibility shows a broad peak with a maximum at T_{max} ~ 4 K, which is essentially independent of field strength. Such a result is consistent with short-range antiferromagnetic order in the 2D Cu planes.[203] For the higher applied field strengths, the peak maximum shifts to lower temperatures with increasing field strength due to the greater influence of the magnetic field over the short-range interactions. Above T_{max}, the susceptibility decays with increasing temperature to a small value at room temperature, indicative of paramagnetic behavior.

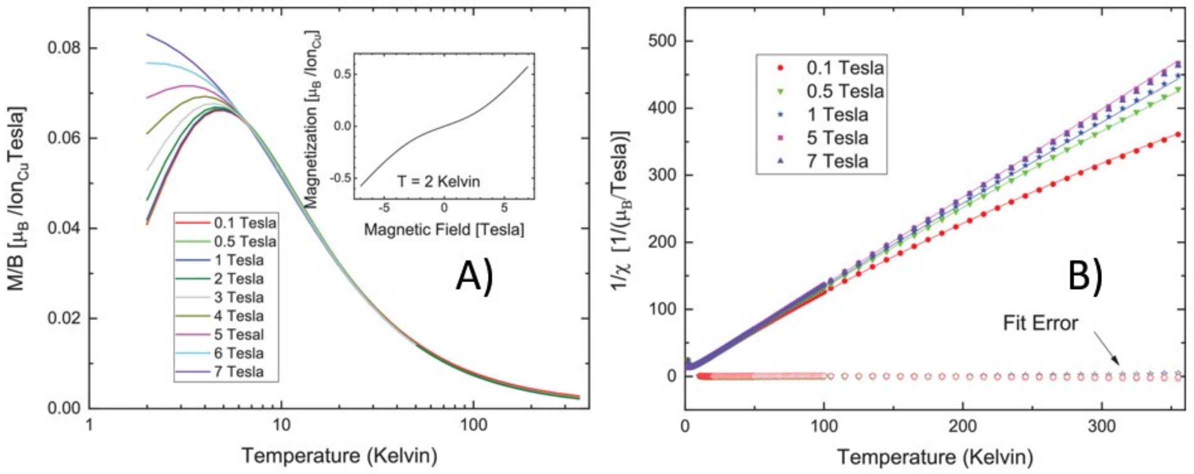

Figure 3.11. *Experimental magnetic measurements.* ***A)*** *Magnetic susceptibility, M/B, as a function of temperature for different values of the applied magnetic field, as obtained from the raw magnetization data. The insert shows the magnetization as a function of the applied field at 2 K.* ***B)*** *Inverse susceptibility, 1/χ, (filled symbols) as a function of temperature for different values of the applied magnetic field, along with fits to the data (solid lines). The deviations between the fits and measured data are also shown (open symbols).*

The inverse susceptibilities, χ^{-1}, which are used to obtain Curie-Weiss fits of the data, are shown in **Figure 3.11–B**. As can be seen, straight lines are only observed at high field strengths, with deviations observed at low field strengths, namely, $\chi^{-1}(T)$ curves downwards at high temperatures due to paramagnetic or ferromagnetic contributions. It should be noted that diamagnetic contributions, if present, would bend $\chi^{-1}(T)$ upwards at high temperatures and be field-independent. A good fit to the susceptibility, χ, over the full temperature range from 10 K to the highest temperature was obtained using **Eqn. 3.2**.

$$\chi = {}^{C_{CW}}\!/_{T-\Theta_{CW}} + \chi_{dia} + {}^{C_B}\!/_{\sqrt{B}} \qquad 3.2$$

Where C_{CW} and Θ_{CW} are the Curie and Curie-Weiss constants, respectively, and χ_{dia} is the diamagnetic contribution. The last field-dependent term, $\chi_B = {}^{C_B}\!/_{\sqrt{B}}$, is introduced to capture the deviations from the Curie-Weiss behavior observed at high temperatures, where C_B is a temperature-independent constant. The observed square root behavior can arise from a small amount of ferromagnetic impurity with soft magnetic properties.[204] The fit gives $C_{CW} = 0.76\ {}^{\mu_B K}\!/_{Ion_{Cu}\,Tesla}$, $\Theta_{CW} = -4.13\ K$, $\chi_{dia} = 110 \times 10^{-6}\ {}^{\mu_B}\!/_{Ion_{Cu}\,Tesla}$, and $C_B =$

$225 \times 10^{-6}\ ^{\mu_B}/_{Ion_{Cu}\sqrt{Tesla}}$. Assuming Cu spins with g=2, the obtained value of the Curie constant, C_{CW}, suggests that ~80% of the Cu spins per mole of spins contribute to the magnetic interactions. The field dependence of the magnetization at 2 K (see insert of **Figure 3.11–A**) shows a change in slope at 2.5 Tesla to paramagnetic behavior. This value of the field corresponds to a Zeeman splitting of 3.4 K for Cu spins, which is consistent with T_{max} ~ 4 K and $\Theta_{CW} =$ -4.13 K. The negative sign of the latter indicates that the interactions are antiferromagnetic. The magnitudes of the ferromagnetic (χ_B) and diamagnetic (χ_{dia}) backgrounds are very small compared to the low-temperature susceptibility values, so they can be safely treated within this fit. The diamagnetic background can arise from the non-magnetic atoms in TUB40.

DFT calculations of the density of states (DOS), projected density of states (pDOS), band gap, band structure (**Appendix Figures A4-A6**), and partial charges of TUB40 were also carried out. **Figure 3.12** shows the optimized structure of the antiferromagnetic (AFM) configuration of TUB40 (the optimized structure of the ferromagnetic (FM) configuration is negligibly different). As seen in **Table 3.4**, the structural differences between the optimized structure and experimental crystal structure are minimal. The exchange energy (i.e., difference between the energies of the AFM and FM configurations) was calculated to be $E_x = E_{AFM} - E_{FM} =$ -1.50 meV, suggesting that the zero-temperature magnetic ground state is the AFM state (in agreement with the magnetic susceptibility data below 5 K).

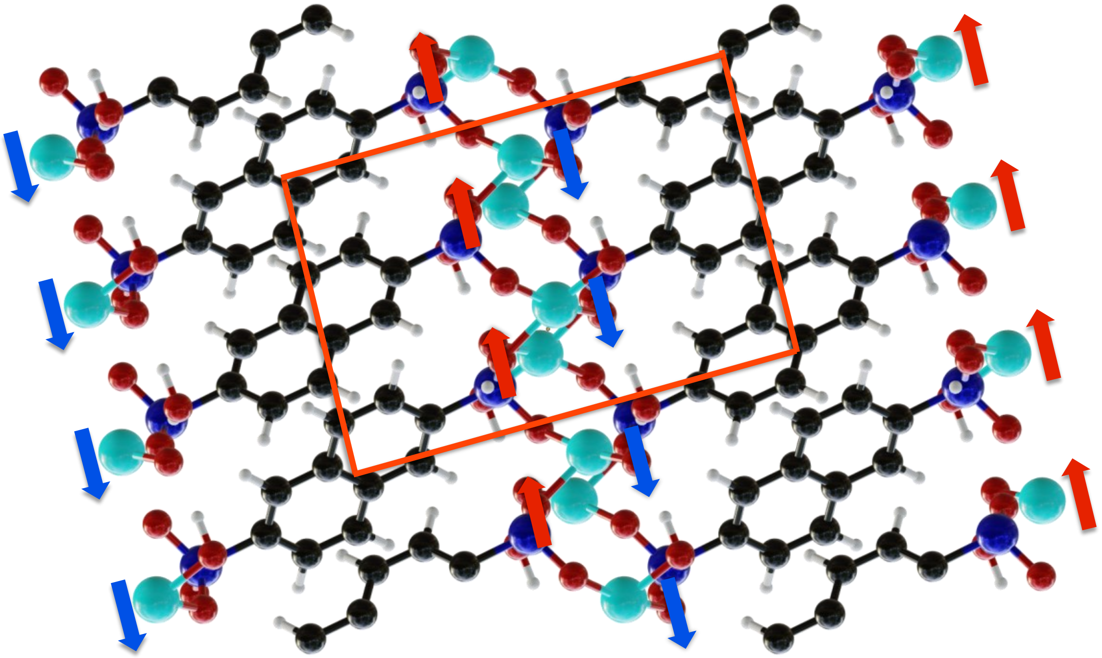

Figure 3.12. *Minimum energy structure of the 2×1×2 supercell of TUB40 in the AFM configuration, obtained at the DZP-PBE-D3 level of theory. The orange box delineates the unit cell. The red and blue arrows denote the α and β spins, respectively, of the unpaired electrons of the copper atoms. For the FM configuration, all the unpaired electrons are taken to be spin-α. (O – red; Cu – cyan; P – blue; C – black; H- white).*

Table 3.4. *Comparison of average bond lengths (in Å) between the TZP PBE-D3-BJ optimized AFM structure and the experimental crystal structure. Standard deviations are given in brackets.*

Bond	**Theory**	**Crystal structure**
Cu-O	1.97 (9.92E-3)	1.95 (1.90E-2)
Cu--O	2.00 (1.32E-2)	1.99 (3.75E-4)
C-P	1.81 (3.15E-4)	1.80 (4.61E-4)
O-P	1.56 (5.01E-3)	1.53 (2.97E-3)
O-H	1.01 (7.12E-3)	0.83 (2.97E-3)
C-H	1.09 (6.23E-4)	0.93 (4.30E-4)
C-C	1.42 (5.24E-3)	1.41 (1.82E-3)
C=C	1.38 (4.43E-3)	1.37 (2.90E-4)

We first present and discuss the HOCO-LUCO gap and pDOS of the AFM configuration (the total DOS and band structure may be found in **Appendix Figure A–4**). The HOCO-LUCO gap was calculated to be 2.320 eV and, as seen in the pDOS (**Figure 3.13**), the HOCO is predominantly dictated by the carbon orbitals of the naphthalenes and the LUCO by the orbitals on the copper and, to a lesser extent, the oxygen atoms. These results suggest that the AFM configuration has a spatially separated HOCO-to-LUCO transition. Further insight into the HOCO-LUCO gap is provided by the pDOSs in **Figure 3.14**, which show the contributions from the p-orbitals of the carbon atoms and the d-orbitals of the copper atoms with excess β- (**Figure 3.14–A**) and α-spins (**Figure 3.14–B**). As can be seen, the spin orientations of the copper d-orbitals contributing to the LUCO depend on the copper atom under consideration (i.e., a copper atom with an excess β-spin or α-spin). Specifically, for the copper atoms with the excess β/α-spins, spin-up/down electrons may populate the copper d-orbitals of the LUCO. Due to the electronic transition selection rule that $\Delta S = 0$ (i.e., the spin of the electron cannot change), our results suggest the possibility of excitations of spin-up/down electrons from the naphthalene π orbitals to the empty d-orbitals of copper atoms with unpaired spin-down/up electrons, i.e., a copper atom with an unpaired spin-up electron will only accept an excited spin-down electron into its empty d-orbitals and vice versa.

Given the small exchange energy, we next present and discuss the HOCO-LUCO gaps and pDOSs of the FM configuration. Based on the spin-up and spin-down band gaps, band structure (**Figure A–5**), total DOS (**Figure A–5**), and pDOS (**Figure 3.14**), we see that the FM configuration's HOCO-LUCO gap is spin-dependent. More specifically, the spin-down states have a band gap of 2.195 eV, in the semiconductor regime, while the spin-up states have a band gap of 3.913 eV, which is closer to that of an insulator. This situation may be contrasted with that of a half-metal, where one spin orientation has a zero band gap and the other has a non-zero band gap.[34,205,206] As can be seen in **Figure A–5**, the HOCO is spin-independent while the LUCO is spin-dependent. To understand how the various atoms contribute to the spin-dependent HOCO-LUCO gap, we calculated the pDOS for carbon, copper, oxygen, and phosphorous shown in **Figure 3.15**. The figure reveals that the HOCO of TUB40 in the FM configuration is predominantly dictated by the carbon orbitals of the naphthalenes (as in the case of the AFM configuration). On the other hand, the spin-down contribution to the LUCO is mainly composed of copper orbitals with a small contribution from the oxygen orbitals (as in the case of the AFM configuration), while the spin-up contribution is due to carbon orbitals. Based on these results, we see that the spin-down states have a spatially separated HOCO-to-LUCO transition (as in the case of the AFM configuration), while that of the spin-up states is localized on the naphthalene carbon atoms. Further insight into the HOCO-LUCO gap is provided by the pDOS in **Figure 3.16**, which shows the contributions from the p-orbitals of the carbon atoms and the d-orbitals of the copper atoms with excess α-spins. As can be seen, spin-down electrons may populate the copper d-orbitals of the LUCO. Due to the electronic transition selection rule that ΔS = 0, this figure suggests the possibility of excitations of spin-down electrons from the naphthalene π orbitals to the empty d-orbitals of the copper atoms, i.e., a β-spin π-d transition with a 2.195 eV gap.

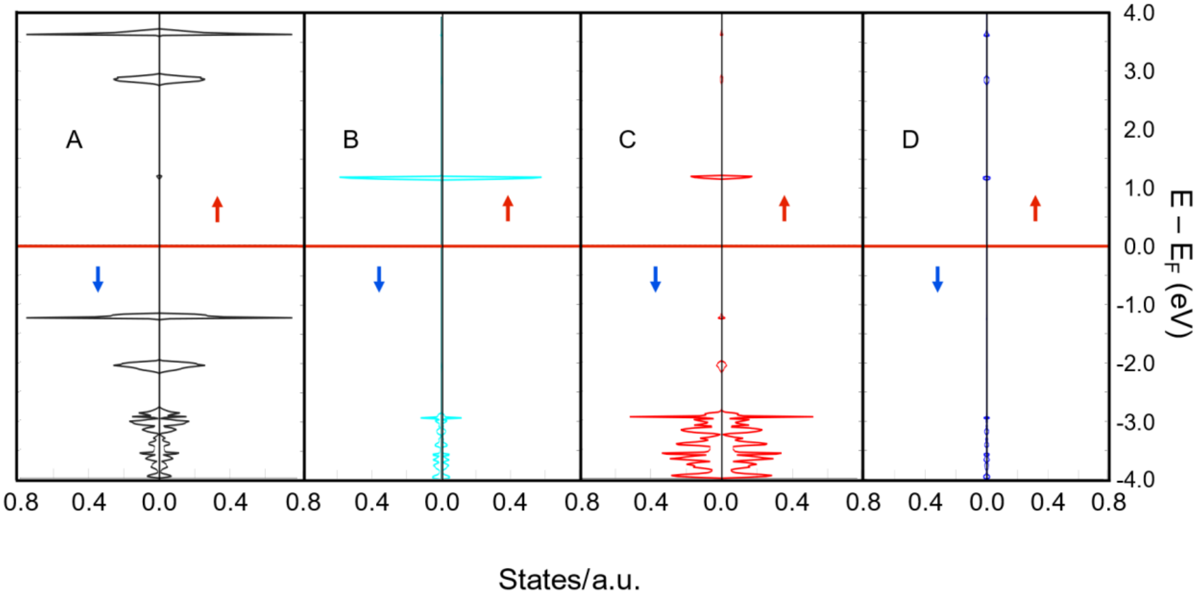

Figure 3.13. *Spin-up (red arrow) and spin-down (blue arrow) projected density of states for TUB40 in the AFM configuration. (A) Carbon, (B) Copper, (C) Oxygen, (D) Phosphorous.*

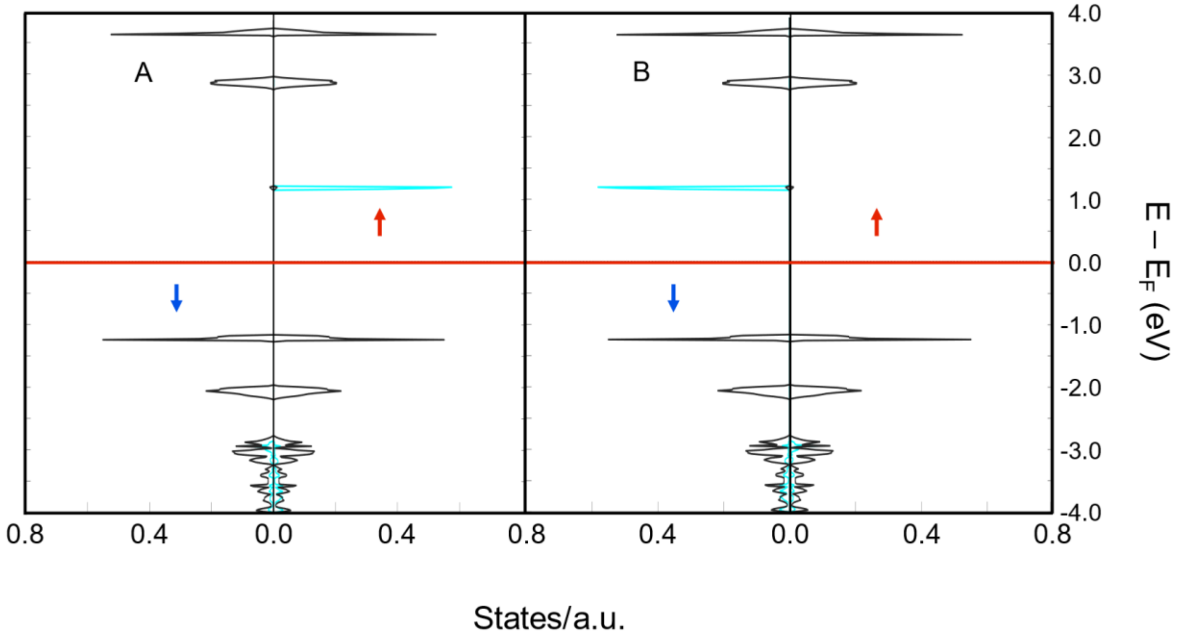

Figure 3.14. *Spin-up (red arrow) and spin-down (blue arrow) projected density of states for TUB40 in the AFM configuration, showing the contributions from p-orbitals of the carbon atoms (black) and d-orbitals of the copper atoms (cyan) with* ***(A)*** *an excess β-spin and* ***(B)*** *an excess α-spin.*

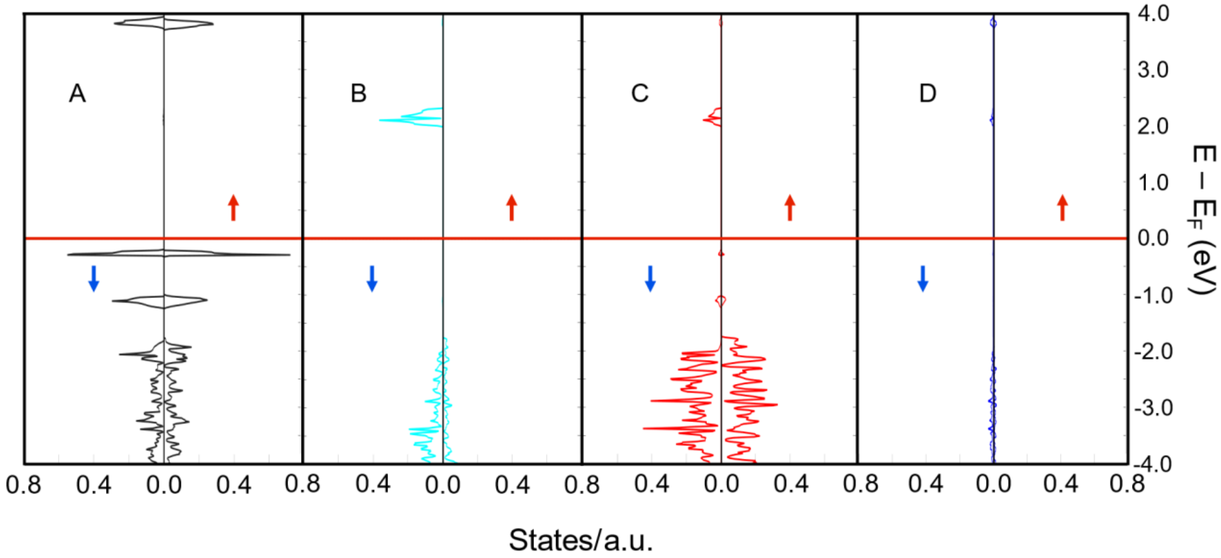

Figure 3.15. *Spin-up (red arrow) and spin-down (blue arrow) projected density of states for TUB40 in the FM configuration. (A) Carbon, (B) Copper, (C) Oxygen, (D) Phosphorous.*

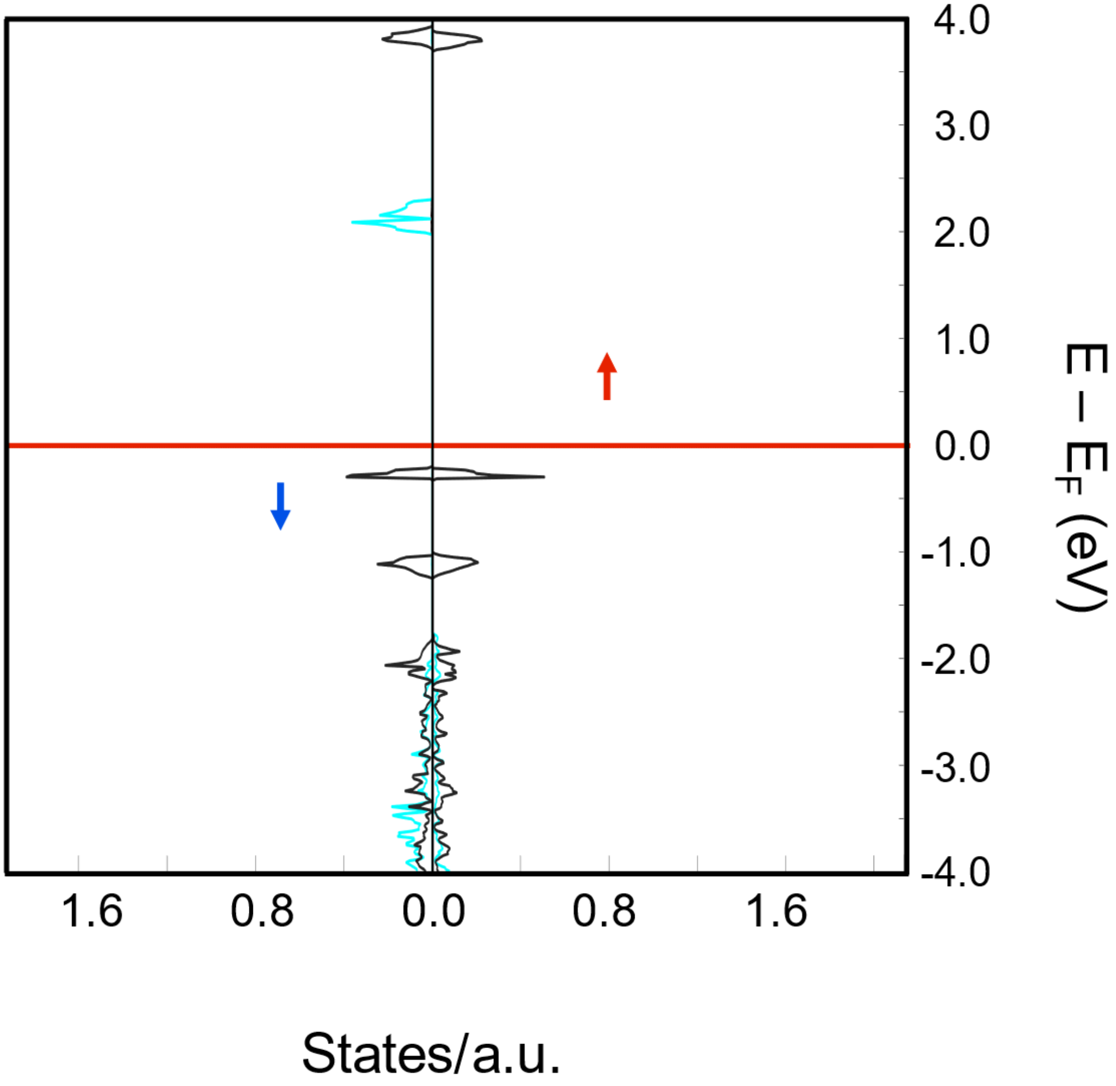

Figure 3.16. *Spin-up (red arrow) and spin-down (blue arrow) projected density of states for TUB40 in the FM configuration, showing the contributions from p-orbitals of the carbon atoms (black) and d-orbitals of the copper atoms (cyan) with an excess α-spin.*

Our smallest calculated HOCO-LUCO gaps (viz., 2.320 eV and 2.195 eV) are somewhat larger than the experimental estimate of the band gap (viz., 1.42 eV). This may be due to a combination of reasons. Firstly, our gaps were calculated at 0 K, while the experimental gap was extracted from a UV-Vis spectrum obtained at room temperature. Secondly, the HSE06 hybrid functional that we used has a parameter that can be varied to switch between the PBE0 hybrid functional[104,207] (ω = 0) and the pure GGA PBE[101] functional (as ω → ∞). Hybrid functionals include Hartree-Fock exchange, which increases long-distance interactions and, in turn, increases

HOCO-LUCO gaps. Given that the default value of $\omega = 0.11$ was used in our calculations and that our calculated HOCO-LUCO gaps overestimate the experimental one, it is possible that too much Hartree-Fock exchange was included in the functional.

Finally, the results of the electronic population analyses (see **Table 3.5**) show that the oxygen atoms surrounding each copper atom have excess electron density (viz., for every three oxygen atoms there is approximately an excess electron), pointing to high electron delocalization within the 2D IBU. The spin density isosurface of the AFM configuration (**Figure 3.17**) shows that the spin density is delocalized onto the copper atoms and oxygen atoms, suggesting that both of these atoms contribute to the magnetic behaviour of TUB40.

Table 3.5. *Average partial charges for each atom in the AFM configuration, as calculated by several population analysis techniques.*

Atom	**Hirshfeld**[145]	**Voronoi**[146]	**CM5**[147,148]	**Mulliken**[144]
Cu	0.574	0.582	0.872	0.947
O	-0.298	-0.344	-0.466	-0.815
P	0.462	0.485	0.399	1.801
C	-0.028	-0.052	-0.055	-0.157
H	0.059	0.114	0.173	0.259

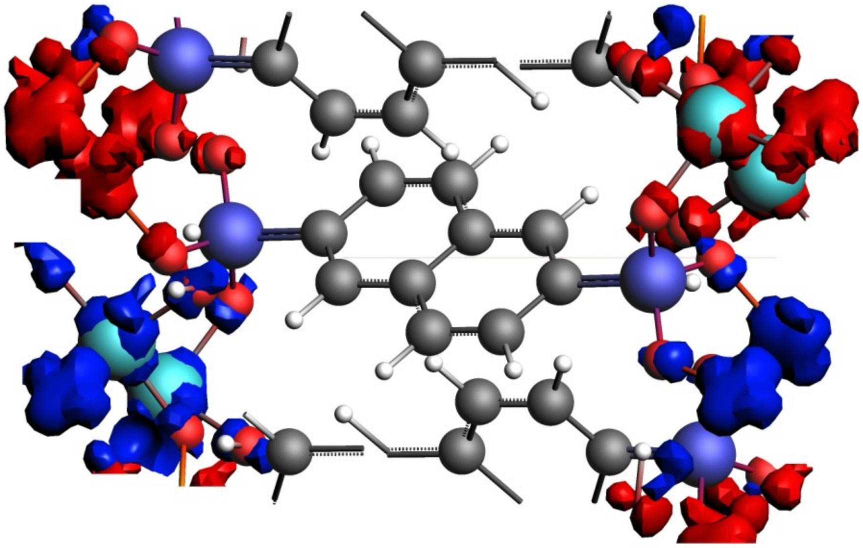

Figure 3.17. *Spin density isosurface of the optimized unit cell of TUB40 in the AFM configuration. β/α spin density is shown in blue/red and corresponds to a difference between the spin-up and spin-down density of 0.005 electrons per $Å^3$. The portions of the isosurface that appear to not have atoms associated with them are consequences of the periodic calculation. Color definitions: O-red; P-blue; Cu-cyan; C-grey; H-white.*

3.3.3 Coordination-Dependent Band Gaps in a Cu-Phosphonate Metal-Organic Framework: TUB1

It is believed that the well-layered aromatic units in such phosphonate MOFs help promote electron hopping and that the continuous arrangement of M-O-P polyhedra in the IBUs extend the conjugation.[58,80] Moreover, due to their exceptionally high thermal and chemical stabilities, phosphonate MOFs could be suitable for applications such as electrodes in supercapacitors for electric vehicles and the storage/supply of energy produced by solar panels and wind turbines.[177,27,208,209] In this work, we report the crystal structure of a newly synthesized phosphonate MOF, termed TUB1, which possesses a unique one-dimensional IBU composed of square planar and distorted trigonal bipyramidal copper(II) ions, and a tris deprotonated methane tetra-p-phenylphosphonic acid (H_5MTPPA^{3-}) linker. Notably, TUB1 was found to have an indirect band gap of 2.4 eV.

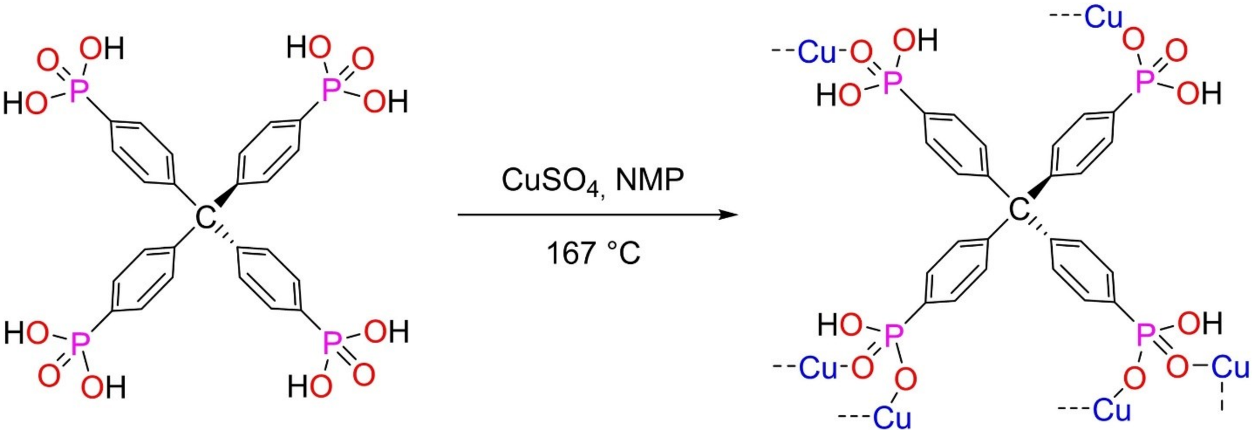

Scheme 3.2. *Solvothermal reaction scheme for the synthesis of TUB1.*

As seen in **Scheme 3.2** and **Figure 3.18–A**, TUB1 is composed of one-dimensional IBUs, which are bridged together by H_5MTPPA^{3-} linkers. Each IBU is composed of corner-sharing eight-membered Cu1-O-P-O-Cu1-O-P-O and Cu2-O-P-O-Cu2-O-P-O rings. Since three of the four phosphonic acid units in the linker are mono-deprotonated, the linker has asymmetric metal-binding modes, viz., the mono-deprotonated units could give rise to ionic interactions while the fully protonated unit provides coordinate covalent binding. Therefore, TUB1 exhibits two different metal-binding options, in contrast to our previously reported Co_2H_4MTPPA and Zn_2H_4MTPPA MOFs.[177,210] In particular, the three mono-deprotonated phosphonic acid units are coordinated to square planar and distorted trigonal bipyramidal copper centres (labelled Cu1 and Cu2, respectively) via ionic bonding, while the fully protonated unit exclusively generates coordinate covalent bonding between the square planar copper centre and the P=O bond of the phosphonic acid. DFT-based charge analysis in **Table 3.6** shows that there is high electron delocalization on the deprotonated oxygens, suggesting the possibility of ionic interactions.) To the best of our knowledge, the presence of both trigonal bipyramidal and square planar copper centres in a one-dimensional IBU has not been previously reported for phosphonate MOFs.[211] The crystal structure of TUB1 indicates the presence of two different types of square- and parallelogram-shaped void channels (see **Figure 3.18**).

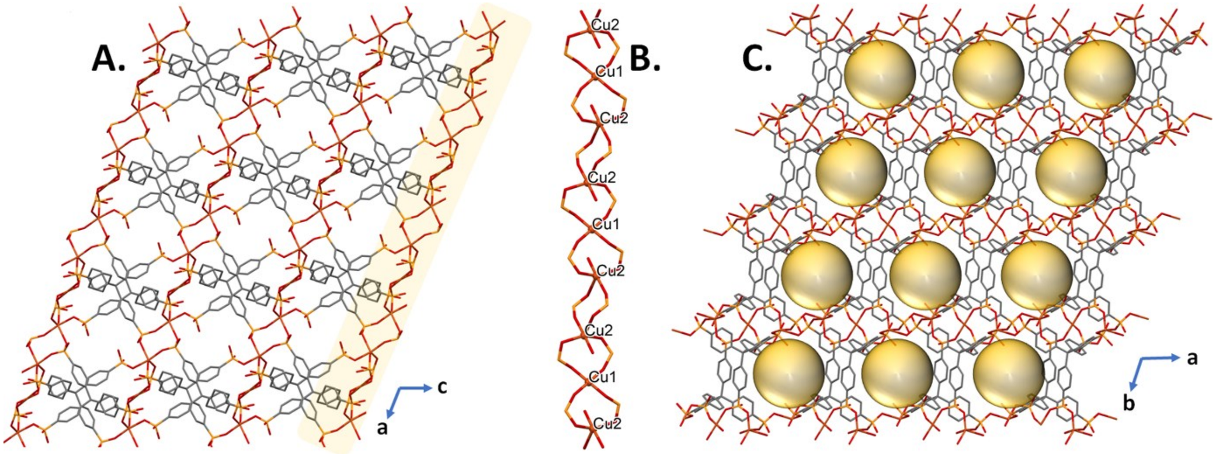

Figure 3.18. *a) View of rectangular void channels (highlighted in yellow) in the ac plane b) Structure of the one-dimensional IBU c) View of parallelogram void channels in the ab plane.*

Next, the indirect and direct band gaps of TUB1 were estimated from Tauc plots of the UV-Vis spectrum (see **Figure 3.19**) to be 2.4 eV and 2.7 eV, respectively. As seen in **Figure 3.19**, the Tauc plots of H_8MTPPA reveal direct and indirect band gaps of ca. 4.2 eV, which are considerably wider than those of TUB1 and contain two jumps as opposed to one in the TUB1 plots. This is likely due to the fact that H_5MTPPA has an insulating sp^3 methane core. The lower band gap of TUB1 arises from the formation of one-dimensional IBUs composed of eight-membered Cu1-O-P-O-Cu1-O-P-O and Cu2-O-P-O-Cu2-O-P-O rings in the MOF. Such a dramatic change in the Tauc plot after the formation of TUB1 suggests the emergence of an electron hopping mechanism, as the sp^3 methane core in H_5MTPPA^{3-} blocks the extension of conjugation in three dimensions.

To gain deeper insight into the electronic structure of TUB1, we performed DFT calculations of the highest occupied crystal orbital (HOCO)-lowest unoccupied crystal orbital (LUCO) gap, projected density of states (pDOS), HOCO and LUCO, average partial charges, and band structure.

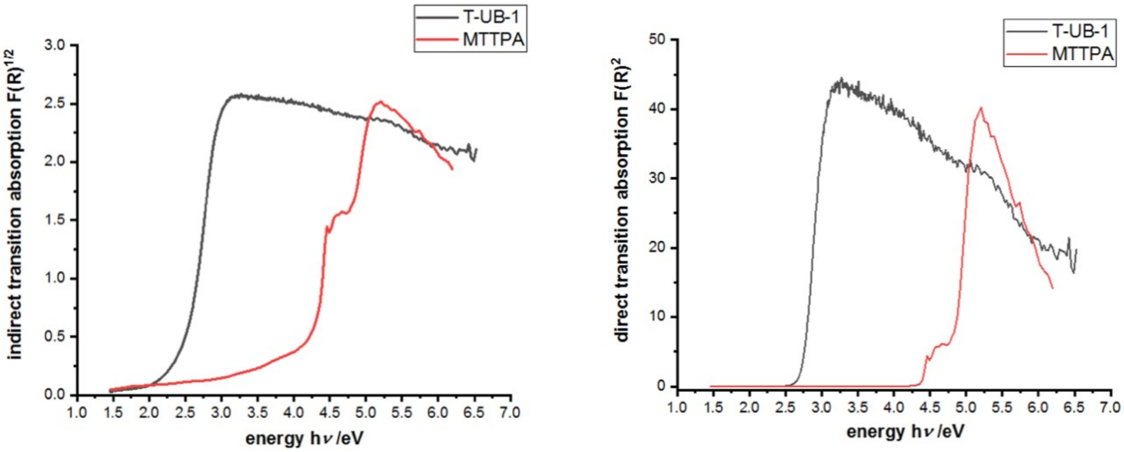

Figure 3.19. *Tauc plots of UV-Vis spectra used to obtain the indirect (left) and direct (right) band gaps of TUB1 and the MTTPA linker.*

The optimized structures of a 2x2x2 supercell and a single unit cell of TUB1 are shown in **Figure 3.20**, with the spin polarizations of each copper atom indicated on the unit cell. The structural differences between the optimized structure and experimental crystal structure are small (see **Appendix Table A1**). As illustrated in **Figure 3.21**, the copper atoms in the unit cell have different coordination environments, with the α-copper atoms (i.e., copper atoms with an excess of spin-up electrons) in the trigonal bipyramidal geometry and the β-copper atom in the square planar geometry.

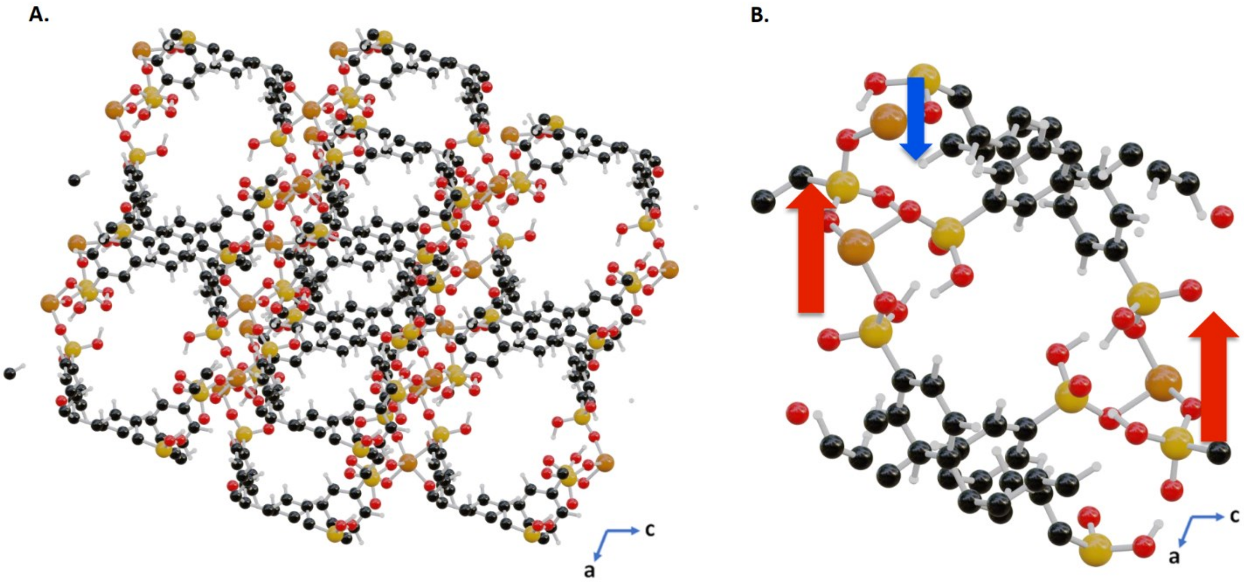

Figure 3.20. *Optimized structure of TUB1. a) A view down the b-axis of the 2x2x2 supercell. b) A view down the b-axis of the unit cell, with the red (spin-up) and blue (spin-down) arrows indicating the minimum-energy spin configuration of the unpaired electrons on the copper atoms (Cu – light brown; P – yellow; O – red; C – black; H – white).*

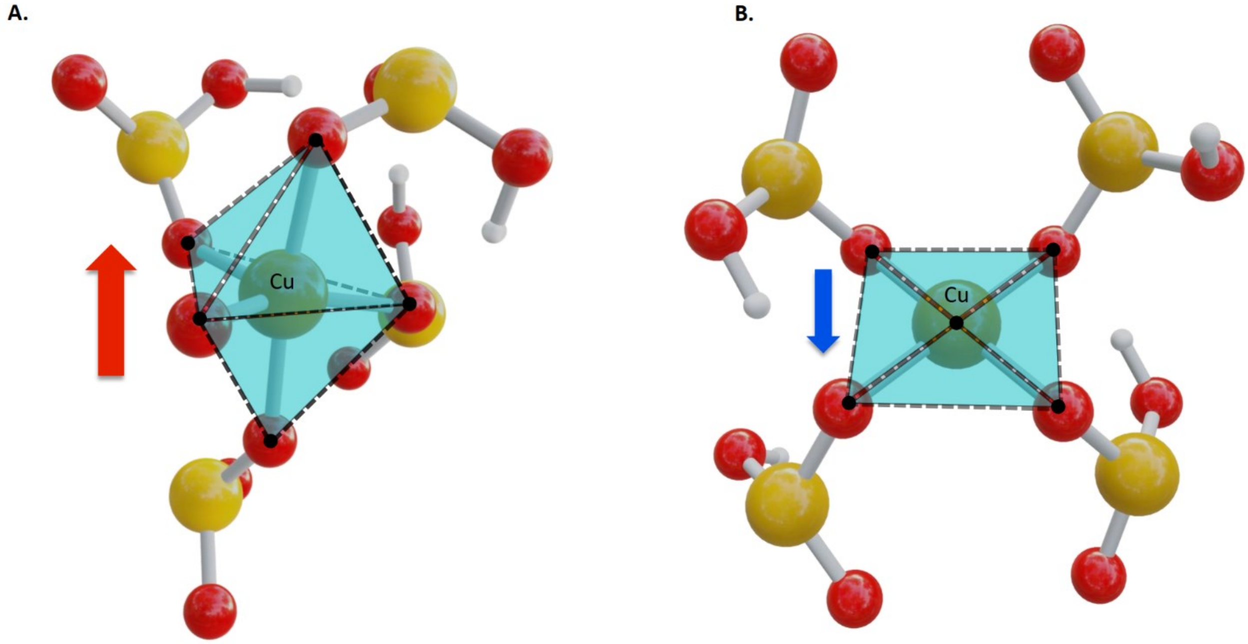

Figure 3.21. *A portion of the TUB1 unit cell, highlighting the two types of copper coordination environments. a) Trigonal bi-pyramidal copper atom coordinated to five oxygen atoms. b) Square*

planar copper atom coordinated to four oxygen atoms (Cu – light brown central atom; P – yellow; O – red; H – white).

Next, the pDOS was calculated using the range-separated hybrid functional HSE06,[103,183,184,185] which is known to yield accurate solid-state HOCO-LUCO gaps.[212,88] An analysis of the pDOS (shown in **Figure 3.22**) reveals a potential electrical conduction mechanism involving two spin-dependent HOCO-LUCO gaps, viz., a spin-up (α) gap of 2.60 eV, which is in good agreement with the experimental estimates of 2.4 eV (indirect) and 2.7 eV (direct), and a spin-down (β) gap of 0.48 eV. As seen in the pDOS, the β-HOCO-LUCO gap, which lies beneath the Fermi energy, is generated by orbitals primarily on the carbon atoms and some on the oxygen and copper atoms. From the β-HOCO and β-LUCO isosurfaces in the top panel of **Figure 3.23**, we see that the β-HOCO is primarily composed of π-orbitals on the sp^2 carbon atoms in half of the phenyl rings down the b-axis. The β-LUCO is composed of the same phenyl carbon π-orbitals, as well as π-orbitals on the oxygen atoms and d-orbitals on the square planar copper atoms (see **Figures 3.24** and **3.25**). The higher energy β-unoccupied crystal orbitals are primarily composed of orbitals on the trigonal bipyramidal copper atoms and yield a gap of 3.72 eV (see **Figure 3.24**). Comparing this value to the β- and α-HOCO-LUCO gaps of 0.48 eV and 2.60 eV, respectively, generated by square planar copper atoms, it is evident that the coordination environment of the copper atoms plays an essential role in narrowing the HOCO-LUCO gap. From the α-HOCO and α-LUCO isosurfaces in the bottom panel of **Figure 3.23**, we see that the α-HOCO is composed of carbon and oxygen π-orbitals along the b-axis, while the α-LUCO is primarily composed of d-orbitals on the square planar copper atom (see **Figures 3.24** and **3.25**) and π-orbitals on the oxygen and carbon atoms. The participation of the carbon, oxygen, and square planar copper atoms in both spin-dependent HOCO-LUCO gaps suggests that they are integral in facilitating electrical conduction in TUB1.

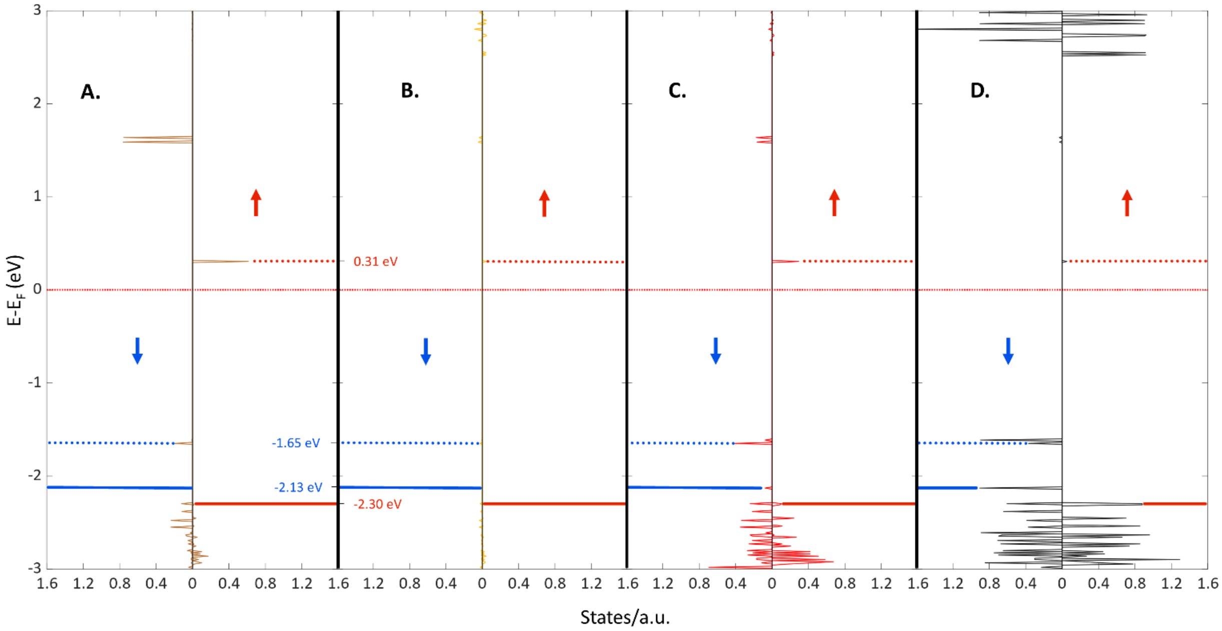

Figure 3.22. *Spin-up (red arrow) and spin-down (blue arrow) projected density of states for TUB1: (A) Copper, (B) Phosphorous, (C) Oxygen, (D) Carbon. The solid red and blue lines indicate the α- and β-HOCO energy levels, respectively. The dotted red and blue lines indicate the α- and β-LUCO energy levels, respectively. The blue numbers in panel A indicate the energies of the β-HOCO and β-LUCO, while the red numbers in panel B indicate the energies of the α-HOCO and α-LUCO.*

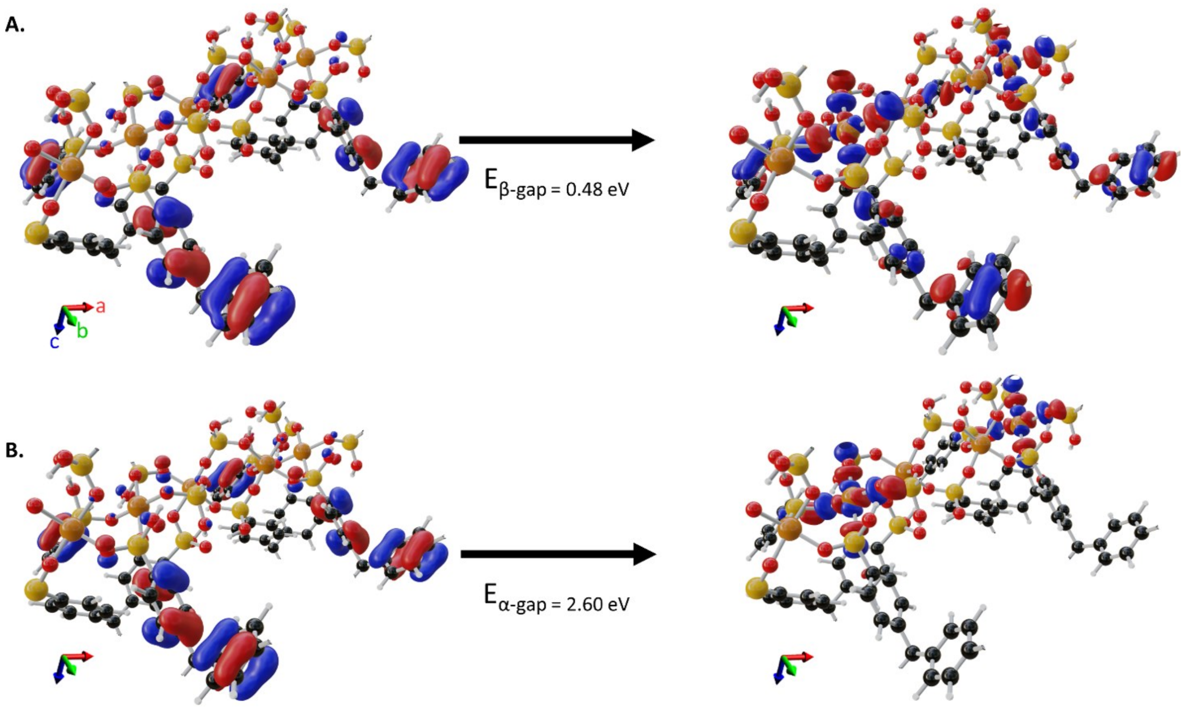

Figure 3.23. *HOCO and LUCO iso-density surfaces, corresponding to a density of 1 electron per 0.03 Å*^{3}*. A) β-spin HOCO-LUCO gap. B) α-spin HOCO-LUCO gap. For clarity, only a portion of the unit cell is shown (Cu – light brown; P – yellow; O – red; C – black; H – white).*

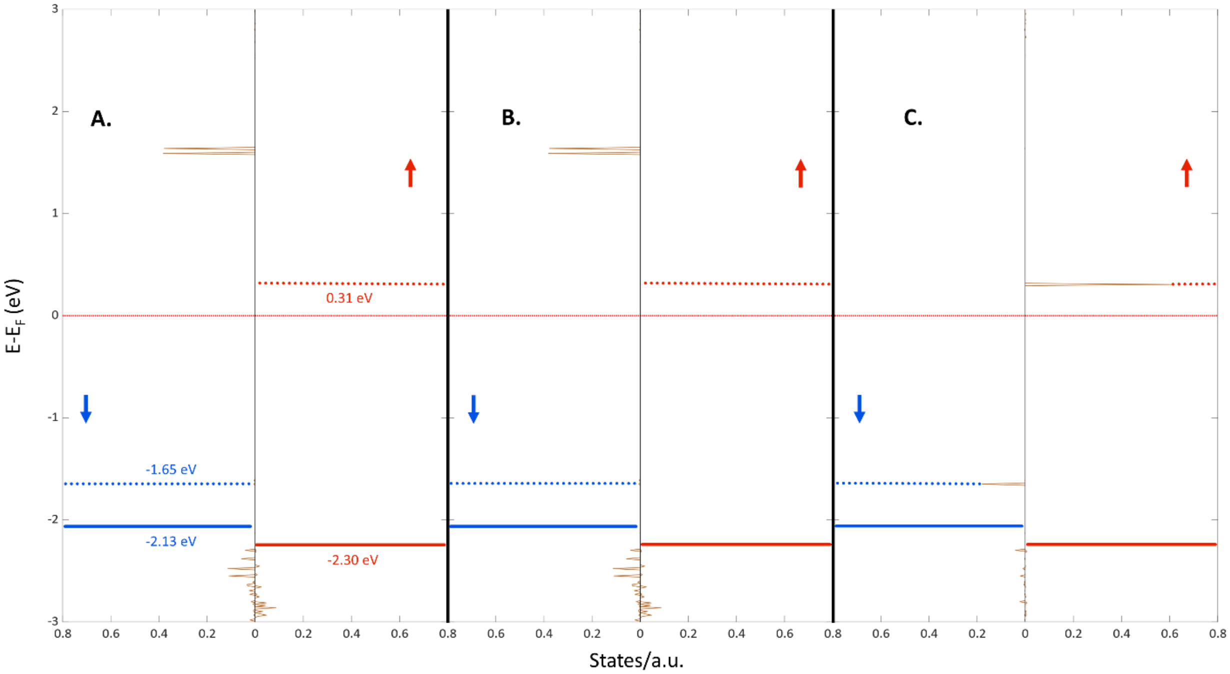

Figure 3.24. *pDOS of the copper atoms in TUB1. A) First trigonal bipyramidal α-copper. B) Second trigonal bipyramidal α-copper. C) Square planar β-copper. The contributions from the spin-up (α) and spin-down (β) electrons are indicated by the red and blue arrows, respectively. The dotted red and blue lines indicate the α- and β-LUCO energy levels, respectively, while the solid red and blue lines indicate the α- and β-HOCO energy levels, respectively. The red and blue numbers in panel A indicate the energies of the HOCO and LUCO for the spin-up and spin-down contributions, respectively.*

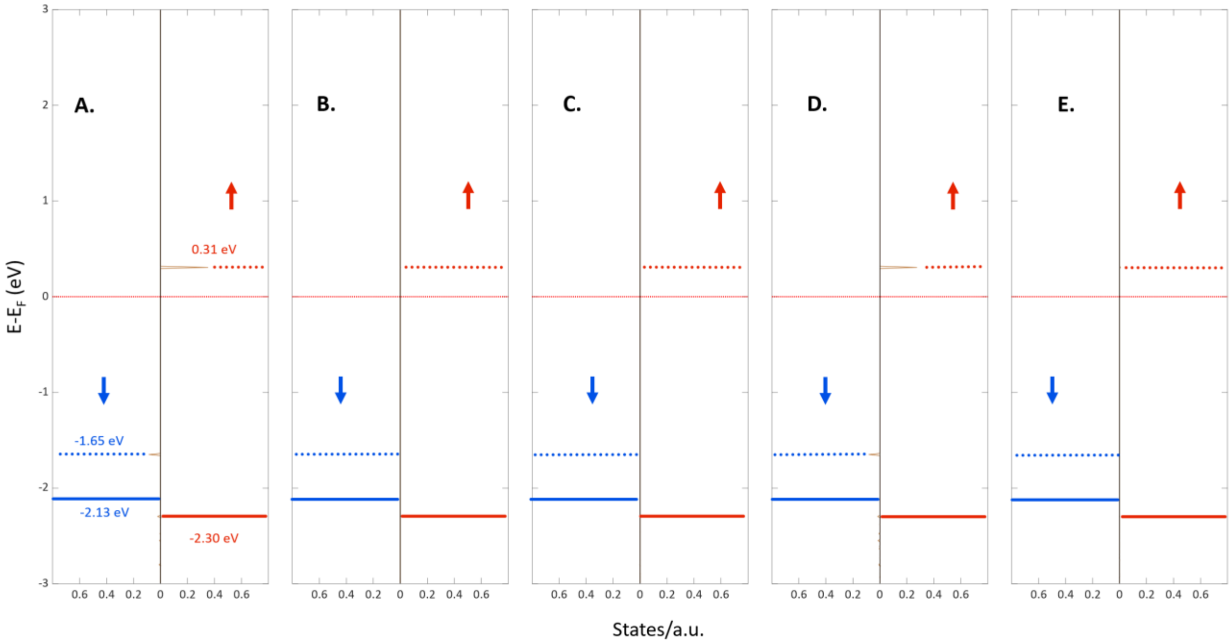

Figure 3.25. *pDOS of the d-orbitals on the square planar copper atom. A)* d_{yz}*; B)* d_{z2}*; C)* d_{xz}*; D)* d_{xy}*; E)* d_{x2-y2}*. The solid red and blue lines indicate the α- and β-HOCO energy levels, respectively, while the dotted red and blue lines indicate the α- and β-LUCO energy levels, respectively. The red and blue numbers in panel A indicate the energies of the HOCO and LUCO for the spin-up and spin-down contributions, respectively.*

The band structure of TUB1 is shown in **Figure 3.26**. As can be seen, there are 120 meV dispersions in the β-LUCO band along the X-Γ, Γ-Y, L-Γ, Γ-Z, N-Γ, Γ-M, and R-Γ paths in k-space. This points to higher electron mobility in several directions compared to typical semiconducting MOFs, which have linear bands or bands with dispersions of less than 50 meV.[167,33]

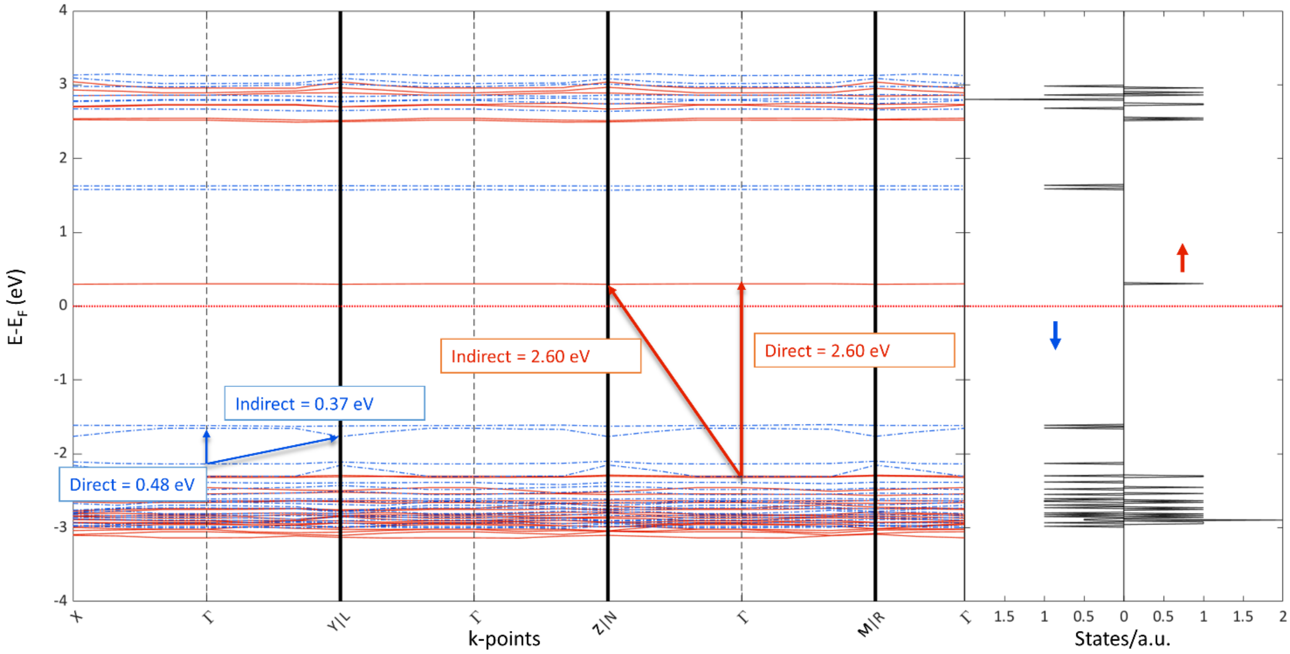

Figure 3.26. *(Left) Band structure of TUB1 calculated using the HSE06 functional with a TZP basis set, normal numerical quality, and an enforced spin polarization of three alpha electrons. The solid red and dotted blue lines denote the spin-up and spin-down bands, respectively. The indirect and direct band gaps are indicated by solid arrows. (Right) Total density of states (DOS) broken down into the spin-up (red arrow) and spin-down (blue arrow) contributions.*

Electronic population analyses were carried out on TUB1, using several different approaches. The resulting average partial charges on the various atoms are presented in **Table 3.6.** As can be seen, the hydrogen atoms that are directly bonded to carbon atoms possess relatively low positive charges (which is consistent with the non-polarizing nature of hydrocarbon bonds), while the hydrogen atoms in the phosphonate groups show a roughly two-fold increase in positive charge. All three types of oxygen atoms in the phosphonate group have significant negative charge on them, pointing to electron delocalization between them. Although the double-bonded oxygen atoms are expected to have higher electron density, we see that the oxygen atoms participating in P-O-Cu bonds possess nearly the same negative charge. Although the copper atoms are found in different coordination environments (**Figure 3.21**), their charges remain almost the same.

Table 3.6. *Average partial charges of oxygen, hydrogen, and copper atoms in TUB1. NB: Each charge presented is the difference between the nuclear charge and the partitioned electronic charge around each atom.*

Atom (bond-type found in)	Hirshfeld[145]	Voronoi[146]	CM5[147,148]	Mulliken[144]
H (H-C)	0.05	0.09	0.11	-0.15
H (P-O-H)	0.10	0.17	0.30	0.28
O (P-O-H)	-0.26	-0.27	-0.41	-0.67
O (P=O)	-0.31	-0.36	-0.40	-0.87
O (P-O-Cu)	-0.31	-0.36	-0.40	-0.82
Cu (bi-pyr)	0.57	0.59	0.90	0.91
Cu (planar)	0.58	0.59	0.94	0.87

3.4 CONCLUSIONS

3.4.1 TUB75

We report on the conductive and magnetic properties of the phosphonate MOF, TUB75. With an experimental band gap value of 1.4 eV, TUB75 is the first semiconducting phosphonate MOF in the literature, paving the way for a new family of semiconductors with an extremely rich structural chemistry. The metal-binding modes of the phosphonic acid group in TUB75 support a 1D IBU composed of a zigzag copper dimer chain, which was found to be antiferromagnetically coupled. The temperature-dependent magnetic susceptibility data was well fit using a combination of a Heisenberg chain model at higher temperatures and Brillouin functions at very low temperatures. Our experimental measurements were accompanied by DFT calculations, which yielded a band gap of 1.77 eV in good agreement with the experimental one and support the AFM nature of the IBU. Given the high thermal/chemical stabilities of phosphonate MOFs and the innumerous metal-binding modes of phosphonates, our findings suggest that they could be used in next-generation electrodes and supercapacitors capable of withstanding harsh operating conditions. The vast structural diversity of phosphonate MOFs could lead to a new generation of porous materials with engineerable surface areas and magnetic/conductive properties. Currently, we are working on the reticular chemistry of phosphonate MOFs to explore these possibilities.

3.4.2 TUB40

In conclusion, we reported on the conductive and magnetic properties of TUB40, which is composed of 2D sheets of copper(II)-phosphonate polyhedra. TUB40 was found to have a narrow band gap of 1.42 eV, well within the semiconducting range. The single-crystal and pellet-based impedance measurements yielded conductivities of 200 S m^{-1} and 142 S m^{-1}, respectively, at room temperature, making TUB40 one of the most conductive three-dimensional MOFs in the literature. Temperature-dependent magnetization measurements showed that the copper(II) atoms are antiferromagnetically coupled at very low temperatures. The DFT results suggested that the electrical conduction in TUB40 is due to excitations between the spatially separated HOCO and LUCO, which are primarily located on the aromatic naphthalene rings and the copper(II) atoms, respectively. Given their high thermal stability and extremely rich phosphonate metal-binding modes, phosphonate MOFs could become the next generation of microporous semiconductors and supercapacitor electrodes.

3.4.3 TUB1

In summary, we have reported on the electronic properties of a low-gap three-dimensional MOF TUB1, which possesses a unique one-dimensional IBU composed of corner-sharing eight-membered Cu1-O-P-O-Cu1-O-P-O and Cu2-O-P-O-Cu2-O-P-O rings containing square planar and distorted trigonal bipyramidal copper(II) centres. TUB1 was found to have an indirect band gap of 2.4 eV. Our DFT calculations confirm the experimental structure, yield spin-dependent HOCO-LUCO gaps of 2.60 eV (α) and 0.48 eV (β), suggest a role of the square planar copper centres in reducing the HOCO-LUCO gap, and point to above-normal non-directional electron mobility. The uniqueness of TUB1's IBU was made possible by the structural diversity afforded by phosphonate metal-binding groups. Such metal phosphonate IBUs may be used to construct semiconductive MOFs with polyaromatic cores for use in next-generation supercapacitors.

3.4.4 General Conclusions on TUB-phosphonate MOFs

These three phosphonate MOFs show promise as low band gap, magnetic materials. Our DFT results indicate that in general the HOCO-LUCO gaps of these materials depends highly on the π-conjugation of the linkers. Particularly, each of the materials presented have a gap that is dependent on the π-conjugated carbon orbitals participating in the HOCO's, suggesting π-conjugation is important in changing the HOCO-LUCO gaps of these systems. However, It is not as evident how the LUCO's of these materials are affected by the linkers as TUB40 and TUB1 both have LUCO's that depend on the d-orbitals of the copper(II) atoms, and TUB75 depends on the π-conjugation of the carbon orbitals from the 4,4'-bipyridine linkers. When magnetic measurements are available, as in the case of TUB75 and TUB40, our DFT results indicate they depend explicitly on the metal centres and the closest-bonded elements. Furthermore, all our charge analyses indicate that when three oxygen atoms from a phosphonate are near a metal atom they have an increased negative charge, suggesting high electron delocalization.

Chapter 4

Phosphonate Hydrogen-Bonded Organic Frameworks Insights from DFT [R2]

4.1 INTRODUCTION

Hydrogen-bonded organic frameworks (HOFs) represent an emerging class of microporous materials.[213,214,42,215,216,217,218] Compared to other microporous compounds such as metal-organic frameworks and covalent organic frameworks, HOFs can be synthesized under milder reaction conditions and can be recycled several times.[219] Although hydrogen bonds are weaker than covalent bonds in general, hydrogen bonds whose lengths are shorter than 2.4 Å can exhibit near-covalent bond stabilities.[220] In a supramolecular system such as a HOF, the high number of hydrogen bonds,[216,221] as well as the van der Waals interactions between the polyaromatic linkers, contribute to the stability of the framework.[220,222] Although crystal structures of hydrogen-bonded organic molecules were already known in the literature, the first synthesis of a permanently stable microporous HOF was only reported a decade ago.[223] Since then, HOFs synthesized with arylcarboxylic acids, boronic acids, azolates, pyridines, sulfonic acids, imides, imines, and amidinium functional groups have been reported, and our group recently reported the first HOF using the phosphonic acid functional group.[213,42,224] Currently, the number of HOFs in the literature is relatively low (compared to MOFs),[42,218] but they have already been used in a number of applications.[214,224,40] For example, HOFs constructed from non-toxic linkers have proven useful in drug delivery.[225,226] HOFs with high proton conductivities have been proposed as materials for

---

[R2] The contents of this chapter have been copied and/or adapted from two separate publications: **1)** Tholen, P.; Peeples, C. A.; Schaper, R.; Bayraktar, C.; Erkal, T. S.; Ayhan, M. M.; Çoşut, B.; Beckmann, J.; Yazaydin, A. O.; Wark, M.; Hanna, G.; Zorlu, Y.; Yücesan, G. Semiconductive Microporous Hydrogen-Bonded Organophosphonic Acid Frameworks. *Nat. Commun.* **2020**, *11* (1), 1–7. **2)** Tholen, P.; Peeples, C. A.; Ayhan, M. M.; Wagner, L.; Thomas, H.; Imbrasas, P.; Zorlu, Y.; Baretzky, C.; Reineke, S.; Hanna, G.; Yücesan, G. Tuning Structural and Optical Properties of Porphyrin-Based Hydrogen-Bonded Organic Frameworks by Metal Insertion. *Small* **2022**, *18* (49), 2204578. The supporting information for this chapter can be found in Appendix B: Figures B1-B5, Tables B1-B8, and section B1.

proton exchange membranes.[213,40,227] They are also known to effectively store small molecules such as hydrogen and to separate gases.[228,229,230]

4.2 METHODOLOGICAL APPROACH

The five HOF systems presented in this chapter were all modeled in a similar fashion. This section will describe the general approach used in both manuscripts, while the subsections will describe the specific differences for the simulations.

4.2.1 Density Functional Theory Approach for Phosphonate HOFs

The geometry optimization of the GTUB-5 series was performed using density functional theory (DFT) and the conjugate gradient method[231] within the Quickstep-CP2K program (version 6.1),[232,233] starting from the experimental crystal structure. Since the GTUB-5 series are bulk material, periodic boundary conditions were applied. The Perdew-Burke-Ernzerhof (PBE)[101] generalized gradient approximation (GGA) functional was used in conjunction with the Grimme D3 dispersion correction[106] and BJ damping.[107] The Gaussian and plane waves method[233,137] was also used, with the valence orbitals expanded in terms of molecularly optimized Gaussian basis sets of double-ζ plus polarization quality and the core electrons represented by norm-conserving Goedecker-Teter-Hutter pseudopotentials[234,235] and Γ-point sampling was used.

4.2.2 DFT methodology for GTUB-5

Atomic-only optimization of GTUB-5 was performed starting from the experimental crystal structure and with the lattice vectors set to their experimental values, using a reoriented 1x1x1 cell (a=25.452 Å, b=22.863 Å, c=7.1798 Å, α=γ= 90.0°, β = 102.325°). The valence electrons were described by a Gaussian basis set of double-ζ plus polarization (MOLOPT-DZVP)[236] quality. The plane-wave cutoff in reciprocal space was set to 550 Ry, with a Gaussian mapping of 60 Ry over five multi-grids. The self-consistent field was converged to 10^{-6} Ry with the 'FULL_ALL' preconditioner using the orbital transformation method with a HOCO-LUCO gap of 1.67 eV. Single point calculations were performed using CP2K to obtain the HOCO-LUCO isosurface plots, orbital populations, and HOCO-LUCO gap. A second single point calculation was performed using the Slater-Type Orbital (STO) software ADF-BAND 2018.104[179,134] to obtain the projected density of states (pDOS), band structure, and band gap. The periodic ADF-BAND calculations were performed using an all-electron double-ζ plus polarization (DZP) basis set, PBE-D3-BJ, and

Γ-point sampling for the 1x1x1 unit cell, with good numerical quality. The HOCO-LUCO gaps obtained from CP2K and ADF-BAND were both 1.65 eV (thus, the HOCO-LUCO isosurfaces and orbital populations obtained from CP2K are expected to be the same as those from ADF-BAND).

4.2.3 DFT methodology for Ni-, Cu-, Zn-, Pd-GTUB-5

Lattice and geometry optimizations were performed on the crystal structures in the crystallographic information files (CIFs). The Goedecker-Teter-Hutter (GTH) short-range basis sets were applied, which describe the valence electrons with double-ζ polarization (DZVP-MOLOPT-SR-GTH)[236] functions. All calculations were performed with the functional as described above, PBE-D3-BJ. The Gaussian-type orbitals (GTOs) were expanded in reciprocal space with an 800 Ry cut-off and a 60 Ry Gaussian mapping over 5 multigrid's using Γ-point sampling. The SCF was converged using the orbital transformation (OT)[237] method and the preconditioner 'FULL_ALL', requiring a self-consistency of $1x10^{-9}$ a.u. Geometry and lattice optimizations were converged with a derivative tolerance of $1x10^{-7}$ a.u./Å and an external pressure of 100 bar for the lattice, while maintaining monoclinic symmetry. The Cu-GTUB-5 system was optimized in both the ferromagnetic (FM) and antiferromagnetic (AFM) spin configurations, using the same geometry and lattice optimization procedure mentioned above. The resulting magnetic exchange energy, $E_{ex} = E_{AFM} – E_{FM} = 0.19$ meV, suggests that the FM configuration is the lower energy Cu-GTUB-5 system, and thus the FM configuration is presented in the manuscript. Single-point calculations were performed using the same SCF convergence criteria to obtain the orbital populations (**Appendix Tables B1-B4**), projected density of states (pDOS), total density of states, RESP-REPEAT partial charges, and HOCO/LUCO isosurfaces. Sphere sampling for the RESP-REPEAT[149,238,239] fitting made use of van der Waals radii from the universal force field (UFF).[240] Vibrational analysis was performed for the Zn-GTUB-5 system using the same SCF convergence criteria as the optimizations. Vibrational analyses were attempted for the other M-GTUB-5 systems, but due to resource constraints they never fully converged.

4.3 RESULTS AND DISCUSSION

4.3.1 Semiconductive Microporous Hydrogen-Bonded Oragnophosphonic Acid Frameworks: GTUB-5

HOFs have attracted immense interest in recent years.[223,241,242] In HOFs, the linker connectivity is achieved via hydrogen-bonded networks rather than inorganic building units (IBUs).[243,178,244,245,54] Hydrogen bonds provide simpler connectivity options compared to the complex molecular, one-, two-, and three-dimensional IBUs of MOFs.[211] Therefore, the design and synthesis of stable hydrogen-bonded supramolecular networks can be more easily achieved compared to that of MOFs. HOFs are also more convenient to recycle and HOFs are free of heavy metal ions providing environmentally friendly solutions. The recent interest in HOFs has resulted in several review articles[214,246,247] summarizing their applications in CO_2 capture,[248,249,250] and proton conductivity.[251,252] However, to date, no semiconductive HOFs have been reported in the literature. Thermally stable and permanently microporous semiconducting HOFs could revolutionize the design of supercapacitors and electrodes due to their simpler chemistry compared to MOFs. In this communication, we present the first example of a HOF (known as GTUB5, where TUB stands for Technische Universität Berlin and G for Gebze), synthesized using phosphonic acid functional groups ($R\text{-}PO_3H_2$), which exhibits a low band gap, proton conductivity, and high thermal stability.

The phosphonic acid functional group has two protons and one oxygen from the $P=O$ bond, which allow it to form multiple hydrogen bonds with other phosphonic acid groups and thereby stabilize the resulting HOF. The phosphonic acid functional group contains two deprotonation modes with pK_a values of 1.7 and 7.4, respectively.[244] Therefore, in order to synthesize our phosphonate HOF, we adopted a crystallization method at pHs between 1.7 and 7.4 with mixed phosphonic acid linkers of phenylphosphonic acid (PPA) and 5,10,15,20-tetrakis [*p*-phenylphosphonic acid] porphyrin (H_8-TPPA) to ensure that at least one of the phosphonic acid moieties is not fully deprotonated. H_8-TPPA exhibits a planar tetratopic geometry with a 90° angle between the phenylphosphonate tethers.[253,254] Given these starting conditions and materials, it is expected that a mixed linker strategy involving H_8-TPPA and PPA could produce two-dimensional HOFs with hexagonal void channels.

The structure of GTUB5 was characterized using single crystal X-ray diffraction (XRD). As seen in **Figure 4.1-A, -B**, GTUB5 is composed of two-dimensional sheets of hydrogen-bonded H_8-TPPA and PPA moieties. The structure contains two different hydrogen-bonding patterns, which are observed between different H_8-TPPA units and between H_8-TPPA and PPA (see **Figure 4.1-E**). In the first pattern, the P = O bond from the H_8-TPPA unit is exclusively involved in creating the (almost linear) double hydrogen-bonding pattern between each unit. In the second pattern, the hydrogen bond forms between the second protonated hydroxyl group of the H_8-TPPA and the deprotonated PPA^{2-}. The four DMF solvent molecules in the HOF structure act as a Lewis base acquiring the PPAs' protons.

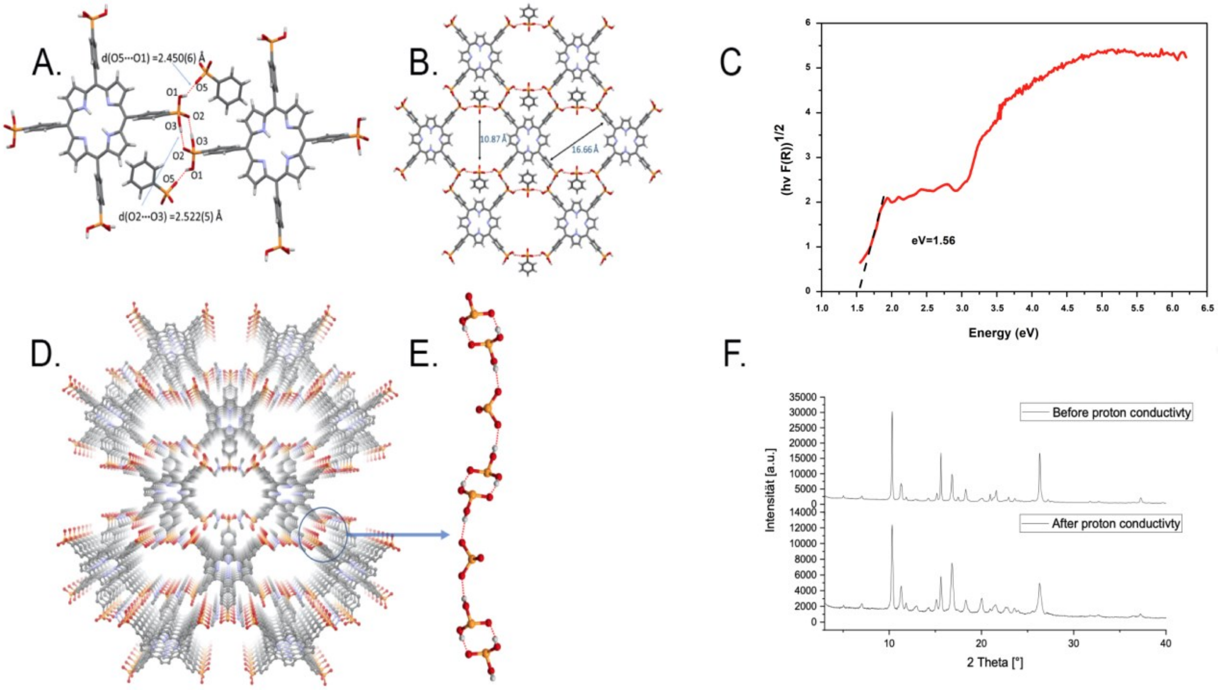

Figure 4.1. *General properties of the GTUB-5 material. A) Portion of hydrogen-bonded network of GTUB-5. B) Depiction of hexagonal void spaces in GTUB-5. C) Tauc plot from the solid-state UV-Vis spectrum of GTUB-5, showing a band gap of 1.56 eV. The second jump at 2.88 eV corresponds to the Soret band of the porphyrin core at 430 nm. D) Layer structure of*

GTUB-5. E) One-dimensional hydrogen-bonded building unit of GTUB-5. F) XRD pattern before and after the proton conductivity measurements.

The band gap was estimated from a solid-state diffuse reflectance UV-Vis spectrum of the GTUB-5 crystals (see **Appendix Figure B1**). As seen in **Figure 4.1–C**, the Tauc plot derived from the spectrum yields a narrow band gap of 1.56 eV. The second jump at 2.88 eV corresponds to the Soret band of the porphyrin core at 430 nm. From a cyclic voltammetry measurement on GTUB-5 in DMSO (see **Appendix Figure B2**), the first oxidation and reduction potentials were measured to be 0.42 V and -1.23 V, respectively, yielding a HOCO–LUCO gap of 1.65 eV supporting this hypothesis.

To gain insight into the semiconductive nature of GTUB-5, we performed density functional theory (DFT) calculations. The details of the calculations, employing hybrid Gaussian plane-wave (GPW) basis sets and Slater Type Orbital basis sets, can be found in the methodology section. **Figure 4.2** shows a periodic representation of the optimized geometry, which is in close agreement with the experimental crystal structure (see **Table 4.1** and **Figures 4.3-4.5**). A single point calculation on the optimized structure yields a band gap of 1.65 eV, in very good agreement with the experimental result of 1.56 eV. As seen in **Figure 4.2**, the HOCO and LUCO are predominantly localized on some of the porphyrins within the supercell (of which, a single unit cell is delineated by the black rectangle), but not all of them; with the LUCO occupying the same porphyrins as the HOCO.

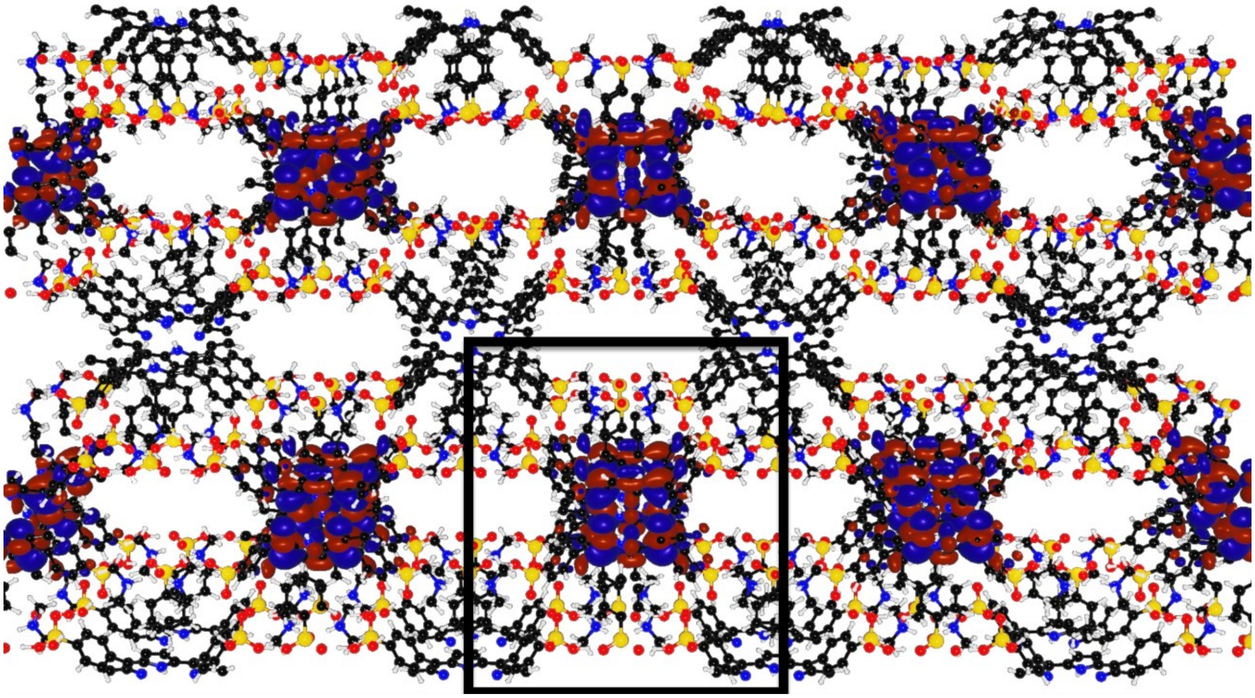

Figure 4.2. *Periodic representation of GTUB-5, with the unit cell indicated by the black box. This represents the HOCO isosurface corresponding to an electron density of 0.01 electrons per Å^3 (negative and positive phases are shown in red and blue, respectively). (O – red; N – blue; P – yellow; C – black; H – white).*

Table 4.1. *Comparison of experimental and calculated average inter-atomic distances (in Å). Standard deviations in distances are given in brackets. The calculated structure was obtained from a geometry optimization of the experimental crystal structure at the PBE-D3-BJ DZVP-550 Ry level of theory.*

Atom pair	Experimental	Calculated
	Figure 4.3	
C-P	1.78	1.80
	(0.018)	(0.008)
P-O	1.53	1.58
	(0.003)	(0.013)
O-H	0.83	1.16
	(0.013)	(0.096)

C-C	1.49	1.46
	(0.000)	(0.023)
C=C	1.39	1.40
	(0.025)	(0.01)
	Figure 4.4	
N-C	1.78	1.80
	(0.018)	(0.008)
N=C	1.53	1.58
	(0.003)	(0.013)
N-H	0.88	1.05
	(0.012)	(0.015)
N--N	2.92	2.93
	(0.000)	(0.000)
	Figure 4.5	
O-O	2.47	2.43
	(0.018)	(0.000)
O--H	1.88	1.75
	(0.164)	(0.005)

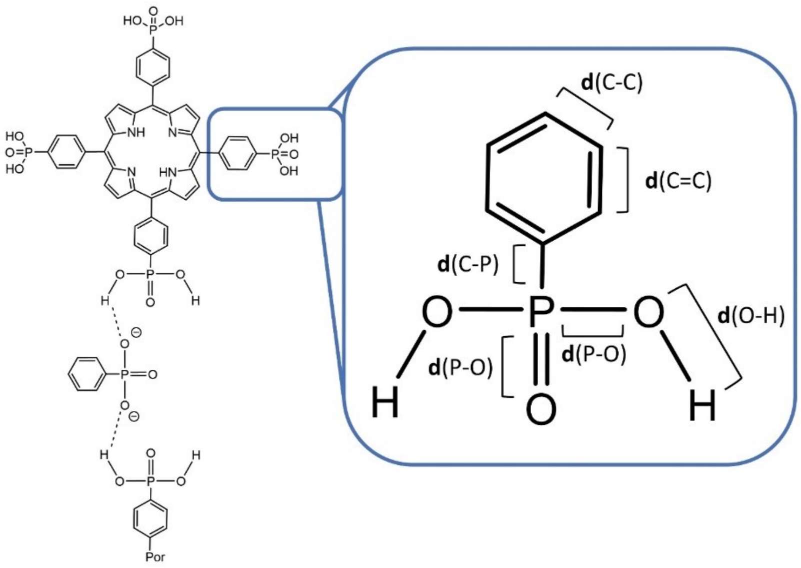

Figure 4.3. *Simplified chemical structure of the* ***GTUB5*** *building block, highlighting one of the phenyl-phosphonic acid groups. The bond distance labeling is used in* ***Table 4.1****.*

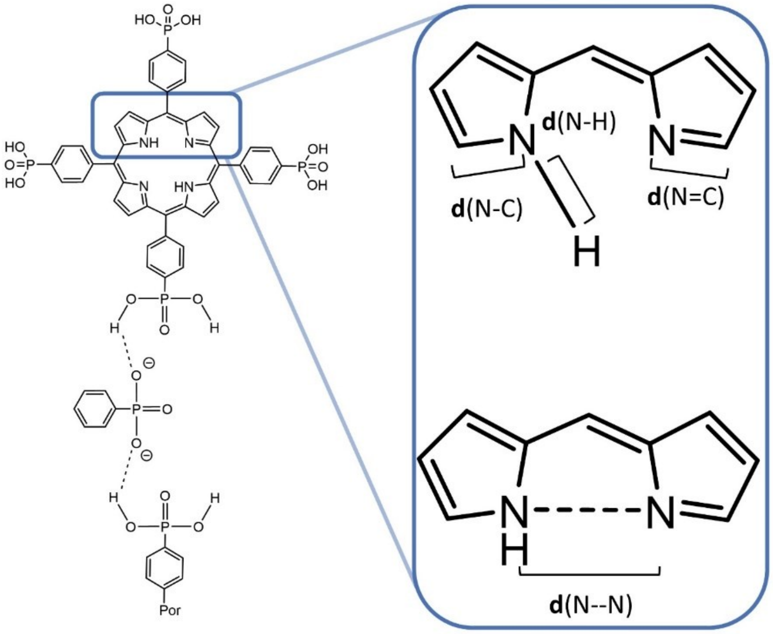

***Figure 4.4.** Simplified chemical structure of the **GTUB5** building block, highlighting the dipyrromethene portion of the porphyrin group. The bond distance labeling is used in **Table 4.1**.*

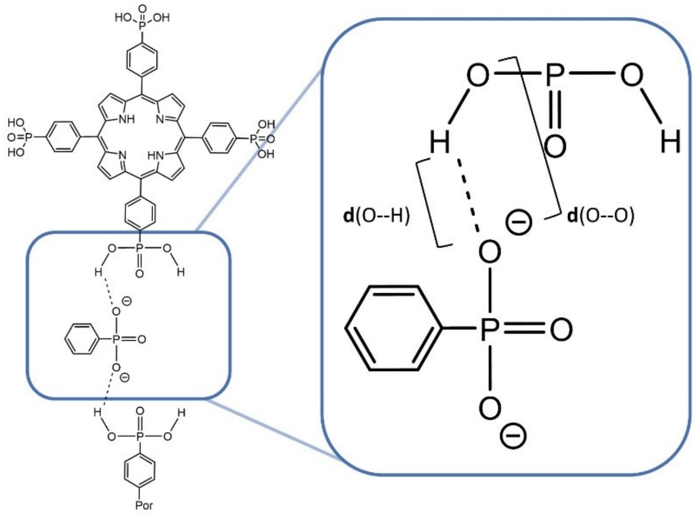

Figure 4.5.** Simplified chemical structure of the GTUB5 building block, highlighting the hydrogen bonding between neighbouring phenyl-phosphonic acid groups. The bond distance labeling is used in **Table 4.1.

Focusing on the portions of the structure that have significant HOCO and LUCO density, we see that the HOCO and LUCO are localized on the same porphyrin (see **Figure 4.6**). Moreover, they are mostly confined to a subset of the carbon and nitrogen atoms. The HOCO is composed of π orbitals mostly on sp^2 hybridized carbons and nitrogens, while the LUCO is composed of π* orbitals on some of the sp^2 carbons and nitrogens. As shown in **Table 4.2**, ~75% of the HOCO and LUCO orbital contributions are from the carbon and nitrogen 2p orbitals of the porphyrin. **Table 4.2** also shows that a HOCO-LUCO transition would lead to an increase in the carbon $2p_x$ orbital population, a slight decrease in the carbon $2p_y$ population, and a slight increase in the carbon $2p_z$ population; while the nitrogen $2p_x$ and $2p_z$ populations both decrease (the $2p_y$ population remains negligible). These results suggest that the semiconductive nature of GTUB-5 is predominantly determined by π- π* transitions involving orbitals localized on some of the porphyrin carbons and nitrogens. Inspection of the projected density of states (pDOS) confirms that the HOCO-LUCO gap is predominantly due to orbitals localized on carbons and nitrogens (see **Figure 4.7**).

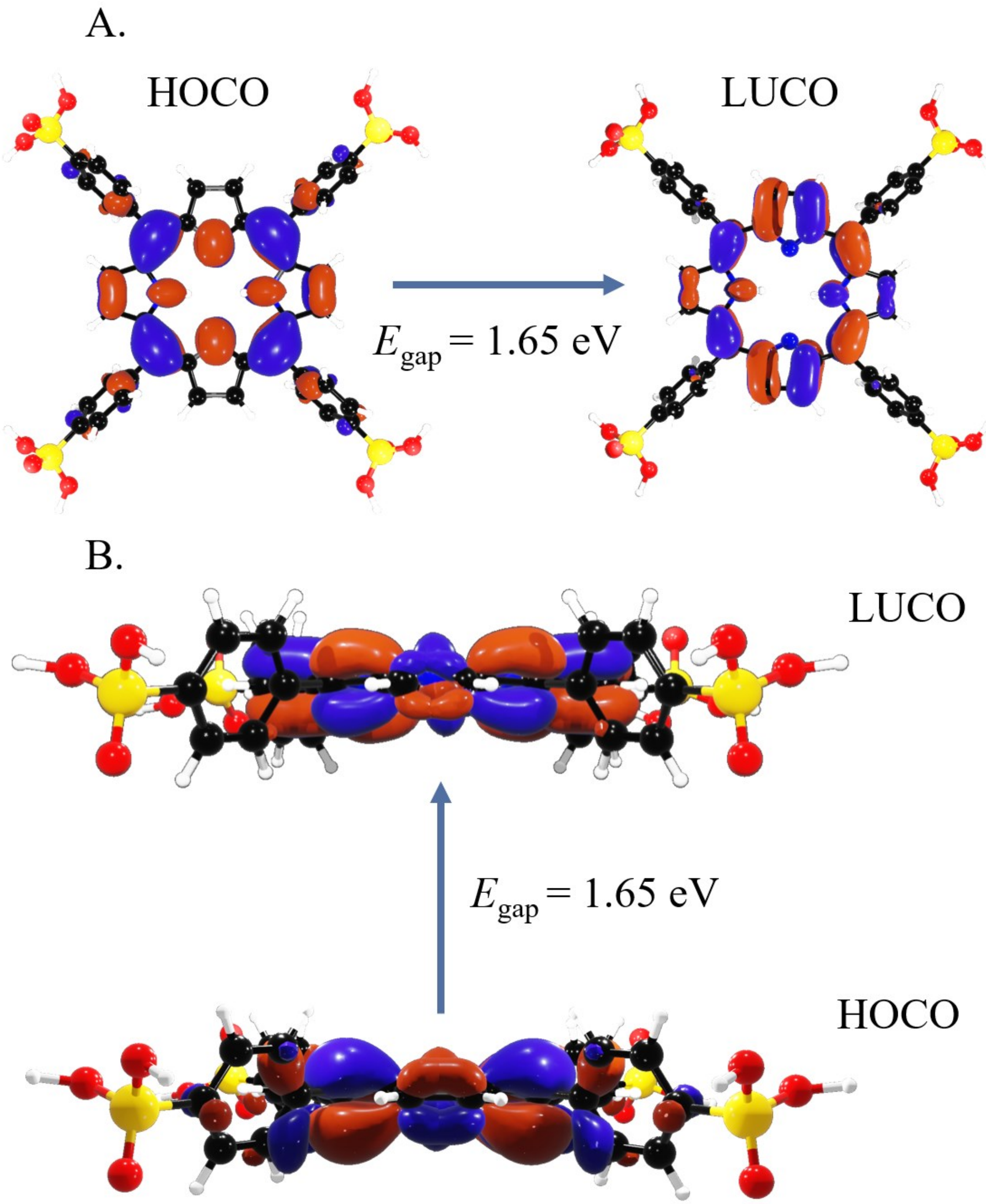

Figure 4.6. *HOCO and LUCO isosurfaces, corresponding to an electron density of 0.01 electrons per* Å^3*.* ***A)*** *Top view.* ***B)*** *Side view. Red/blue correspond to the negative/positive phases. (O – red; N – blue; P – yellow; C – black; H – white).*

Table 4.2. *Contributions from the 2p orbitals on the porphyrin carbons and nitrogens to the HOCO and LUCO.*

Carbon	**2p$_x$**	**2p$_y$**	**2p$_z$**	**Sum**
HOCO	0.366	0.042	0.134	0.541
LUCO	0.484	0.020	0.170	0.674

Nitrogen	**2p$_x$**	**2p$_y$**	**2p$_z$**	
HOCO	0.163	$4.70\text{x}10^{-07}$	0.053	0.216
LUCO	0.048	$5.22\text{x}10^{-4}$	0.020	0.067

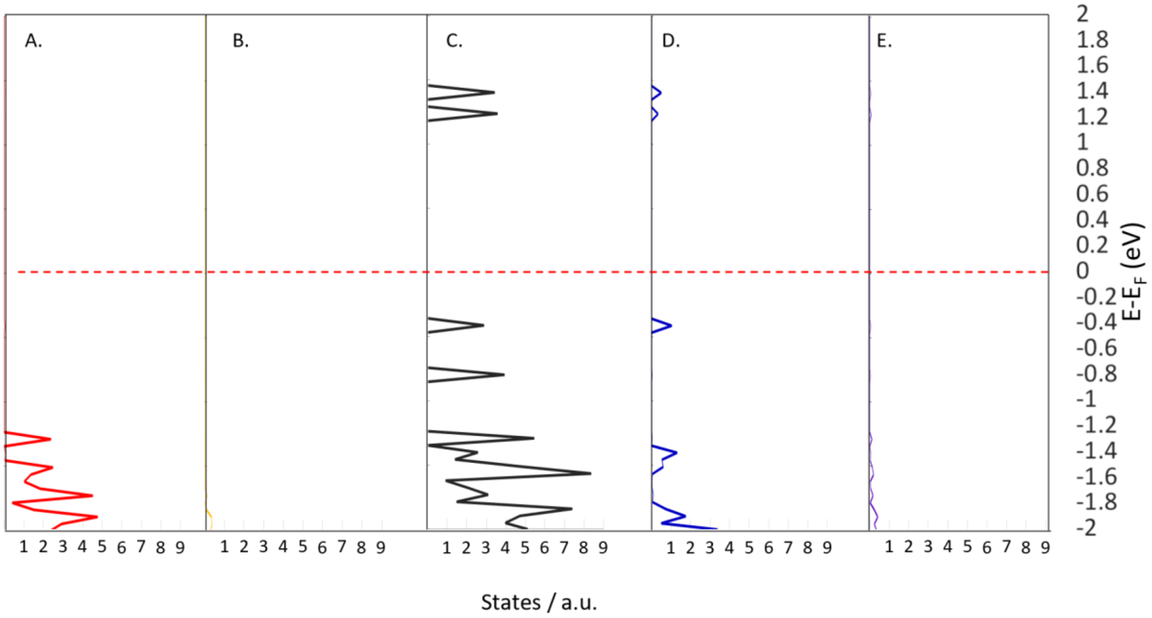

Figure 4.7. *Projected density of states (pDOS) for O(A.), P(B.), C(C.), N(D.), and H(E.) in GTUB-5, generated using ADF-BAND.*[51]

Given the presence of –PO_3H_2 groups in its hydrogen-bonded framework, the proton conductivity of GTUB-5 was measured. Electrochemical impedance spectroscopy measurements were carried out at 75% and 90% relative humidity (%r.h.) and temperatures in the range of 25°C to 75°C (see **Appendix B**, **section B1**, and Ref.[255] for setup details). At 75%r.h., we see that the proton conductivity of GTUB-5 increases from 8.29×10^{-7} to 3.00×10^{-6} S cm^{-1} as the temperature is increased from 25°C to 75°C, while a non-monotonic increase is observed at 90%r.h. (see **Table 4.3**). Furthermore, at a given temperature, we observe an increase in the proton conductivity with increasing relative humidity. The activation energies, as sum of the migration energy and the formation energy of defects, were extracted from the slopes of the Arrhenius plots (see **Appendix Figure B3**) to be $E_A = 0.26$ eV and $E_A = 0.14$ eV at 75°C and 90°C, respectively. These low activation energy values suggest that a Grotthuss mechanism with high proton movability and therefore low migration energy is the predominant mechanism for proton conduction through the framework. As seen in **Figure 4.1–F**, the XRD pattern of the sample recorded before and after the proton conductivity experiments slightly changes, indicating that the structure was slightly affected by the humidified atmosphere and the applied temperatures up to 75°C during the measurements.

Table 4.3. *Proton conductivities and activation energies (E_A) of GTUB-5 at different relative humidities.*

Relative humidity [%rh]	Temp.	75	90
Conductivity [S cm^{-1}]	25 °C	$8.29 \cdot 10^{-7}$	$3.55 \cdot 10^{-6}$
	50 °C	$1.67 \cdot 10^{-6}$	$3.26 \cdot 10^{-6}$
	75 °C	$3.00 \cdot 10^{-6}$	$4.20 \cdot 10^{-6}$
E_A [eV]		0.26	0.14

4.3.2 Tuning Structural Properties of Porphyrin-based Hydrogen-Bonded Organic Frameworks by Metal Insertion: Ni-, Cu-, Zn-, Pd-GTUB-5

Until our recent report,[213] there were no HOFs constructed using aryl phosphonic acids in the literature. The reported HOF, termed GTUB-5, is permanently porous, proton-conductive, highly thermally and chemically stable, and possesses an indirect band gap of 1.56 eV, which is comparable to those of semiconductors like GaAs (1.42 eV) and metal halide perovskites (1.60 eV).[256,257] Phosphonic acid functional groups are known to form strong hydrogen-bonded networks.[213] They have two protons and three oxygen atoms, making them ideal for constructing permanently porous HOFs, while carboxylic acids have only one proton and two oxygen atoms.[191] The presence of higher numbers of hydrogen and oxygen atoms around a concentrated tetrahedral geometry imparts phosphonic acids with structural richness and stability.[178,211,258,64,53] Thus, phosphonate HOFs are unique compared to other HOF families due to the multiple number of hydrogen bonds they can form and their high stabilities.

GTUB-5 was originally synthesized with a metal-free porphyrin ring.[213] In this study, we inserted different metal atoms in the central porphyrin ring of the *p*-H_8-TPPA linker as a way of modifying the structural and optical properties of GTUB-5. In particular, we synthesized three isostructural HOFs, viz., Cu-GTUB-5, Pd-GTUB-5, Zn-GTUB-5, and one structural isomer Ni-GTUB-5, solved their crystal structures, estimated their band gaps using solid-state diffuse reflectance spectroscopy (DRS). We also performed DFT calculations to calculate the band gaps and gain insight into the electronic structures of these HOFs and performed molecular simulations to estimate their textural properties. In our previous study, it was found that the semiconductivity of GTUB-5 originates from electronic interactions between the π-stacked porphyrin rings, which are held together by the phosphonic acid groups.[213] Introducing different metal atoms into the central porphyrin core is therefore expected to change the electronic structure of the HOF by modifying the relative orientations of the porphyrin rings. This modification, in turn, has implications on the geometric properties of the unit cell, and band gap of the resulting HOF, as will be discussed below.

Single crystal diffraction revealed that Cu-GTUB-5, Pd-GTUB-5, and Zn-GTUB-5 are isostructural to each other, while Ni-GTUB-5 has a twisted structure and different hydrogen bonding pattern compared to the others (see **Figure 4.8**). To gain a more accurate picture of the hydrogen bonding, we performed geometry and lattice optimizations of the crystal structures using density functional theory (DFT) (the full details of the periodic DFT calculations using the CP2K-Quickstep[92] program are in the methodology). **Table 4.4** shows the average lengths of the bonds exhibiting the largest differences across the M-GTUB-5 series (the remainder of the average bond lengths are given in **Table B5** of the **Appendix**). Given the close agreement between the calculated and experimental bond distances and lattice vectors (see **Appendix Tables B5 and 4.5**), the optimized structures of the M-GTUB-5 systems (see **Figure 4.9**) are considered to be good representations of the actual structures. As seen in **Figure 4.9–C**, the Ni-GTUB-5 porphyrin structure is rotated around the *a*-axis. Our DFT results suggest this is partly due to the short Ni-N bonds in the centre of the porphyrin (as seen in **Table 4.4**, the Ni-N bonds are the shortest of the M-N bonds across the series). As seen in **Figure 4.7–A,** Cu-GTUB-5, Pd-GTUB-5, and Zn-GTUB-5 have unique hydrogen bonding units, which are composed of rod-shaped hydrogen-bonded phosphonic acid groups from phenylphosphonic acid and H_8TPPA linkers. This rod-shaped hydrogen bonding pattern is further crosslinked into layered hydrogen-bonded building units via dimethyl-ammonium (DMA^+) cations. Ni-GTUB-5 also has a similar pattern but with twisted porphyrins (See **Figure 4.7–B**).

As seen in the optimized structures (**Figures 4.6** and **4.7**), there are significant differences between Cu-/Pd-/Zn-GTUB-5 and Ni-GTUB-5 in terms of hydrogen bond numbers and O--H lengths. The three isostructural HOFs, Cu-, Pd-, and Zn-GTUB-5, are built up like the previously reported GTUB-5 with the fully deprotonated phenylphosphonic acid molecules and dimethylammonium cations involved in several hydrogen bonds. In the Cu-, Pd-, and Zn-GTUB-

5 unit cells, there are two O--H-O hydrogen bonds between each phenyl-phosphonate and 5,10,15,20-Tetrakis[*p*-phenylphosphonic acid] porphyrin (for a total of 16 O--H-O bonds per unit cell), while in the Ni-GTUB-5 unit cell, each phenyl-phosphonate not bonded to the porphyrin forms one O--H-O hydrogen bond (for a total of 12 per unit cell). This difference in numbers is due to the shorter Ni-N bonds, which in turn cause the Ni-based porphyrin to twist along the a-axis, allowing each porphyrin-phosphonate access to only one O--H-O phenyl-based hydrogen bond (see **Table 4.4** and **Figure 4.10**). As seen in **Table 4.4**, there are differences in the average donor-proton (O-H), proton-acceptor (O--H), and donor-acceptor distances (O---O) across the M-GTUB-5 series. The longest donor-proton (O-H) bonds are in Cu-GTUB-5, followed by Zn-, Pd-, and Ni-GTUB-5 with the shortest bonds. This trend is reversed for the proton-acceptor bonds (O--H). With regards to the average O--H-O hydrogen bond angle, Cu-GTUB-5 has the smallest angle, followed by Zn-, Ni-, and Pd-GTUB-5 with the largest angle (see **Table 4.6**). The average donor-acceptor bond length (O---O) is longest in Cu-GTUB-5, followed by Ni-, Pd-, and Zn-GTUB-5 with the shortest bonds. Typically, the strength of a hydrogen bond depends on the donor-acceptor bond length and angle, with shorter bond lengths and angles closer to 180° yielding stronger hydrogen bonds.[259] When considering the standard deviations in the distances and angles (shown in **Tables 4.4** and **4.6**), we find that the donor-acceptor bond lengths and angles are statistically similar to each other; thus, it appears that all systems have similar hydrogen bond strengths. The presence of short O---O hydrogen bonds (~2.5 Å) and angles close to 180° (~176°) in all of the reported M-HOFs is indicative of strong hydrogen bonding.

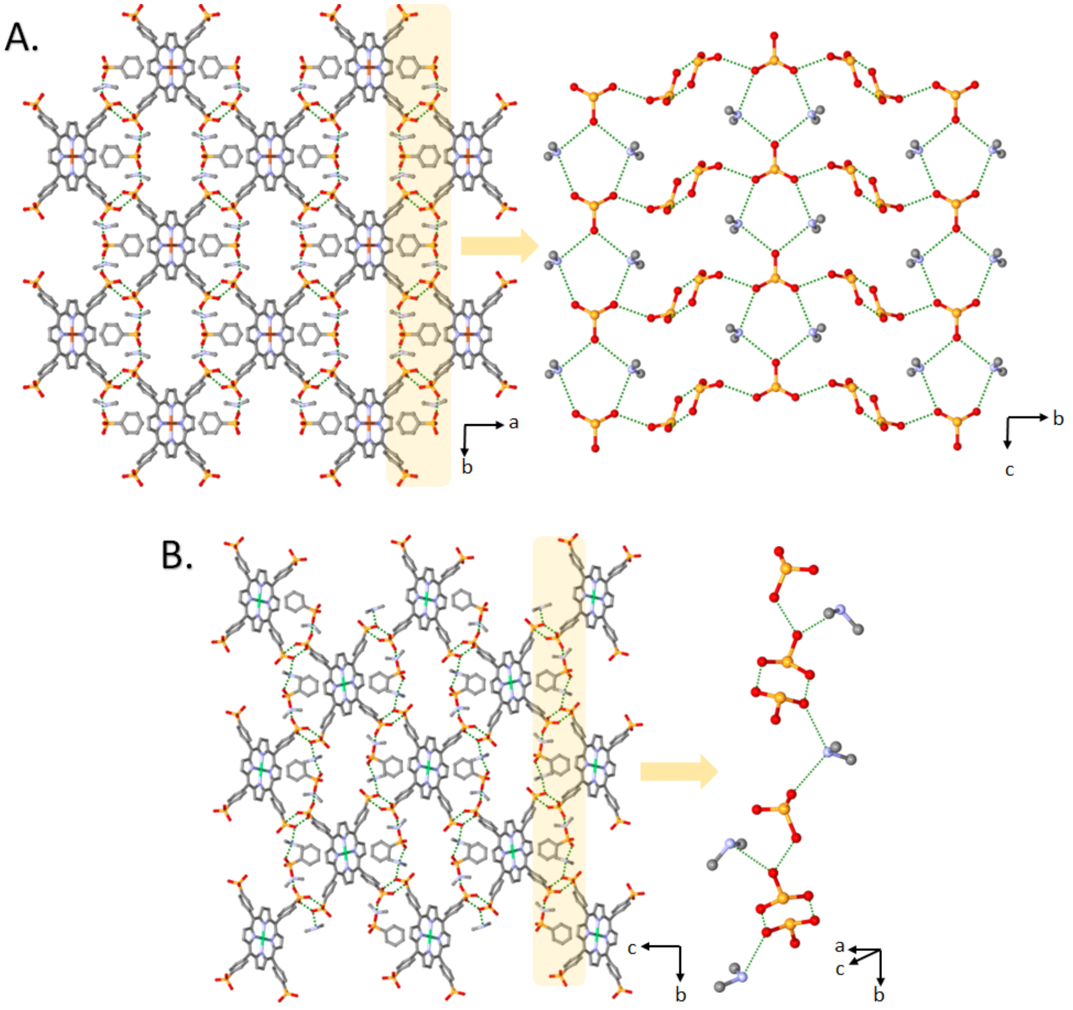

Figure 4.8. *A) Illustration of the porous HOF of M-GTUB-5 (M = Cu, Pd, Zn) showing their 2D network formed by O···O and O···N hydrogen bonding interactions between phosphonate arms and DMA cation. Cu-GTUB-5 structure is shown for representation. B) Schematic diagram of the porous HOF of Ni-GTUB-5 showing 1D hydrogen-bonded chains by O···O and O···N hydrogen bonding interactions between phosphonate arms and DMA cation.*

Table 4.4. *DFT-calculated average interatomic distances for select pairs of atoms. M-N refers to the metal-nitrogen pairs in the porphyrins; O-H refers to the hydrogen bond donor oxygen-proton pair; O--H$_{(O\text{-}H\text{-}O)}$ refers to the hydrogen bond acceptor oxygen-proton pair in oxygen-oxygen hydrogen bonds; O---O refers to the donor oxygen-acceptor oxygen pair; N-H refers to the hydrogen bond donor oxygen-proton pair; O--H$_{(O\text{-}H\text{-}N)}$ refers to the hydrogen bond acceptor oxygen-proton pair in oxygen-nitrogen hydrogen bonds; and O---N refers to the donor oxygen-acceptor nitrogen pair; Por (H--H)axis refers to the distance between H atoms on opposite sides*

of the porphyrin unit along a particular axis. All distances are in Å and angles and standard deviations are given in brackets.

Atom Pairs	**Ni-GTUB-5**	**Cu-GTUB-5**	**Zn-GTUB-5**	**Pd-GTUB-5**
M-N	1.96 (0.00)	2.02 (0.01)	2.05 (0.02)	2.04 (0.01)
O-H	1.05 (0.02)	1.11 (0.11)	1.08 (0.04)	1.06 (0.02)
O--$H_{(O-H-O)}$	1.47 (0.05)	1.39 (0.08)	1.40 (0.09)	1.44 (0.07)
O---O	2.52 (0.03)	2.53 (0.32)	2.48 (0.05)	2.50 (0.04)
N-H	1.06 (0.01)	1.06 (0.00)	1.06 (0.00)	1.05 (0.00)
O--$H_{(O-H-N)}$	1.65 (0.01)	1.70 (0.02)	1.66 (0.00)	1.73 (0.04)
O---N	2.71 (0.06)	2.73 (0.01)	2.72 (0.00)	2.77 (0.03)
Por $(H\text{--}H)_{b\text{-axis}}$	10.03	10.19	10.26	10.19
Por $(H\text{--}H)_{a/c\text{-axis}}$	10.07	10.13	10.16	10.16

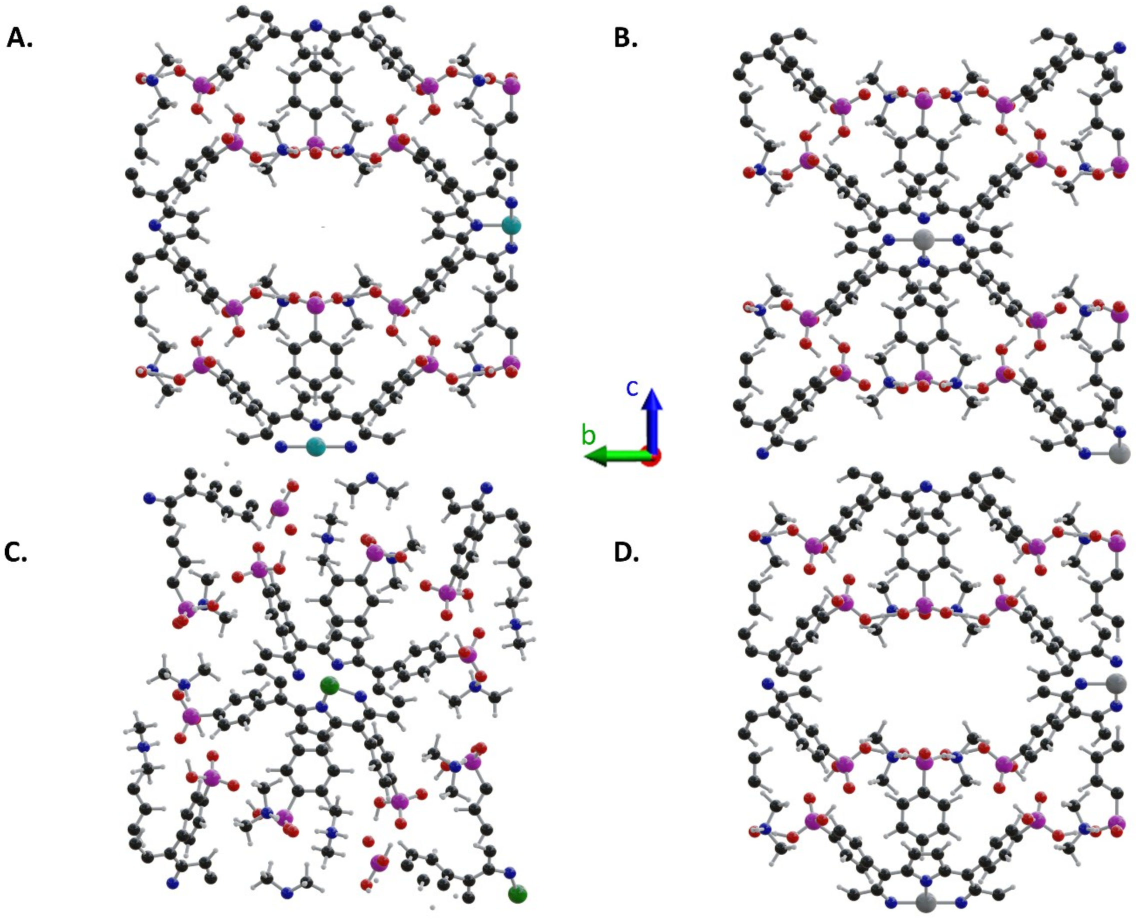

Figure 4.9. *DFT-optimized structures of the M-GTUB-5 systems. A) Cu-GTUB-5, B) Pd-GTUB-5, C) Ni-GTUB-5, D) Zn-GTUB-5. (Colour scheme: Phosphorous – purple; Oxygen – red; Nitrogen – blue; Carbon – black; Hydrogen – white; Copper – cyan; Palladium – light gray; Nickel – green; Zinc – dark gray).*

Table 4.5. *Experimental and DFT-calculated monoclinic lattice vectors, angles, and unit cell volumes of the M-GTUB-5 systems. Lattice vectors are in Å, angles are in degrees, and volumes are in Å^3. The DFT-calculated lattice vectors and volumes are in shown in brackets.*

	Ni-GTUB-5	Cu-GTUB-5	Zn-GTUB-5	Pd-GTUB-5
$\vec{a}$	7.251 (6.658)	7.106 (6.881)	7.090 (6.853)	6.990 (6.915)
$\vec{b}$	23.77 (22.32)	22.91 (22.80)	22.98 (22.62)	23.16 (22.93)
$\vec{c}$	23.64 (24.83)	25.87 (25.84)	25.03 (25.90)	24.88 (25.08)
$\angle\beta$	95.3	93.05	94.51	94.71

∠α = ∠γ	90.0	90.0	90.0	90.0
Volume	4057 (3675)	4205 (4048)	4066 (4003)	4013 (3962)

Table 4.6. *DFT-calculated average bond angles for hydrogen bonds in the porphyrins. All angles are in degrees and standard deviations are given in brackets.*

Atoms in angles	Ni-GTUB-5	Cu-GTUB-5	Zn-GTUB-5	Pd-GTUB-5
∠O-H--O	176.5 (1.97)	175.9 (2.74)	176.0 (2.52)	177.5 (1.60)
∠N-H--O	172.5 (2.90)	165.6 (8.43)	176.8 (0.84)	170.1 (6.09)

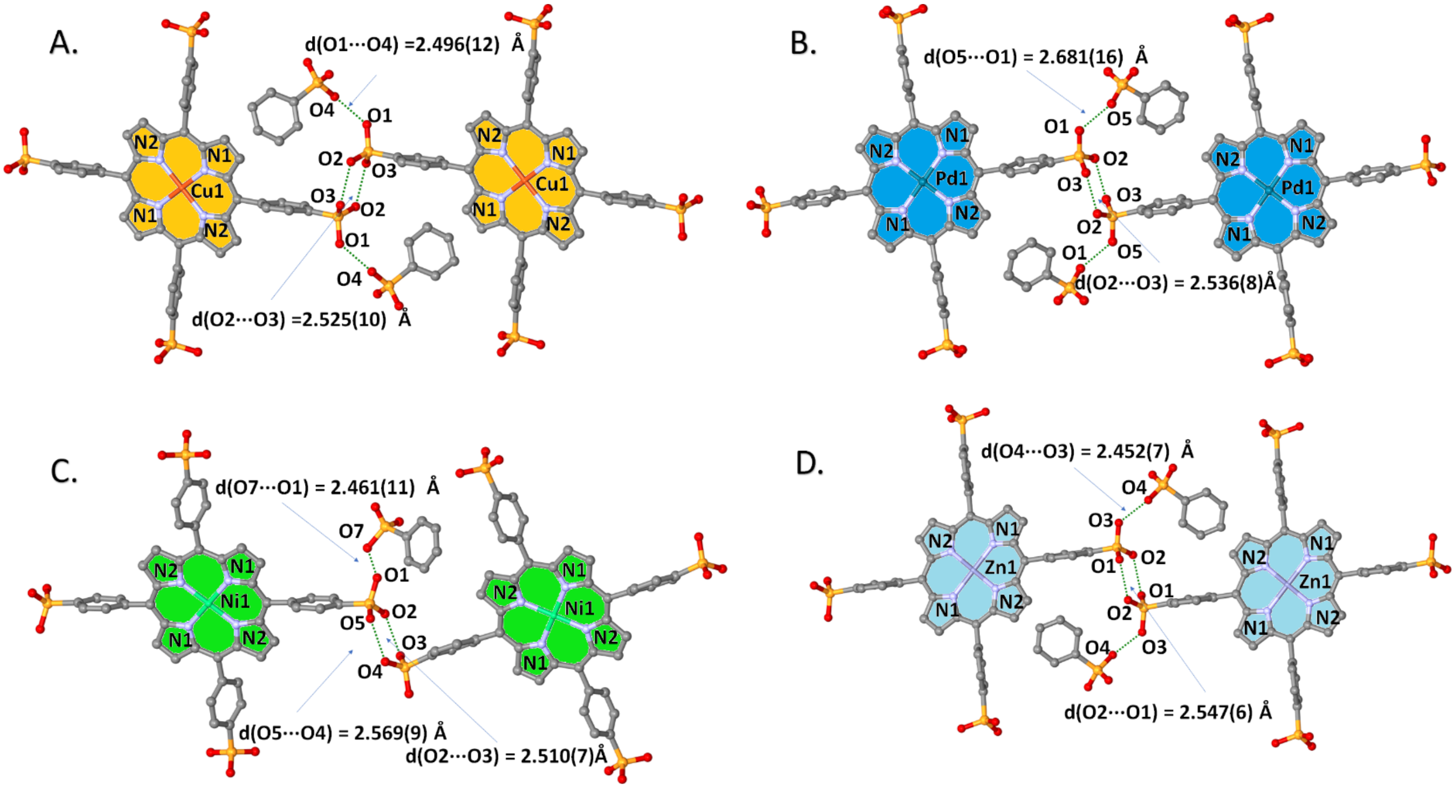

Figure 4.10. *Perspective views of hydrogen-bonding motifs showing strong O···O hydrogen bonding (~2.5 Å) between the phosphonate groups. A, B, C, and D represent M-GTUB-5 crystal structures, where M = Cu, Pd, Ni, and Zn, respectively.*

A vibrational analysis on Zn-GTUB-5 reveals that the O-H stretching mode (belonging to the O--H-O bond) lies between 2286-2458 cm^{-1} (see **Table 4.7**). Upon examination of the experimental FTIR spectra of the M-GTUB-5 systems (**Figures 4.11 and 4.12**) and the simulated

FTIR spectrum of Zn-GTUB-5 (**Figure 4.12**), it becomes apparent that the broad feature centred around 2350 cm^{-1} corresponds to this O-H stretching mode. This peak does not shift across the M-GTUB-5 series, which further suggests that there is no significant change in the hydrogen bonding strength upon changing the metal.

Table 4.7. *Description of IR-active modes in the simulated spectrum of Zn-GTUB-5.*

Scaled frequency (cm^{-1})	**IR-active mode**
750	Wiggling of sp$_2$ carbons involved in phenyl and porphyrin
800	Wiggling of phosphorous and hydrogen atoms
880	C-N-C stretching in dimethylammonium ions
950	Hydrogens in porphyrin waving
980	O-H bending
1116-1171	C-H group rocking
1253	C-N bending and C-C bending on porphyrin phenyl-phosphonates
1478	Phenyl puckering
1678	H scissoring on N
2286-2458	O-H stretching
2698-2749	N-H stretching
2949	N-H stretching
3061	C-H stretching

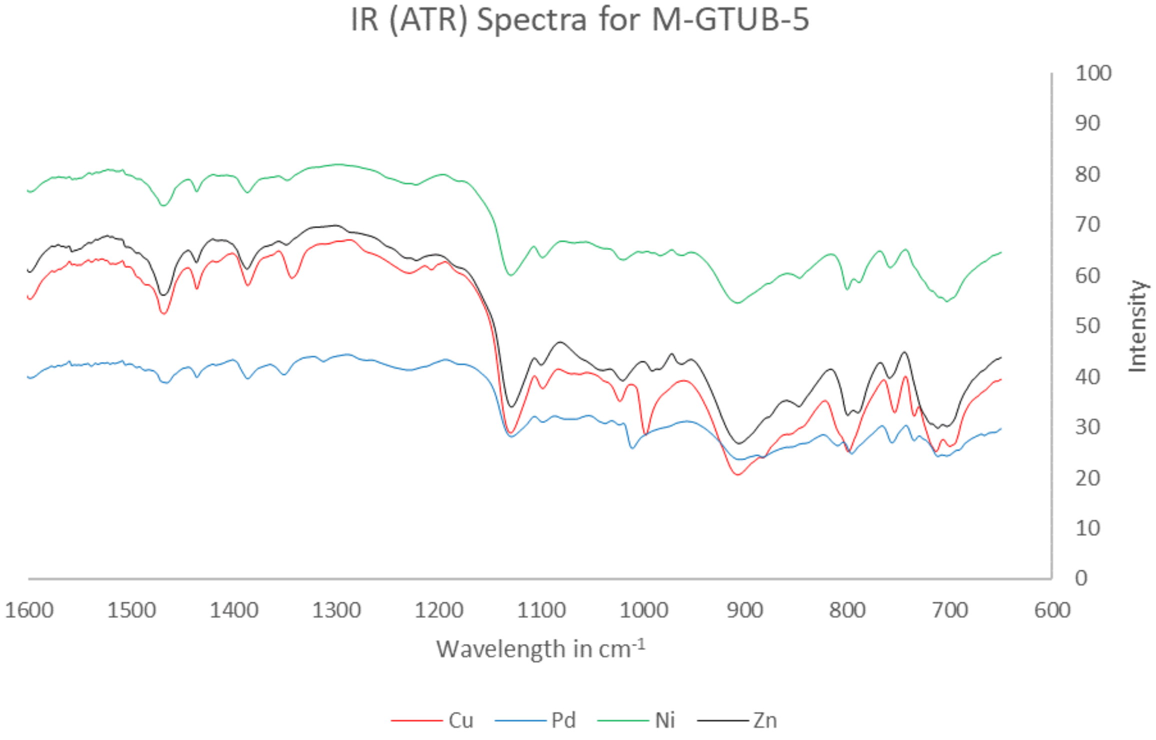

Figure 4.11. *IR (ATR) spectra of Cu-GTUB-5 (Red), Ni-GTUB-5 (Green), Pd-GTUB-5 (Blue), and Zn-GTUB-5 (Black) from 600 to 1600 cm*$^{-1}$.

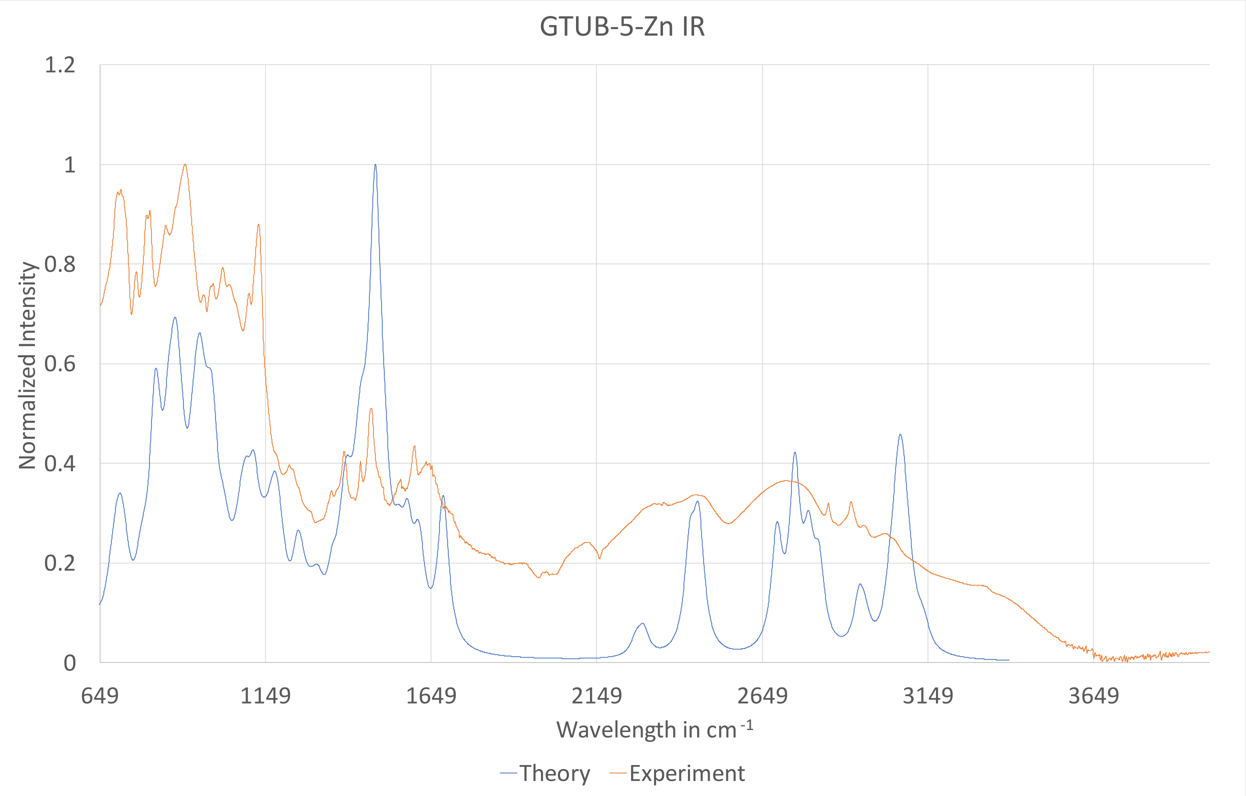

Figure 4.12. *Simulated and experimental IR spectra for Zn-GTUB-5. The simulated spectrum was generated using a Lorentzian line shape with a half-width of 20.0. Both intensities were normalized and the DFT-frequencies were scaled by 0.97.*

Another difference between Cu/Pd/Zn-GTUB-5 and Ni-GTUB-5 is the angle between the phenylphosphonic anion and the porphyrin unit. For Cu-, Pd- and Zn-GTUB-5, the P-C_{para}-H_{para} axis of the phenylphosphonic acid forms a ~ 40° angle (α) with the N_4-plane of the porphyrin core, while for Ni-GTUB-5 this angle is 49.5° (β) (see **Appendix Figure B5**). As a result, Cu-, Pd-, and Zn-GTUB-5 have similar rectangular pores to GTUB-5,[213] while Ni-GTUB-5 has smaller pores due to the twisted porphyrin moieties.

Geometric surface areas and pore size and volume characteristics of Cu-, Ni-, Pd- and Zn-GTUB-5 were calculated with the Poreblazer (v4.0) software[260] using their crystallographically determined unit cells (See **Appendix section B.1** and **Tables B7 & B8** for details of these calculations). The geometric accessible surface areas, were calculated using the method of Düren *et al.*[261] The surface areas were calculated to be 230 m^2 g^{-1}, 85 m^2 g^{-1}, 100 m^2 g^{-1}, and 201 m^2 g^{-1}

for Cu-, Ni-, Pd-, and Zn-GTUB-5, respectively [c.f. 422 m^2 g^{-1} for the metal-free GTUB-5[213]]. Overall, the surface areas of M-GTUB-5 are smaller than that of GTUB-5 because the porphyrin centers are occupied by metal ions. The significantly lower surface areas of Ni- and Pd-GTUB-5 are caused by the twist in the overall structure and large ionic radius of Pd, respectively. Results for the remaining textural properties may be found in Appendix B. In this work, the optical band gap is tuned by inserting metal ions into the porphyrin cores of GTUB-5. The band gaps of Cu-, Pd-, Ni-, and Zn-GTUB-5 in their crystalline states were first estimated via diffuse reflectance spectroscopy (DRS) using an ISR-2600-Plus Shimadzu spectrophotometer (see **Appendix B** for DRS spectra). **Figure 4.13** shows the Tauc plots derived from the leftmost edge of the spectra, yielding narrow band gaps of 1.44, 1.58, 1.37, and 1.62 eV for Cu-, Ni-, Pd-, and Zn-GTUB-5, respectively (see **Appendix B** for Tauc plotting details). The band gaps of the M-GTUB-5's and GTUB-5 are summarized in **Table 1**. Overall, these results show that the band gaps of HOFs may be fine-tuned by inserting different metal ions into the porphyrin cores.

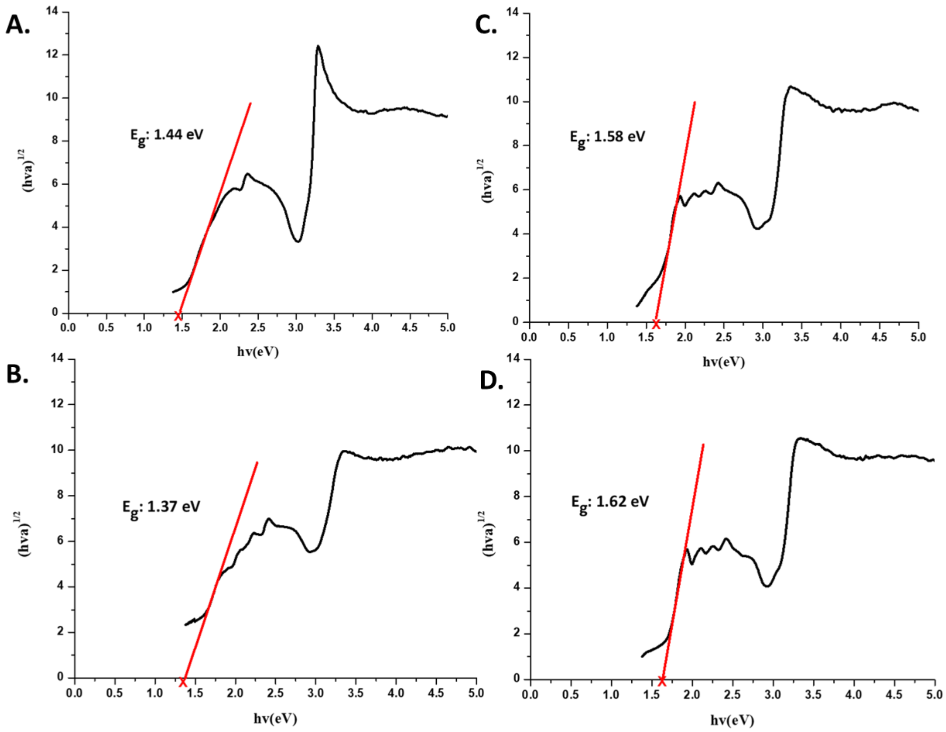

Figure 4.13. *Tauc plots of the diffuse reflectance spectra of (a) Cu-GTUB-5, (b) Ni-GTUB-5, (c) Pd-GTUB-5, and (d) Zn-GTUB-5 in their crystalline states, showing the resulting band gaps.*

DFT provides further insight into the band gaps of the M-GTUB-5 series. The calculated highest occupied crystal orbital (HOCO) to lowest unoccupied crystal orbital (LUCO) gaps for each system are 1.81/1.89 eV for Cu-GTUB-5 (β/α), 1.64 eV for Ni-GTUB-5, 1.87 eV for Pd-GTUB-5, and 1.77 eV for Zn-GTUB-5. Overall, these values are in very good agreement with the estimates from the Tauc plots.

The orbitals which form the HOCO and LUCO of each M-GTUB-5 system are elucidated in the projected density of states (pDOS) in **Figure 4.14** and the orbital diagrams in **Figure 4.15**. (The total DOS for each system is shown in **Figure 4.16**.) As seen in **Figure 4.14**, carbon, and nitrogen p_x and p_z orbitals participate in the HOCO-LUCO gaps of Cu-α-, Cu-β-, Zn-, and Pd-GTUB-5. In addition, several of the copper d-orbitals participate in the LUCO of Cu-β-GTUB-5. In the case of Ni-GTUB-5, the nickel d-orbitals are the primary contributors to the HOCO and LUCO, with minor contributions from carbon and nitrogen p-orbitals. The significant valence orbital contributions of the HOCO and LUCO for each system are given in **Tables B1-B4** of **Appendix B**.

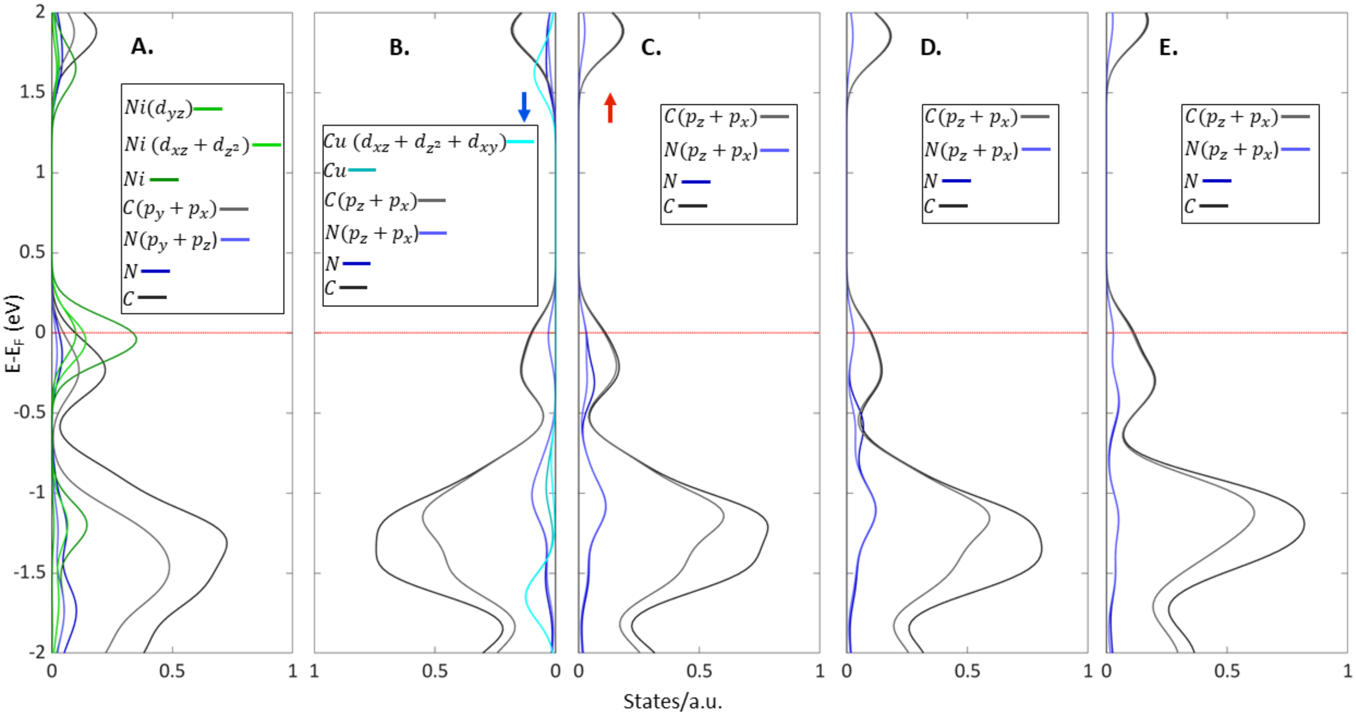

Figure 4.14. *pDOS of each M-GTUB-5 system showing the dominant valence orbital contributions and the total valence orbital contributions for key atoms. A) Ni-GTUB-5, B) Cu-β-GTUB-5, C) Cu-α-GTUB-5, D) Zn-GTUB-5, and E) Pd-GTUB-5. The red/blue arrows denote the contributions from the α/β-spins to the Cu-GTUB-5 pDOS.*

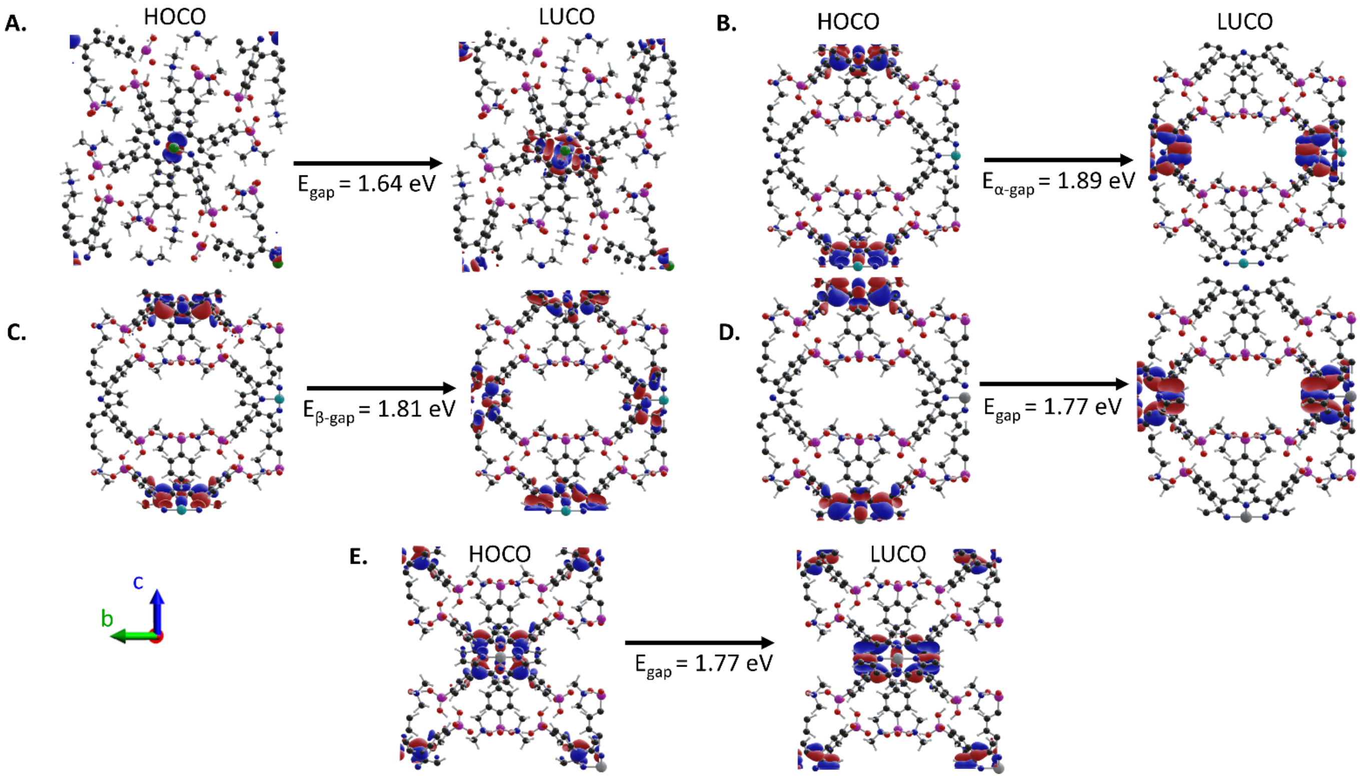

Figure 4.15. *HOCO and LUCO isosurfaces corresponding to an electron density of 1 electron per 0.02 Å^3 for A) Ni-GTUB-5, B) Cu-α-GTUB-5, C) Cu-β-GTUB-5, D) Zn-GTUB-5, and E) Pd-GTUB-5 (Colour scheme: Phosphorous – purple; Oxygen – red; Nitrogen – blue; Carbon – black; Hydrogen – white; Nickel – green; Copper – cyan; Zinc – dark gray; Palladium – light gray).*

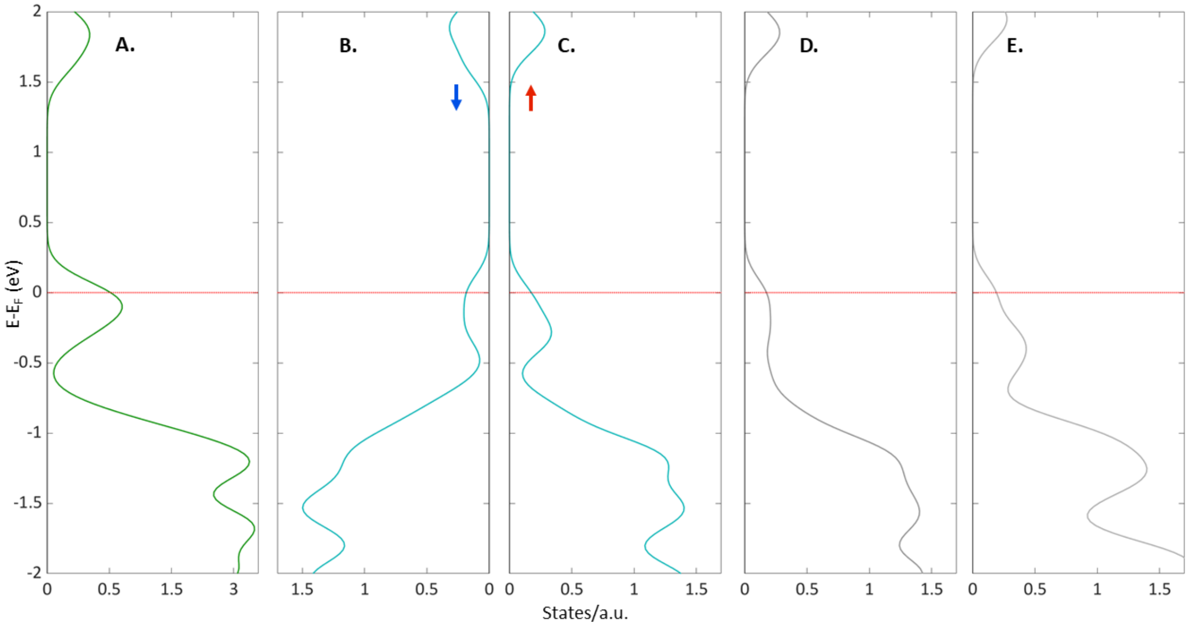

Figure 4.16. *Total density of states for the M-GTUB-5 systems. A) Ni-GTUB-5, B) Cu-β-GTUB-5, C) Cu-α-GTUB-5, D) Zn-GTUB-5, E) Pd-GTUB-5. The red/blue arrow indicates the contribution from α/β-spins.*

The restrained electrostatic potential (RESP),[149] obtained using the repeating electrostatic potential extracted atomic (REPEAT)[238] charges method, was used to determine the local electrostatic charge environment around each atom (see **Table 4.8**). The nickel atoms in Ni-GTUB-5 were found to have the least positive charges (0.579) among the metals, which indicates that the nickel atom's electrons are more evenly shared with the surrounding porphyrin. The copper atoms in Cu-GTUB-5 and palladium atoms in Pd-GTUB-5 have slightly higher positive charges (0.648 and 0.633, respectively) than the nickel atoms, while the zinc atoms in Zn-GTUB-5 have effectively lost a full electron (1.099) to the surrounding porphyrin. In Zn-GTUB-5, there is a large disparity between the zinc and nitrogen charges, indicating a reduced sharing of electrons and poor orbital overlap between the zinc and nitrogen atoms. This deficient overlap is further confirmed by the Zn-N bond lengths (see **Table 4.4**), as they are the largest in the M-GTUB-5 series. For the Ni-N bond, the difference between the charges is the least, indicating good orbital overlap and leading to the shortest M-N bond in the series.

Table 4.8. *Average RESP-REPEAT fitting charges for all atoms in each M-GTUB-5 system. Units are in elementary charge and standard deviations are in brackets.* ***N****-M denotes charges on nitrogen atoms directly bonded to metals, while N denotes all nitrogen atoms in each system.*

Atom	Ni-GTUB-5	Cu-GTUB-5	Zn-GTUB-5	Pd-GTUB-5
M	0.579 (2.48E-04)	0.648 (6.23E-02)	1.099 (2.57E-02)	0.633 (1.41E-06)
O	-0.672 (1.15E-01)	-0.654 (9.00E-02)	-0.628 (1.02E-01)	-0.659 (7.07E-02)
P	1.072 (1.18E-01)	1.139 (7.42E-02)	1.099 (1.07E-01)	1.122 (1.06E-01)
C	-0.110 (2.63E-01)	-0.103 (2.81E-01)	-0.098 (3.32E-01)	-0.101 (3.06E-01)
H	0.145 (1.10E-01)	0.086 (1.01E-01)	0.155 (9.64E-01)	0.153 (1.06E-01)
N	-0.020 (4.39E-01)	-0.056 (4.10E-01)	-0.197 (5.06E-01)	-0.043 (4.54E-01)
N-M	-0.483 (1.35E-02)	-0.450 (4.19E-02)	-0.687 (3.39E-02)	-0.481 (4.56E-02)
		Errors		
Root-mean square error	3.51E-06	2.64E-06	2.80E-06	2.98E-06
Relative root-mean square error	1.29E-02	1.14E-02	1.21E-02	1.22E-02

4.4 CONCLUSIONS

4.4.1 GTUB-5

In conclusion, we presented the first member, GTUB-5, of a novel family of two-dimensional, microporous phosphonic acid HOFs. Given its low band gap (as confirmed by solid-state/solution measurements and DFT calculations), GTUB-5 paves the way for the creation of new semiconductive microporous compounds. Within the context of semiconductive microporous compounds, GTUB-5 is the first HOF in the literature exhibiting such a small band gap. The use of hydrogen bonds in constructing a framework comes with the advantage of less complex connectivity options and eliminate the presence of toxic metal ions in capacitors and batteries providing environmentally friendlier solutions. Among, other HOFs, phosphonic acid HOFs provide more structural diversity and further potential applications. In addition, GTUB-5 exhibits proton conductive behavior as well. Currently, we are focusing on different linker geometries and pH modulations to further optimize the pore sizes and conductive behavior of phosphonate-HOFs. Given the high surface area and narrow band gap of GTUB-5, phosphonate-HOFs have the potential to revolutionize the semiconductive materials industry with applications in electrodes and supercapacitors.

4.4.2 Ni-, Cu-, Zn-, Ni-GTUB-5

In this paper, we reported on the synthesis and characterization of a series of transition metal-functionalized porphyrin phosphonate HOFs, namely Cu-GTUB-5, Ni-GTUB-5, Pd-GTUB-5, and Ni-GTUB-5. These HOFs were synthesized according to a new methodology for functionalizing the porphyrin core with different transition metal ions including Zn, Cu, Ni, and Pd. Introduction of metals with different ionic radii into the porphyrin cores alters the interactions between the HOF building units, leading to tuning of the textural properties of the resulting HOFs. The electronic interactions between the metal ions and the porphyrin cores cause small changes (on the order of few tenths of an eV) in the band gap compared to GTUB-5. These results establish HOFs as an emerging class of microporous materials with tunable semiconductive and photoluminescent properties.

Our DFT results indicate that the inclusion of different metals into the porphyrin centres affects the orbital contributions to the HOCOs and LUCOs, with the majority of the HOCOs and LUCOs being composed of carbon and nitrogen p-orbitals, except for Ni-GTUB-5 whose HOCO and LUCO are mainly composed of d-orbitals (with minor carbon and nitrogen p-orbital contributions). In addition, the inclusion of different metals results in changes to the hydrogen bonding in each M-GTUB-5 system, as well as the metal-to-nitrogen bonds within the porphyrin cores. The Ni d-orbital composition of the HOCO, short Ni-N bonds, and substantial sharing of electron density in the Ni-N bond, has profound effects on the structure of Ni-GTUB-5. We believe that the combination of these features causes the porphyrin to rotate about the a-axis (in contrast to the other M-GTUB-5 systems), which may be the reason why Ni-GTUB-5 has fewer O--H-O hydrogen bonds overall. This rotation both lowers the unit cell volume, and reduces the pore sizes and surface area in Ni-GTUB-5, imparting it with the lowest accessible surface area of the series. In addition, ionic sizes of different metal ions also change the textural properties of M-GTUB-5 systems. We have shown an easy method to insert a variety of metal ions into porphyrin cores. This methodology could be further applied to a variety of hydrogen bonding functional groups such as: carboxylates, sulfonates, and azolates that include porphyrin cores for metal binding. Furthermore, the presence of multiple hydrogen bonding moieties from the phosphonic acid functional group has created four permanently porous HOF structures, where the hydrogen bonds exhibit near covalent bond strength. Based on our results, we believe that metal insertion could be used as a strategy for optimizing porphyrin HOFs for optoelectronics and small-molecule capture applications.

4.4.3 General Conclusions on GUTB-5-like HOFs

Overall, our results suggest that phosphonate-based HOFs tend to be stable under ambient conditions and tend to have a low band gap. The stability likely stems from the phosphonate building units allowing for considerably shorter hydrogen-bonding lengths. The frontier orbitals are nearly exclusively made up of orbitals from the carbon and nitrogen atoms localized within the core of the porphyrin structures, except for Ni-GTUB-5. While the insertion of metals tends to minutely affect the HOCO-LUCO gaps, it has significant effect on the structure. Excluding Ni-GTUB-5, the GTUB-5 family is iso-structural. While the differences in Ni-GTUB-5 come from both the reliance of the frontier orbitals on the d-orbitals of the nickel atom, and the compression of the porphyrin due to favourable interactions of the nickel with the nitrogen atoms within the porphyrin core.

Chapter 5

Mechanistic Insights into the Proton Transport in Phosphonate Hydrogen-Bonded Organic Frameworks: A Born-Oppenheimer Molecular Dynamics and Metadynamical Study[R3]

5.1 INTRODUCTION

The need for renewable sources of energy is a critical factor in reducing carbon-based anthropogenic pollution.[262,263,264] Producing efficient and cheap green energy sources that avoid CO_2 emissions has become an active research area in material science, with the overall goal of moving away from traditional fossil fuels.[265] The reduction of CO_2 pollution can be achieved in several ways, e.g., using materials that harvest solar energy as in photovoltaic technologies[266], using catalysts which can recycle spent CO_2 to produce hydrocarbons, which in turn may be used as feedstock for fuel (known as the circular carbon economy).[267,268] Another approach involves capturing the energy stored in H_2 by reacting it with O_2 from the air to form water (known as the hydrogen economy).[269,270] This can be achieved using a hydrogen fuel-cell[10] (**Scheme 5.1**), which splits gaseous H_2 into $2H^+ + 2e^-$ at the anode, after which the electrons are transported from the anode to the cathode where gaseous $\frac{1}{2}O_2$ reacts with $2H^+$, finally, water and heat are produced as by-products. Fuel-cells have three interdependent components: a catalytic anode in which H_2 is split into $2H^+ + 2e^-$ (**Figure 5.1-A**), a proton-exchange membrane (PEM), which allows for proton transport between the anode and cathode (**Figure 5.1-B**), and a cathode where the reaction $2H^+ + \frac{1}{2} O_2 \rightarrow H_2O$ takes place (**Figure 5.1-C**).

[R3] This chapter contains research to be submitted. The supporting information for this chapter can be found in Appendix C: Figures C1-C6 and Tables C1-C6.

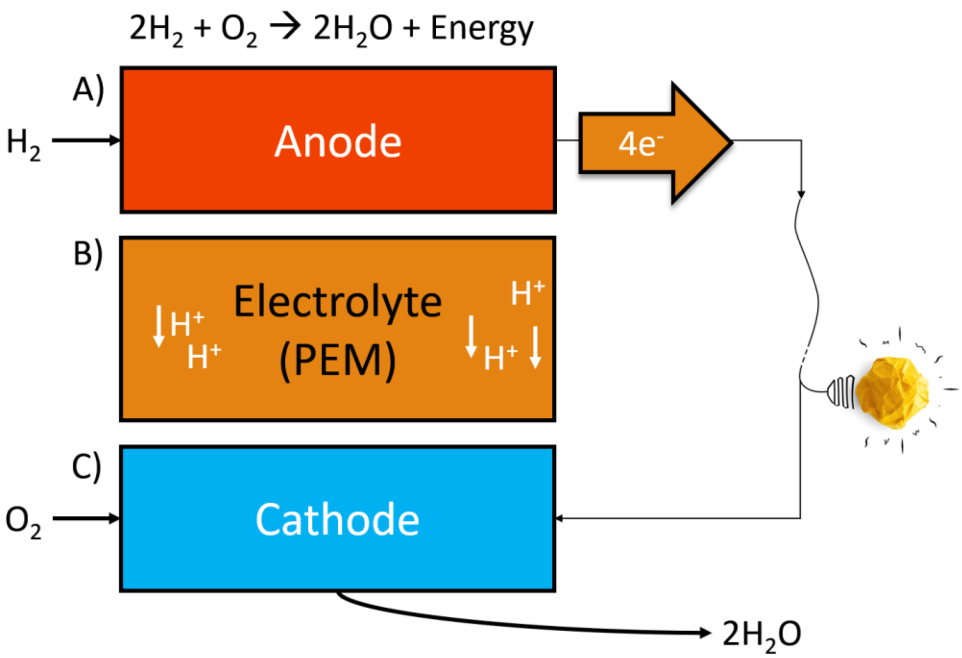

Scheme 5.1. *Depiction of a hydrogen fuel-cell. A) Anode catalyst in which H_2 is split into 2 protons and 2 electrons. B) Proton-exchange membrane (PEM). C) Cathode in which O_2 reacts with protons to create heat and water.*

The anode material, which is typically platinum based[271], catalyzes the H_2 oxidation half-cell reaction (**Eqn. 5.1**), resulting in a chemical potential of $E^0 = 0$ V.[10] The cathode material, which is typically a platinum alloy[271], catalyzes the reduction half-cell reaction of O_2 with H^+ (**Eqn. 5.2**), resulting in a chemical potential of $E^0 = 1.2291$ V.[10] Combining **Eqn. 5.1** and **Eqn. 5.2** yields the overall redox reaction (**Eqn. 5.3**) and a voltage of 1.2291 V under standard conditions (i.e., 1 atm and 25 °C).[10] A suitable PEM should be heat-stable[10], proton-conductive[55], and preferably a solid.[55,12] The protons resulting from the oxidation reaction at the anode require an efficient PEM to transport the protons away, preventing charge recombination and allowing for energy generation.

$$H_2 \leftrightarrow 2H^+ + 2e^- \qquad 5.4$$

$$O_2 + 4H^+ + 4e^- \leftrightarrow 2H_2O \qquad 5.5$$

$$H_2 + \frac{1}{2} O_2 \leftrightarrow H_2O \qquad 5.6$$

PEM fuel cells can be constructed to operate between 25 °C to 80 °C, with higher temperatures typically giving rise to higher proton conductivity of the PEM.[10,213,12] One also needs to consider the relative humidity (%r.h.) in which the PEM is exposed to; a higher %r.h. leads to more water molecules in the membrane the medium, which leads to increased proton conductivity.[10,213,12] Currently, Nafion,[69] a sulfonated tetrafluoroethylene-based fluoropolymer-copolymer, is the leading PEM used in solid-state fuel-cell technology, exhibiting proton conductivities up to 0.2 S cm^{-1}.

Recently, there has emerged a new family of solid-state porous materials, known as hydrogen-bonded organic frameworks (HOFs),[251,272] whose structure is held together by hydrogen bonding. As HOFs are held together by an extensive network of hydrogen bonds, it has been proposed that these materials could serve as solid-state proton-conductive PEMs.[273] The building blocks of most HOFs to date have been carboxylate-based linkers;[37] however, these carboxylate HOFs are typically not stable under ambient temperatures.[274,44] On the other hand, phosphonate-based HOFs, which came on the scene over the last several years,[12,213] characteristically more thermally stable due to strong hydrogen bonding interactions between adjacent PO_3H_2, **Figure 5.1**, groups in the structure. Phosphonate compounds are also known for their ability to conduct protons.[275] Given these properties, a solid-state phosphonate HOF makes an intuitive choice for a PEM. Two such phosphonate HOFs have been recently reported in the literature, namely our previous work on GTUB-5[213] and the work of Wang *et al.*[12] on UPC-H5a. UPC-H5a and GTUB-5 both contain mostly benign elements, and both conduct protons.

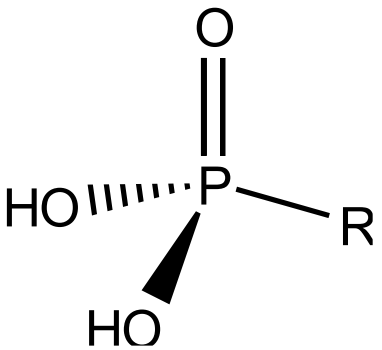

Figure 5.1. The phosphonate (PO_3H_2) group. R can be any other functional group.

In our previous work, GTUB-5 (**Figure 5.2-A**) was synthesized and characterized as a porous HOF composed of repeating units of 5,10,15,20-tetrakis [*p*-phenylphosphonic acid] porphyrin with a phenylphosphonic acid linker, stabilized by charge balancing dimethylammonium (DMA) ions. GTUB-5 was found to remain stable under conditions of 90 %r.h. and up to 75 °C, and the proton conductivity under these conditions was measured to be 4.20 x 10^{-6} S cm^{-1}, which is low relative to other proton-conductive materials. Wang *et al.*[12] recently synthesized and characterized a similar porous HOF, UPC-H5a (**Figure 5.2-B**), which is composed of repeating units of 5,10,15,20-tetrakis [*p*-phenylphosphonic acid] Ni-porphyrin, stabilized by charge-balancing DMA ions. UPC-H5a remains stable at 99 %r.h. and up to 80 °C, with proton conductivities reaching 3.42 x 10^{-2} S cm^{-1} under these conditions (which is comparable to that of Nafion). The main difference between the two structures is the phenylphosphonic acid linker from GTUB-5 is not present in UPC-H5a, and introduction of Ni^{2+} atoms into the porphyrin cores of UPC-H5a (**Figure 5.1**). Thus, despite being constructed of similar porphyrin-based phosphonates, the proton conductivity of UPC-H5a is four orders of magnitude higher compared to that of GTUB-5 (viz., 3.42 x 10^{-2} S cm^{-1} vs. 4.20 x 10^{-6} S cm^{-1}). An understanding of the proton conduction mechanism(s) in these HOFs will help shed light on this large difference and, in turn, may give rise to strategies for designing highly proton conductive HOFs.

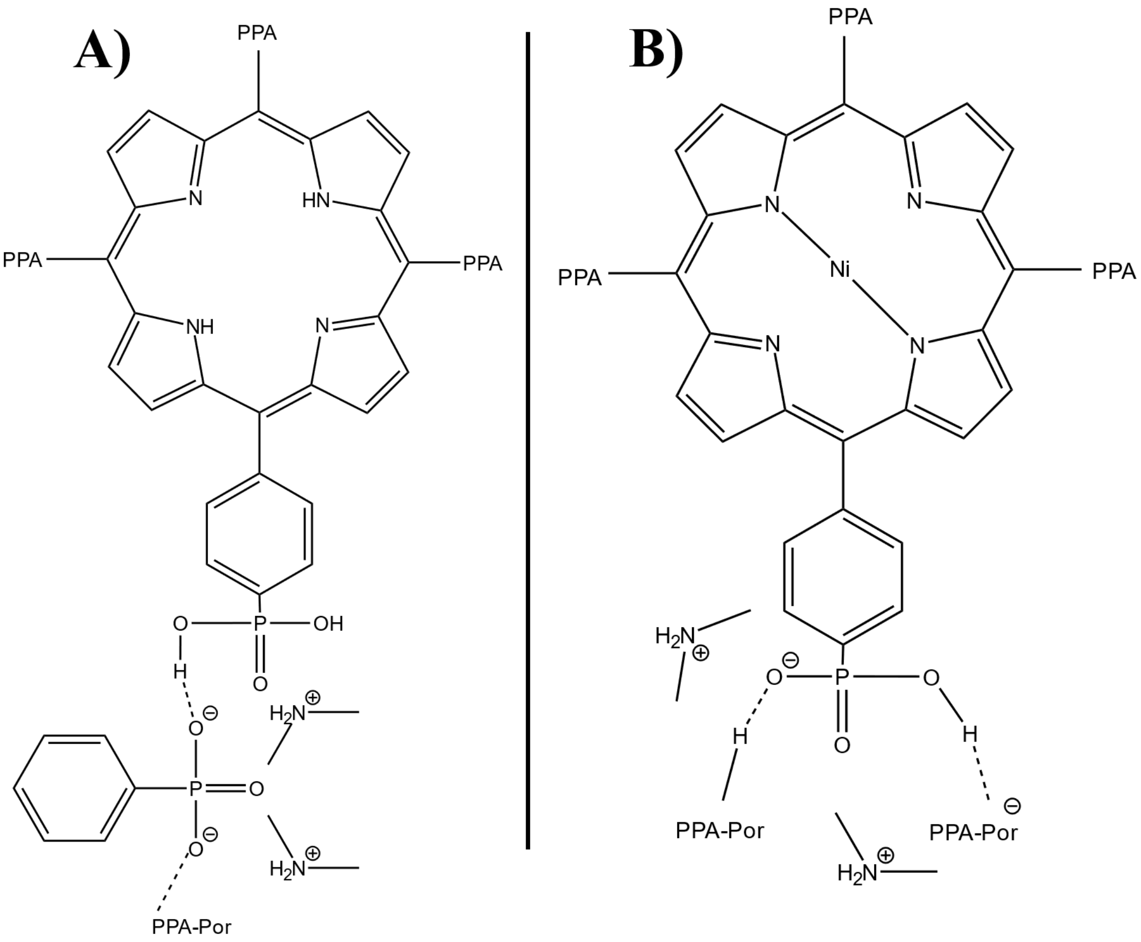

Figure 5.2. *A) A cut-out section of the crystal structure of GTUB-5 showing the phenyl-phosphonate porphyrin hydrogen bonded to the phenylphosphonic acid stand-alone linker. B) A cut-out section of the crystal structure of UPC-H5a showing the hydrogen bonding between phenyl-phosphonate Ni-porphyrins.* (*H---O denotes a H that is hydrogen bonded to an O, PPA= phenylphosphonic acid linker, and Por = porphyrin unit*).

5.2 METHODOLOGY

The goal of this computational study is to elucidate the microscopic details of the proton transport mechanisms in GTUB-5 and UPC-H5a. The experimental activation energies that are obtained through Arrhenius fitting of proton conductivities for GTUB-5 and UPC-H5a (viz., 0.14 eV at 90 %r.h. and 0.20 eV at 95 %r.h., respectively[12,213]) indicate that the proton transport occurs via a Grotthuss mechanism. The Grotthuss mechanism is typically accepted to have an activation energy which is lower than 0.40 eV,[72,54] as breaking hydrogen bonds require energy between 0.1 – 0.3 eV,[54,276] and higher energies are required for proton mobility via a vehicle mechanism.[72,277] Thus, we will assume a Grotthuss-like mechanism in setting up our simulations.

A number of different computational approaches have been used previously to study proton transport in solids.[75,278,279] One approach is to use static post-Hartree-Fock electronic structure calculations to study the kinetics and thermodynamics through transition state searches and minimum energy pathways.[109] Depending on the size of the system, however, this approach could be highly computationally costly and neglects dynamical effects. Furthermore, when invoking periodic boundary conditions, one is highly limited in post-Hartree-Fock approaches, as the exact exchange diverges at long ranges and requires special approximations to incorporate.[131] Proton transport can also be studied using force-field-based, non-reactive classical molecular dynamics, which allows for simulations of large systems out to long timescales.[279] However, without the possibility of reactions, one cannot simulate a Grotthuss-like mechanism of proton transport. Another approach that has been used to study proton transport is Born-Oppenheimer molecular dynamics (BOMD).[75,280,126] BOMD allows one to simulate Grotthuss-like proton hopping, albeit at lower levels of theory and for shorter times. For example, AIMD has been combined with metadynamics (MTD) to study proton transport between water molecules in differing sizes of porous graphene membranes[75], decomposition of carbonic acid in water to carbon dioxide,[280,281,282] and proton transport along oxygen atoms in a porous zirconia framework.[126] In Ref. [126], Rabone *et al.* inserted a proton into a ZrO_2 solid-state structure in which they used MTD to bias the proton in moving to the centre of the ZrO_2 structure, using the MTD energy barriers to approximate the diffusion of the proton. Herein, we follow a similar methodology for estimation of the free energy as Rabone *et al.*, by taking the energy difference between the beginning of a proton transfer and the transition and use it to study proton transport in the water-filled pores of GTUB-5 and UPC-H5a. This methodology is used to gain insight into specific proton mechanistic pathways in the pores.

5.2.1 Electronic structure calculations

Geometry and lattice optimizations of GTUB-5 and UPC-H5a were first performed using the Quickstep-CP2K program (v. 9.1).[232,233] As these HOFs are solid-state materials, periodic boundary conditions were applied. CP2K makes use of density functional theory (DFT) and a

Gaussian plane-wave hybrid approach[233,137] to describe the electronic structure. Goedecker-Teter-Hutter (GTH) PBE-optimized basis sets were used to describe the main-group valence orbitals, while GTH short-range orbitals were used to describe the Ni valence electrons.[236] All valence basis sets were of the double-ζ with a valence polarization function (DZVP) type, GTH pseudopotentials[234,235] were used to describe the core electrons, and Γ-point sampling was used. The calculations were done with the PBE-D3-BJ functional.[101,106,107] Atomic and lattice optimizations were performed for both systems excluding water in the pores, followed by geometry optimizations with 10 water molecules in each HOF. The initial structure of GTUB-5 was taken from the optimized CIF of our previous work,[213] and then its lattice and geometry were optimized simultaneously. The initial structure of UPC-H5a was constructed from the supporting information in Ref.[12] (where the initial $NiH_4TPPP(Me_2NH_2)_4(DMF)(H_2O)_4$ structure was refined, removing the lattice DMF and water molecules to make the pristine $NiH_4TPPP(Me_2NH_2)_4$ framework), and then the lattice and atomic coordinates were optimized, **Figure 5.3**.

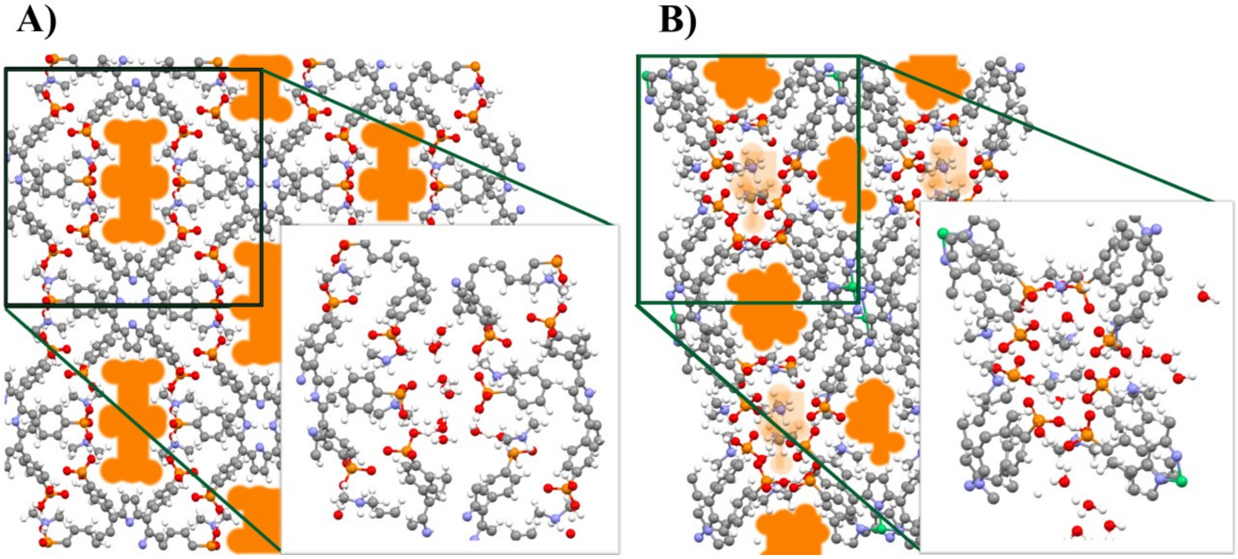

Figure 5.3. *DFT-optimized supercells of A) GTUB5 and B) UPC-H5a. The orange highlighted regions indicate the pores in which the water guest molecules and protons are inserted. Colour coding: carbon-grey, nitrogen-blue, oxygen-red, phosphorous-orange, nickel-green, hydrogen-white.*

5.2.2 Born-Oppenheimer Molecular Dynamics

BOMD simulations of the two HOF systems were performed using the Quickstep-CP2K program (v. 9.1) with a 0.5 fs time-step using PBE-D3-BJ, with a DZVP basis and GTH pseudopotentials to estimate the quantum potential. The initial configuration for each system was taken to be the DFT-optimized structure with 10 water molecules in the pores of each HOF and 3/1 excess protons in UPC-H5a/GTUB5. The number of protons added to each framework reflects the number of unique pores in it. The excess positive charges resulting from the insertion of protons were neutralized by adding a static homogenous negative background charge. An NVT equilibration using the canonical sampling through velocity rescaling (CSVR) thermostat with a 1 ps time constant was performed at 393 K and 403 K over 10 ps for GTUB5 and UPC-H5a, respectively. A second NVT equilibration of 9 ps was performed using the CSVR thermostat with a 10 fs time constant and at the same temperatures. Six unbiased microcanonical (NVE) production runs of 10 ps were generated for each system, starting from the configurations at 2.5 ps, 5 ps, 6 ps, 7 ps, 8 ps, and 9 ps in the second equilibration trajectory. The resulting xyz trajectories were post-processed and reorganized based on molecular building blocks using the Trajectory Analyzer and Visualizer (TRAVIS)[283] software to allow for easy visual identification of the water molecules of interest. The resulting coordinate-trajectory files were also converted to protein data base (PDB) configuration files using the Open Babel software (v. 3.1.1)[284] and subsequently converted to xtc trajectory files by GROMACS (v. 2021)[285,286], to be analyzed by the PLUMED[127] software. The unbiased runs give more accurate dynamical information about hydrogen movement throughout both HOFs, the results were used to parameterize the metadynamical (MTD) simulations, giving values for average hydrogen to oxygen lengths. H-O radial distribution functions (RDFs) were calculated for each of the six NVE production trajectories for both UPC-H5a and GTUB-5 using the unit cells and VMD (v. 1.9.3) software.[287] The results were averaged to produce a single RDF for each HOF.

RESP-REPEAT[149,238] calculations were performed after the unbiased simulations. To do these calculations extracted coordinates from the beginning, middle, and end of a proton transfer were used for single-point calculations on each to obtain the local charges relevant to the proton transfers. The RESP-REPEAT charge calculations require more computational time, approximately twice the time per MD step, which is an immensely expensive computational cost, particularly when considering AIMD simulations, thus the calculations were performed on post-processed snapshots of the NVE trajectories. The RESP-REPEAT charges are calculated for an atom, however, the RESP potential is fitted grid of points surrounding the atom defined by a radii, in this case the universal force field (UFF) radii,[240] the potential calculated by the RESP-REPEAT charges is corrected to model the electrostatic potential on the grid points correctly.

5.2.3 Metadynamics

Well-tempered MTD[125] simulations of UPC-H5a and GTUB-5 were performed starting from the final configuration of the first production run of each system, three 2 ps MTD trajectories were generated for each of GTUB-5 and UPC-H5a. These were carried out using CP2K+PLUMED (v. 2.8) with a CSVR thermostat (10 fs time constant), with a 0.5 fs time-step using PBE-D3-BJ, with a DZVP basis and GTH pseudopotentials to estimate the quantum potential. Gaussian hills with a height of k_BT (where T is the temperature set by the thermostat) were added to the potential every 5 fs, and a bias factor of 10 was used.

MTD simulations add a bias potential along particular variables, CVs, in a trajectory; the goal of which is to push the CVs over energy barriers that trajectories would otherwise not be able to explore sufficiently, either due to time-scale constraints, or barrier heights.[123] An often-used description is to think of the free energy surface as varying hills, with local maxima and minima, and one adds the bias potential as '*sand*' to the surface. This sand is added starting with the local minima until the well is filled up and the variable crosses over a maximum and is allowed to explore an adjacent local minimum. To perform MTD simulations, one needs to define CVs in which to bias the system. Here it was decided to use the coordination number (CN) between select oxygen atoms and all hydrogen atoms in the system. Thus, the bias will be added to any proton bonded to one of the selected oxygen-atoms and be pushed away until the hydrogen is bonded to an adjacent oxygen atom. The bias potential for the oxygen CNs is described by the atomic-pair **Eqn. 5.4**, for which i, and j is the O, and H pairing, respectfully,

$$s_{ij} = \frac{1-\left(\frac{r_{ij}-d_0}{r_0}\right)^n}{1-\left(\frac{r_{ij}-d_0}{r_0}\right)^m} \qquad 5.7$$

where the CV s_{ij} is the CN between atoms i and j, r_{ij} is the current distance between atoms i and j, r_0 is the difference between d_0 and the centre of the first minimum peak from the RDFs, n, m, and d_0, are switching function parameters.

To determine the likely proton transport mechanism(s) in the HOF pores, we considered the following three proton transport routes for the MTD simulations: (i) Proton transfers from one water molecule to the next, i.e., water-to-water (WtW) or vice versa; and (ii) Proton transfers from a water molecule to the framework or vice versa, i.e., water-to-framework (WtF). (iii) Proton transfers from framework group to framework group, i.e., framework-to-framework (FtF) or vice versa. These routes dictated the following choices of collective variables (CVs):

1. **WtW** → CVs only involve water-based oxygen atoms. (**Figures 5.4–A, 5.5–A)**
2. **WtF** → CVs force protons onto the framework from H_2O molecules **Figures (5.4–B, 5.5–B)**
3. **FtF** → CVs force proton movement from within the framework. **Figures (5.4–C, 5.5–C)**.

These three general pathways incorporate how the confined space will affect the waters' ability to move protons, how willing a framework will accept an excess proton from surrounding waters, and finally how easily protons are transferred throughout the framework, which should be a sufficient encapsulation of the potential proton movements within each HOF. The choice of CVs for the WtF pathway in UPC-H5a has also allowed for extraction of some FtF transfers as well, providing more statistics for the FtF pathway. The full CV profiles can be found in **Figures C1-C6.**

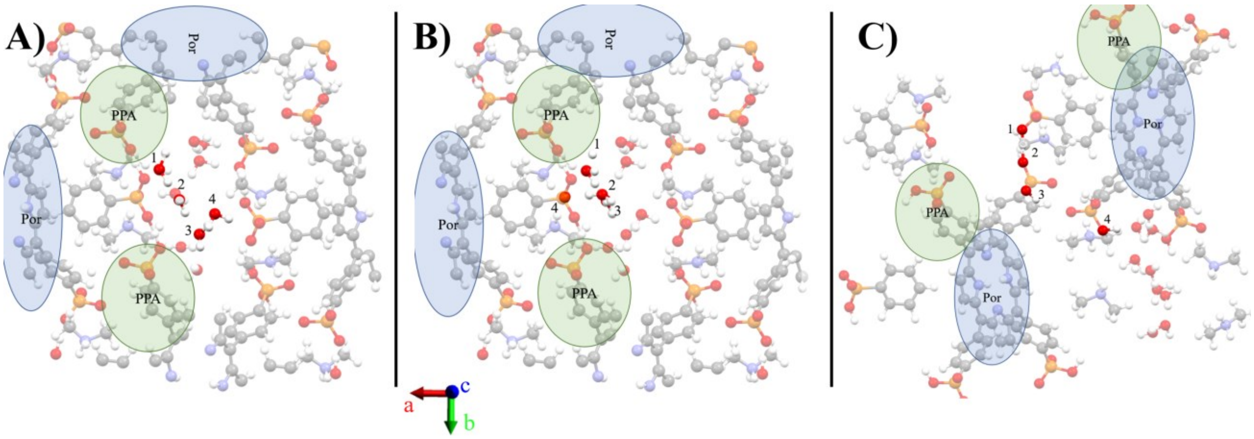

Figure 5.4. *MTD routes for proton transport in GTUB-5, the numbers indicate the 4 oxygen atoms in which the bias is being applied. A) WtW using the same GTUB-5 orientation as* ***Figure 5.3****. B) WtF using the same GTUB-5 orientation as* ***Figure 5.3****. C) FtF rotated orientation using TRAVIS to put the phosphonate framework in the centre of the unit cell, oxygen atoms 1, 2, and 3 are near the top of the c-axis in the unit cell, and 4 is near the bottom of the c-axis in the unit cell. PPA group is indicated by the green highlight, porphyrin backbone is indicated by blue highlights. Colour coding: carbon-grey, nitrogen-blue, oxygen-red, phosphorous-orange, hydrogen-white.*

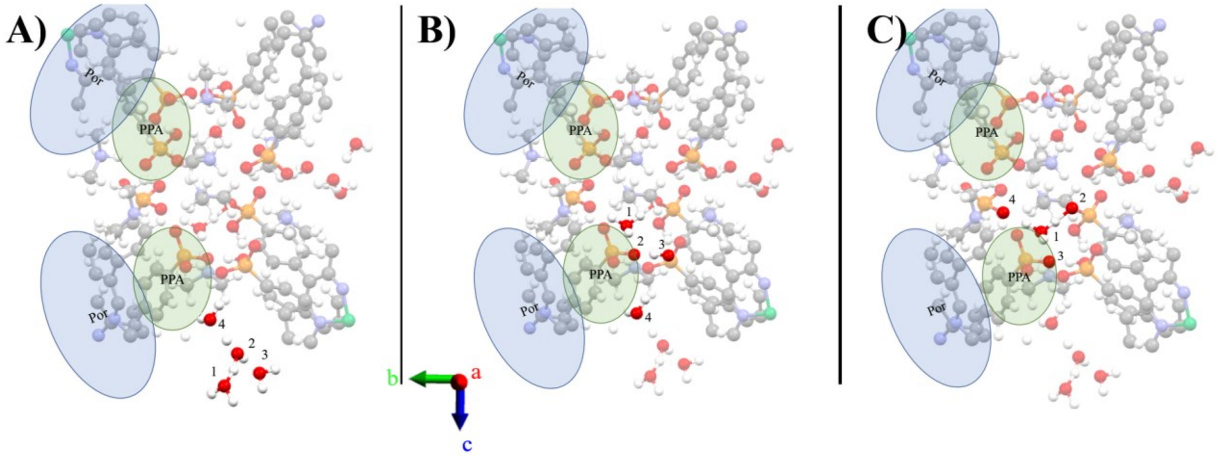

Figure 5.5. *MTD routes for proton transport in UPC-H5a, the numbers indicate the 4 oxygen atoms in which the bias is being applied to. A) WtW using the same UPC-H5a orientation as* ***Figure 5.3****. B) WtF using the same UPC-H5a orientation as* ***Figure 5.3****. C) FtF UPC-H5a orientation as* ***Figure 5.3****. PPA group is indicated by the green highlight, porphyrin backbone is indicated by blue highlights. Colour coding: carbon-grey, nitrogen-blue, oxygen-red, phosphorous-orange, hydrogen-white, nickel-green.*

In analyzing the trajectories, the following rules were applied to ensure consistency in counting proton transfer events for both HOFs:

1. If a proton transfers from one oxygen atom to another and then back again, it is not counted unless the time for the backwards transfer is > 0.05 ps (50 fs).
2. The CN of the oxygen from which the proton is transferring must change by at least 0.8 over the course of the transfer.

3. Include only the estimates of free energies of transport of the specific pathway, viz., for WtW, the free energy difference from the time the proton begins transit from a water molecule to another and the time in which the proton is halfway between two water molecules, for WtF, the free energy difference from the time the proton begins transit from a water molecule to a framework oxygen and the time in which the proton is halfway between the transfer, and for FtF, the free energy difference from the time the proton begins transit from a framework oxygen to a framework oxygen, and the time in which the proton is halfway between the transfer.

5.3 RESULTS AND DISCUSSION

There are two general observations that are made from the unbiased trajectories: (i) the intrinsic protons supplied by the DMA ions do not participate in any of the proton transfers over any of the NVE trajectories; (ii) the routes for the CVs are the primary mode of transport observed within the unbiased trajectories.

The H-O RDFs for GTUB-5 and UPC-H5a are shown in **Figure 5.6**, these RDFs include any hydrogen to any oxygen throughout the unbiased runs. Although there are some quantitative differences between the two RDFs, they have the same overall structure. The first (high) peak centred at 0.995 Å corresponds to the H-O hydrogen bond distance, this peak is a combination of H-O_{donor}, and lone H-O distances. The second (low) peak centred at 1.505/1.595 Å corresponds to H-$O_{acceptor}$ and (DMA^+) N-H-$O_{acceptor}$ hydrogen bond distances for GTUB-5/UPC-H5a. The third (low) peak centred at 3.240/3.600 Å corresponds to the H-O distances from hydrogens to their 2^{nd} next nearest neighbouring oxygen atoms. The main differences between the two RDFs are in the height/width of the first peak and position of the second peak. More specifically, there is a slight contraction in the average H-O distance and slightly narrower range of H-O bond distances in UPC-H5a compared to in GTUB-5. The range of H-$O_{acceptor}$ distances begin and ends at lower values for GTUB-5 compared to UPC-H5a, with the peaks centred at 1.505 Å and 1.595 Å, respectively. Furthermore, the O-O RDFs for GTUB-5 and UPC-H5a are shown in **Figure 5.7**, these RDFs include any oxygen to any oxygen throughout the unbiased runs. The first (high) peak centred at 2.575/2.585 Å corresponds to the O_{donor}-$O_{acceptor}$ distance for GTUB-5/UPC-H5a. These results indicate that GTUB-5 has stronger relative hydrogen bonding strength.

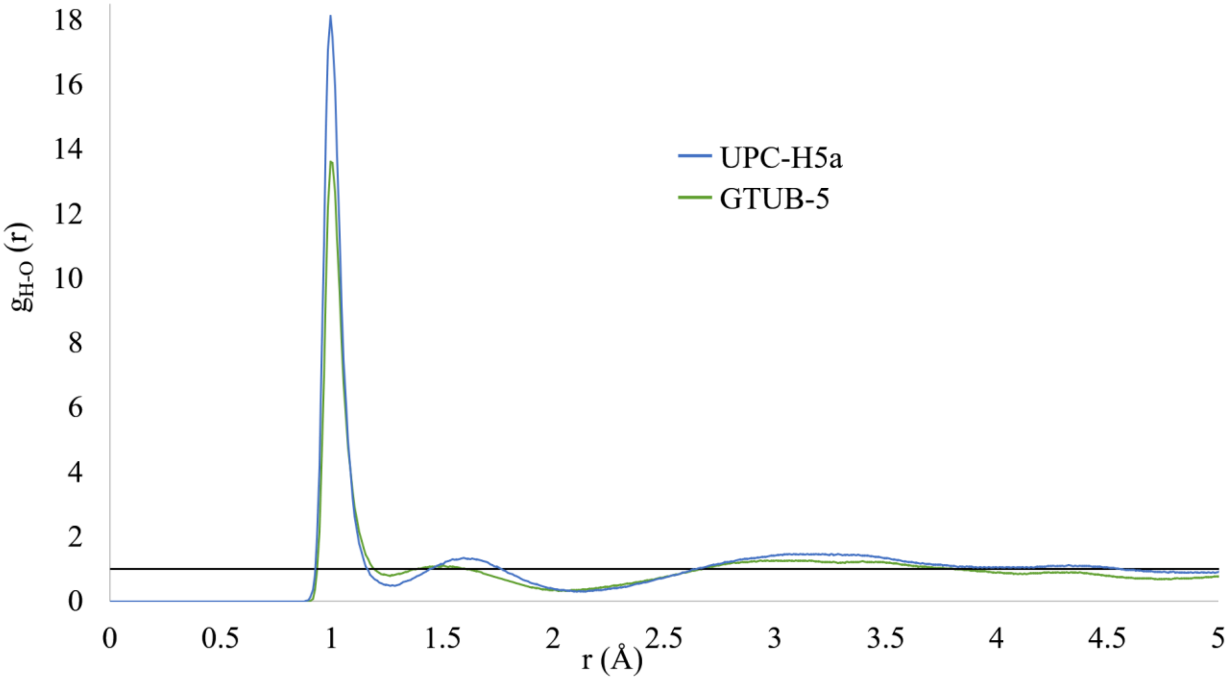

Figure 5.6. *All hydrogen to all oxygen RDFs for UPC-H5a (blue) and GTUB-5 (green). The graphs shown are averaged over the six NVE trajectories of each HOF.*

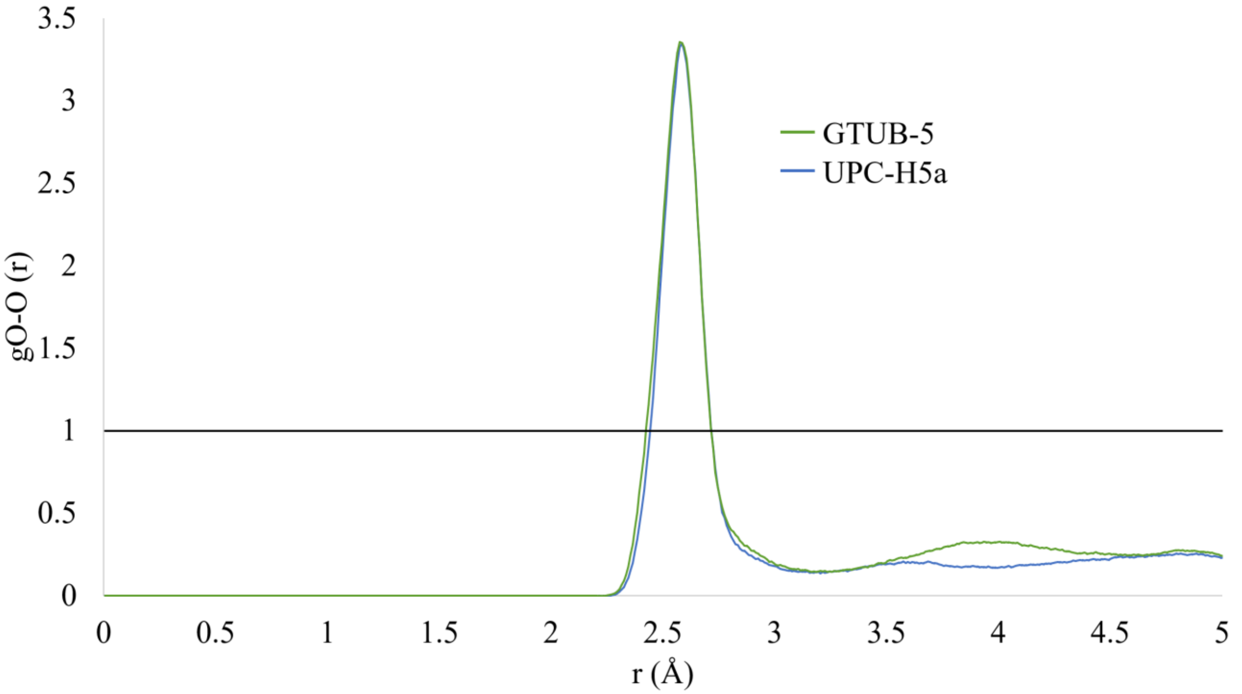

Figure 5.7. *All oxygen to all oxygen RDFs for UPC-H5a (blue) and GTUB-5 (green). The graphs shown are averaged over the six NVE trajectories of each HOF.*

The average RESP-REPEAT charges on the O_{donor}, $O_{acceptor}$, and H^+ atoms in GTUB-5 and UPC-H5a for several proton transfer events in the unbiased trajectories are shown in **Table 5.1**. As can be seen, the charges on these atoms in the reactant, transition, and product states are similar for both HOFs, where a positively charged proton bound to a negatively charged oxygen atom (donor) transfers to another negatively charged oxygen atom (acceptor). For both GTUB-5 and UPC-H5a, the donor/acceptor oxygen at the beginning of the proton transfer is more/less negatively charged than at the end of the transfer, with the negative charges reaching their most/least negative values after the proton has fully transferred to the acceptor. This suggests that there is an electronic charge transfer from the acceptor oxygen to the donor oxygen over the course of the proton transfer. As for the charges on the Ni atoms in UPC-H5a, they change negligibly over the course of the transfers, most likely due to the fact that the Ni atoms are not close enough to the pores to significantly affect and/or feel the effect of the proton transfers. The full listing of charges can be found in Appendix C, **Tables C1 – C6**.

Table 5.1. *Average RESP-REPEAT charges of key atoms over the course of a proton transfer for GTUB-5 and UPC-H5a. These values are averaged over the first three unbiased NVE trajectories, explicitly averaging a transfer per trajectory that correspond to each of WtW, WtF, and FtF (9 transfers for GTUB-5 and 9 transfers for UPC-H5a). All charges are reported in elementary charge units, and the values in brackets are the standard deviations.*

	GTUB-5			UPC-H5a				
	O_{donor}	H^+	$O_{acceptor}$	O_{donor}	H^+	$O_{acceptor}$	Ni_1	Ni_2
Reactant	-0.72	0.46	-0.74	-0.70	0.46	-0.75	0.51	0.48
	(0.11)	(0.03)	(0.11)	(0.12)	(0.05)	(0.10)	(0.03)	(0.02)
Transition	-0.80	0.52	-0.75	-0.72	0.45	-0.68	0.51	0.47
	(0.17)	(0.05)	(0.09)	(0.05)	(0.02)	(0.03)	(0.04)	(0.00)
Product	-0.81	0.47	-0.68	-0.77	0.48	-0.66	0.53	0.49
	(0.11)	(0.02)	(0.10)	(0.10)	(0.04)	(0.06)	(0.03)	(0.01)

Next, we analyzed the MTD trajectories to gain insight into the possible proton transport mechanisms and obtain the free energy of the proton transfer. An estimate of the free energies can be obtained by calculating the amount of biased energy added from the MTD simulations, along the predefined CVs. To define the CVs, we made use of the distances between hydrogen and oxygen atoms from the RDF in the unbiased runs, we can obtain an estimate of when a proton transfer begins, and when it has been fully transferred to an adjacent oxygen. The unbiased RDFs determined that the values of the parameters in **Eqn. 5.4** are n=6 and m=18 (for both systems), r_0 = 0.748 Å and d_0 = 0.517 Å for UPC-H5a, and r_0 = 0.815 Å and d_0 = 0.450 Å for GTUB-5. These values were chosen to begin significant reduction of the applied bias, s_{ij}, after the hydrogen is outside the H-O direct bonding range, corresponding to 1.285/1.275 on the H-O RDF for UPC-H5a/GTUB-5. The parameters for s_{ij} were also chosen so they go through an inflection point at the second (low) peak centred at 1.595/1.505 Å corresponding to the H-$O_{acceptor}$ hydrogen bond distance for UPC-H5a/GTUB-5. The bias is a minimum at distances > 2.0 Å (**Figure 5.8**). Therefore, if one of the oxygen atoms in the predetermined pathways is bonded to *any* hydrogen atom, the bias will actively be applied until the hydrogen atom has moved away a significant distance.

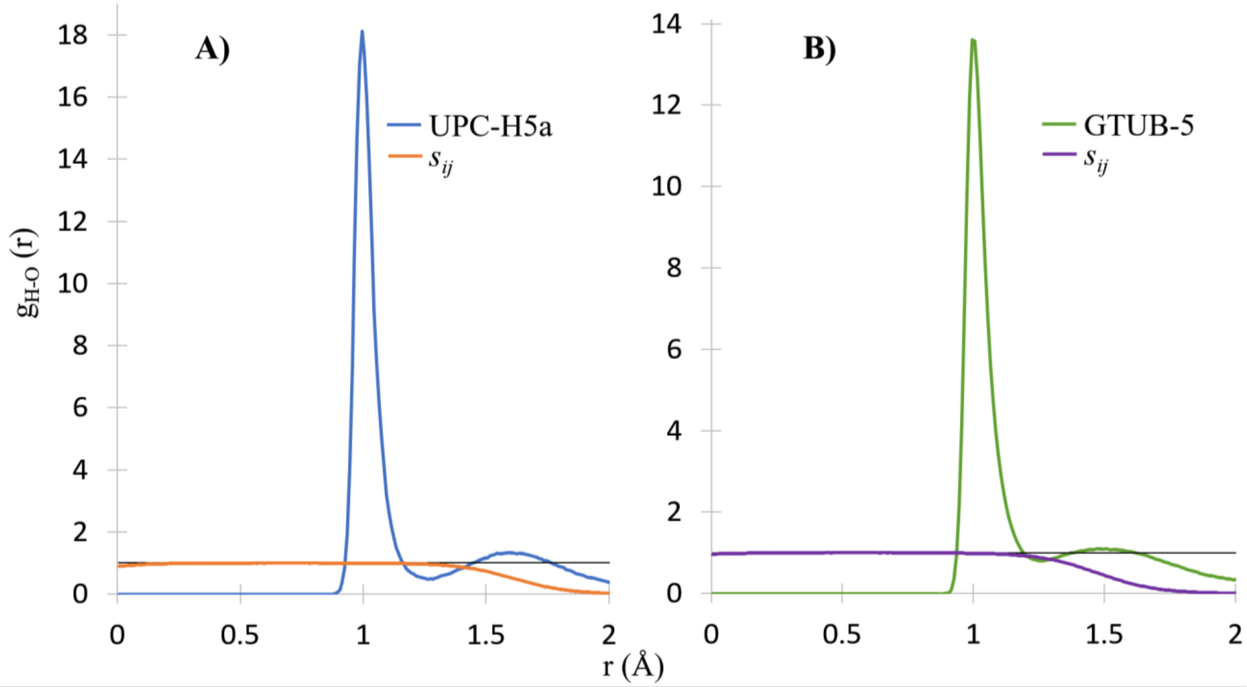

Figure 5.8. *CN (s_{ij}) as a function of distance, r, overlaid upon the RDFs for A) UPC-H5a and B) GTUB-5. Beyond 2 Å, S_{ij} reaches < 0.03 for UPC-H5a and < 0.01 for GTUB-5.*

There are several proton transport mechanisms that are seen throughout the MTD trajectories, these incorporate single proton transfer, stepwise,[109] and concerted type-mechanisms, the descriptions that follow are seen in both HOFs. The single proton transfer mechanisms are seen readily with single WtW, and WtF transfers, **Figures 5.9 & 5.10**. Typically, the single transfer mechanism occurs when the proton transfer is from an isolated water molecule (WtW), or to a phosphonate on the framework (WtF) where there is an oxygen not currently participating in hydrogen bonding. The stepwise mechanisms take place when a chain formation of waters occurs (WtW), and one transfer begets a second transfer on the next water, **Figure 5.11**. The stepwise mechanism also occurs when a proton from a framework oxygen transfers to a water oxygen, forcing the proton on the water to transfer to an adjacent framework oxygen (WtF), (**Figure 5.12**). Another version of the stepwise mechanism is a framework oxygen pushes a proton to a hydrogen bonded phosphonate (FtF), forcing one of the adjacent oxygen atoms on the other side of the phosphonate to push off a proton that was participating in a different hydrogen bond, (**Figure 5.13**). The concerted mechanism occurs when two phosphonate groups are participating in two parallel hydrogen bonds (FtF), and one proton transfers from the first phosphonate to the second, causing the proton in the second hydrogen bond to pass to the initial phosphonate, **Figure 5.14**.

In **Figure 5.14** the second phosphonate oxygen does not have any bias applied, but the mechanistic pictures (**Figure 5.15-E**) shown later illustrate the reaction.

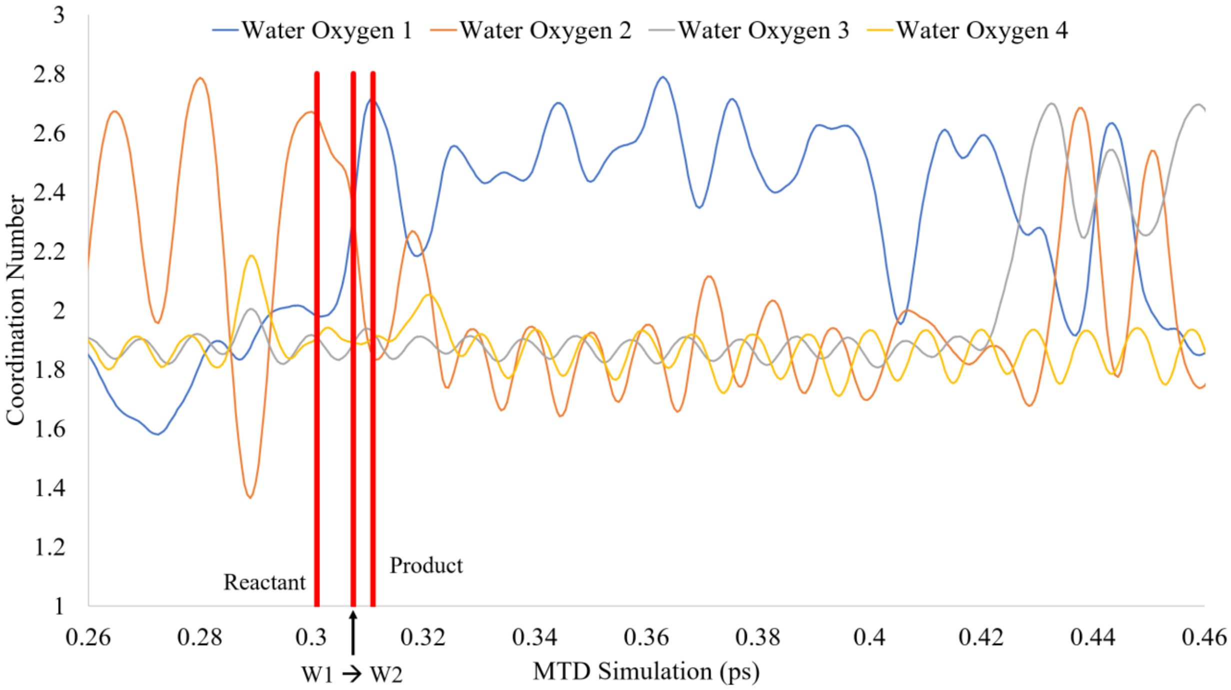

Figure 5.9. *Highlighted portion of the oxygen CNs along a WtW-MTD run for UPC-H5a showing a single proton transfer. Grey, blue, orange, and yellow lines correspond to oxygen atoms from water molecules in the pore. W1→ W2 indicates which waters the protons are transferred from and to. W stands for water-based oxygen atom in which the bias is applied. The red lines indicate*

the beginning of a proton transfer (reactant), the transition point (W1→ W2), and the point at which the proton as fully transferred (product).

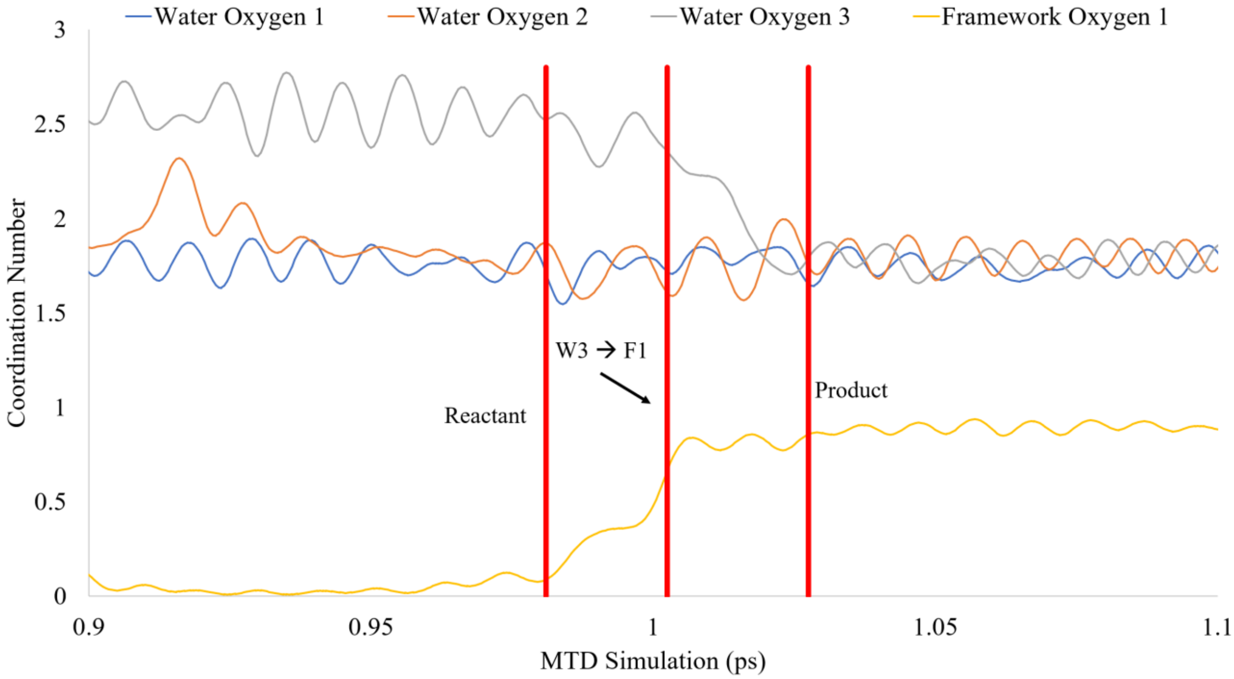

Figure 5.10. *Highlighted portion of the oxygen CNs along a WtF-MTD run for GTUB-5 showing a single proton transfer. Grey, blue, and orange lines correspond to oxygen atoms from water molecules in the pore, while the yellow line corresponds to an oxygen atom on the phenyl-phosphonate. W3→ F1 indicate the proton transfer from a water oxygen atom to a framework oxygen atom. W stands for water-based oxygen atom in which the bias is applied, and F stands for a framework-based oxygen atom in which the bias is applied. The red lines indicate the beginning of a proton transfer (reactant), the transition point (W3→ F1), and the point at which the proton as fully transferred (product).*

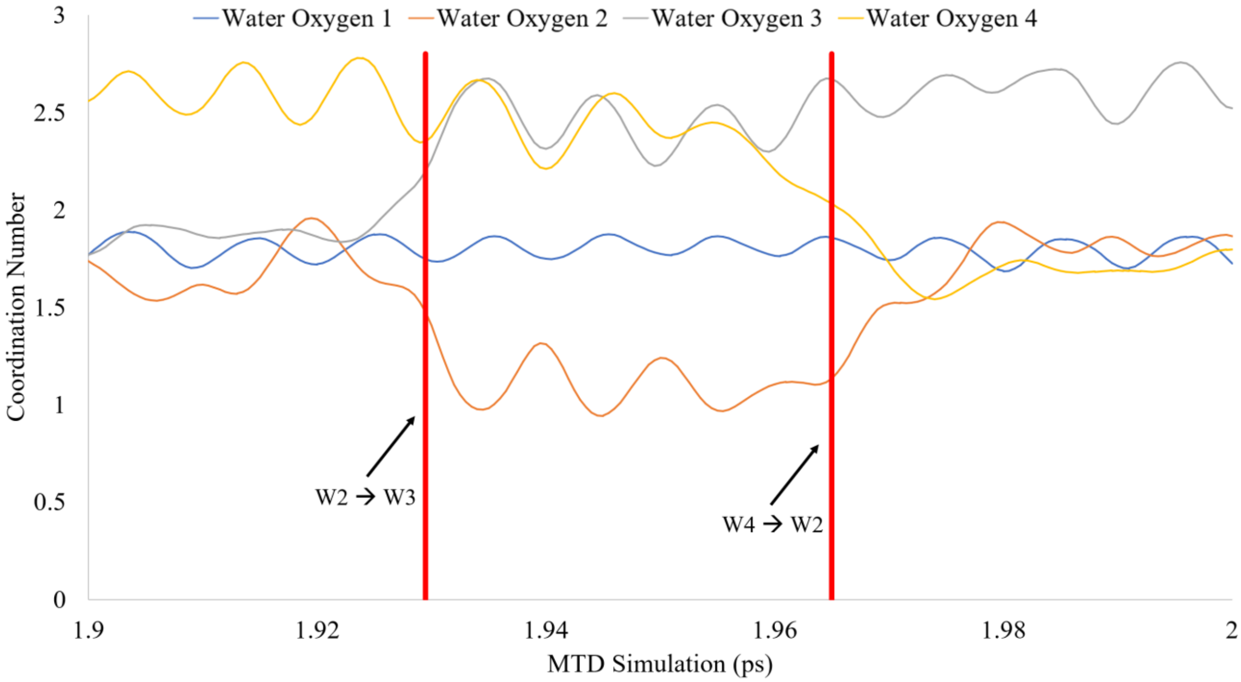

Figure 5.11. *Highlighted portion of the oxygen CNs along a WtW-MTD run for GTUB-5 showing a stepwise proton transfer. Grey, blue, orange, and yellow lines correspond to oxygen atoms from water molecules in the pore. W2→ W3 indicates the initiation of the transfer, and W4→ W2 finishes the stepwise transfer; W stands for water-based oxygen atom in which the bias is applied. The red lines the two transition points in the stepwise mechanism W2→ W3, and W4→W2.*

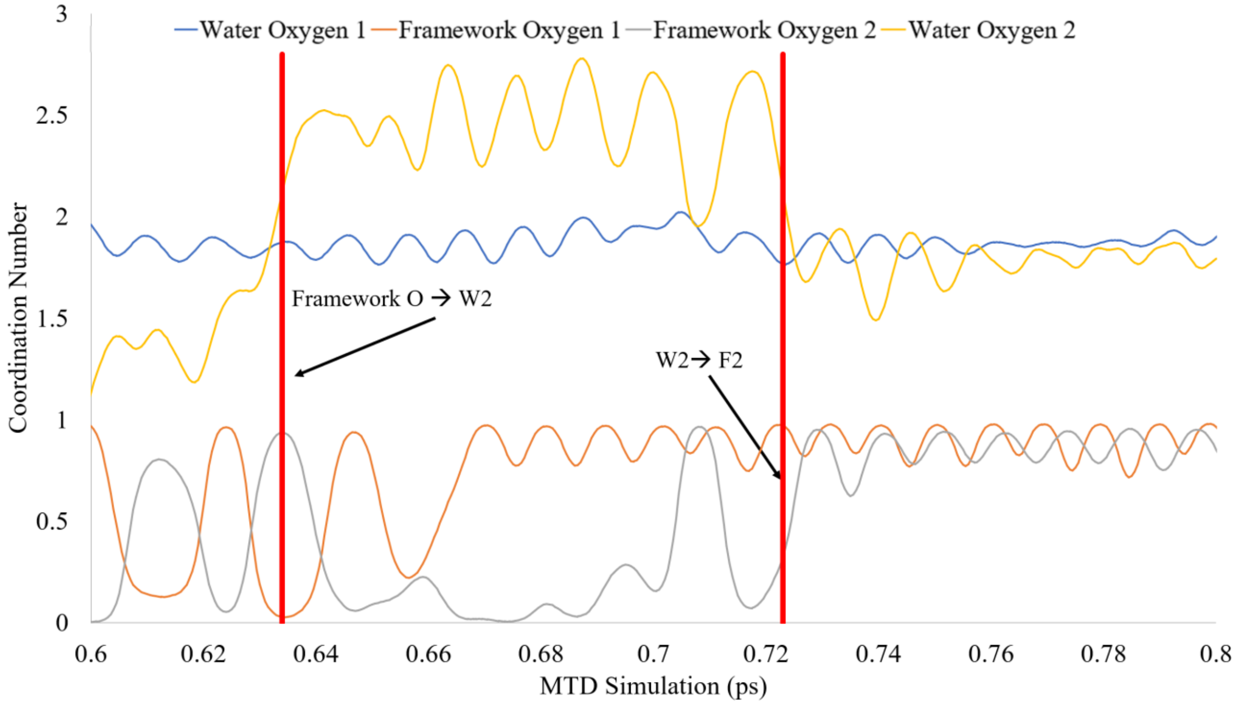

Figure 5.12. *Highlighted portion of the oxygen CNs along a WtF-MTD run for UPC-H5a showing a stepwise proton transfer. Blue, and yellow lines correspond to oxygen atoms from water molecules in the pore. Grey, and orange lines correspond to oxygen atoms from the framework. Framework O→ W2 indicates the initiation of the transfer, and W2→ F2 finishes the stepwise transfer; W stands for water-based oxygen atom in which the bias is applied, F stands for framework-based oxygen atom in which the bias is applied, and unbiased O is an oxygen atom on the framework without bias added. The red lines the two transition points in the stepwise mechanism unbiased O→ W2, and W2 →F2.*

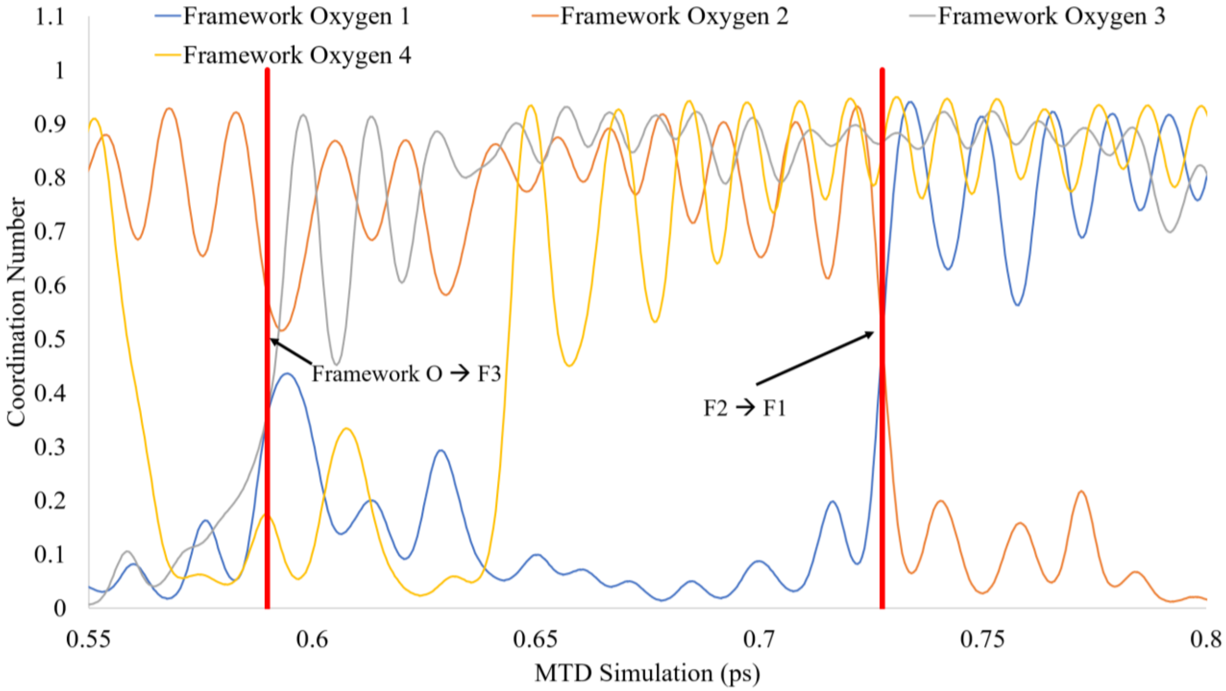

Figure 5.13. *Highlighted portion of the oxygen CNs along a FtF-MTD run for GTUB-5 showing stepwise proton transfer. Grey, orange, blue, and yellow lines correspond to oxygen atoms on the framework. Unbiased O→ F2 indicates the initiation of the transfer, and F2→ F1 indicate the proton transfer to and from a framework oxygen atom. Framework O is a transfer from a framework oxygen atom which is not affected by the bias. F stands for a framework-based oxygen atom in which the bias is applied. The red lines the two transition points in the stepwise mechanism Framework O→ F3, and F2→F1.*

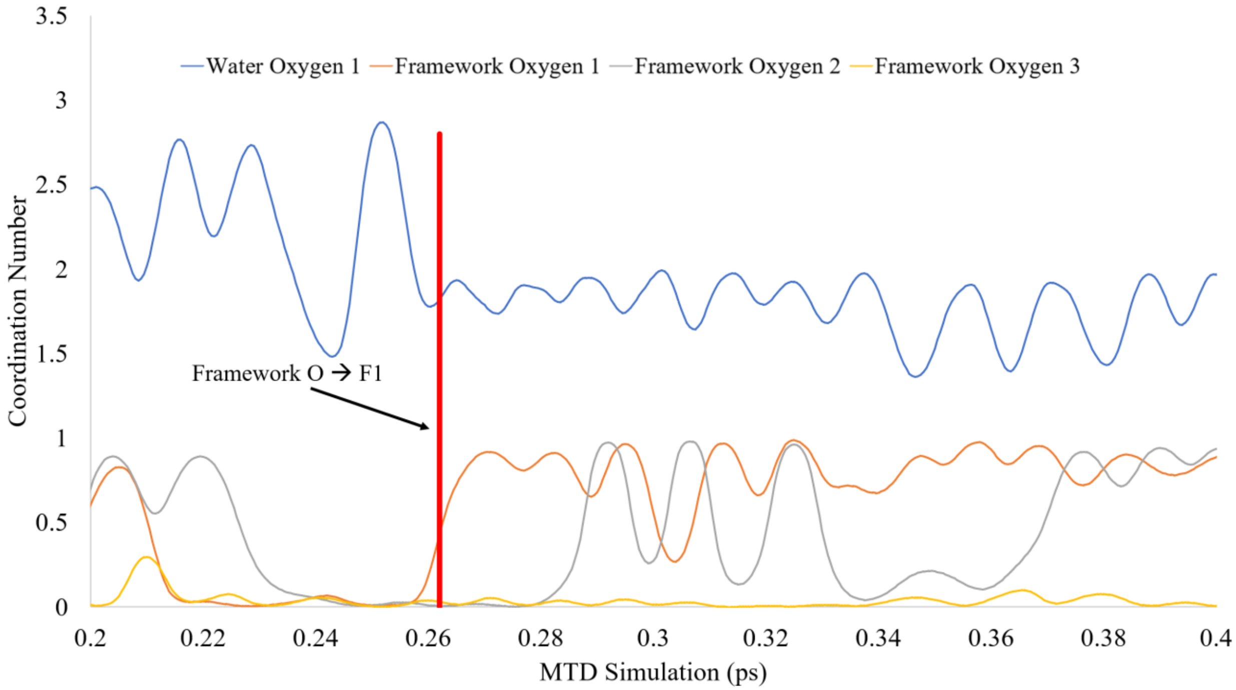

Figure 5.14. *Highlighted portion of the oxygen CNs along a FtF-MTD run for UPC-H5a showing a concerted proton transfer. Grey, orange, and yellow lines correspond to oxygen atoms on the framework. Blue lines correspond to oxygen atoms from water molecules in the pore. F1 is the oxygen which the bias potential is being added, unbiased O is an oxygen atom on the framework without added bias. The red lines the transition in the concerted mechanism unbiased O→F1.*

To obtain an approximate value of the free energy (ΔG_{PT}) of proton transfers within the HOFs, we make use of the energy applied from the bias of the MTD simulations. The bias potential is added every 5 fs, thus, to calculate the ΔG_{PT}, we use PLUMED to convert the Gaussian hills to free energy over the simulation giving access to the free energy applied along all the CVs with respect to time. To capture an approximation to ΔG_{PT} of a proton transport, the energy at the beginning of a proton transfer is considered the reactant and when the proton is mid-way between two oxygen atoms it is considered the transition state. For example, within the WtF-MTD pathway for GTUB-5 (**Figure 5.10**) there is a proton transfer starting at 0.981 ps, which reaches the transition point at 1.003 ps. The transfer is indicated by the '*Water Oxygen 3*' CN reducing from ~2.5 to ~1.7, while the '*Framework Oxygen 1*' CN increases from ~0 to ~1. Since the bias is added every 5 fs, we use the difference in free energy that initiated the proton transfer at 0.98 ps, and the free energy added near the transition at 1.00 ps to approximate the ΔG (**Eqns. 5.5, 5.6**).

$$\Delta G_{PT} = G_{transiton} - G_{reactant} \qquad 5.8$$

$$\Delta G_{PT} = G_{1.00\ ps} - G_{0.98\ \ ps} = (1.158 - 1.167)x10^{3} = 8.53\ meV \qquad 5.6$$

The calculated proton ΔG_{PT} for the various routes in GTUB-5 and UPC-H5a are given in **Table 5.2**. Between the two HOFs it is evident the barrier for transmission is in general lower for UPC-H5a, compared to GTUB-5, that is, from our MTD simulations the protons have easier proton transport within UPC-H5a. When considering the statistics from the error bars, the WtW and FtF transfers are both lower in ΔG_{PT} in UPC-H5a compared to GTUB-5, while the WtF error bars for GTUB-5 extend beyond those of UPC-H5a. As can be seen for GTUB-5, the results indicate that the lowest energy for transfer occurs for protons to the framework from waters in the pore (i.e., WtF), followed by protons moving between water molecules in the pores (i.e., WtW), and then protons moving through the framework (i.e., FtF). The results for UPC-H5a indicate the lowest ΔG is for transfers from the pore to the framework (i.e., WtF), followed by protons moving between water molecules in the pores (i.e., WtW), with the highest energies being associated with movement of protons through the framework (i.e., FtF).

Table 5.2. *Estimated proton ΔG for each transport route in GTUB-5 & UPC-H5a. For each route, the values are obtained by averaging over the proton transfers in the corresponding MTD trajectories (with standard deviations shown along with each average). WtW is averaged over 9/9 proton transfers over the 2ps WtW-MTD simulation for GTUB-5/UPC-H5a; WtF is averaged over 2/7 proton transfers from the 2ps WtF-MTD simulations for GTUB-5/UPC-H5a; FtF is averaged over 10 proton transfers from the 2ps FtF-MTD simulation of GTUB-5, and 5 proton transfers from the FtF-MTD & 4 proton transfers from the W2F-MTD UPC-H5a, totaling 9 proton transfers for FtF-MTD within UPC-H5a.*

Route	**ΔG_{PT} (meV) GTUB-5**	**ΔG_{PT} (meV) UPC-H5a**
WtW	5.61 ±3.20	1.72 ±2.12
WtF	4.84 ±5.22	0.884 ± 0.72
FtF	7.14	3.50

	±4.68	± 4.74

Snapshots from the MTD trajectory results for both UPC-H5a and GTUB-5 are shown in **Figure 5.15**. These figures are a sample of the proton transfer mechanisms that were seen in both the biased and unbiased trajectories, each of the individual proton transfers shown occurred in both HOFs, and the results presented are focused on the MTD trajectories. Based on **Figures 5.9, 5.11**, we see that the WtW route proceeds via either a single proton transport or stepwise mechanism (see **Figure 5.15-A, B**, respectively). In particular, a single proton transport mechanism occurs between two semi-isolated water molecules in the pore (**Figure 5.15 – A, Figure 5.9)**, while the stepwise mechanism occurs when a chain of water molecules forms in the pore (**Figure 5.15 – B, Figure 5.11)**.

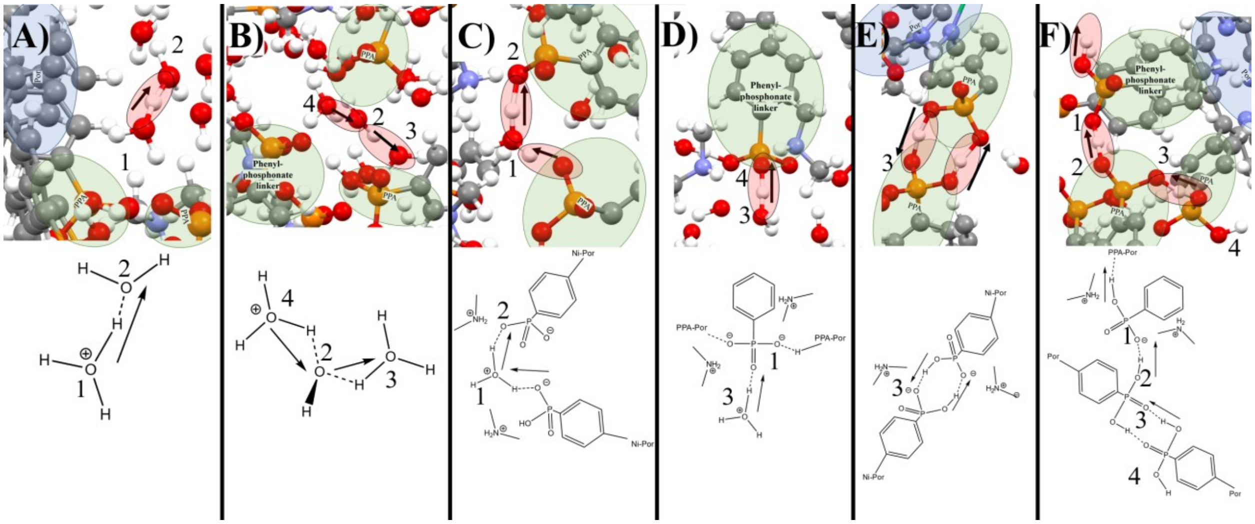

Figure 5.15. *Snapshots along MTD trajectories of proton transport mechanisms observed in the trajectories for UPC-H5a and GTUB-5. All mechanisms shown occur in both UPC-H5a and GTUB-5. A) Single proton WtW transfer in UPC-H5a, as shown in* ***Figure 5.9****. B) Stepwise WtW mechanism in GTUB-5, as shown in* ***Figure 5.11****. C) Stepwise WtF mechanism in UPC-H5a, as shown in* ***Figure 5.12****. D) Single proton WtF transfer in GTUB-5, as seen in* ***Figure 5.10****. E) Concerted F2F mechanism in UPC-H5a, as shown in* ***Figure 5.14****. F) Stepwise mechanism in GTUB-5, as shown in* ***Figure 5.13****. Colour coding: carbon-grey, nitrogen-blue, oxygen-red, phosphorous-orange, hydrogen-white, the numbers refer to the oxygen atoms in which the bias is applied (****Figure 5.4, Figure 5.5****).*

The WtF route occurs by either a single proton transfer or stepwise Grotthuss mechanism (**Figure 5.10, Figure 5.12**). This route requires proximity of water molecules and free oxygen atoms on the phosphonates for transfer of a proton, the phosphonate oxygens participate in a three-body transition state with the water (**Figure 5.10, Figure 5.15 – D)**. The stepwise mechanism occurs when a proton is passed along a chain of oxygens from/to the framework (**Figures 5.12, Figure 5.15 – C)**. The proton will then be donated to a phosphonate already actively participating in a hydrogen bond within the framework; the donated proton can cause the framework to donate its proton to an adjacent framework oxygen. The FtF route (**Figure 5.13, Figure 5.14**) occurs via either a concerted or stepwise mechanism. The former happens readily as the phosphonate hydrogen bonds have freely available protons between adjacent phosphonates, hydrogen bonding in paralell (**Figure 5.15 – E**). The later stepwise mechanism typically happens if a proton hops from one phosphonate to another, causing a proton on the opposite side of the phosphonate to push off (**Figure 5.15 – F**).

Based on **(Figures 5.9-5.15)**, we propose potential routes for proton conduction through the UPC-H5A and GTUB-5 super-structures. As can be seen in **Figure 5.16 – A**, the UPC-H5a pore is lined with phosphonates along the a-axis. Such pores allow for proton transport predominantly along the a-axis via single proton transport into/or a stepwise mechanism (WtW) amongst waters in the pores, along with a single proton transport mechanism from water to the framework (WtF), and lastly through a stepwise mechanism among oxygen atoms in the framework (FtF). On the other hand, as seen in **Figure 5.10 – B**, GTUB-5 has sheets of phosphonates that run along the c-axis. In this case, the pores allow for proton transport via the WtW, WtF, and FtF routes predominantly along the c-axis. The transport is done via single proton transport into/or stepwise mechanism to transport protons (WtW) amongst themselves, a stepwise mechanism for the waters to transport protons to the framework (WtF), and transport through the framework itself through a stepwise FtF mechanism.

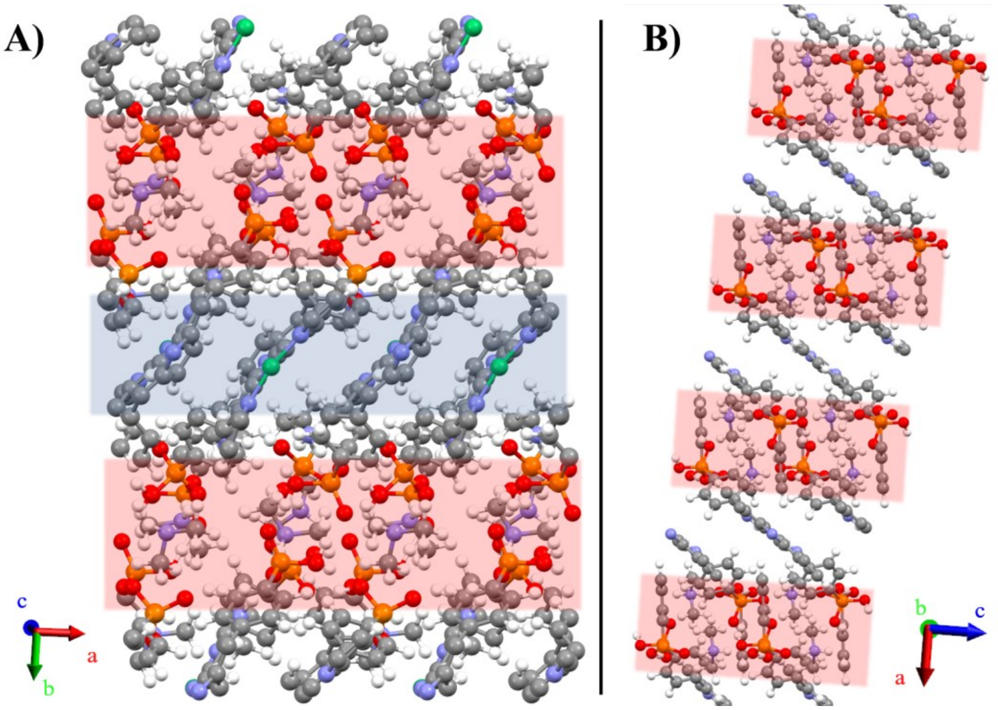

Figure 5.16. *2x2x2 expanded supercells (based on the lattice/geometrically optimized unit-cell pre hydration) depicting the phosphonate-lined pores (highlighted in red and blue) in A) UPC-H5a and B) GTUB-5. The red highlighted pore in UPC-H5a describes two pores, while the blue describes the third pore.*

5.4 CONCLUSIONS

Proton conduction mechanisms of two HOFs have been studied, namely GTUB-5 and UPC-H5a. Where UPC-H5a and GTUB-5 have similar structural makeup, with the structures primarily composed of 5,10,15,20-tetrakis [*p*-phenylphosphonic acid] porphyrin, the difference being UPC-H5a has nickel atoms introduced into the porphyrin core, and GTUB-5 has a phenylphosphonic acid linker between adjacent porphyrins. Experimentally, these HOFs conduct protons at 4.20 x 10^{-6}/3.42 x 10^{-2} S cm^{-1}, under 90%/99% at 75 °C/80 °C for GTUB-5/UPC-H5a, respectively. The temperature dependent proton conductivities correspond to activation energies (E_a) of 0.14/0.20 eV under 90/95 %r.h. for GTUB-5/UPC-H5a, respectfully, which suggests a Grotthuss-like mechanism of proton transport in both HOFs. To study these HOFs, the structures were optimized using DFT and PBC-based electronic structure refinement of their experimental XRD structures, and dynamically analyzed by use of BOMD and MTD simulations.

The results of the unbiased BOMD simulations indicate that GTUB-5 has a higher relative hydrogen bonding strength, as the O-O RDF distances are lower compared to UPC-H5a, this agrees with the contracted hydrogen-$O_{acceptor}$ distances for GTUB-5, compared to UPC-H5a as seen in the H-O RDF. The average RESP-REPEAT charges of several snapshot reactant, transition, and product proton transfers indicate an electronic charge transport from the $O_{acceptor}$ to the O_{donor} from a proton transport this is seen as the donor/acceptor oxygen at the beginning of the proton transfer is more/less negatively charged than at the end of the transfer. Three potential routes for proton transport were identified and MTD was used to drive protons along these pathways, to obtain both approximate free energies and mechanisms, the routes being water-to-water (WtW), water-to-frame (WtF), and frame-to-frame (FtF). The results of the averaged free energies of proton hops in the MTD simulations indicate a lower energy requirement for transport in UPC-H5a. Within UPC-H5a the WtF (0.757 +/- 0.66 meV) had the lowest ΔG_{PT} followed by WtW (1.10 +/- 1.06 meV), and FtF (4.90 +/- 6.61 meV). Also, the averaged free energies from the GTUB-5 MTD trajectories follow the same pattern, where the WtF (4.84 +/- 5.22 meV) had the lowest ΔG_{PT} followed by WtW (5.21 +/- 3.26 meV), and FtF (7.47 +/- 5.33 meV).

There are three proton transport mechanisms in both systems, these are single proton transport, a stepwise transport, and a concerted transport. The single proton transport occurs in the WtW and WtF pathways, the stepwise mechanism is seen in the WtW, and FtF pathways, and the concerted transport takes place in the FtF pathway. Lastly, due to the orientation of the phosphonate groups in the super-structure of the HOFs, proton transport takes place along the a-/c-axis of UPC-H5a/GTUB-5, for which the overall transport is likely a combination of single proton and stepwise mechanisms.

Chapter 6

CONCLUSIONS AND FUTURE WORK

6.1 SUMMARY

The modeling of MOFs and HOFs is challenging due to the high numbers of atoms, electrons, oxidation states available to metals (in the case of MOFs), and hydrogen bonding (in the case of HOFs). Choosing sufficiently accurate, computationally feasible, and reproducible methodologies is paramount in studying these materials, e.g., optimizing geometries, determining spin configurations, calculating frontier orbital gaps, simulating nuclear dynamics, etc. Commonly used methodologies include DFT, hybrid-DFT, and DFT-based BOMD due to their favourable balance between computational speed and accuracy. DFT and hybrid-DFT approaches can yield useful information about the static electronic structure of a system (i.e., orbital configurations), energies, frontier orbital gaps, magnetic contributions, and local electrostatic environments around atoms. On the other hand, BOMD yields information about how nuclei move in time, reactions between host molecules in the framework, reactions between host molecules and the framework, proton transfer, etc. Throughout this thesis, we applied DFT, hybrid-DFT, and BOMD to gain insight into the electronic structure, electrical conductivity, proton conductivity, magnetic behaviour, and local electrostatic environments of a number of phosphonate MOFs and HOFs.

In Chapter 3, we investigated three different phosphonate MOFs: TUB75, TUB40, and TUB1. These MOFs contain copper(II) phosphonate IBUs with differing SBU linkers, namely, 4,4'-bipyridine and 1,4-naphthalendiphosphonic acid in TUB75, 2,6-naphthalendiphosphonic acid in TUB40, and methane tetra-p-phenylphosphonic acid in TUB1. We used DFT to optimize their structures to characterize their electrical conduction and magnetic mechanisms. The HOCO-LUCO gap in TUB75 was calculated to be 1.77 eV, in good agreement with the experimental value of 1.4 eV (estimated from a Tauc plot of the UV-Vis spectrum). The TUB75 HOCO and LUCO orbitals are spatially separated, with the HOCO on the naphthalene-based carbon atoms and the

LUCO on the nitrogen and carbon atoms on the bipyridine, suggesting a through-space conduction mechanism. Furthermore, the magnetic exchange energy was calculated to be -37.3 meV, which agrees with the experimental finding that the AFM configuration is the most stable configuration at low temperatures. In the case of TUB40, Tauc plotting of the UV-Vis spectrum yields a 1.42 eV gap, and the temperature-dependent magnetic susceptibility at different applied magnetic fields also indicates that the AFM configuration is most stable at low temperatures. Our calculations yielded a HOCO-LUCO gap of 2.32 eV and a magnetic exchange energy of -1.50 meV, indicating that the AFM configuration is the more stable configuration. That being said, since the magnitude of the magnetic exchange energy was small, we also studied the FM configuration. The FM configuration was found to have two spin-dependent gaps, viz., 2.195 and 3.913 eV for the spin-down and spin-up configurations, respectively. For the AFM configuration, the pDOS results show that the HOCO is localized on the naphthalene carbon atoms and the LUCO has contributions from the copper d-orbitals. On the other hand, for the FM configuration, an excitation of an alpha-electron would transfer the electron from the naphthalene carbon HOCO to a naphthalene carbon LUCO, while an excitation of a beta-electron would transfer an electron from the naphthalene carbon atoms HOCO to a LUCO on the copper atoms in the system, suggesting a through-bond conduction mechanism for beta excitation, and through space conduction mechanism for an alpha excitation. In the case of TUB1, the crystal structure shows two different copper(II) phosphonate coordination environments in the system, viz., square planar and distorted trigonal bipyramidal. Furthermore, Tauc plotting of the UV-Vis spectrum reveals an indirect band gap of 2.4 eV and a direct gap of 2.7 eV. Our DFT calculations predict an α-spin gap of 2.60 eV and a β-spin gap of 0.48 eV. Both the alpha-spin and beta-spin LUCOs are mainly composed of the square planar copper atom d-orbitals with some oxygen p-orbitals, and both HOCOs are mainly composed of the π-orbitals of the carbon atoms in half the phenyl rings and π-orbitals of oxygen atoms, thus indicating a through-bond conduction mechanism. Interestingly, the LUCO's dependence on the d-orbitals of the square planar copper atoms indicates a lowered frontier orbital gap in this geometric configuration compared to the distorted trigonal bipyramidal copper atom coordination environment. Upon inspection of the band structure of TUB1, one observes 120 meV dispersions in the β-LUCO band, suggestive of high electron mobility in multiple directions. All of the above TUB-MOFs have electron delocalization around the three oxygen atoms of the phosphonate, as deduced from the charge model calculations; the three oxygen atoms have a charge of ~ -1, indicating an excess of 1 electron in the group. In general, for these phosphonate MOFs all of the HOCOs are dependent on the carbon atoms within the SBUs. However, the LUCO is highly structurally dependent, with contributions from the carbon and nitrogen atoms in the bipyridine in TUB75, from the copper atoms in TUB40, and from the copper atoms in TUB1.

In Chapter 4, we investigated five HOF materials, namely, GTUB-5, Cu-GTUB-5, Ni-GTUB-5, Zn-GTUB-5, and Pd-GTUB-5. The GTUB-5 HOF material is constructed of 5,10,15,20-tetrakis [*p*-phenylphosphonic acid] porphyrins connected through phenyl-phosphonate linkers. The metalated versions of with the *M*-prefix have the same building units, however, they contain a metal within the core of the porphyrin, which has ramifications on the structure and HOCO/LUCO orbital gaps. These systems were studied in a similar fashion to the MOF materials, however, instead of making use of the hybrid-DFT approach, we use a pure GGA-DFT approach for analysis. To investigate these materials, we made use of structural optimizations, DOS plots, charge, and IR analysis. Experimentally, GTUB-5 had an indirect gap of 1.56 eV, and our DFT calculations resulted in good agreement with the UV-Vis experiment, where the HOCO-LUCO gap is estimated to be 1.65 eV in both codes used, CP2K and ADF-BAND. The HOCO to LUCO transition both take place within the carbon and nitrogen atoms in the porphyrin core. The orbital populations for the carbon atoms indicate a reduction in from the HOCO to LUCO along the y-axis and an increase from the HOCO to LUCO along the x-axis, indicating a directional dependence of an electronic excitation. For the metalated GTUB-5 materials, XRD showed that the nickel substitution, Ni-GTUB-5, caused a twist along the a-axis. Our calculations revealed that there is a contraction of the porphyrin size when Ni is substituted into the porphyrin core. The contraction is likely due to a combination of localization of the HOCO on the d-orbitals within Ni-GTUB-5, and the short Ni-nitrogen bond lengths caused by an even sharing of electron density between the Ni and nitrogen atoms. Zn-GTUB-5 has the largest porphyrin size likely due to a poor sharing of electron density, causing long Zn-nitrogen bond lengths. For Cu- and Pd-GTUB-5, their porphyrin sizes are similar and the density distribution (and bond lengths) of the metals and nitrogen atoms are in-between those of Zn- and Ni-GTUB-5. Partial Hessians were obtained for Zn-GTUB-5 and allowed for assignment of several IR stretching frequencies. In particular, the DFT-IR results indicate that the O-H stretching modes are between 2286 cm^{-1} – 2458 cm^{-1}. All of the experimental IR spectra of the metalated GTUB-5 systems show a similar peak structure/width at a similar wavenumber, suggesting that there is no significant difference in the hydrogen bonding strength between the systems. The UV-Vis spectra yield frontier orbital gaps of 1.44, 1.58, 1.37, and 1.62 eV for Cu-, Ni-, Pd-, and Zn-GTUB-5, respectively. While our DFT calculations do not reproduce the trend in the HOCO-LUCO gaps, they are in decent agreement with experiment (viz., 1.81(α)/1.89(β), 1.64, 1.87, 1.77 eV for Cu(α)/Cu(β)-, Ni-, Pd-, and Zn-GTUB-5, respectively). Our DOS plots reveal that Zn-, Pd-, and α-spin Cu-GTUB-5 all have HOCO/LUCO characters on the porphyrin carbon and nitrogen atoms, similar to GTUB-5. While the HOCO of β-spin Cu-GTUB-5 lies on the porphyrin carbon and nitrogen atoms, the LUCO has contributions from the d-orbitals of the copper atom. Lastly, Ni-GTUB-5 stands, with both its HOCO and LUCO having contributions from the d-orbitals of the Ni.

In Chapter 5, we investigated the proton conductive mechanism of two HOFs, the GTUB-5 HOF of Chapter 4, and a HOF from literature, constructed of similar building units, namely, UPC-H5a. Both HOFs are constructed of 5,10,15,20-tetrakis [*p*-phenylphosphonic acid] porphyrin linkers, while GTUB-5 has an additional phenylphosphonate linker compared to UPC-H5a, which UPC-H5a has a nickel atom in the porphyrin core. Despite this seemingly small difference in structural makeup, experimentally GTUB-5 is for orders of magnitude slower at conducting protons compared to UPC-H5a. Where GTUB-5 has a proton conductivity of 4.20 x 10^{-6} S cm^{-1} under 90 %r.h. and 75 °C, and UPC-H5a has a proton conductivity of 3.42 x 10^{-2} S cm^{-1} under 99 %r.h. and 80 °C. The experimental activation energies which corresponds to the sum of migration and defect formation at different temperatures were determined to be 0.14 eV for GTUB-5 (under 90 %r.h.) and 0.20 eV (under 95% r.h.) for UPC-H5a. Activation energies in this range correspond to a Grotthuss-like mechanism. We optimized both GTUB-5 and UPC-H5a structures, added 10 guest water molecules into the pores, and 3/1 protons into the pores (where 3/1 are the number of unique pores for GTUB-5/UPC-H5a), and performed BOMD, and MTD simulations to investigate the protonic movement. The unbiased BOMD-based RDFs indicated that GTUB-5 has shorter O-O bonding, and the H-O bond distance is slightly contracted in the UPC-H5a HOF, indicating relatively stronger hydrogen bonding in GTUB-5. Furthermore, the charge analysis indicates that there is a charge transfer from $O_{acceptor}$ to O_{donor} from the transit of a proton from the donors to the acceptors in both systems. The MTD simulations were parameterized based on the RDF results of the unbiased trajectories and used to push protons around through three pre-defined pathways that were identified in the unbiased runs: (i) Water-to-water (WtW). (ii) Water-to-framework (WtF). (iii) Framework-to-framework (FtF). The MTD results were used to estimate the free energy (ΔG_{PT}) of proton transport and indicate that UPC-H5a has lower ΔG_{PT} requirement for proton transport than GTUB-5. Within GTUB-5 the WtF (4.84 +/- 5.22 meV) had the lowest ΔG_{PT} followed by WtW (5.21 +/- 3.26 meV), and FtF (7.47 +/- 5.33 meV). Similarly, for UPC-H5a the WtF (0.757 +/- 0.66 meV) had the lowest ΔG_{PT} followed by WtW (1.10 +/- 1.06 meV), and FtF (4.90 +/- 6.61 meV). There were three proton transport mechanisms identified: (i) Single proton transport. (ii) Stepwise proton transport. (iii) Concerted proton transport. The single proton transport mechanism happens in the WtW and WtF pathways, the stepwise mechanism takes place in WtW, and FtF pathways, and the concerted proton transport occurs in the FtF pathway. Single proton is either between isolated water molecules or water molecules to the framework. The stepwise mechanism occurs between a chain of waters, or a chain of phosphonates in the framework. The concerted mechanism takes place when a proton transits between two phosphonates hydrogen-bonded in parallel, causing the second phosphonate to push off its proton to the initial phosphonate. Lastly, based on the locations of the phosphonates in the pores of the structures of GTUB-5 and UPC-H5a, we suggested long-range proton transport occurs in the pores by using the single proton transport and stepwise mechanisms along the a-/c-axes of UPC-H5a/GTUB-5.

6.2 FUTURE WORK

In Chapter 3, we investigated the electrical conductivity and magnetic characteristics of TUB75. However, it has been experimentally determined that this material also captures CO_2 in the presence of H_2O with high selectivity, a property that is highly sought after for greenhouse gas reduction. The material itself is synthesized under hydrothermal conditions, yet the crystal structure has no H_2O molecules in its pores after refinement. Currently, there is a limited understanding of how CO_2 behaves in the pores in the presence of H_2O. Based on the structure of TUB75, it is hypothesized that the hydrophobic SBUs help reduce H_2O uptake while allowing bonding with CO_2. To shed light on this, one must study (i) the dynamics of CO_2 and H_2O within the pores and (ii) the nature of the binding of CO_2 in the pores (i.e., chemisorption or physisorption). The combination of AIMD with MTD used in Chapter 5 could also be used to simulate the $CO_2 + H_2O$ dynamics in TUB75. Furthermore, the resulting trajectories could be used as a starting point for higher-level quantum chemistry calculations for investigating the binding of

CO_2 within the pores. There is also interest in using the phosphonate MOF materials for ion transport applications, e.g., Li^+ transport. Again, a similar dynamics methodology to that used in Chapter 5 would be useful to study the transport of Li^+ ions in the pores of various phosphonate MOFs.

In Chapter 5, we investigated the proton conductivity mechanisms of two proton-conductive HOFs, viz., GTUB-5 and UPC-H5a. While the results point to three potential mechanisms of proton transport, the large statistical uncertainties in the activation energies and charges could be reduced by gathering more statistics. The charges, which were averaged over three proton jumps in three unbiased trajectories for each HOF, could be improved by averaging over more jumps in all the unbiased trajectories and more proton transports in each trajectory. Furthermore, the well-tempered MTD approach improves with longer trajectories; thus, one could likely improve the uncertainty in the activation energies in three ways: (i) increase the length of the MTD trajectories from 2 ps to 4 ps, (ii) perform more MTD simulations starting from different initial conditions, and (iii) perform more MTD simulations incorporating different oxygen-based pathways.

6.3 CONCLUSIONS

The computational results presented in this thesis helped open a new area of study in phosphonate-MOF chemistry. In particular, our DFT results revealing the narrow frontier orbital gap in TUB75 spawned studies of the electrical conductivity of several phosphonate MOF and HOF materials. The computational methodologies for studying MOFs have been well-established for some time, and the work presented in this thesis shows that they can be successfully applied to previously un-studied systems. While formerly there has been extensive research on electrical conductivity in traditional MOF materials, there was little exploration of the frontier orbital gaps in phosphonate-MOF/HOFs, which was the main focus of the research presented in this thesis. Furthermore, studies of proton transport mechanisms in HOFs have also been limited, so the results presented in Chapter 5 shed light on them. Overall, the work presented in this thesis sheds light on the electrical/proton conductive nature of the phosphonate MOFs and HOFs through a variety of computational chemistry methods.

A critical question in studying the proton/electrical conductivity of MOFs and HOFs is which components of the frameworks are involved in the conduction. The results presented in this thesis indicate that one possible path to low gap materials are linkers formed of highly conjugated organic building blocks, as the materials studied herein all have HOCOs containing π-conjugated carbon rings. As mentioned in the introduction, improving the interactions between π-conjugated linkers is one avenue for improving conductivity in highly porous materials, and our collaborative work corroborates this. However, there is no clear and systematic route for improvement, as the introduction of metals and different IBUs into the frameworks vastly changes the localization of the unoccupied orbitals, as seen in both the highly conjugated HOFs in Chapter 4 and in the MOFs in Chapter 3. In summary, this thesis explores the intricate electronic structure landscape of phosphonate MOF/HOFs, and dynamics within HOFs, using DFT and BOMD simulations. These findings could provide valuable insights into the properties of these materials, particularly in the fundamental understanding of their electronic properties, one day leading to more advanced energy-related devices.

BIBLIOGRAPHY

(1) Armand, M.; Tarascon, J. M. Building Better Batteries. *Nature*. Nature Publishing Group February 7, 2008, pp 652–657. https://doi.org/10.1038/451652a.

(2) Nayak, P. K.; Mahesh, S.; Snaith, H. J.; Cahen, D. Photovoltaic Solar Cell Technologies: Analysing the State of the Art. *Nat. Rev. Mater.* **2019**, *4* (4), 269–285. https://doi.org/10.1038/s41578-019-0097-0.

(3) Staffell, I.; Scamman, D.; Velazquez Abad, A.; Balcombe, P.; Dodds, P. E.; Ekins, P.; Shah, N.; Ward, K. R. The Role of Hydrogen and Fuel Cells in the Global Energy System. *Energy and Environmental Science*. Royal Society of Chemistry February 1, 2019, pp 463–491. https://doi.org/10.1039/c8ee01157e.

(4) Manthiram, A. An Outlook on Lithium Ion Battery Technology. *ACS Cent. Sci.* **2017**, *3* (10), 1063–1069. https://doi.org/10.1021/acscentsci.7b00288.

(5) Goodenough, J. B.; Park, K. S. The Li-Ion Rechargeable Battery: A Perspective. *Journal of the American Chemical Society*. UTC January 30, 2013, pp 1167–1176. https://doi.org/10.1021/ja3091438.

(6) Redondo-Iglesias, E.; Venet, P.; Pelissier, S. Efficiency Degradation Model of Lithium-Ion Batteries for Electric Vehicles. *IEEE Trans. Ind. Appl.* **2019**, *55* (2), 1932–1940. https://doi.org/10.1109/TIA.2018.2877166.

(7) Paul, T.; Mesbahi, T.; Durand, S.; Flieller, D.; Uhring, W. Sizing of Lithium-Ion Battery/Supercapacitor Hybrid Energy Storage System for Forklift Vehicle. *Energies* **2020**, *13* (17), 14–17. https://doi.org/10.3390/en13174518.

(8) Marin Halper James C Ellenbogen, V. S. *3 Supercapacitors: A Brief Overview MITRE*; 2006.

(9) Sheberla, D.; Bachman, J. C.; Elias, J. S.; Sun, C. J.; Shao-Horn, Y.; Dincă, M. Conductive MOF Electrodes for Stable Supercapacitors with High Areal Capacitance. *Nat. Mater.* **2017**, *16* (2), 220–224. https://doi.org/10.1038/nmat4766.

(10) Zhang, J.; Zhang, H.; Wu, J.; Zhang, J. PEM Fuel Cell Fundamentals. In *Pem Fuel Cell Testing and Diagnosis*; Elsevier, 2013; pp 1–42. https://doi.org/10.1016/b978-0-444-53688-4.00001-2.

(11) Spohr, E. Molecular Dynamics Simulations of Proton Transfer in a Model Nafion Pore. In *Molecular Simulation*; Taylor & Francis GroupAbingdon, UK, 2004; Vol. 30, pp 107–115. https://doi.org/10.1080/0892702301000152208.

(12) Wang, Y.; Yin, J.; Liu, D.; Gao, C.; Kang, Z.; Wang, R.; Sun, D.; Jiang, J. Guest-Tuned Proton Conductivity of a Porphyrinylphosphonate-Based Hydrogen-Bonded Organic Framework. *J. Mater. Chem. A* **2021**, *9* (5), 2683–2688. https://doi.org/10.1039/d0ta07207a.

(13) Seth, S.; Jhulki, S. Porous Flexible Frameworks: Origins of Flexibility and Applications. *Mater. Horizons* **2020**. https://doi.org/10.1039/d0mh01710h.

(14) Zentner, C. A.; Lai, H. W. H.; Greenfield, J. T.; Wiscons, R. A.; Zeller, M.; Campana, C. F.; Talu, O.; Fitzgerald, S. A.; Rowsell, J. L. C. High Surface Area and Z′ in a Thermally Stable 8-Fold Polycatenated Hydrogen-Bonded Framework. *Chem. Commun.* **2015**, *51* (58), 11642–11645. https://doi.org/10.1039/C5CC04219D.

(15) Eddaoudi, M.; Kim, J.; Rosi, N.; Vodak, D.; Wachter, J.; O'Keeffe, M.; Yaghi, O. M. Systematic Design of Pore Size and Functionality in Isoreticular MOFs and Their Application in Methane Storage. *Science.* **2002**, *295* (5554), 469–472. https://doi.org/10.1126/science.1067208.

(16) Zhou, H. C.; Long, J. R.; Yaghi, O. M. Introduction to Metal-Organic Frameworks. *Chemical Reviews*. February 8, 2012, pp 673–674. https://doi.org/10.1021/cr300014x.

(17) Yaghi, O. M.; O'Keeffe, M.; Ockwig, N. W.; Chae, H. K.; Eddaoudi, M.; Kim, J. Reticular Synthesis and the Design of New Materials. *Nature*. June 12, 2003, pp 705–714. https://doi.org/10.1038/nature01650.

(18) Xie, L. S.; Skorupskii, G.; Dincă, M. Electrically Conductive Metal-Organic Frameworks. *Chemical Reviews*. American Chemical Society 2020. https://doi.org/10.1021/acs.chemrev.9b00766.

(19) Wang, H.; Li, B.; Wu, H.; Hu, T. L.; Yao, Z.; Zhou, W.; Xiang, S.; Chen, B. A Flexible Microporous Hydrogen-Bonded Organic Framework for Gas Sorption and Separation. *J. Am. Chem. Soc.* **2015**, *137* (31), 9963–9970. https://doi.org/10.1021/JACS.5B05644/SUPPL_FILE/JA5B05644_SI_003.CIF.

(20) Batten, S. R.; Champness, N. R.; Chen, X. M.; Garcia-Martinez, J.; Kitagawa, S.; Öhrström, L.; O'Keeffe, M.; Suh, M. P.; Reedijk, J. Terminology of Metal-Organic Frameworks and Coordination Polymers (IUPAC Recommendations 2013). *Pure Appl. Chem.* **2013**, *85* (8), 1715–1724. https://doi.org/10.1351/PAC-REC-12-11-20.

(21) Li, H.; Eddaoudi, M.; O'Keeffe, M.; Yaghi, O. M. Design and Synthesis of an Exceptionally Stable and Highly Porous Metal- Organic Framework. *Nature* **1999**, *402* (6759), 276–279. https://doi.org/10.1038/46248.

(22) Lyle, S. J.; Flaig, R. W.; Cordova, K. E.; Yaghi, O. M. Facilitating Laboratory Research Experience Using Reticular Chemistry. *J. Chem. Educ.* **2018**, *95* (9), 1512–1519. https://doi.org/10.1021/ACS.JCHEMED.8B00265/ASSET/IMAGES/MEDIUM/ED-2018-00265X_0006.GIF.

(23) Rosen, A. S.; Iyer, S. M.; Ray, D.; Yao, Z.; Aspuru-Guzik, A.; Gagliardi, L.; Notestein, J. M.; Snurr, R. Q. Machine Learning the Quantum-Chemical Properties of Metal–Organic Frameworks for Accelerated Materials Discovery. *Matter* **2021**, *4* (5), 1578–1597. https://doi.org/10.1016/j.matt.2021.02.015.

(24) Moghadam, P. Z.; Li, A.; Wiggin, S. B.; Tao, A.; Maloney, A. G. P.; Wood, P. A.; Ward, S. C.; Fairen-Jimenez, D. Development of a Cambridge Structural Database Subset: A Collection of Metal-Organic Frameworks for Past, Present, and Future. *Chemistry of Materials*. 2017, pp 2618–2625. https://doi.org/10.1021/acs.chemmater.7b00441.

(25) Farha, O. K.; Eryazici, I.; Jeong, N. C.; Hauser, B. G.; Wilmer, C. E.; Sarjeant, A. A.; Snurr, R. Q.; Nguyen, S. T.; Yazaydin, A. Ö.; Hupp, J. T. Metal-Organic Framework Materials with Ultrahigh Surface Areas: Is the Sky the Limit? *J. Am. Chem. Soc.* **2012**, *134* (36), 15016–15021. https://doi.org/10.1021/ja3055639.

(26) Lin, J. Bin; Nguyen, T. T. T.; Vaidhyanathan, R.; Burner, J.; Taylor, J. M.; Durekova, H.;

Akhtar, F.; Mah, R. K.; Ghaffari-Nik, O.; Marx, S.; Fylstra, N.; Iremonger, S. S.; Dawson, K. W.; Sarkar, P.; Hovington, P.; Rajendran, A.; Woo, T. K.; Shimizu, G. K. H. A Scalable Metal-Organic Framework as a Durable Physisorbent for Carbon Dioxide Capture. *Science.* **2021**, *374* (6574), 1464–1469. https://doi.org/10.1126/SCIENCE.ABI7281/SUPPL_FILE/SCIENCE.ABI7281_SM.PDF.

(27) Zhu, Y. P.; Yin, J.; Abou-Hamad, E.; Liu, X.; Chen, W.; Yao, T.; Mohammed, O. F.; Alshareef, H. N. Highly Stable Phosphonate-Based MOFs with Engineered Bandgaps for Efficient Photocatalytic Hydrogen Production. *Adv. Mater.* **2020**, *32* (16), 1906368. https://doi.org/10.1002/adma.201906368.

(28) Valenzano, L.; Civalleri, B.; Chavan, S.; T., P. G.; Arean, C. O.; Bordiga, S. Computational and Experimental Studies on the Adsorption of CO, N_2, and CO_2 on Mg-MOF-74. *J. Phys. Chem. C* **2010**, *114* (25), 11185–11191. https://doi.org/10.1021/jp102574f.

(29) Bloch, E. D.; Queen, W. L.; Krishna, R.; Zadrozny, J. M.; Brown, C. M.; Long, J. R. Hydrocarbon Separations in a Metal-Organic Framework with Open Iron(II) Coordination Sites. *Science.* **2012**, *335* (6076), 1606–1610. https://doi.org/10.1126/science.1217544.

(30) Britt, D.; Furukawa, H.; Wang, B.; Glover, T. G.; Yaghi, O. M. Highly Efficient Separation of Carbon Dioxide by a Metal-Organic Framework Replete with Open Metal Sites. *Proc. Natl. Acad. Sci.* **2009**, *106* (49), 20637–20640. https://doi.org/10.1073/pnas.0909718106.

(31) Hartlieb, K. J.; Ferris, D. P.; Holcroft, J. M.; Kandela, I.; Stern, C. L.; Nassar, M. S.; Botros, Y. Y.; Stoddart, J. F. Encapsulation of Ibuprofen in CD-MOF and Related Bioavailability Studies. *Mol. Pharm.* **2017**, *14* (5), 1831–1839. https://doi.org/10.1021/acs.molpharmaceut.7b00168.

(32) Horcajada, P.; Serre, C.; Maurin, G.; Ramsahye, N. A.; Balas, F.; Vallet-Regí, M.; Sebban, M.; Taulelle, F.; Férey, G. Flexible Porous Metal-Organic Frameworks for a Controlled Drug Delivery. *J. Am. Chem. Soc.* **2008**, *130* (21), 6774–6780. https://doi.org/10.1021/ja710973k.

(33) Pathak, A.; Shen, J. W.; Usman, M.; Wei, L. F.; Mendiratta, S.; Chang, Y. S.; Sainbileg, B.; Ngue, C. M.; Chen, R. S.; Hayashi, M.; Luo, T. T.; Chen, F. R.; Chen, K. H.; Tseng, T. W.; Chen, L. C.; Lu, K. L. Integration of a (–Cu–S–) n Plane in a Metal–Organic Framework Affords High Electrical Conductivity. *Nat. Commun.* **2019**, *10* (1), 1–7. https://doi.org/10.1038/s41467-019-09682-0.

(34) Li, W.; Sun, L.; Qi, J.; Jarillo-Herrero, P.; Dincă, M.; Li, J. High Temperature Ferromagnetism in π-Conjugated Two-Dimensional Metal-Organic Frameworks. *Chem. Sci.* **2017**, *8* (4), 2859–2867. https://doi.org/10.1039/c6sc05080h.

(35) Yang, C.; Dong, R.; Wang, M.; Petkov, P. S.; Zhang, Z.; Wang, M.; Han, P.; Ballabio, M.; Bräuninger, S. A.; Liao, Z.; Zhang, J.; Schwotzer, F.; Zschech, E.; Klauss, H.-H.; Cánovas, E.; Kaskel, S.; Bonn, M.; Zhou, S.; Heine, T.; Feng, X. A Semiconducting Layered Metal-Organic Framework Magnet. *Nat. Commun.* **2019**, *10* (1), 3260. https://doi.org/10.1038/s41467-019-11267-w.

(36) Simard, M.; Su, D.; Wuest, J. D. Use of Hydrogen Bonds to Control Molecular Aggregation. Self-Assembly of Three-Dimensional Networks with Large Chambers. *J. Am. Chem. Soc.* **1991**, *113* (12), 4696–4698. https://doi.org/10.1021/ja00012a057.

(37) Duchamp, D. J.; Marsh, R. E.; Duchampt, D. J.; Marsh, R. E. The Crystal Structure of Trimesic Acid (Benzene-1,3,5-Tricarboxylic Acid). **1969**, *25* (1), 5–19.

(38) He, Y.; Xiang, S.; Chen, B. A Microporous Hydrogen-Bonded Organic Framework for Highly Selective C 2H2/C2H4 Separation at Ambient Temperature. *J. Am. Chem. Soc.* **2011**, *133* (37), 14570–14573. https://doi.org/10.1021/JA2066016/SUPPL_FILE/JA2066016_SI_001.PDF.

(39) Hu, L.; Slebodnick, C.; Gandour, R. D.; Hanson, B. E. The Role of 4,4′-Trimethylene-Dipyridine Flexibility in the Construction of Hybrid Networks Templated on Aromatic Alcohols. *Inorganica Chim. Acta* **2008**, *361* (8), 2439–2446. https://doi.org/10.1016/j.ica.2007.12.029.

(40) Wang, B.; Lin, R. B.; Zhang, Z.; Xiang, S.; Chen, B. Hydrogen-Bonded Organic Frameworks as a Tunable Platform for Functional Materials. *Journal of the American*

Chemical Society. American Chemical Society August 26, 2020, pp 14399–14416. https://doi.org/10.1021/jacs.0c06473.

(41) Holman, K. T.; Pivovar, A. M.; Swift, J. A.; Ward, M. D. Metric Engineering of Soft Molecular Host Frameworks. *Acc. Chem. Res.* **2001**, *34* (2), 107–118. https://doi.org/10.1021/ar970272f.

(42) Li, P.; Ryder, M. R.; Stoddart, J. F. Hydrogen-Bonded Organic Frameworks: A Rising Class of Porous Molecular Materials. *Accounts Mater. Res.* **2020**, *1* (1), 77–87. https://doi.org/10.1021/accountsmr.0c00019.

(43) Wu, Y. L.; Horwitz, N. E.; Chen, K. S.; Gomez-Gualdron, D. A.; Luu, N. S.; Ma, L.; Wang, T. C.; Hersam, M. C.; Hupp, J. T.; Farha, O. K.; Snurr, R. Q.; Wasielewski, M. R. G-Quadruplex Organic Frameworks. *Nat. Chem.* **2017**, *9* (5), 466–472. https://doi.org/10.1038/nchem.2689.

(44) Pal, S. C.; Mukherjee, D.; Sahoo, R.; Mondal, S.; Das, M. C. Proton-Conducting Hydrogen-Bonded Organic Frameworks. *ACS Energy Lett.* **2021**, *6* (12), 4431–4453. https://doi.org/10.1021/ACSENERGYLETT.1C02045/ASSET/IMAGES/LARGE/NZ1C02045_0009.JPEG.

(45) Ghasempour, H.; Wang, K.-Y.; Powell, J. A.; Zarekarizi, F.; Lv, X.-L.; Morsali, A.; Zhou, H.-C. Metal-Organic Frameworks Based on Multicarboxylate Linkers. **2020**. https://doi.org/10.1016/j.ccr.2020.213542.

(46) Lu, W.; Wei, Z.; Gu, Z. Y.; Liu, T. F.; Park, J.; Park, J.; Tian, J.; Zhang, M.; Zhang, Q.; Gentle, T.; Bosch, M.; Zhou, H. C. Tuning the Structure and Function of Metal-Organic Frameworks via Linker Design. *Chemical Society Reviews*. The Royal Society of Chemistry July 22, 2014, pp 5561–5593. https://doi.org/10.1039/c4cs00003j.

(47) Chae, H. K.; Siberio-Pérez, D. Y.; Kim, J.; Go, Y. B.; Eddaoudi, M.; Matzger, A. J.; O'Keeffe, M.; Yaghi, O. M. A Route to High Surface Area, Porosity and Inclusion of Large Molecules in Crystals. *Nat. 2004 4276974* **2004**, *427* (6974), 523–527. https://doi.org/10.1038/nature02311.

(48) Yuan, D.; Zhao, D.; Sun, D.; Zhou, H. C. An Isoreticular Series of Metal-Organic

Frameworks with Dendritic Hexacarboxylate Ligands and Exceptionally High Gas-Uptake Capacity. *Angew. Chemie - Int. Ed.* **2010**, *49* (31), 5357–5361. https://doi.org/10.1002/ANIE.201001009.

(49) Burtch, N. C.; Jasuja, H.; Walton, K. S. Water Stability and Adsorption in Metal-Organic Frameworks. *Chemical Reviews*. American Chemical Society October 22, 2014, pp 10575–10612. https://doi.org/10.1021/cr5002589.

(50) Joharian, M.; Morsali, A.; Azhdari Tehrani, A.; Carlucci, L.; Proserpio, D. M. Water-Stable Fluorinated Metal–Organic Frameworks (F-MOFs) with Hydrophobic Properties as Efficient and Highly Active Heterogeneous Catalysts in Aqueous Solution. *Green Chem.* **2018**, *20* (23), 5336–5345. https://doi.org/10.1039/C8GC02367K.

(51) Abdolalian, P.; Morsali, A.; Makhloufi, G.; Janiak, C. Acid- and Base-Stable Porous Mechanically Interlocked 2D Metal-Organic Polyrotaxane for in Situ Organochlorine Insecticide Encapsulation, Sensing and Removal. *New J. Chem.* **2018**, *42* (22), 18152–18158. https://doi.org/10.1039/c8nj03302a.

(52) Zhu, Y. P.; Yuan, Z. Y.; Alshareef, H. N. New Opportunities for Functional Materials from Metal Phosphonates. *ACS Materials Letters*. UTC 2020, pp 582–594. https://doi.org/10.1021/acsmaterialslett.0c00095.

(53) Yücesan, G.; Zorlu, Y.; Stricker, M.; Beckmann, J. Metal-Organic Solids Derived from Arylphosphonic Acids. *Coordination Chemistry Reviews*. Elsevier B.V. August 15, 2018, pp 105–122. https://doi.org/10.1016/j.ccr.2018.05.002.

(54) Ramaswamy, P.; Wong, N. E.; Shimizu, G. K. H. MOFs as Proton Conductors-Challenges and Opportunities. *Chemical Society Reviews*. Royal Society of Chemistry July 21, 2014, pp 5913–5932. https://doi.org/10.1039/c4cs00093e.

(55) Bao, S. S.; Shimizu, G. K. H.; Zheng, L. M. Proton Conductive Metal Phosphonate Frameworks. *Coord. Chem. Rev.* **2019**, *378*, 577–594. https://doi.org/10.1016/J.CCR.2017.11.029.

(56) Metal Phosphonate Chemistry: From Synthesis to Applications. **2011**. https://doi.org/10.1039/9781849733571.

(57) Peeples, C. A.; Çetinkaya, A.; Tholen, P.; Schmitt, F. J.; Zorlu, Y.; Bin Yu, K.; Yazaydin, O.; Beckmann, J.; Hanna, G.; Yücesan, G. Coordination-Induced Band Gap Reduction in a Metal–Organic Framework. *Chem. - A Eur. J.* **2022**, *28* (8), e202104041. https://doi.org/10.1002/chem.202104041.

(58) Siemensmeyer, K.; Peeples, C. A.; Tholen, P.; Schmitt, F. J.; Çoşut, B.; Hanna, G.; Yücesan, G. Phosphonate Metal–Organic Frameworks: A Novel Family of Semiconductors. *Adv. Mater.* **2020**, *32* (24), 2000474. https://doi.org/10.1002/adma.202000474.

(59) Gagnon, K. J.; Perry, H. P.; Clearfield, A. Conventional and Unconventional Metal-Organic Frameworks Based on Phosphonate Ligands: MOFs and UMOFs. *Chemical Reviews*. American Chemical Society February 8, 2012, pp 1034–1054. https://doi.org/10.1021/cr2002257.

(60) Shimizu, G.; Vaidhyanathan, R.; Taylor, J. Phosphonate and Sulfonate Metal Organic Frameworks. *Chem. Soc. Rev.* **2009**, *38* (5), 1430–1449. https://doi.org/10.1039/b802423p.

(61) Ma, T. Y.; Li, H.; Deng, Q. F.; Liu, L.; Ren, T. Z.; Yuan, Z. Y. Ordered Mesoporous Metal-Organic Frameworks Consisting of Metal Disulfonates. *Chem. Mater.* **2012**, *24* (12), 2253–2255. https://doi.org/10.1021/CM301256R/SUPPL_FILE/CM301256R_SI_001.PDF.

(62) Zhu, Y. P.; Ren, T. Z.; Yuan, Z. Y. Insights into Mesoporous Metal Phosphonate Hybrid Materials for Catalysis. *Catalysis Science and Technology*. The Royal Society of Chemistry August 17, 2015, pp 4258–4279. https://doi.org/10.1039/c5cy00107b.

(63) Herdes, C.; Valente, A.; Lin, Z.; Rocha, J.; Coutinho, J. A. P.; Medina, F.; Vega, L. F. Selective Adsorption of Volatile Organic Compounds in Micropore Aluminum Methylphosphonate-α: A Combined Molecular Simulation-Experimental Approach. *Langmuir* **2007**, *23* (13), 7299–7305. https://doi.org/10.1021/LA063518A/ASSET/IMAGES/MEDIUM/LA063518AN00001.GIF.

(64) Gagnon, K. J.; Perry, H. P.; Clearfield, A. Conventional and Unconventional Metal-Organic Frameworks Based on Phosphonate Ligands: MOFs and UMOFs. *Chemical Reviews*. February 8, 2012, pp 1034–1054. https://doi.org/10.1021/cr2002257.

(65) Bazaga-García, M.; Papadaki, M.; Colodrero, R. M. P.; Olivera-Pastor, P.; Losilla, E. R.; Nieto-Ortega, B.; Aranda, M. Á. G.; Choquesillo-Lazarte, D.; Cabeza, A.; Demadis, K. D. Tuning Proton Conductivity in Alkali Metal Phosphonocarboxylates by Cation Size-Induced and Water-Facilitated Proton Transfer Pathways. *Chem. Mater.* **2015**, *27* (2), 424–435. https://doi.org/10.1021/CM502716E/SUPPL_FILE/CM502716E_SI_001.PDF.

(66) Sun, Z. B.; Li, Y. L.; Zhang, Z. H.; Li, Z. F.; Xiao, B.; Li, G. A Path to Improve Proton Conductivity: From a 3D Hydrogen-Bonded Organic Framework to a 3D Copper-Organic Framework. *New J. Chem.* **2019**, *43* (26), 10637–10644. https://doi.org/10.1039/c9nj02025j.

(67) Gándara, F.; Uribe-Romo, F. J.; Britt, D. K.; Furukawa, H.; Lei, L.; Cheng, R.; Duan, X.; O'Keeffe, M.; Yaghi, O. M. Porous, Conductive Metal-Triazolates and Their Structural Elucidation by the Charge-Flipping Method. *Chem. - A Eur. J.* **2012**, *18* (34), 10595–10601. https://doi.org/10.1002/chem.201103433.

(68) Chen, D.; Xing, H.; Su, Z.; Wang, C. Electrical Conductivity and Electroluminescence of a New Anthracene-Based Metal-Organic Framework with π-Conjugated Zigzag Chains. *Chem. Commun.* **2016**, *52* (10), 2019–2022. https://doi.org/10.1039/c5cc09065b.

(69) Sone, Y.; Ekdunge, P.; Simonsson, D. Proton Conductivity of Nafion 117 as Measured by a Four-Electrode AC Impedance Method. *J. Electrochem. Soc.* **1996**, *143* (4), 1254–1259. https://doi.org/10.1149/1.1836625.

(70) Samms, S. R.; Wasmus, S.; Savinell, R. F. Thermal Stability of Nafion® in Simulated Fuel Cell Environments. *J. Electrochem. Soc.* **1996**, *143* (5), 1498–1504. https://doi.org/10.1149/1.1836669/XML.

(71) Yin, C.; Li, J.; Zhou, Y.; Zhang, H.; Fang, P.; He, C. Phase Separation and Development of Proton Transport Pathways in Metal Oxide Nanoparticle/Nafion Composite Membranes during Water Uptake. *J. Phys. Chem. C* **2018**, *122* (17), 9710–9717.

https://doi.org/10.1021/ACS.JPCC.8B02535/ASSET/IMAGES/LARGE/JP-2018-02535F_0002.JPEG.

(72) Lim, D. W.; Kitagawa, H. Proton Transport in Metal-Organic Frameworks. *Chemical Reviews*. American Chemical Society August 26, 2020, pp 8416–8467. https://doi.org/10.1021/acs.chemrev.9b00842.

(73) Umeyama, D.; Horike, S.; Inukai, M.; Itakura, T.; Kitagawa, S. Inherent Proton Conduction in a 2D Coordination Framework. *J. Am. Chem. Soc.* **2012**, *134* (30), 12780–12785. https://doi.org/10.1021/JA304693R/SUPPL_FILE/JA304693R_SI_002.CIF.

(74) Musho, T.; Wu, N. Ab Initio Calculation of Electronic Charge Mobility in Metal-Organic Frameworks. *Phys. Chem. Chem. Phys.* **2015**, *17* (39), 26160–26165. https://doi.org/10.1039/c5cp03920g.

(75) Shi, L.; Xu, A.; Pan, D.; Zhao, T. Aqueous Proton-Selective Conduction across Two-Dimensional Graphyne. *Nat. Commun.* **2019**, *10* (1). https://doi.org/10.1038/s41467-019-09151-8.

(76) Choi, P.; Jalani, N. H.; Datta, R. Thermodynamics and Proton Transport in Nafion. *J. Electrochem. Soc.* **2005**, *152* (3), E123. https://doi.org/10.1149/1.1859814.

(77) Mínguez Espallargas, G.; Coronado, E. Magnetic Functionalities in MOFs: From the Framework to the Pore. *Chem. Soc. Rev.* **2018**, *47* (2), 533–557. https://doi.org/10.1039/c7cs00653e.

(78) Verdaguer, M.; Girolami, G. S. Magnetic Prussian Blue Analogs. In *Magnetism: Molecules to Materials V*; John Wiley & Sons, Ltd, 2005; pp 283–346. https://doi.org/10.1002/3527604383.ch9.

(79) Dietzel, P. D. C.; Morita, Y.; Blom, R.; Fjellvåg, H. An in Situ High-Temperature Single-Crystal Investigation of a Dehydrated Metal-Organic Framework Compound and Field-Induced Magnetization of One-Dimensional Metal-Oxygen Chains. *Angew. Chemie - Int. Ed.* **2005**, *44* (39), 6354–6358. https://doi.org/10.1002/anie.200501508.

(80) Peeples, C. A.; Kober, D.; Schmitt, F. J.; Tholen, P.; Siemensmeyer, K.; Halldorson, Q.; Çoşut, B.; Gurlo, A.; Yazaydin, A. O.; Hanna, G.; Yücesan, G. A 3D Cu-Naphthalene-

Phosphonate Metal–Organic Framework with Ultra-High Electrical Conductivity. *Adv. Funct. Mater.* **2021**, *31* (3), 2007294. https://doi.org/10.1002/adfm.202007294.

(81) Clemente-León, M.; Coronado, E.; Martí-Gastaldo, C.; Romero, F. M. Multifunctionality in Hybrid Magnetic Materials Based on Bimetallic Oxalate Complexes. *Chem. Soc. Rev.* **2011**, *40* (2), 473–497. https://doi.org/10.1039/c0cs00111b.

(82) Park, S. S.; Hontz, E. R.; Sun, L.; Hendon, C. H.; Walsh, A.; Van Voorhis, T.; Dincə, M. Cation-Dependent Intrinsic Electrical Conductivity in Isostructural Tetrathiafulvalene-Based Microporous Metal-Organic Frameworks. *J. Am. Chem. Soc.* **2015**, *137* (5), 1774–1777. https://doi.org/10.1021/ja512437u.

(83) Teale, A. M.; Helgaker, T.; Savin, A.; Adamo, C.; Aradi, B.; Arbuznikov, A. V.; Ayers, P. W.; Baerends, E. J.; Barone, V.; Calaminici, P.; Cancès, E.; Carter, E. A.; Chattaraj, P. K.; Chermette, H.; Ciofini, I.; Crawford, T. D.; De Proft, F.; Dobson, J. F.; Draxl, C.; Frauenheim, T.; Fromager, E.; Fuentealba, P.; Gagliardi, L.; Galli, G.; Gao, J.; Geerlings, P.; Gidopoulos, N.; Gill, P. M. W.; Gori-Giorgi, P.; Görling, A.; Gould, T.; Grimme, S.; Gritsenko, O.; Jensen, H. J. A.; Johnson, E. R.; Jones, R. O.; Kaupp, M.; Köster, A. M.; Kronik, L.; Krylov, A. I.; Kvaal, S.; Laestadius, A.; Levy, M.; Lewin, M.; Liu, S.; Loos, P. F.; Maitra, N. T.; Neese, F.; Perdew, J. P.; Pernal, K.; Pernot, P.; Piecuch, P.; Rebolini, E.; Reining, L.; Romaniello, P.; Ruzsinszky, A.; Salahub, D. R.; Scheffler, M.; Schwerdtfeger, P.; Staroverov, V. N.; Sun, J.; Tellgren, E.; Tozer, D. J.; Trickey, S. B.; Ullrich, C. A.; Vela, A.; Vignale, G.; Wesolowski, T. A.; Xu, X.; Yang, W. DFT Exchange: Sharing Perspectives on the Workhorse of Quantum Chemistry and Materials Science. *Phys. Chem. Chem. Phys.* **2022**, *24* (47), 28700–28781. https://doi.org/10.1039/d2cp02827a.

(84) Schmidtmann, M.; Coster, P.; Henry, P. F.; Ting, V. P.; Weller, M. T.; Wilson, C. C. Determining Hydrogen Positions in Crystal Engineered Organic Molecular Complexes by Joint Neutron Powder and Single Crystal X-Ray Diffraction. *CrystEngComm* **2014**, *16* (7), 1232–1236. https://doi.org/10.1039/c3ce42070a.

(85) Muller, P.; Herbst-Irmer, R.; Spek, A.; Schneider, T.; Sawaya, M. *Crystal Structure Refinement: A Crystallographer's Guide to SHELXL (International Union of*

Crystallography Texts on Crystallography); 2006.

(86) Riley, K. E.; Pitoňák, M.; Cerný, J.; Hobza, P. On the Structure and Geometry of Biomolecular Binding Motifs (Hydrogen-Bonding, Stacking, X-H⋯π): WFT and DFT Calculations. *J. Chem. Theory Comput.* **2010**, *6* (1), 66–80. https://doi.org/10.1021/ct900376r.

(87) Lejaeghere, K.; Van Speybroeck, V.; Van Oost, G.; Cottenier, S. Error Estimates for Solid-State Density-Functional Theory Predictions: An Overview by Means of the Ground-State Elemental Crystals. *Crit. Rev. Solid State Mater. Sci.* **2014**, *39* (1), 1–24. https://doi.org/10.1080/10408436.2013.772503.

(88) Perdew, J. P.; Yang, W.; Burke, K.; Yang, Z.; Gross, E. K. U.; Scheffler, M.; Scuseria, G. E.; Henderson, T. M.; Zhang, I. Y.; Ruzsinszky, A.; Peng, H.; Sun, J.; Trushin, E.; Görling, A. Understanding Band Gaps of Solids in Generalized Kohn-Sham Theory. *Proc. Natl. Acad. Sci. U. S. A.* **2017**, *114* (11), 2801–2806. https://doi.org/10.1073/pnas.1621352114.

(89) Mancuso, J. L.; Mroz, A. M.; Le, K. N.; Hendon, C. H. Electronic Structure Modeling of Metal-Organic Frameworks. *Chemical Reviews*. 2020, pp 8641–8715. https://doi.org/10.1021/acs.chemrev.0c00148.

(90) Niklasson, A. M. N.; Steneteg, P.; Odell, A.; Bock, N.; Challacombe, M.; Tymczak, C. J.; Holmström, E.; Zheng, G.; Weber, V. Extended Lagrangian Born-Oppenheimer Molecular Dynamics. *J. Chem. Phys.* **2009**, *130*, 164123. https://doi.org/10.1063/1.3148075.

(91) Philipsen, P. H. T.; te Velde, G. te; Baerends, E. J.; Berger, J. A.; Boeij, P. L. de; Franchini, M.; Groeneveld, J. A.; Kadantsev, E. S.; Klooster, R.; Kootstra, F.; Romaniello, P.; Raupach, M.; Skachkov, D. G.; Snijders, J. G.; Verzijl, C. J. O.; Gil, J. A. C.; J. M. Thijssen, G.; Wiesenekker, G.; Peeples, C. A.; Schreckenbach, G.; Ziegler., T. BAND 2019.3, SCM, Theoretical Chemistry, Vrije Universiteit, Amsterdam, The Netherlands, Http://Www.Scm.Com. 2019.

(92) Kühne, T. D.; Iannuzzi, M.; Del Ben, M.; Rybkin, V. V; Seewald, P.; Stein, F.; Laino, T.;

Khaliullin, R. Z.; Schütt, O.; Schiffmann, F.; Golze, D.; Wilhelm, J.; Chulkov, S.; Bani-Hashemian, M. H.; Weber, V.; Borštnik, U.; Taillefumier, M.; Jakobovits, A. S.; Lazzaro, A.; Pabst, H.; Müller, T.; Schade, R.; Guidon, M.; Andermatt, S.; Holmberg, N.; Schenter, G. K.; Hehn, A.; Bussy, A.; Belleflamme, F.; Tabacchi, G.; Glöß, A.; Lass, M.; Bethune, I.; Mundy, C. J.; Plessl, C.; Watkins, M.; VandeVondele, J.; Krack, M.; Hutter, J. CP2K: An Electronic Structure and Molecular Dynamics Software Package -Quickstep: Efficient and Accurate Electronic Structure Calculations. *Journal of Chemical Physics*. 2020, p 194103. https://doi.org/10.1063/5.0007045.

(93) Koch, W.; Holthausen, M. C. *A Chemist's Guide to Density Functional Theory*; 2001; Vol. 3. https://doi.org/10.1002/3527600043.

(94) Hohenberg, P.; Kohn, W. Inhomogeneous Electron Gas. *Phys. Rev.* **1964**, *136* (3B), B864–B871. https://doi.org/10.1103/PhysRev.136.B864.

(95) Kohn, W.; Sham, L. J. Self-Consistent Equations Including Exchange and Correlation Effects. *Phys. Rev.* **1965**, *140* (4A). https://doi.org/10.1103/PhysRev.140.A1133.

(96) Dirac, P. A. M. Note on Exchange Phenomena in the Thomas Atom. *Math. Proc. Cambridge Philos. Soc.* **1930**, *26* (3), 376–385. https://doi.org/10.1017/S0305004100016108.

(97) Parr, R. G.; Yang, W. *Density-Functional Theory of Atoms and Molecules - Robert G. Parr, Yang Weitao*; Oxford University Press, 1994.

(98) Cramer, C. J. *Essentials of Computational Chemistry Theories and Models*, Second.; 2004. https://doi.org/10.1021/ci010445m.

(99) Ceperley, D. M.; Alder, B. J. Ground State of the Electron Gas by a Stochastic Method.Pdf. *Phys. Rev. Lett.* **1980**, *45* (7), 566–569.

(100) Vosko, s. h.; Wilk, L.; Nusair, M. Accurate Spin-Dependent Electron Liquid Correlation Energies for Local Spin Density Calculations: A Critical Analysis. *Can. J. Phys.* **1980**, *58* (8), 1200–1211. https://doi.org/10.1139/p80-159.

(101) Perdew, J.; Burke, K.; Ernzerhof, M. Generalized Gradient Approximation Made Simple. *Phys. Rev. Lett.* **1996**, *77*, 3865–3868. https://doi.org/10.1103/PhysRevLett.77.3865.

(102) Becke, A. D. A New Mixing of Hartree-Fock and Local Density-Functional Theories. *J. Chem. Phys.* **1993**, *98* (2), 1372–1377. https://doi.org/10.1063/1.464304.

(103) Heyd, J.; Scuseria, G. E.; Ernzerhof, M. Hybrid Functionals Based on a Screened Coulomb Potential. *J. Chem. Phys.* **2003**, *118* (18), 8207–8215. https://doi.org/10.1063/1.1564060.

(104) Adamo, C.; Barone, V. Toward Reliable Density Functional Methods without Adjustable Parameters: The PBE0 Model. *J. Chem. Phys.* **1999**, *110* (13), 6158–6170. https://doi.org/10.1063/1.478522.

(105) Grimme, S.; Antony, J.; Schwabe, T.; Mück-Lichtenfeld, C. Density Functional Theory with Dispersion Corrections for Supramolecular Structures, Aggregates, and Complexes of (Bio)Organic Molecules. *Org. Biomol. Chem.* **2007**, *5* (5), 741–758. https://doi.org/10.1039/b615319b.

(106) Grimme, S.; Antony, J.; Ehrlich, S.; Krieg, H. A Consistent and Accurate Ab Initio Parametrization of Density Functional Dispersion Correction (DFT-D) for the 94 Elements H-Pu. *J. Chem. Phys.* **2010**, *132* (15), 154104-1-154104–154119. https://doi.org/10.1063/1.3382344.

(107) Grimme, S.; Ehrlich, S.; Goerigk, L. Effect of the Damping Function in Dispersion Corrected Density Functional Theory. *J. Comput. Chem.* **2011**, *32* (7), 1456–1465. https://doi.org/10.1002/jcc.21759.

(108) Wellendorff, J.; Silbaugh, T. L.; Garcia-Pintos, D.; Nørskov, J. K.; Bligaard, T.; Studt, F.; Campbell, C. T. A Benchmark Database for Adsorption Bond Energies to Transition Metal Surfaces and Comparison to Selected DFT Functionals. *Surf. Sci.* **2015**, *640*, 36–44. https://doi.org/10.1016/j.susc.2015.03.023.

(109) Tautermann, C. S.; Voegele, A. F.; Loerting, T.; Kohl, I.; Hallbrucker, A.; Mayer, E.; Liedl, K. R. Towards the Experimental Decomposition Rate of Carbonic Acid (H2CO3) in Aqueous Solution. *Chem. - A Eur. J.* **2002**, *8* (1), 66–73. https://doi.org/10.1002/1521-3765(20020104)8:1<66::AID-CHEM66>3.0.CO;2-F.

(110) Das, T.; Ghule, S.; Vanka, K. Insights Into the Origin of Life: Did It Begin from HCN and

H_2O? *ACS Cent. Sci.* **2019**, *5* (9), 1532–1540. https://doi.org/10.1021/acscentsci.9b00520.

(111) Tuckerman, M. E. (Mark E. *Statistical Mechanics : Theory and Molecular Simulation*; Oxford University Press, 2010.

(112) Berendsen, H. J. C.; Postma, J. P. M.; van Gunsteren, W. F.; Hermans, J. Interaction Models for Water in Relation to Protein Hydration; Springer, Dordrecht, 1981; pp 331–342. https://doi.org/10.1007/978-94-015-7658-1_21.

(113) Oostenbrink, C.; Villa, A.; Mark, A. E.; Gunsteren, W. F. Van. A Biomolecular Force Field Based on the Free Enthalpy of Hydration and Solvation: The GROMOS Force-Field Parameter Sets 53A5 and 53A6. *J. Comput. Chem.* **2004**, *25* (13), 1656–1676. https://doi.org/10.1002/JCC.20090.

(114) Marx, D.; Hutter, J. *Ab Initio Molecular Dynamics: Basic Theory and Advanced Methods*; Cambridge University Press, 2009. https://doi.org/10.1017/CBO9780511609633.

(115) Leforestier, C. Classical Trajectories Using the Full Ab Initio Potential Energy Surface H- + CH4 → CH4 + H-. *J. Chem. Phys.* **1978**, *68* (10), 4406–4410. https://doi.org/10.1063/1.435520.

(116) Helgaker, T.; Uggerud, E.; Jensen, H. J. A. Integration of the Classical Equations of Motion on Ab Initio Molecular Potential Energy Surfaces Using Gradients and Hessians: Application to Translational Energy Release upon Fragmentation. *Chem. Phys. Lett.* **1990**, *173* (2–3), 145–150. https://doi.org/10.1016/0009-2614(90)80068-O.

(117) Swope, W. C.; Andersen, H. C.; Berens, P. H.; Wilson, K. R. A Computer Simulation Method for the Calculation of Equilibrium Constants for the Formation of Physical Clusters of Molecules: Application to Small Water Clusters. *J. Chem. Phys.* **1982**, *76* (1), 637–649. https://doi.org/10.1063/1.442716.

(118) Hockney, R. W.; Goel, S. P.; Eastwood, J. W. Quiet High-Resolution Computer Models of a Plasma. *J. Comput. Phys.* **1974**, *14* (2), 148–158. https://doi.org/10.1016/0021-9991(74)90010-2.

(119) Berendsen, H. J. C.; Postma, J. P. M.; Van Gunsteren, W. F.; Dinola, A.; Haak, J. R. Molecular Dynamics with Coupling to an External Bath. *J. Chem. Phys.* **1984**, *81* (8),

3684–3690. https://doi.org/10.1063/1.448118.

(120) Bussi, G.; Donadio, D.; Parrinello, M. Canonical Sampling through Velocity Rescaling. *J. Chem. Phys.* **2007**, *126* (1), 2635. https://doi.org/10.1063/1.2408420.

(121) Iftimie, R.; Minary, P.; Tuckerman, M. E. Ab Initio Molecular Dynamics: Concepts, Recent Developments, and Future Trends. *Proceedings of the National Academy of Sciences of the United States of America*. National Academy of Sciences May 10, 2005, pp 6654–6659. https://doi.org/10.1073/pnas.0500193102.

(122) Kolafa, J. Time-Reversible Always Stable Predictor-Corrector Method for Molecular Dynamics of Polarizable Molecules. *J. Comput. Chem.* **2004**, *25* (3), 335–342. https://doi.org/10.1002/jcc.10385.

(123) Laio, A.; Gervasio, F. L. Metadynamics: A Method to Simulate Rare Events and Reconstruct the Free Energy in Biophysics, Chemistry and Material Science. *Reports Prog. Phys.* **2008**, *71* (12), 126601. https://doi.org/10.1088/0034-4885/71/12/126601.

(124) Biswas, S.; Kwon, H.; Barsanti, K. C.; Myllys, N.; Smith, J. N.; Wong, B. M. Ab Initio Metadynamics Calculations of Dimethylamine for Probing p K Bvariations in Bulk vs. Surface Environments. *Phys. Chem. Chem. Phys.* **2020**, *22* (45), 26265–26277. https://doi.org/10.1039/d0cp03832f.

(125) Barducci, A.; Bussi, G.; Parrinello, M. Well-Tempered Metadynamics: A Smoothly Converging and Tunable Free-Energy Method. *Phys. Rev. Lett.* **2008**, *100* (2), 020603. https://doi.org/10.1103/PHYSREVLETT.100.020603/FIGURES/3/MEDIUM.

(126) Rabone, J.; Van Uffelen, P. DFT-Based Metadynamics Simulation of Proton Diffusion in Tetragonal Zirconia at 1500 K. *J. Nucl. Mater.* **2015**, *459*, 30–36. https://doi.org/10.1016/J.JNUCMAT.2015.01.002.

(127) Bonomi, M.; Branduardi, D.; Bussi, G.; Camilloni, C.; Provasi, D.; Raiteri, P.; Donadio, D.; Marinelli, F.; Pietrucci, F.; Broglia, R. A.; Parrinello, M. PLUMED: A Portable Plugin for Free-Energy Calculations with Molecular Dynamics. *Comput. Phys. Commun.* **2009**, *180* (10), 1961–1972. https://doi.org/10.1016/J.CPC.2009.05.011.

(128) Makov, G.; Payne, M. C. Periodic Boundary Conditions in Ab Initio Calculations. *Phys.*

Rev. B **1995**, *51* (7), 4014–4022. https://doi.org/10.1103/PhysRevB.51.4014.

(129) Truhlar, D. G.; Garrett, B. C.; Klippenstein, S. J. Current Status of Transition-State Theory. *J. Phys. Chem.* **1996**, *100* (31), 12771–12800. https://doi.org/10.1021/jp953748q.

(130) Jähnigen, S.; Zehnacker, A.; Vuilleumier, R. Computation of Solid-State Vibrational Circular Dichroism in the Periodic Gauge. *J. Phys. Chem. Lett. 2021* **2021**, *12*. https://doi.org/10.1021/acs.jpclett.1c01682.

(131) Guidon, M.; Hutter, J.; Vandevondele, J. Auxiliary Density Matrix Methods for Hartree-Fock Exchange Calculations. https://doi.org/10.1021/ct1002225.

(132) Bloch, F. Über Die Quantenmechanik Der Elektronen in Kristallgittern. *Z. Phys.* **1929**, *52* (7–8), 555–600. https://doi.org/10.1007/BF01339455.

(133) Monkhorst, H. J.; Pack, J. D. Special Points for Brillouin-Zone Integrations. *Phys. Rev. B* **1976**, *13* (12), 5188–5192. https://doi.org/10.1103/PhysRevB.13.5188.

(134) Philipsen, P. H. T.; te Velde, G. te; Baerends, E. J.; Berger, J. A.; Boeij, P. L. de; Franchini, M.; Groeneveld, J. A.; Kadantsev, E. S.; Klooster, R.; Kootstra, F.; Romaniello, P.; Raupach, M.; Skachkov, D. G.; Snijders, J. G.; Verzijl, C. J. O.; Gil, J. A. C.; J. M. Thijssen, G.; Wiesenekker, G.; Peeples, C. A.; Schreckenbach, G.; Ziegler., T. BAND 2018.104, SCM, Theoretical Chemistry, Vrije Universiteit, Amsterdam, The Netherlands, Http://Www.Scm.Com.

(135) Slater, J. C. Atomic Shielding Constants. *Phys. Rev.* **1930**, *36* (1), 57–64. https://doi.org/10.1103/PhysRev.36.57.

(136) Boys, S. F. Electronic Wave Functions - I. A General Method of Calculation for the Stationary States of Any Molecular System. *Proc. R. Soc. London. Ser. A. Math. Phys. Sci.* **1950**, *200* (1063), 542–554. https://doi.org/10.1098/rspa.1950.0036.

(137) Lippert, G.; Hutter, J.; Parrinello, M. A Hybrid Gaussian and Plane Wave Density Functional Scheme. *Mol. Phys.* **1997**, *92* (3), 477–488. https://doi.org/10.1080/002689797170220.

(138) Schwerdtfeger, P. The Pseudopotential Approximation in Electronic Structure Theory.

ChemPhysChem **2011**, *12* (17), 3143–3155. https://doi.org/10.1002/cphc.201100387.

(139) Jensen, F. Polarization Consistent Basis Sets: Principles. *J. Chem. Phys.* **2001**, *115* (20), 9113–9125. https://doi.org/10.1063/1.1413524.

(140) Thompson, J. D.; Xidos, J. D.; Sonbuchner, T. M.; Cramer, C. J.; Truhlar, D. G. More Reliable Partial Atomic Charges When Using Diffuse Basis Sets. *PhysChemComm* **2002**, *5*, 117–134. https://doi.org/10.1039/b206369g.

(141) Woodall, C. H.; Fuertes, S.; Beavers, C. M.; Hatcher, L. E.; Parlett, A.; Shepherd, H. J.; Christensen, J.; Teat, S. J.; Intissar, M.; Rodrigue-Witchel, A.; Suffren, Y.; Reber, C.; Hendon, C. H.; Tiana, D.; Walsh, A.; Raithby, P. R. Tunable Trimers: Using Temperature and Pressure to Control Luminescent Emission in Gold(i) Pyrazolate-Based Trimers. *Chem. - A Eur. J.* **2014**, *20* (51), 16933–16942. https://doi.org/10.1002/chem.201404058.

(142) GAVEZZOTTI, A. Periodic Systems: Crystal Orbitals and Lattice Dynamics. *Mol. Aggreg.* **2006**, 153–171. https://doi.org/10.1093/ACPROF:OSO/9780198570806.003.0006.

(143) Hinuma, Y.; Pizzi, G.; Kumagai, Y.; Oba, F.; Tanaka, I. Band Structure Diagram Paths Based on Crystallography. *Comput. Mater. Sci.* **2017**, *128*, 140–184. https://doi.org/10.1016/j.commatsci.2016.10.015.

(144) Mulliken, R. S. Electronic Population Analysis on LCAO-MO Molecular Wave Functions. I. *J. Chem. Phys.* **1955**, *23* (10), 1833–1840. https://doi.org/10.1063/1.1740588.

(145) Hirshfeld, F. L. Bonded-Atom Freagments for Describing Molecular Charge Densities. *Theor. Chim. Acta* **1977**, *44*, 129–138. https://doi.org/10.1007/BF00549096.

(146) Fonseca Guerra, C.; Handgraaf, J. W.; Baerends, E. J.; Bickelhaupt, F. M. Voronoi Deformation Density (VDD) Charges: Assessment of the Mulliken, Bader, Hirshfeld, Weinhold, and VDD Methods for Charge Analysis. *J. Comput. Chem.* **2004**, *25*, 189–210. https://doi.org/10.1002/jcc.10351.

(147) Marenich, A. V.; Jerome, S. V.; Cramer, C. J.; Truhlar, D. G. Charge Model 5: An Extension of Hirshfeld Population Analysis for the Accurate Description of Molecular

Interactions in Gaseous and Condensed Phases. *J. Chem. Theory Comput.* **2012**, *8* (2), 527–541. https://doi.org/10.1021/ct200866d.

(148) Peeples, C. A.; Schreckenbach, G. Implementation of the SM12 Solvation Model into ADF and Comparison with COSMO. *J. Chem. Theory Comput.* **2016**, *12* (8), 4033–4041. https://doi.org/10.1021/acs.jctc.6b00410.

(149) Bayly, C. I.; Cieplak, P.; Cornell, W. D.; Kollman, P. A. A Well-Behaved Electrostatic Potential Based Method Using Charge Restraints for Deriving Atomic Charges: The RESP Model. *J. Phys. Chem.* **1993**, *97* (40), 10269–10280. https://doi.org/10.1021/j100142a004.

(150) Campañá, C.; Mussard, B.; Woo, T. K. Electrostatic Potential Derived Atomic Charges for Periodic Systems Using a Modified Error Functional. *J. Chem. Theory Comput.* **2009**, *5* (10), 2866–2878. https://doi.org/10.1021/ct9003405.

(151) Zhou, H.-C.; Long, J. R.; Yaghi, O. M. Introduction to Metal−Organic Frameworks. *Chem. Rev.* **2012**, *112*, 673–674. https://doi.org/10.1021/cr300014x.

(152) Furukawa, H.; Cordova, K. E.; O'Keeffe, M.; Yaghi, O. M. The Chemistry and Applications of Metal-Organic Frameworks. *Science*. 2013, p 974. https://doi.org/10.1126/science.1230444.

(153) Zhou, H.-C. 'Joe'; Kitagawa, S. Metal-Organic Frameworks (MOFs). *Chemical Society Reviews*. Royal Society of Chemistry August 21, 2014, pp 5415–5418. https://doi.org/10.1039/c4cs90059f.

(154) Kalmutzki, M. J.; Hanikel, N.; Yaghi, O. M. Secondary Building Units as the Turning Point in the Development of the Reticular Chemistry of MOFs. *Science Advances*. American Association for the Advancement of Science October 5, 2018, pp 1–16. https://doi.org/10.1126/sciadv.aat9180.

(155) Schoedel, A.; Li, M.; Li, D.; O'Keeffe, M.; Yaghi, O. M. Structures of Metal-Organic Frameworks with Rod Secondary Building Units. *Chemical Reviews*. American Chemical Society October 12, 2016, pp 12466–12535. https://doi.org/10.1021/acs.chemrev.6b00346.

(156) Cohen, S. M. The Postsynthetic Renaissance in Porous Solids. *J. Am. Chem. Soc.* **2017**, *139* (8), 2855–2863. https://doi.org/10.1021/jacs.6b11259.

(157) Wang, Z.; Cohen, S. M. Postsynthetic Covalent Modification of a Neutral Metal-Organic Framework. *J. Am. Chem. Soc.* **2007**, *129* (41), 12368–12369. https://doi.org/10.1021/ja074366o.

(158) Tanabe, K. K.; Cohen, S. M. Postsynthetic Modification of Metal-Organic Frameworks - A Progress Report. *Chemical Society Reviews*. February 2011, pp 498–519. https://doi.org/10.1039/c0cs00031k.

(159) Kapelewski, M. T.; Runčevski, T.; Tarver, J. D.; Jiang, H. Z. H.; Hurst, K. E.; Parilla, P. A.; Ayala, A.; Gennett, T.; Fitzgerald, S. A.; Brown, C. M.; Long, J. R. Record High Hydrogen Storage Capacity in the Metal-Organic Framework Ni_2(*m*-Dobdc) at Near-Ambient Temperatures. *Chem. Mater.* **2018**, *30* (22), 8179–8189. https://doi.org/10.1021/acs.chemmater.8b03276.

(160) Ding, M.; Flaig, R. W.; Jiang, H. L.; Yaghi, O. M. Carbon Capture and Conversion Using Metal-Organic Frameworks and MOF-Based Materials. *Chemical Society Reviews*. Royal Society of Chemistry May 21, 2019, pp 2783–2828. https://doi.org/10.1039/c8cs00829a.

(161) Horcajada, P.; Gref, R.; Baati, T.; Allan, P. K.; Maurin, G.; Couvreur, P.; Férey, G.; Morris, R. E.; Serre, C. Metal-Organic Frameworks in Biomedicine. *Chemical Reviews*. February 8, 2012, pp 1232–1268. https://doi.org/10.1021/cr200256v.

(162) Rojas, S.; Baati, T.; Njim, L.; Manchego, L.; Neffati, F.; Abdeljelil, N.; Saguem, S.; Serre, C.; Najjar, M. F.; Zakhama, A.; Horcajada, P. Metal-Organic Frameworks as Efficient Oral Detoxifying Agents. *J. Am. Chem. Soc.* **2018**, *140* (30), 9581–9586. https://doi.org/10.1021/jacs.8b04435.

(163) Ranocchiari, M.; Bokhoven, J. A. Van. Catalysis by Metal-Organic Frameworks: Fundamentals and Opportunities. *Physical Chemistry Chemical Physics*. April 14, 2011, pp 6388–6396. https://doi.org/10.1039/c0cp02394a.

(164) Dhakshinamoorthy, A.; Li, Z.; Garcia, H. Catalysis and Photocatalysis by Metal Organic Frameworks. *Chemical Society Reviews*. Royal Society of Chemistry November 21, 2018,

pp 8134–8172. https://doi.org/10.1039/c8cs00256h.

(165) Coronado, E.; Mínguez Espallargas, G. Dynamic Magnetic MOFs. *Chemical Society Reviews*. February 21, 2013, pp 1525–1539. https://doi.org/10.1039/c2cs35278h.

(166) Coronado, E.; Giménez-Marqués, M.; Espallargas, G. M.; Brammer, L. Tuning the Magneto-Structural Properties of Non-Porous Coordination Polymers by HCl Chemisorption. *Nat. Commun.* **2012**, *3* (828), 1–8. https://doi.org/10.1038/ncomms1827.

(167) Sun, L.; Campbell, M. G.; Dincă, M. Electrically Conductive Porous Metal-Organic Frameworks. *Angewandte Chemie - International Edition*. Wiley-VCH Verlag March 7, 2016, pp 3566–3579. https://doi.org/10.1002/anie.201506219.

(168) Ohkoshi, S. I.; Tokoro, H. Photomagnetism in Cyano-Bridged Bimetal Assemblies. *Acc. Chem. Res.* **2012**, *45* (10), 1749–1758. https://doi.org/10.1021/ar300068k.

(169) Ouellette, W.; Prosvirin, A. V.; Whitenack, K.; Dunbar, K. R.; Zubieta, J. A Thermally and Hydrolytically Stable Microporous Framework Exhibiting Single-Chain Magnetism: Structure and Properties of $[Co_2(H_{0.67}Bdt)_3]\cdot 20H_2O$. *Angew. Chemie - Int. Ed.* **2009**, *48* (12), 2140–2143. https://doi.org/10.1002/anie.200804805.

(170) Faust, T. B.; D'Alessandro, D. M. Radicals in Metal-Organic Frameworks. *RSC Advances*. Royal Society of Chemistry 2014, pp 17498–17512. https://doi.org/10.1039/c4ra00958d.

(171) Maspoch, D.; Ruiz-Molina, D.; Wurst, K.; Domingo, N.; Cavallini, M.; Biscarini, F.; Tejada, J.; Rovira, C.; Veciana, J. A Nanoporous Molecular Magnet with Reversible Solvent-Induced Mechanical and Magnetic Properties. *Nat. Mater.* **2003**, *2* (3), 190–195. https://doi.org/10.1038/nmat834.

(172) Farha, O. K.; Eryazici, I.; Jeong, N. C.; Hauser, B. G.; Wilmer, C. E.; Sarjeant, A. A.; Snurr, R. Q.; Nguyen, S. T.; Yazaydin, A. Ö.; Hupp, J. T. Metal-Organic Framework Materials with Ultrahigh Surface Areas: Is the Sky the Limit? *J. Am. Chem. Soc.* **2012**, *134* (36), 15016–15021. https://doi.org/10.1021/ja3055639.

(173) Yucesan, G.; Golub, V.; O'Connor, C. J.; Zubieta, J. Temperature Dependence of the Crystal Chemistry of the Oxovanadium–Ethylenediphosphonate/Copper(II)--Bipyridine

System. Crystal Structures of the Two-Dimensional [Cu(Bpy)VO2(O3PCH2CH2PO3H)]•1.5H2O and of the One-Dimensional [Cu(Bpy)VO2(O3PCH2CH2PO3H)]. *Solid State Sci.* **2005**, *7* (1), 133–139. https://doi.org/10.1016/j.solidstatesciences.2004.10.010.

(174) AlDamen, M. A.; Cardona-Serra, S.; Clemente-Juan, J. M.; Coronado, E.; Gaita-Ariño, A.; Martí-Gastaldo, C.; Luis, F.; Montero, O. Mononuclear Lanthanide Single Molecule Magnets Based on the Polyoxometalates [Ln(W5O$_{18}$)2]9- and [Ln(B2-SiW11O39)2]13- (LnIII = Tb, Dy, Ho, Er, Tm, and Yb). *Inorg. Chem.* **2009**, *48* (8), 3467–3479. https://doi.org/10.1021/ic801630z.

(175) Tran, D. T.; Fan, X.; Brennan, D. P.; Zavalij, P. Y.; Oliver, S. R. J. Open Metal-Organic Framework Containing Cuprate Chains. *Inorg. Chem.* **2005**, *44* (18), 6192–6196. https://doi.org/10.1021/ic050024c.

(176) Taddei, M.; Costantino, F.; Vivani, R. Robust Metal-Organic Frameworks Based on Tritopic Phosphonoaromatic Ligands. *European Journal of Inorganic Chemistry*. September 2016, pp 4300–4309. https://doi.org/10.1002/ejic.201600207.

(177) Zorlu, Y.; Erbahar, D.; Çetinkaya, A.; Bulut, A.; Erkal, T. S.; Yazaydin, A. O.; Beckmann, J.; Yücesan, G. A Cobalt Arylphosphonate MOF-Superior Stability, Sorption and Magnetism. *Chem. Commun.* **2019**, *55* (21), 3053–3056. https://doi.org/10.1039/c8cc09655d.

(178) Shearan, S. J. I.; Stock, N.; Emmerling, F.; Demel, J.; Wright, P. A.; Demadis, K. D.; Vassaki, M.; Costantino, F.; Vivani, R.; Sallard, S.; Salcedo, I. R.; Cabeza, A.; Taddei, M. New Directions in Metal Phosphonate and Phosphinate Chemistry. *Crystals* **2019**, *9* (5). https://doi.org/10.3390/cryst9050270.

(179) te Velde, G.; Bickelhaupt, F. M.; Baerends, E. J.; Fonseca Guerra, C.; van Gisbergen, S. J. A.; Snijders, J. G.; Ziegler, T. Chemistry with ADF. *J. Comput. Chem.* **2001**, *22* (9), 931–967. https://doi.org/10.1002/jcc.1056.

(180) Baerends, E. J.; Ziegler, T.; Atkins, A. J.; Autschbach, J.; Bashford, D.; Baseggio, O.; Bérces, A.; Bickelhaupt, F. M.; Bo, C.; Boerritger, P. M.; Cavallo, L.; Daul, C.; Chong, D.

P.; Chulhai, D. V; Deng, L.; Dickson, R. M.; Dieterich, J. M.; Ellis, D. E.; van Faassen, M.; Ghysels, A.; Giammona, A.; van Gisbergen, S. J. A.; Goez, A.; Götz, A. W.; Gusarov, S.; Harris, F. E.; van den Hoek, P.; Hu, Z.; Jacob, C. R.; Jacobsen, H.; Jensen, L.; Joubert, L.; Kaminski, J. W.; van Kessel, G.; König, C.; Kootstra, F.; Kovalenko, A.; Krykunov, M.; van Lenthe, E.; McCormack, D. A.; Michalak, A.; Mitoraj, M.; Morton, S. M.; Neugebauer, J.; Nicu, V. P.; Noodleman, L.; Osinga, V. P.; Patchkovskii, S.; Pavanello, M.; Peeples, C. A.; Philipsen, P. H. T.; Post, D.; Pye, C. C.; Ramanantoanina, H.; Ramos, P.; Ravenek, W.; Rodríguez, J. I.; Ros, P.; Rüger, R.; Schipper, P. R. T.; Schlüns, D.; van Schoot, H.; Schreckenbach, G.; Seldenthuis, J. S.; Seth, M.; Snijders, J. G.; Solà, M.; M., S.; Swart, M.; Swerhone, D.; te Velde, G.; Tognetti, V.; Vernooijs, P.; Versluis, L.; Visscher, L.; Visser, O.; Wang, F.; Wesolowski, T. A.; van Wezenbeek, E. M.; Wiesenekker, G.; Wolff, S. K.; Woo, T. K.; Yakovlev, A. L. ADF2019, SCM, Theoretical Chemistry, Vrije Universiteit, Amsterdam, The Netherlands, Https://Www.Scm.Com. 2019.

(181) Barth, U. von; Hedin, L. A Local Exchange-Correlation Potential for the Spin Polarized Case. I. *J. Phys. C Solid State Phys.* **1972**, *5* (13), 1629–1642. https://doi.org/10.1088/0022-3719/5/13/012.

(182) Jacob, C. R.; Reiher, M. Spin in Density-Functional Theory. *Int. J. Quantum Chem.* **2012**, *112* (23), 3661–3684. https://doi.org/10.1002/qua.24309.

(183) Heyd, J.; Scuseria, G. E. Efficient Hybrid Density Functional Calculations in Solids: Assessment of the Heyd-Scuseria-Ernzerhof Screened Coulomb Hybrid Functional. *J. Chem. Phys.* **2004**, *121* (3), 1187–1192. https://doi.org/10.1063/1.1760074.

(184) Heyd, J.; Scuseria, G. E.; Ernzerhof, M. Erratum: Hybrid Functionals Based on a Screened Coulomb Potential. *Journal of Chemical Physics*. June 7, 2006, p 219906. https://doi.org/10.1063/1.2204597.

(185) Krukau, A. V.; Vydrov, O. A.; Izmaylov, A. F.; Scuseria, G. E. Influence of the Exchange Screening Parameter on the Performance of Screened Hybrid Functionals. *J. Chem. Phys.* **2006**, *125* (22), 224106-1-224106–5. https://doi.org/10.1063/1.2404663.

(186) Bitzek, E.; Koskinen, P.; Gähler, F.; Moseler, M.; Gumbsch, P. Structural Relaxation

Made Simple. *Phys. Rev. Lett.* **2006**, *97* (17), 170201-1-170201–170204. https://doi.org/10.1103/PhysRevLett.97.170201.

(187) Kadantsev, E. S.; Klooster, R.; De Boeij, P. L.; Ziegler, T. The Formulation and Implementation of Analytic Energy Gradients for Periodic Density Functional Calculations with STO/NAO Bloch Basis Set. *Mol. Phys.* **2007**, *105* (19–22), 2583–2596. https://doi.org/10.1080/00268970701598063.

(188) Lee, C.; Yang, W.; Parr, R. G. Development of the Colle-Salvetti Correlation-Energy Formula into a Functional of the Electron Density. *Phys. Rev. B* **1988**, *37*, 785–789.

(189) Becke, A. D. A Multicenter Numerical Integration Scheme for Polyatomic Molecules. *J. Chem. Phys.* **1988**, *88* (4), 2547–2553. https://doi.org/10.1063/1.454033.

(190) Wilbraham, L.; Adamo, C.; Ciofini, I. Communication: Evaluating Non-Empirical Double Hybrid Functionals for Spin-State Energetics in Transition-Metal Complexes. *J. Chem. Phys.* **2018**, *148* (4), 041103. https://doi.org/10.1063/1.5019641.

(191) Coxall, R. A.; Harris, S. G.; Henderson, D. K.; Parsons, S.; Tasker, P. A.; Winpenny, R. E. P. Inter-Ligand Reactions: In Situ Formation of New Polydentate Ligands. *J. Chem. Soc. Dalt. Trans.* **2000**, No. 14, 2349–2356. https://doi.org/10.1039/b001404o.

(192) Bulut, A.; Zorlu, Y.; Wörle, M.; Çetinkaya, A.; Kurt, H.; Tam, B.; Yazaydın, A. Ö.; Beckmann, J.; Yücesan, G. Short Naphthalene Organophosphonate Linkers to Microporous Frameworks. *ChemistrySelect* **2017**, *2* (24), 7050–7053. https://doi.org/10.1002/slct.201701411.

(193) Zanatta, A.; Chambouleyron, I. Absorption Edge, Band Tails, and Disorder of Amorphous Semiconductors. *Phys. Rev. B - Condens. Matter Mater. Phys.* **1996**, *53* (7), 3833–3836. https://doi.org/10.1103/PhysRevB.53.3833.

(194) Tauc, J.; Grigorovici, R.; Vancu, A. Optical Properties and Electronic Structure of Amorphous Germanium. *Phys. status solidi* **1966**, *15* (2), 627–637. https://doi.org/10.1002/pssb.19660150224.

(195) Hatfield, W. E.; Weller, R. R.; Hall, J. W. Exchange Coupling in the Sulfur-Bridged Quasi-Linear-Chain Compound Bis(Dimethyldithiocarbamato)Copper(II). Observations

on Exchange in Sulfur-Bridged Copper(II) Compounds. *Inorg. Chem.* **1980**, *19* (12), 3825–3828. https://doi.org/10.1021/ic50214a047.

(196) Bonner, J. C.; Fisher, M. E. Linear Magnetic Chains with Anisotropic Coupling. *Phys. Rev.* **1964**, *135* (3A). https://doi.org/10.1103/PhysRev.135.A640.

(197) Buschow, K. H. J. *Handbook of Magnetic Materials*, 1st ed.; North Holland, 1997. https://doi.org/10.1016/s0925-8388(96)03098-8.

(198) Klyushina, E. S.; Islam, A. T. M. N.; Park, J. T.; Goremychkin, E. A.; Wheeler, E.; Klemke, B.; Lake, B. Hamiltonian of the S= 1/2 Dimerized Antiferromagnetic-Ferromagnetic Quantum Spin Chain $BaCu_2V_2O_8$. *Phys. Rev. B* **2018**, *98* (10). https://doi.org/10.1103/PhysRevB.98.104413.

(199) Eggert, S.; Affleck, I.; Takahashi, M. Susceptibility of the Spin 1/2 Heisenberg Antiferromagnetic Chain. *Phys. Rev. Lett.* **1994**, *73* (2), 332–335. https://doi.org/10.1103/PhysRevLett.73.332.

(200) Bulut, A.; Zorlu, Y.; Wörle, M.; Paşa, S.; Kurt, H.; Zubieta, J.; Beckmann, J.; Yücesan, G. Rational Design of Two-Dimensional Bimetallic Wave Structures from Zigzag Chains via Site-Specific Coordination around the 2,6-Naphthalenediphosphonic Acid Motif. *Eur. J. Inorg. Chem.* **2016**, *2016* (21), 3506–3512. https://doi.org/10.1002/ejic.201600309.

(201) Dhineshbabu, N. R.; Rajendran, V.; Nithyavathy, N.; Vetumperumal, R. Study of Structural and Optical Properties of Cupric Oxide Nanoparticles. *Appl. Nanosci.* **2016**, *6* (6), 933–939. https://doi.org/10.1007/s13204-015-0499-2.

(202) Grima-Gallardo, P.; Salas, M.; Contreras, O.; Power, C.; Quintero, M.; Cabrera, H.; Zumeta-Dubé, I.; Rodríguez, A.; Aitken, J.; Brämer-Escamilla, W. Cu_3TaSe_4 and Cu_3NbSe_4: X-Ray Diffraction, Differential Thermal Analysis, Optical Absorption and Raman Scattering. *J. Alloys Compd.* **2016**, *658*, 749–756. https://doi.org/10.1016/j.jallcom.2015.10.283.

(203) Lederová, L.; Orendáčová, A.; Chovan, J.; Strečka, J.; Verkholyak, T.; Tarasenko, R.; Legut, D.; Sýkora, R.; ČiŽmár, E.; Tkáč, V.; Orendáč, M.; Feher, A. Realization of a Spin- 1/2 Spatially Anisotropic Square Lattice in a Quasi-Two-Dimensional Quantum

Antiferromagnet Cu(En)(H2 O)2SO4. *Phys. Rev. B* **2017**, *95* (5), 054436. https://doi.org/10.1103/PhysRevB.95.054436.

(204) Pellicer, E.; Varea, A.; Pané, S.; Nelson, B. J.; Menéndez, E.; Estrader, M.; Suriñach, S.; Baró, M. D.; Nogués, J.; Sort, J. 983-991 Nanocrystalline Electroplated Cu-Ni: Metallic Thin Films with Enhanced Mechanical Properties and Tunable Magnetic Behavior. *Adv. Funct. Mater.* **2010**, *20* (6), 983–991. https://doi.org/10.1002/adfm.200901732.

(205) De Groot, R. A.; Mueller, F. M.; Engen, P. G. V.; Buschow, K. H. J. New Class of Materials: Half-Metallic Ferromagnets. *Phys. Rev. Lett.* **1983**, *50* (25), 2024–2027. https://doi.org/10.1103/PhysRevLett.50.2024.

(206) Coey, J. M. D.; Venkatesan, M. Half-Metallic Ferromagnetism: Example of CrO_2. *J. Appl. Phys.* **2002**, *91* (10 I), 8345–8350. https://doi.org/10.1063/1.1447879.

(207) Ernzerhof, M.; Scuseria, G. E. Assessment of the Perdew-Burke-Ernzerhof Exchange-Correlation Functional. *J. Chem. Phys.* **1999**, *110* (11), 5029–5036. https://doi.org/10.1063/1.478401.

(208) Gao, C. Y.; Ai, J.; Tian, H. R.; Wu, D.; Sun, Z. M. An Ultrastable Zirconium-Phosphonate Framework as Bifunctional Catalyst for Highly Active CO2 Chemical Transformation. *Chem. Commun.* **2017**, *53* (7), 1293–1296. https://doi.org/10.1039/c6cc08773f.

(209) Zheng, T.; Yang, Z.; Gui, D.; Liu, Z.; Wang, X.; Dai, X.; Liu, S.; Zhang, L.; Gao, Y.; Chen, L.; Sheng, D.; Wang, Y.; DIwu, J.; Wang, J.; Zhou, R.; Chai, Z.; Albrecht-Schmitt, T. E.; Wang, S. Overcoming the Crystallization and Designability Issues in the Ultrastable Zirconium Phosphonate Framework System. *Nat. Commun.* **2017**, *8* (1), 1–11. https://doi.org/10.1038/ncomms15369.

(210) Schütrumpf, A.; Bulut, A.; Hermer, N.; Zorlu, Y.; Kirpi, E.; Stock, N.; Yazaydın, A. Ö.; Yücesan, G.; Beckmann, J. From Tetrahedral Tetraphosphonic Acids E[p-C6H4P(O)(OH)2]4 (E=C, Si) to Porous Cu- and Zn-MOFs with Large Surface Areas. *ChemistrySelect* **2017**, *2* (10), 3035–3038. https://doi.org/10.1002/slct.201700573.

(211) Tholen, P.; Zorlu, Y.; Beckmann, J.; Yücesan, G. Probing Isoreticular Expansions in Phosphonate MOFs and Their Applications. *Eur. J. Inorg. Chem.* **2020**.

https://doi.org/10.1002/ejic.201901291.

(212) Garza, A. J.; Scuseria, G. E. Predicting Band Gaps with Hybrid Density Functionals. *J. Phys. Chem. Lett.* **2016**, *7* (20), 4165–4170. https://doi.org/10.1021/acs.jpclett.6b01807.

(213) Tholen, P.; Peeples, C. A.; Schaper, R.; Bayraktar, C.; Erkal, T. S.; Ayhan, M. M.; Çoşut, B.; Beckmann, J.; Yazaydin, A. O.; Wark, M.; Hanna, G.; Zorlu, Y.; Yücesan, G. Semiconductive Microporous Hydrogen-Bonded Organophosphonic Acid Frameworks. *Nat. Commun.* **2020**, *11* (1), 1–7. https://doi.org/10.1038/s41467-020-16977-0.

(214) Lin, R. B.; He, Y.; Li, P.; Wang, H.; Zhou, W.; Chen, B. Multifunctional Porous Hydrogen-Bonded Organic Framework Materials. *Chemical Society Reviews*. Royal Society of Chemistry March 4, 2019, pp 1362–1389. https://doi.org/10.1039/c8cs00155c.

(215) Hisaki, I.; Ikenaka, N.; Gomez, E.; Cohen, B.; Tohnai, N.; Douhal, A. Hexaazatriphenylene-Based Hydrogen-Bonded Organic Framework with Permanent Porosity and Single-Crystallinity. *Chem. - A Eur. J.* **2017**, *23* (48), 11611–11619. https://doi.org/10.1002/chem.201701893.

(216) Hisaki, I.; Suzuki, Y.; Gomez, E.; Cohen, B.; Tohnai, N.; Douhal, A. Docking Strategy To Construct Thermostable, Single-Crystalline, Hydrogen-Bonded Organic Framework with High Surface Area. *Angew. Chemie* **2018**, *130* (39), 12832–12837. https://doi.org/10.1002/ange.201805472.

(217) Hisaki, I.; Suzuki, Y.; Gomez, E.; Ji, Q.; Tohnai, N.; Nakamura, T.; Douhal, A. Acid Responsive Hydrogen-Bonded Organic Frameworks. *J. Am. Chem. Soc.* **2019**, *141* (5), 2111–2121. https://doi.org/10.1021/jacs.8b12124.

(218) Chen, L.; Zhang, B.; Chen, L.; Liu, H.; Hu, Y.; Qiao, S. Hydrogen-Bonded Organic Frameworks: Design, Applications, and Prospects. *Materials Advances*. RSC May 11, 2022, pp 3680–3708. https://doi.org/10.1039/d1ma01173a.

(219) Yaghi, O. M.; Kalmutzki, M. J.; Diercks, C. S. *Introduction to Reticular Chemistry: Metal-Organic Frameworks and Covalent Organic Frameworks*; Wiley Blackwell, 2019. https://doi.org/10.1002/9783527821099.

(220) Jeffrey, G. A. An Introduction to Hydrogen Bonding. **1997**, 303.

(221) Wang, B.; Lv, X. L.; Lv, J.; Ma, L.; Lin, R. B.; Cui, H.; Zhang, J.; Zhang, Z.; Xiang, S.; Chen, B. A Novel Mesoporous Hydrogen-Bonded Organic Framework with High Porosity and Stability. *Chem. Commun.* **2019**, *56* (1), 66–69. https://doi.org/10.1039/c9cc07802a.

(222) Yang, W.; Greenaway, A.; Lin, X.; Matsuda, R.; Blake, A. J.; Wilson, C.; Lewis, W.; Hubberstey, P.; Kitagawa, S.; Champness, N. R.; Schröder, M. Exceptional Thermal Stability in a Supramolecular Organic Framework: Porosity and Gas Storage. *J. Am. Chem. Soc.* **2010**, *132* (41), 14457–14469. https://doi.org/10.1021/ja1042935.

(223) Yin, Q.; Lü, J.; Li, H. F.; Liu, T. F.; Cao, R. Robust Microporous Porphyrin-Based Hydrogen-Bonded Organic Framework for Highly Selective Separation of C2 Hydrocarbons versus Methane. *Cryst. Growth Des.* **2019**, *19* (7), 4157–4161. https://doi.org/10.1021/acs.cgd.9b00628.

(224) Karmakar, A.; Illathvalappil, R.; Anothumakkool, B.; Sen, A.; Samanta, P.; Desai, A. V.; Kurungot, S.; Ghosh, S. K. Hydrogen-Bonded Organic Frameworks (HOFs): A New Class of Porous Crystalline Proton-Conducting Materials. *Angew. Chemie - Int. Ed.* **2016**, *55* (36), 10667–10671. https://doi.org/10.1002/anie.201604534.

(225) Yin, Q.; Zhao, P.; Sa, R. J.; Chen, G. C.; Jian, L.; Liu, T. F.; Cao, R. An Ultra-Robust and Crystalline Redeemable Hydrogen-Bonded Organic Framework for Synergistic Chemo-Photodynamic Therapy. *Angew. Chemie Int. Ed.* **2018**, *57* (26), 7691–7696. https://doi.org/10.1002/ANIE.201800354.

(226) He, X. T.; Luo, Y. H.; Hong, D. L.; Chen, F. H.; Zheng, Z. Y.; Wang, C.; Wang, J. Y.; Chen, C.; Sun, B. W. Atomically Thin Nanoribbons by Exfoliation of Hydrogen-Bonded Organic Frameworks for Drug Delivery. *ACS Appl. Nano Mater.* **2019**, *2* (4), 2437–2445. https://doi.org/10.1021/acsanm.9b00303.

(227) Xing, G.; Yan, T.; Das, S.; Ben, T.; Qiu, S. Synthesis of Crystalline Porous Organic Salts with High Proton Conductivity. *Angew. Chemie - Int. Ed.* **2018**, *57* (19), 5345–5349. https://doi.org/10.1002/anie.201800423.

(228) Bao, Z.; Xie, D.; Chang, G.; Wu, H.; Li, L.; Zhou, W.; Wang, H.; Zhang, Z.; Xing, H.; Yang, Q.; Zaworotko, M. J.; Ren, Q.; Chen, B. Fine Tuning and Specific Binding Sites

with a Porous Hydrogen-Bonded Metal-Complex Framework for Gas Selective Separations. *J. Am. Chem. Soc.* **2018**, *140* (13), 4596–4603. https://doi.org/10.1021/JACS.7B13706/SUPPL_FILE/JA7B13706_SI_003.CIF.

(229) Li, P.; He, Y.; Arman, H. D.; Krishna, R.; Wang, H.; Weng, L.; Chen, B. A Microporous Six-Fold Interpenetrated Hydrogen-Bonded Organic Framework for Highly Selective Separation of C_2H_4/C_2H_6. *Chem. Commun.* **2014**, *50* (86), 13081–13084. https://doi.org/10.1039/c4cc05506c.

(230) Yang, W.; Wang, J.; Wang, H.; Bao, Z.; Zhao, J. C. G.; Chen, B. Highly Interpenetrated Robust Microporous Hydrogen-Bonded Organic Framework for Gas Separation. *Cryst. Growth Des.* **2017**, *17* (11), 6132–6137. https://doi.org/10.1021/acs.cgd.7b01322.

(231) Hestenes, M. R.; Stiefel, E. Methods of Conjugate Gradients for Solving Linear Systems. *J. Res. Natl. Bur. Stand. (1934).* **1952**, *49* (6), 409. https://doi.org/10.6028/jres.049.044.

(232) VandeVondele, J.; Krack, M.; Mohamed, F.; Parrinello, M.; Chassaing, T.; Hutter, J. Quickstep: Fast and Accurate Density Functional Calculations Using a Mixed Gaussian and Plane Waves Approach. *Comput. Phys. Commun.* **2005**, *167* (2), 103–128. https://doi.org/10.1016/j.cpc.2004.12.014.

(233) Hutter, J.; Iannuzzi, M.; Schiffmann, F.; Vandevondele, J. CP2K: Atomistic Simulations of Condensed Matter Systems. *Wiley Interdiscip. Rev. Comput. Mol. Sci.* **2014**, *4* (1), 15–25. https://doi.org/10.1002/wcms.1159.

(234) Goedecker, S.; Teter, M. Separable Dual-Space Gaussian Pseudopotentials. *Phys. Rev. B - Condens. Matter Mater. Phys.* **1996**, *54* (3), 1703–1710. https://doi.org/10.1103/PhysRevB.54.1703.

(235) Hartwigsen, C.; Goedecker, S.; Hutter, J. Relativistic Separable Dual-Space Gaussian Pseudopotentials from H to Rn. *Phys. Rev. B - Condens. Matter Mater. Phys.* **1998**, *58* (7), 3641–3662. https://doi.org/10.1103/PhysRevB.58.3641.

(236) VandeVondele, J.; Hutter, J. Gaussian Basis Sets for Accurate Calculations on Molecular Systems in Gas and Condensed Phases. *J. Chem. Phys.* **2007**, *127*, 114105. https://doi.org/10.1063/1.2770708.

(237) VandeVondele, J.; Hutter, J. An Efficient Orbital Transformation Method for Electronic Structure Calculations. *J. Chem. Phys.* **2003**, *118* (10), 4365–4369. https://doi.org/10.1063/1.1543154.

(238) Campañá, C.; Mussard, B.; Woo, T. K. Electrostatic Potential Derived Atomic Charges for Periodic Systems Using a Modified Error Functional. *J. Chem. Theory Comput.* **2009**, *5* (10), 2866–2878. https://doi.org/10.1021/ct9003405.

(239) Golze, D.; Hutter, J.; Iannuzzi, M. Wetting of Water on Hexagonal Boron Nitride@Rh(111): A QM/MM Model Based on Atomic Charges Derived for Nano-Structured Substrates. *Phys. Chem. Chem. Phys.* **2015**, *17* (22), 14307–14316. https://doi.org/10.1039/c4cp04638b.

(240) Rappé, A. K.; Casewit, C. J.; Colwell, K. S.; Goddard, W. A.; Skiff, W. M. UFF, a Full Periodic Table Force Field for Molecular Mechanics and Molecular Dynamics Simulations. *J. Am. Chem. Soc.* **1992**, *114* (25), 10024–10035. https://doi.org/10.1021/JA00051A040/SUPPL_FILE/JA00051A040_SI_001.PDF.

(241) Huang, Q.; Li, W.; Mao, Z.; Qu, L.; Li, Y.; Zhang, H.; Yu, T.; Yang, Z.; Zhao, J.; Zhang, Y.; Aldred, M. P.; Chi, Z. An Exceptionally Flexible Hydrogen-Bonded Organic Framework with Large-Scale Void Regulation and Adaptive Guest Accommodation Abilities. *Nat. Commun. 2019 101* **2019**, *10* (1), 1–8. https://doi.org/10.1038/s41467-019-10575-5.

(242) Yoon, T. U.; Baek, S. Bin; Kim, D.; Kim, E. J.; Lee, W. G.; Singh, B. K.; Lah, M. S.; Bae, Y. S.; Kim, K. S. Efficient Separation of C2 Hydrocarbons in a Permanently Porous Hydrogen-Bonded Organic Framework. *Chem. Commun.* **2018**, *54* (67), 9360–9363. https://doi.org/10.1039/c8cc04139c.

(243) Wei, Y. S.; Hu, X. P.; Han, Z.; Dong, X. Y.; Zang, S. Q.; Mak, T. C. W. Unique Proton Dynamics in an Efficient MOF-Based Proton Conductor. *J. Am. Chem. Soc.* **2017**, *139* (9), 3505–3512. https://doi.org/10.1021/jacs.6b12847.

(244) Sevrain, C. M.; Berchel, M.; Couthon, H.; Jaffrès, P. A. Phosphonic Acid: Preparation and Applications. *Beilstein J. Org. Chem.* **2017**, *13*, 2186–2213.

https://doi.org/10.3762/bjoc.13.219.

(245) Schoedel, A.; Li, M.; Li, D.; O'Keeffe, M.; Yaghi, O. M. Structures of Metal-Organic Frameworks with Rod Secondary Building Units. *Chemical Reviews*. October 12, 2016, pp 12466–12535. https://doi.org/10.1021/acs.chemrev.6b00346.

(246) Luo, J.; Wang, J. W.; Zhang, J. H.; Lai, S.; Zhong, D. C. Hydrogen-Bonded Organic Frameworks: Design, Structures and Potential Applications. *CrystEngComm* **2018**, *20* (39), 5884–5898. https://doi.org/10.1039/c8ce00655e.

(247) Hisaki, I.; Xin, C.; Takahashi, K.; Nakamura, T. Designing Hydrogen-Bonded Organic Frameworks (HOFs) with Permanent Porosity. *Angewandte Chemie - International Edition*. Wiley-VCH Verlag August 12, 2019, pp 11160–11170. https://doi.org/10.1002/anie.201902147.

(248) Liu, B.; Li, W.; Xu, Y.; Lin, Q.; Jiang, F.; Liu, X. Insight into the Intrinsic Active Site for Selective Production of Light Olefins in Cobalt-Catalyzed Fischer-Tropsch Synthesis. *ACS Catal.* **2019**, *9* (8), 7073–7089. https://doi.org/10.1021/acscatal.9b00352.

(249) Patil, R. S.; Banerjee, D.; Zhang, C.; Thallapally, P. K.; Atwood, J. L. Selective CO2 Adsorption in a Supramolecular Organic Framework. *Angew. Chemie - Int. Ed.* **2016**, *55* (14), 4523–4526. https://doi.org/10.1002/anie.201600658.

(250) Luo, X. Z.; Jia, X. J.; Deng, J. H.; Zhong, J. L.; Liu, H. J.; Wang, K. J.; Zhong, D. C. A Microporous Hydrogen-Bonded Organic Framework: Exceptional Stability and Highly Selective Adsorption of Gas and Liquid. *J. Am. Chem. Soc.* **2013**, *135* (32), 11684–11687. https://doi.org/10.1021/ja403002m.

(251) Karmakar, A.; Illathvalappil, R.; Anothumakkool, B.; Sen, A.; Samanta, P.; Desai, A. V.; Kurungot, S.; Ghosh, S. K. Hydrogen-Bonded Organic Frameworks (HOFs): A New Class of Porous Crystalline Proton-Conducting Materials. *Angew. Chemie - Int. Ed.* **2016**, *55* (36), 10667–10671. https://doi.org/10.1002/anie.201604534.

(252) Yang, W.; Yang, F.; Hu, T. L.; King, S. C.; Wang, H.; Wu, H.; Zhou, W.; Li, J. R.; Arman, H. D.; Chen, B. Microporous Diaminotriazine-Decorated Porphyrin-Based Hydrogen-Bonded Organic Framework: Permanent Porosity and Proton Conduction.

Cryst. Growth Des. **2016**, *16* (10), 5831–5835. https://doi.org/10.1021/acs.cgd.6b00924.

(253) Rhauderwiek, T.; Zhao, H.; Hirschle, P.; Döblinger, M.; Bueken, B.; Reinsch, H.; De Vos, D.; Wuttke, S.; Kolb, U.; Stock, N. Highly Stable and Porous Porphyrin-Based Zirconium and Hafnium Phosphonates-Electron Crystallography as an Important Tool for Structure Elucidation. *Chem. Sci.* **2018**, *9* (24), 5467–5478. https://doi.org/10.1039/c8sc01533c.

(254) Maares, M.; Ayhan, M. M.; Yu, K. B.; Yazaydin, A. O.; Harmandar, K.; Haase, H.; Beckmann, J.; Zorlu, Y.; Yücesan, G. Alkali Phosphonate Metal–Organic Frameworks. *Chem. - A Eur. J.* **2019**, *25* (48), 11214–11217. https://doi.org/10.1002/chem.201902207.

(255) Homburg, T.; Tschense, C. B. L.; Wolkersdoerfer, K.; Reinsch, H.; Wark, M.; Többens, D.; Zander, S.; Senker, J.; Stock, N. Magnesium Doped Gallium Phosphonates Ga1–XMgx[H3+x(O3PCH2)3N] (x = 0, 0.20) and the Influence on Proton Conductivity. *Zeitschrift fur Anorg. und Allg. Chemie* **2018**, *644* (2), 86–91. https://doi.org/10.1002/ZAAC.201700371.

(256) Bhadeshia, H. K. D. H. Encyclopedia of Materials: Science and Technology. *Encycl. Mater. Sci.* **2001**, 5203–5206.

(257) Dong, C. R.; Wang, Y.; Zhang, K.; Zeng, H. Halide Perovskite Materials as Light Harvesters for Solar Energy Conversion. *EnergyChem*. Elsevier January 1, 2020, p 100026. https://doi.org/10.1016/j.enchem.2020.100026.

(258) *Metal Phosphonate Chemistry: From Synthesis to Applications*; Clearfield, A., Demadis, K., Eds.; Royal Society of Chemistry: Cambridge, UK, 2011. https://doi.org/10.1039/9781849733571.

(259) Herschlag, D.; Pinney, M. M. Hydrogen Bonds: Simple after All? *Biochemistry*. American Chemical Society June 19, 2018, pp 3338–3352. https://doi.org/10.1021/acs.biochem.8b00217.

(260) Sarkisov, L.; Bueno-Perez, R.; Sutharson, M.; Fairen-Jimenez, D. Materials Informatics with PoreBlazer v4.0 and the CSD MOF Database. *Chem. Mater.* **2020**, *32* (23), 9849–9867. https://doi.org/10.1021/acs.chemmater.0c03575.

(261) Düren, T.; Millange, F.; Férey, G.; Walton, K. S.; Snurr, R. Q. Calculating Geometric

Surface Areas as a Characterization Tool for Metal - Organic Frameworks. *J. Phys. Chem. C* **2007**, *111* (42), 15350–15356. https://doi.org/10.1021/jp074723h.

(262) Ripple, W. J.; Wolf, C.; Newsome, T. M.; Gregg, J. W.; Lenton, T. M.; Palomo, I.; Eikelboom, J. A. J.; Law, B. E.; Huq, S.; Duffy, P. B.; Rockström, J. World Scientists' Warning of a Climate Emergency 2021. *Bioscience* **2021**, *71* (9), 894–898. https://doi.org/10.1093/biosci/biab079.

(263) United States of America, Environmental Protection Agency. Sources of Greenhouse Gas Emissions. https://www.epa.gov/ghgemissions/sources-greenhouse-gas-emissions (accessed Feb 8, 2022).

(264) Zhang, J.; Sewell, C. D.; Huang, H.; Lin, Z. Closing the Anthropogenic Chemical Carbon Cycle toward a Sustainable Future via CO_2 Valorization. *Adv. Energy Mater.* **2021**, *11* (47), 1–38. https://doi.org/10.1002/aenm.202102767.

(265) Carmo, M.; Fritz, D. L.; Mergel, J.; Stolten, D. A Comprehensive Review on PEM Water Electrolysis. *Int. J. Hydrogen Energy* **2013**, *38* (12), 4901–4934. https://doi.org/10.1016/j.ijhydene.2013.01.151.

(266) Jäger-Waldau, A.; Kougias, I.; Taylor, N.; Thiel, C. How Photovoltaics Can Contribute to GHG Emission Reductions of 55% in the EU by 2030. *Renewable and Sustainable Energy Reviews*. Elsevier Ltd July 1, 2020. https://doi.org/10.1016/j.rser.2020.109836.

(267) Moretti, C.; López-Contreras, A.; de Vrije, T.; Kraft, A.; Junginger, M.; Shen, L. From Agricultural (by-)Products to Jet Fuels: Carbon Footprint and Economic Performance. *Sci. Total Environ.* **2021**, *775*. https://doi.org/10.1016/j.scitotenv.2021.145848.

(268) Schmack, R.; Friedrich, A.; Kondratenko, E. V.; Polte, J.; Werwatz, A.; Kraehnert, R. A Meta-Analysis of Catalytic Literature Data Reveals Property-Performance Correlations for the OCM Reaction. *Nat. Commun. 2019 101* **2019**, *10* (1), 1–10. https://doi.org/10.1038/s41467-019-08325-8.

(269) Brandon, N. P.; Kurban, Z. Clean Energy and the Hydrogen Economy. *Philos. Trans. R. Soc. A Math. Phys. Eng. Sci.* **2017**, *375* (2098). https://doi.org/10.1098/rsta.2016.0400.

(270) Crabtree, G. W.; Dresselhaus, M. S.; Buchanan, M. V. The Hydrogen Economy. *Physics*

Today. 2004, pp 39–44. https://doi.org/10.1063/1.1878333.

(271) Antolini, E. Iron-Containing Platinum-Based Catalysts as Cathode and Anode Materials for Low-Temperature Acidic Fuel Cells: A Review. *RSC Advances*. Royal Society of Chemistry January 4, 2016, pp 3307–3325. https://doi.org/10.1039/c5ra22035a.

(272) Xin Chen; Kiyonori Takahashi; Kenta Kokado; Takayoshi Nakamura; Ichiro Hisaki. A Proton Conductive Hydrogen-Bonded Framework Incorporating 18-Crown-6-Ether and Dicarboxy- o -Terphenyl Moieties. *Mater. Adv.* **2021**, *2* (17), 5639–5644. https://doi.org/10.1039/D1MA00411E.

(273) Yang, J.; Wang, J.; Hou, B.; Huang, X.; Wang, T.; Bao, Y.; Hao, H. Porous Hydrogen-Bonded Organic Frameworks (HOFs): From Design to Potential Applications. *Chemical Engineering Journal*. Elsevier B.V. November 1, 2020. https://doi.org/10.1016/j.cej.2020.125873.

(274) Feng, J.; Li, Y.; Qin, Y.; Li, G. Preparation, Crystal Structure and Proton Conductive Properties of a Water-Stable Ferrocenyl Carboxylate Framework. *J. Solid State Chem.* **2023**, *318*, 123739. https://doi.org/10.1016/j.jssc.2022.123739.

(275) Murahashi, T. Fuel Cells - Phosphoric Acid Fuel Cells | Electrolytes. In *Encyclopedia of Electrochemical Power Sources*; Elsevier, 2009; pp 564–567. https://doi.org/10.1016/B978-044452745-5.00278-1.

(276) Sheu, S. Y.; Yang, D. Y.; Selzle, H. L.; Schlag, E. W. Energetics of Hydrogen Bonds in Peptides. *Proc. Natl. Acad. Sci. U. S. A.* **2003**, *100* (22), 12683–12687. https://doi.org/10.1073/pnas.2133366100.

(277) Kreuer, K. -D; Rabenau, A.; Weppner, W. Vehicle Mechanism, A New Model for the Interpretation of the Conductivity of Fast Proton Conductors. *Angew. Chemie Int. Ed. English* **1982**, *21* (3), 208–209. https://doi.org/10.1002/anie.198202082.

(278) Ludueña, G. A.; Kühne, T. D.; Sebastiani, D. Mixed Grotthuss and Vehicle Transport Mechanism in Proton Conducting Polymers from Ab Initio Molecular Dynamics Simulations. *Chem. Mater.* **2011**, *23* (6), 1424–1429. https://doi.org/10.1021/cm102674u.

(279) Salcedo, I. R.; Colodrero, R. M. P.; Bazaga-García, M.; López-González, M.; Del Río, C.;

Xanthopoulos, K.; Demadis, K. D.; Hix, G. B.; Furasova, A. D.; Choquesillo-Lazarte, D.; Olivera-Pastor, P.; Cabeza, A. Phase Transformation Dynamics in Sulfate-Loaded Lanthanide Triphosphonates. Proton Conductivity and Application as Fillers in PEMFCs. *ACS Appl. Mater. Interfaces* **2021**, *13* (13), 15279–15291. https://doi.org/10.1021/acsami.1c01441.

(280) Galib, M.; Hanna, G. The Role of Hydrogen Bonding in the Decomposition of H 2 CO 3 in Water: Mechanistic Insights from Ab Initio Metadynamics Studies of Aqueous Clusters. **2014**. https://doi.org/10.1021/jp5029195.

(281) Galib, M.; Hanna, G. Mechanistic Insights into the Dissociation and Decomposition of Carbonic Acid in Water via the Hydroxide Route: An Ab Initio Metadynamics Study. *J. Phys. Chem. B* **2011**, *115* (50), 15024–15035. https://doi.org/10.1021/jp207752m.

(282) Galib, M.; Hanna, G. Molecular Dynamics Simulations Predict an Accelerated Dissociation of H2CO3 at the Air-Water Interface. *Phys. Chem. Chem. Phys.* **2014**, *16* (46), 25573–25582. https://doi.org/10.1039/c4cp03302g.

(283) Brehm, M.; Kirchner, B. TRAVIS - A Free Analyzer and Visualizer for Monte Carlo and Molecular Dynamics Trajectories. *J. Chem. Inf. Model.* **2011**, *51* (8), 2007–2023. https://doi.org/10.1021/CI200217W/SUPPL_FILE/CI200217W_SI_002.TXT.

(284) O'Boyle, N. M.; Banck, M.; James, C. A.; Morley, C.; Vandermeersch, T.; Hutchison, G. R. Open Babel: An Open Chemical Toolbox. *J. Cheminform.* **2011**, *3* (10), 1–14. https://doi.org/10.1186/1758-2946-3-33/TABLES/2.

(285) Lindahl; Abraham; Hess; Spoel, van der. GROMACS 2021 Manual. **2021**. https://doi.org/10.5281/ZENODO.4457591.

(286) Abraham, M. J.; Murtola, T.; Schulz, R.; Páll, S.; Smith, J. C.; Hess, B.; Lindah, E. GROMACS: High Performance Molecular Simulations through Multi-Level Parallelism from Laptops to Supercomputers. *SoftwareX* **2015**, *1–2*, 19–25. https://doi.org/10.1016/J.SOFTX.2015.06.001.

(287) Humphrey, W.; Dalke, A.; Schulten, K. VMD: Visual Molecular Dynamics. *J. Mol. Graph.* **1996**, *14* (1), 33–38. https://doi.org/10.1016/0263-7855(96)00018-5.

(288) Sarkisov, L.; Harrison, A. Computational Structure Characterisation Tools in Application to Ordered and Disordered Porous Materials. *Mol. Simul.* **2011**, *37* (15), 1248–1257. https://doi.org/10.1080/08927022.2011.592832.

(289) Talu, O.; Myers, A. L. Molecular Simulation of Adsorption: Gibbs Dividing Surface and Comparison with Experiment. *AIChE J.* **2001**, *47* (5), 1160–1168. https://doi.org/10.1002/aic.690470521.

(290) Molecular Theory of Gases and Liquids. J. O. Hirschfelder, C. F. Curtiss, and R. B. Bird. Wiley, New York, 1954. Xxvi. *J. Polym. Sci.* **1955**, *17* (83), 116–116. https://doi.org/10.1002/pol.1955.120178311.

Appendix A: Supplementary Data for Chapter 3

Phosphonate Metal-Organic Frameworks

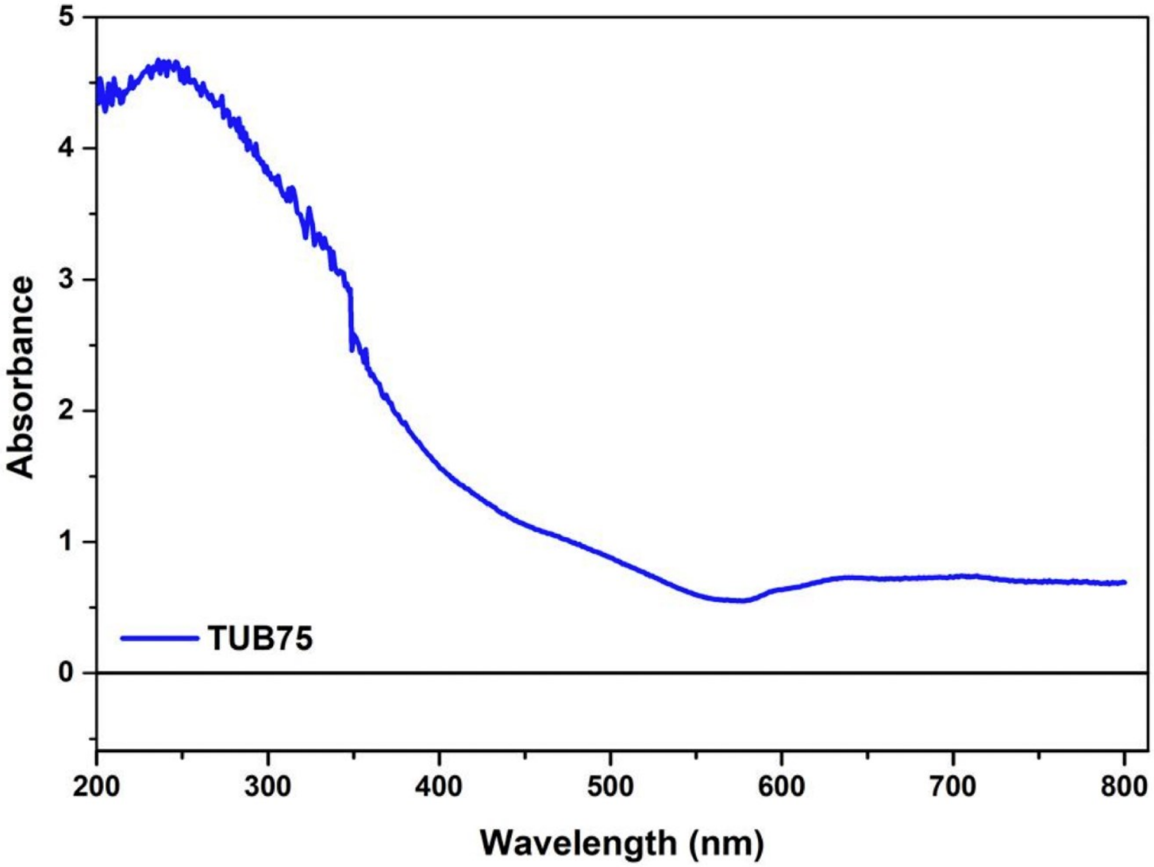

Figure A1. UV-Vis *absorption* spectrum *of TUB75.*

Table A1. *Average distances between bonded atoms in the TUB1 unit cell resulting from optimizations at different levels of theory and with different enforced spin polarizations (the experimental distances are shown at the bottom of the table). All optimizations used the D3-BJ dispersion correction. Standard deviations are shown in parentheses. NB: The PBE - TZP (3-α)-optimized structure is the lowest energy structure.*

Spin polarization	Functional – Basis set	Average atomic distance (Å)					
		Cu-O	O-H	P-O	P-C	C-C	H-C
(2-α, 1-β)	BLYP - TZP	2.04 (0.136)	1.02 (0.017)	1.57 (0.034)	1.80 (0.008)	1.42 (0.051)	1.09 (0.003)
(2-α, 1-β)	PBE - TZP/DZP	2.01 (0.067)	1.03 (0.017)	1.57 (0.026)	1.80 (0.008)	1.42 (0.050)	1.09 (0.001)
(2-α, 1-β)	PBE - TZP	2.03 (0.124)	1.02 (0.013)	1.56 (0.031)	1.80 (0.008)	1.42 (0.050)	1.09 (0.001)
(3-α)	PBE - TZP	2.01 (0.067)	1.03 (0.017)	1.57 (0.027)	1.80 (0.008)	1.42 (0.050)	1.09 (0.001)
Experiment		2.03 (0.157)	0.84 (0.000)	1.54 (0.031)	1.79 (0.004)	1.41 (0.049)	0.95 (0.000)

Table A2. *Copper atom Mulliken populations based on the various PBE-optimized structures and HSE06 single-point calculations. Cu1 denotes the square planar copper atom, and Cu2/Cu3 denotes the trigonal bipyramidal copper atoms.*

Level of theory	Population of α electrons	Population of β electrons
PBE-D3-BJ (3-α)		
Cu1	14.104	14.145
Cu2	14.460	13.732
Cu3	14.460	13.732
PBE-D3-BJ (2-α, 1-β)		
Cu1	14.117	14.136
Cu2	14.300	13.897
Cu3	14.300	13.897
BLYP-D3-BJ (2-α, 1-β)		
Cu1	14.008	14.103
Cu2	14.274	13.865

Cu3	14.274	13.865
PBE-D3-BJ (1-α, 1-β)		
Cu1	14.125	14.125
Cu2	14.437	13.759
Cu3	13.759	14.436
PBE-D3-BJ (2-α)		
Cu1	14.107	14.145
Cu2	14.418	13.784
Cu3	14.418	13.784
HSE06 (3-α)		
Cu1	13.841	14.294
Cu2	14.429	13.659
Cu3	14.429	13.659
HSE06 (2-α, 1-β)		
Cu1	13.833	14.303
Cu2	13.666	14.421
Cu3	14.430	13.658
HSE06 (1-α, 1-β)		
Cu1	13.850	14.288
Cu2	13.663	14.422
Cu3	14.423	13.661
HSE06 (2-α)		
Cu1	13.846	14.293
Cu2	14.425	13.661
Cu3	14.424	13.663

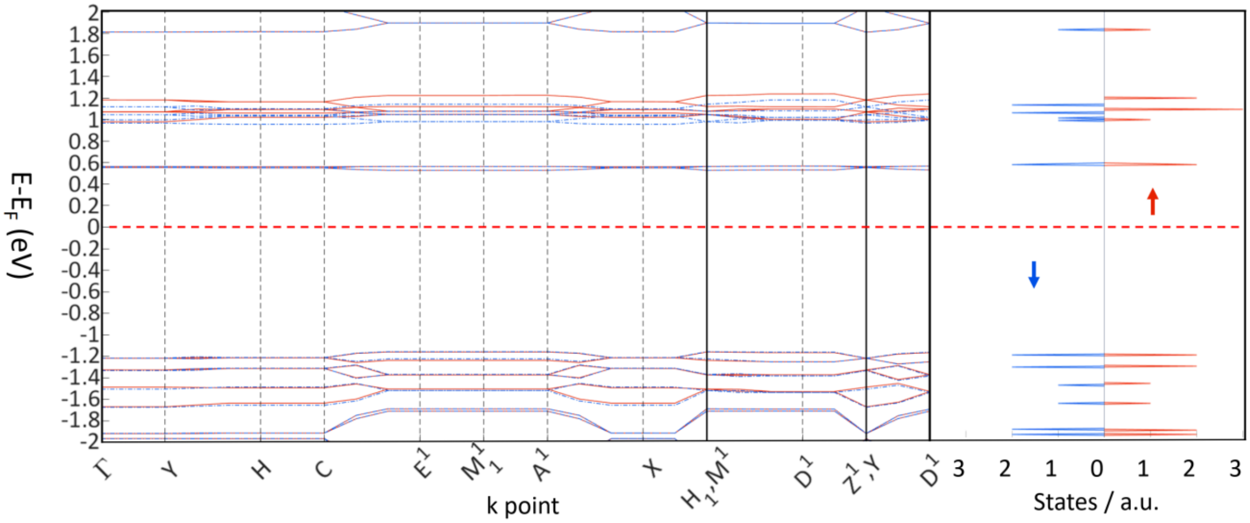

Figure A2. (Left) *Band structure of TUB75. The dashed blue and red solid lines correspond to the spin down and spin up contributions, respectively.* ***(Right)*** *The corresponding total density of states for spin up (red) and spin down (blue).*

A.1 Magnetic susceptibility fitting

To fit our magnetic susceptibility data, we considered a Heisenberg chain (HC) coupled to *m* other chains. A numerical approximation[195] to the Bonner-Fisher model[196] yields the following expression for the susceptibility of the *S*=½ HC:

$$\chi_{HC} = \frac{3C}{T}\frac{0.25+0.14995x+0.30094x^2}{1+1.9862x+0.68854x^2+6.0626x^3}+\frac{C_{Para}}{T-\theta}+c_{Dia} \quad (1)$$

where,

$$x = \frac{J_{Chain}}{kT} \ (2)$$

T is the temperature, and the Curie constant (in units of μ_B/ion) is

$$C = \frac{n\mu_B g^2 s(s+1)}{3k_B} \ (3)$$

In the above equation, *n* is the number of Cu ions per formula unit and is treated as a fitting parameter. The magnetic susceptibility, taking into account the interaction with the *m* other chains, is given by Hatfield *et al.*[195]

$$\chi_m = \frac{\chi_{HC}}{1-\dfrac{2mJ'\chi_{HC}}{n\mu_B g^2}} (4)$$

where J' is the inter-chain interaction. The best fit was obtained with a double chain (i.e., m=1), J_{chain} = 16.8 K, J' = -22 K, and a value of n that suggests the presence of two such double chains, i.e., two independent HC's as depicted in **Figure 3.6–B** of the main text.

We also considered the dimer chain model to fit the magnetic susceptibility data. For this model, the magnetic susceptibility is given by Klyushina *et al.*[198] and Eggert *et al.*[199]:

$$\chi_{DC} = \frac{3C}{T\left(3 + Exp\left(\frac{J_{Dimer}}{k_B T}\right) + \frac{J_{Chain}}{k_B T}\right)} + \frac{C_{Para}}{T-\theta} + \chi_{Dia} \quad (5)$$

where the Curie constant, C, is given by Eq. 3, χ_{dia} is a constant diamagnetic term, and C_{para} is the paramagnetic impurity term.

The best fit to the data above 10 K was obtained with J_{dimer} = 54 K and J_{chain} = -2.6 K. We found that the value of J_{dimer} was quite stable with respect to changes within the fitted (temperature) range, whereas the value of J_{chain} depended somewhat on the dataset and fitted (temperature) range. Below 10 K, the susceptibility remains finite and positive, while the fit yields small negative values. A Curie constant was obtained with g = 2, n = 2 Cu ions per formula unit, and S = ½.

A Curie-Weiss fit to the high temperature portion of the inverse magnetic susceptibility is shown in Fig. 4D of the main text. Given Cu^{2+} spins with S= ½ and g=2, we find from the Curie-Weiss constant that 80% of the Cu^{2+} ions in TUB75 contribute to the high-temperature paramagnetic signal. The Curie temperature is found to be T_C = 25 K, above which the material becomes paramagnetic.

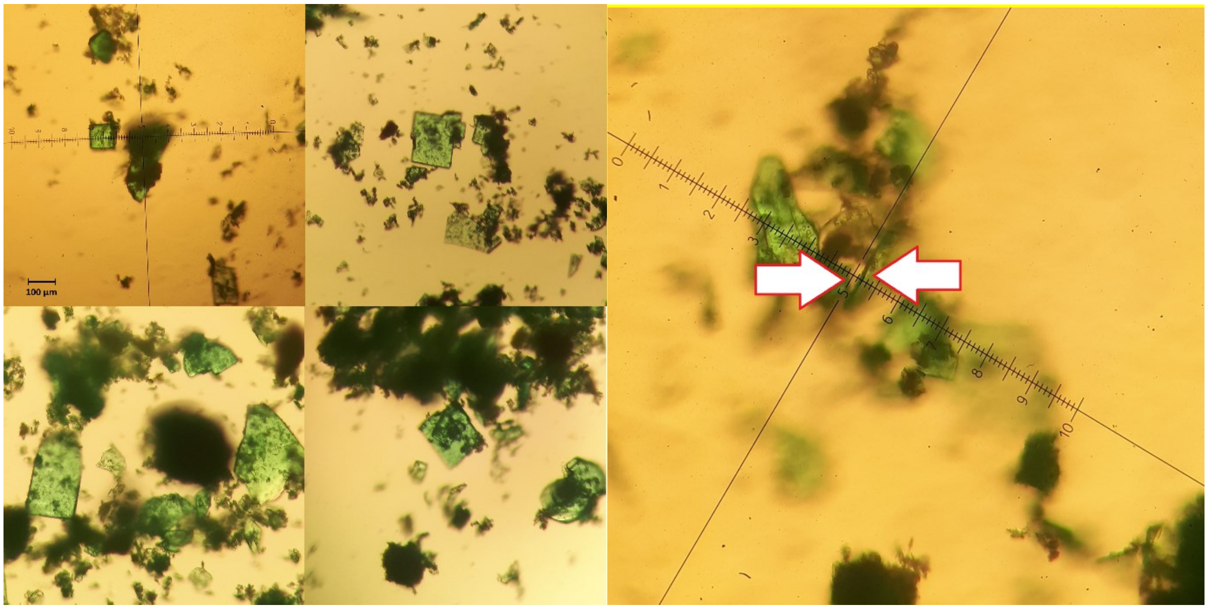

Figure A3. *Single TUB40 crystals under the light microscope. The black bar indicates 100 µm and the internal micrometer scaling corresponds to 100 µm/division (10 µm/subdivision).*

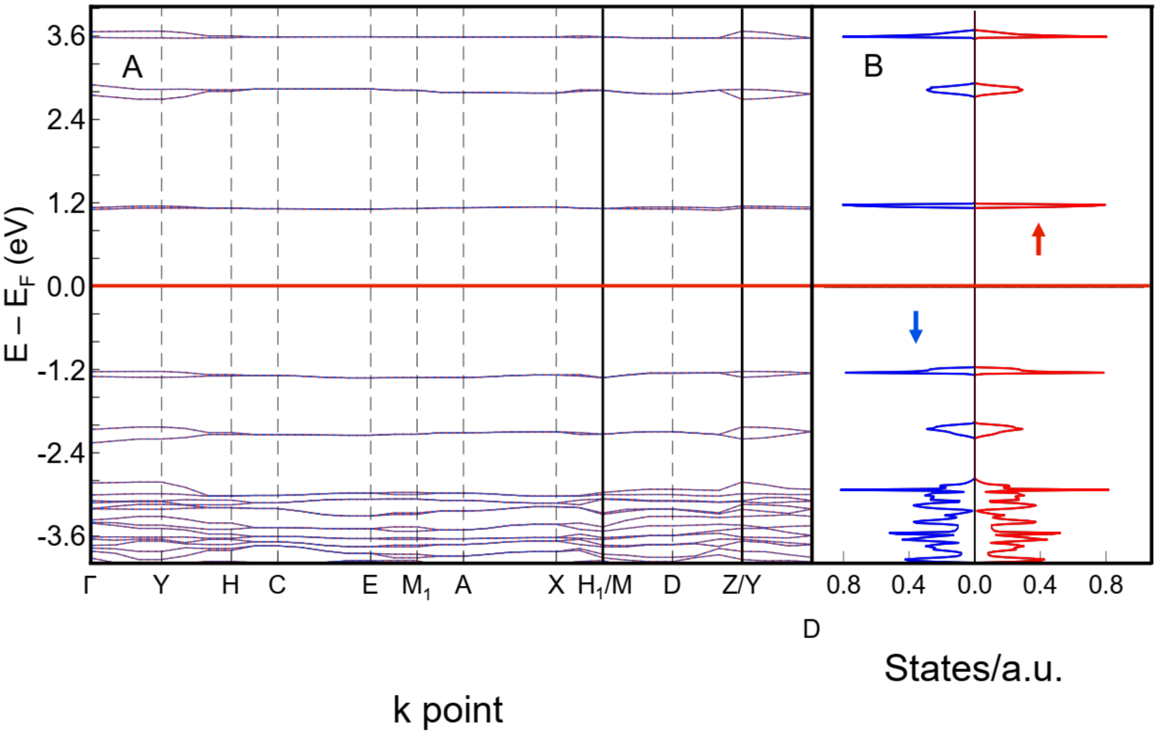

Figure A4. (A) *Electronic band structure of TUB40 in the AFM configuration. The blue and red lines denote the spin-down and spin-up contributions, respectively.* ***(B)*** *Spin-up (red) and spin-down (blue) contributions to the total density of states.*

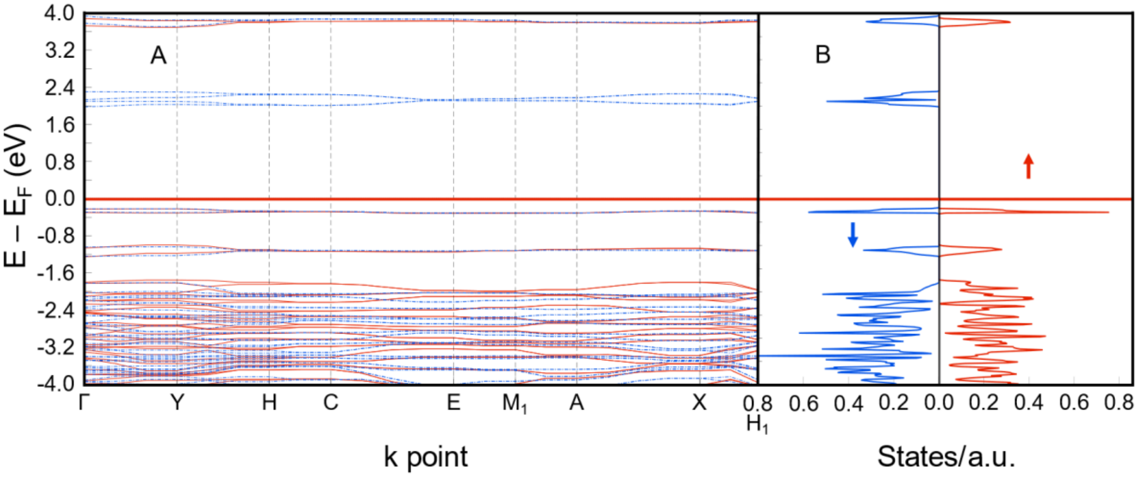

Figure A5. (A) *Electronic band structure of TUB40 in the FM configuration. The blue and red lines denote the spin-down and spin-up contributions, respectively.* ***(B)*** *Spin-up (red) and spin-down (blue) contributions to the total density of states.*

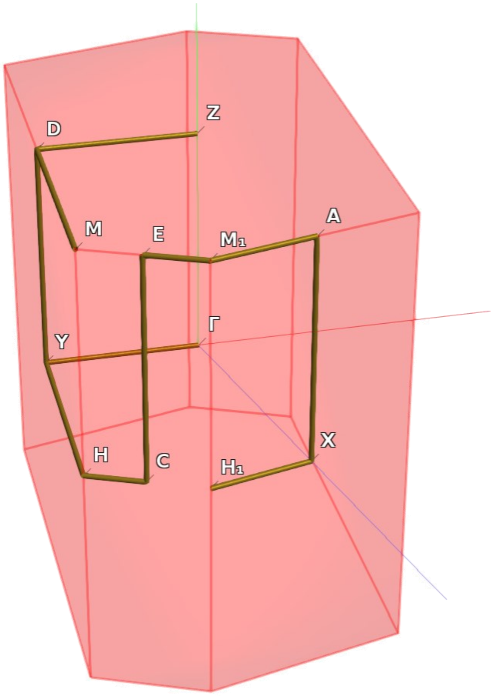

Figure A6. *The k-path followed in the Brillouin zone for determining the electronic band structures of the AFM and FM configurations.*

A.2 Light microscopy for crystal selection TUB40

Single crystals were selected after identification under a light microscope (Axiostar plus, Carl Zeiss, Germany) equipped with 20× objective and 200× total amplification. For the single-crystal conductivity measurements, a series of ten crystals measuring about 100 x 100 µm with a thickness of about ten µm were identified (see Fig. S5) according to the given scaling in the microscope and measured as described in our former study. The resistance of the system with the clamped crystals varied between 1.2 and 12.6 Ω. The contact resistance was measured to be 0.6 Ω resulting in crystal resistances from 0.6 to 12.0 Ω with an average of 4.9 ± 3.2 Ω The average conductivity was therefore calculated to be $\sigma = \frac{l}{RA} = \frac{1e^{-5}m}{5\Omega\cdot((1e^{-4}m)^2)}$ = 200 S m^{-1}, with values ranging from 100 to 10^3 S m^{-1}. Since the TUB40 single crystals are not perfectly monocrystalline (as can be seen in Fig. S5), they do not make perfect contacts with the gold surfaces and the actual conductance's may be even higher than our reported values. We are currently working on growing larger crystals and an optimized electrical workstation for conductivity measurements to maximize the contact surface area in order to more accurately measure TUB40's conductivity.

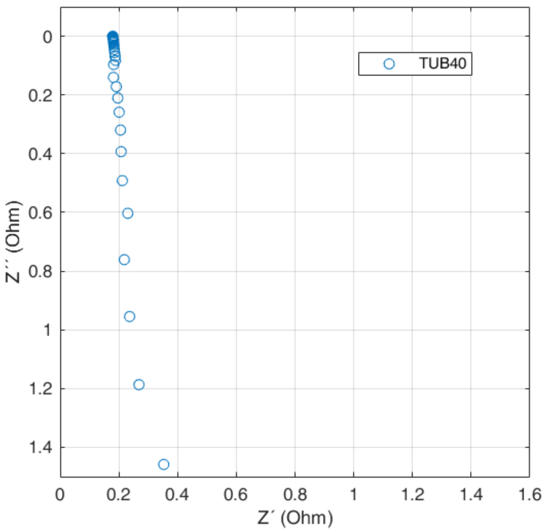

Figure A7. *Impedance spectrum of TUB40 in the Nyquist representation. Above ~500 Hz, Z´´ increases due to the increasing parasitic contributions from the connectors and cables in the setup.*

Appendix B: Supplementary Data for Chapter 4 Phosphonate Hydrogen-Bonded Organic Frameworks

Table B1. *pDOS orbital contributions of the most dominant atoms in the HOCO and LUCO of Ni-GTUB-5. The sum of the HOCO/LUCO contributions shown is 99%/99%.*

Ni-GTUB-5	**s**	**p_y**	**p_z**	**p_x**	**d_{-2}**	**d_{-1}**	**d_0**	**d_{+1}**	**d_{+2}**
C HOCO	4.45E-04	1.96E-03	7.77E-03	1.53E-02	6.59E-04	2.13E-03	3.95E-03	8.67E-04	6.82E-04
C LUCO	1.55E-02	2.51E-02	3.19E-02	1.56E-02	2.00E-03	1.16E-02	8.46E-03	6.63E-03	6.95E-03
N HOCO	9.34E-03	1.14E-02	1.34E-02	2.65E-03	1.52E-04	1.23E-04	5.06E-04	1.48E-03	6.05E-04
N LUCO	5.60E-02	9.54E-02	7.43E-02	3.48E-02	7.57E-04	1.70E-03	1.15E-03	5.68E-03	2.08E-03
Ni HOCO	3.96E-02	0.00E+00	0.00E+00	0.00E+00	8.05E-02	1.26E-01	1.19E-01	5.11E-01	3.78E-02
Ni LUCO	6.90E-07	0.00E+00	0.00E+00	0.00E+00	1.94E-02	1.19E-01	2.73E-02	1.26E-01	3.04E-01

Table B2. *pDOS orbital contributions of the most dominant atoms in the HOCO and LUCO of Zn-GTUB-5. The sum of the HOCO/LUCO contributions shown is 98%/97%.*

Zn-GTUB-5	**s**	**p_y**	**p_z**	**p_x**	**d_{-2}**	**d_{-1}**	**d_0**	**d_{+1}**	**d_{+2}**
C HOCO	7.15E-03	3.02E-02	2.84E-01	2.48E-01	4.85E-02	4.83E-02	7.72E-02	3.77E-03	2.71E-02
C LUCO	2.89E-03	1.43E-02	3.24E-01	3.16E-01	5.80E-02	6.40E-02	6.27E-02	4.15E-03	2.34E-02

N HOCO	1.20E-06	9.43E-02	9.12E-02	1.69E-04	3.88E-04	3.87E-04	1.14E-06	1.35E-04	1.20E-06
N LUCO	4.95E-04	3.89E-02	4.78E-02	3.00E-08	4.60E-07	4.91E-03	1.55E-05	1.73E-03	4.95E-04
Zn HOCO	0.00E+00	0.00E+00	1.08E-02	5.65E-03	1.40E-07	3.20E-06	0.00E+00	0.00E+00	0.00E+00
Zn LUCO	1.37E-04	0.00E+00	0.00E+00	0.00E+00	0.00E+00	0.00E+00	4.63E-03	4.14E-04	6.99E-04

***Table B3**. pDOS orbital contributions of the most dominant atoms in the HOCO and LUCO of Cu-GTUB-5. The sum of the α-HOCO/LUCO and β-HOCO/LUCO contributions shown are 98%/97% and 98%/99%, respectively.*

α-Cu-GTUB-5	**s**	**p_y**	**p_z**	**p_x**	**d_{-2}**	**d_{-1}**	**d_0**	**d_{+1}**	**d_{+2}**
C HOCO	6.78E-03	3.72E-02	2.81E-01	2.50E-01	4.98E-02	4.72E-02	7.67E-02	4.38E-03	2.75E-02
C LUCO	2.72E-03	1.60E-02	3.16E-01	3.20E-01	6.04E-02	6.04E-02	6.40E-02	4.84E-03	2.36E-02
N HOCO	1.59E-05	9.20E-07	8.88E-02	9.03E-02	1.28E-04	3.23E-04	2.57E-04	1.12E-06	9.87E-05
N LUCO	1.28E-04	5.93E-04	3.56E-02	5.08E-02	8.00E-08	5.50E-07	4.62E-03	1.29E-05	1.76E-03
Cu HOCO	0.00E+00	0.00E+00	8.50E-03	4.07E-03	4.00E-08	6.00E-08	0.00E+00	0.00E+00	0.00E+00
Cu LUCO	1.16E-04	0.00E+00	0.00E+00	0.00E+00	0.00E+00	0.00E+00	6.26E-03	6.55E-04	6.93E-04
β-Cu-GTUB-5	**s**	**p_y**	**p_z**	**p_x**	**d_{-2}**	**d_{-1}**	**d_0**	**d_{+1}**	**d_{+2}**
C HOCO	-0.20677	6.87E-03	3.65E-02	2.77E-01	2.46E-01	4.98E-02	4.73E-02	7.68E-02	4.31E-03
C LUCO	1.688336	1.32E-02	2.20E-02	7.03E-02	3.61E-02	3.72E-03	1.63E-02	2.04E-02	7.26E-03

N HOCO	1.56E-05	8.40E-07	9.25E-02	9.41E-02	1.20E-04	3.14E-04	2.47E-04	9.30E-07	9.39E-05
N LUCO	5.18E-02	9.36E-02	8.33E-02	1.92E-02	1.00E-08	3.30E-07	3.30E-03	5.29E-03	1.52E-03
Cu HOCO	0.00E+00	0.00E+00	9.21E-03	4.44E-03	5.00E-08	7.00E-08	0.00E+00	0.00E+00	0.00E+00
Cu LUCO	1.41E-04	0.00E+00	0.00E+00	0.00E+00	0.00E+00	0.00E+00	5.35E-02	1.28E-01	3.53E-01

***Table B4**. pDOS orbital contributions of the most dominant atoms in the HOCO and LUCO of Pd-GTUB-5. The sum of the HOCO/LUCO contributions shown is 99%/99%.*

Pd-GTUB-5	**s**	**p_y**	**p_z**	**p_x**	**d_{-2}**	**d_{-1}**	**d_0**	**d_{+1}**	**d_{+2}**
C HOCO	4.21E-02	2.96E-01	2.43E-01	4.83E-02	4.85E-02	7.61E-02	5.51E-03	2.80E-02	2.71E-02
C LUCO	2.05E-02	3.27E-01	2.74E-01	5.01E-02	6.91E-02	6.35E-02	6.85E-03	2.00E-02	2.34E-02
N HOCO	1.46E-05	3.05E-06	8.84E-02	8.34E-02	1.42E-04	3.23E-04	2.55E-04	5.00E-08	1.27E-04
N LUCO	1.30E-03	7.77E-04	5.88E-02	3.36E-02	1.06E-06	1.47E-06	4.49E-03	1.72E-04	8.03E-04
Pd HOCO	0.00E+00	0.00E+00	5.71E-03	3.02E-03	3.70E-07	1.49E-06	0.00E+00	0.00E+00	0.00E+00
Pd LUCO	2.13E-05	9.00E-08	0.00E+00	0.00E+00	0.00E+00	0.00E+00	1.41E-02	1.64E-04	2.08E-02

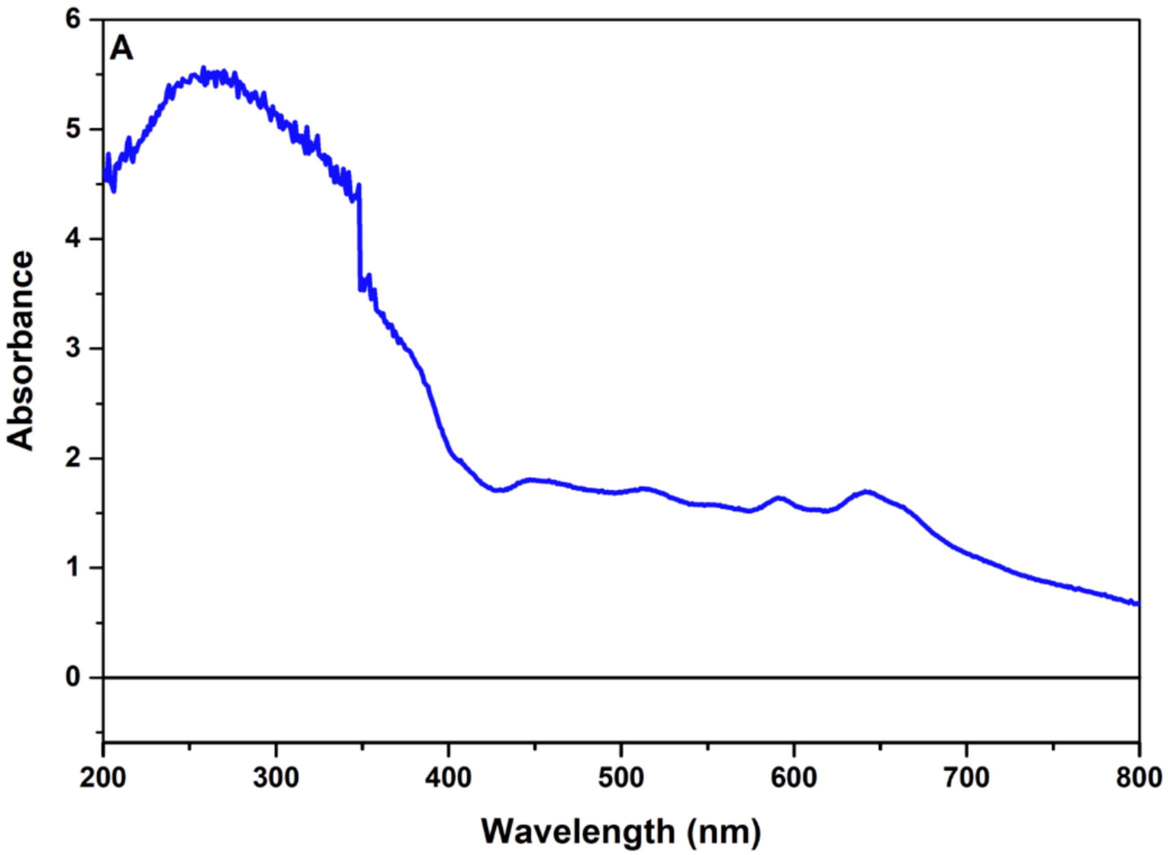

Figure B1. *Solid-sate UV-Vis spectrum of GTUB-5. The solid-state diffuse reflectance ultraviolet–visible (UV-Vis) spectrum of GTUB-5 crystals was collected on a Varian Cary 300 UV-Vis Spectrophotometer.*

B.1 Proton Conductivity

The proton conductivity of GTUB-5 was determined by electrochemical impedance spectroscopy. A Zahner Zennium electrochemical workstation was used with an oscillation voltage of 10 mV over a frequency from 1 to 10 6 Hz. The needles were compressed between two glassy carbon electrodes by a torque of 30 cNm to obtain pellets of 82 mm in diameter and ca. 0.114 mm thickness. The stack was placed in a PTFE sample holder. The sample holder was placed in a stainless-steel chamber with an attached water reservoir. The relative humidity (%rh) was determined by the Clausius-Clapeyron relation and controlled by heating the cell and water reservoir. The sample is held overnight at the desired %r.h. and temperature before measuring each data point. To ensure reproducibility, each data point was measured three times.

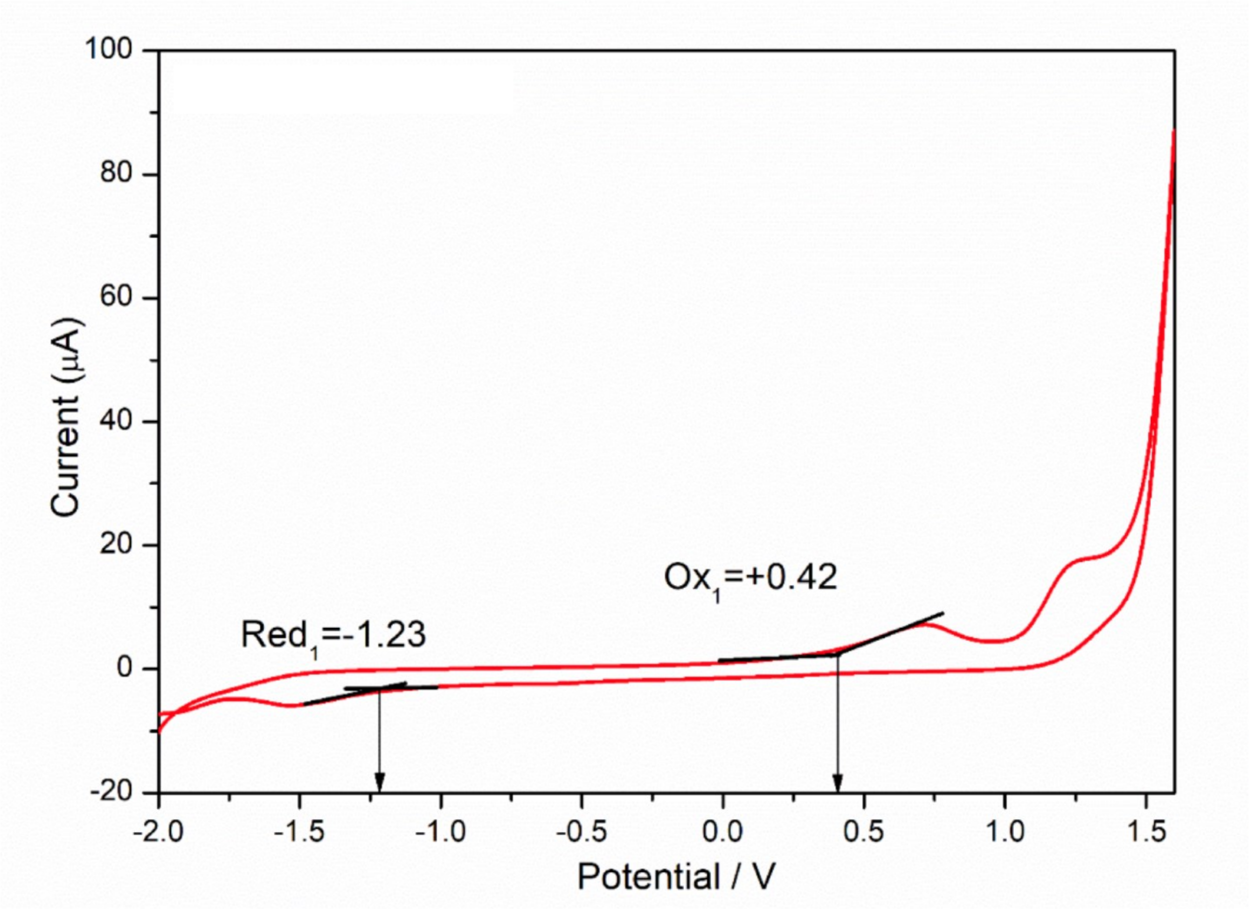

Figure B2. *Cyclic voltammetry of GTUB-5. The HOMO-LUMO gap of GTUB-5 was extracted using cyclic voltammetry*[32]*. From the measurement, the first oxidation and reduction potentials of GTUB-5 in DMSO were determined to be 0.42 V and -1.23 V, which give rise to a HOMO-LUMO gap of 1.65 eV.*

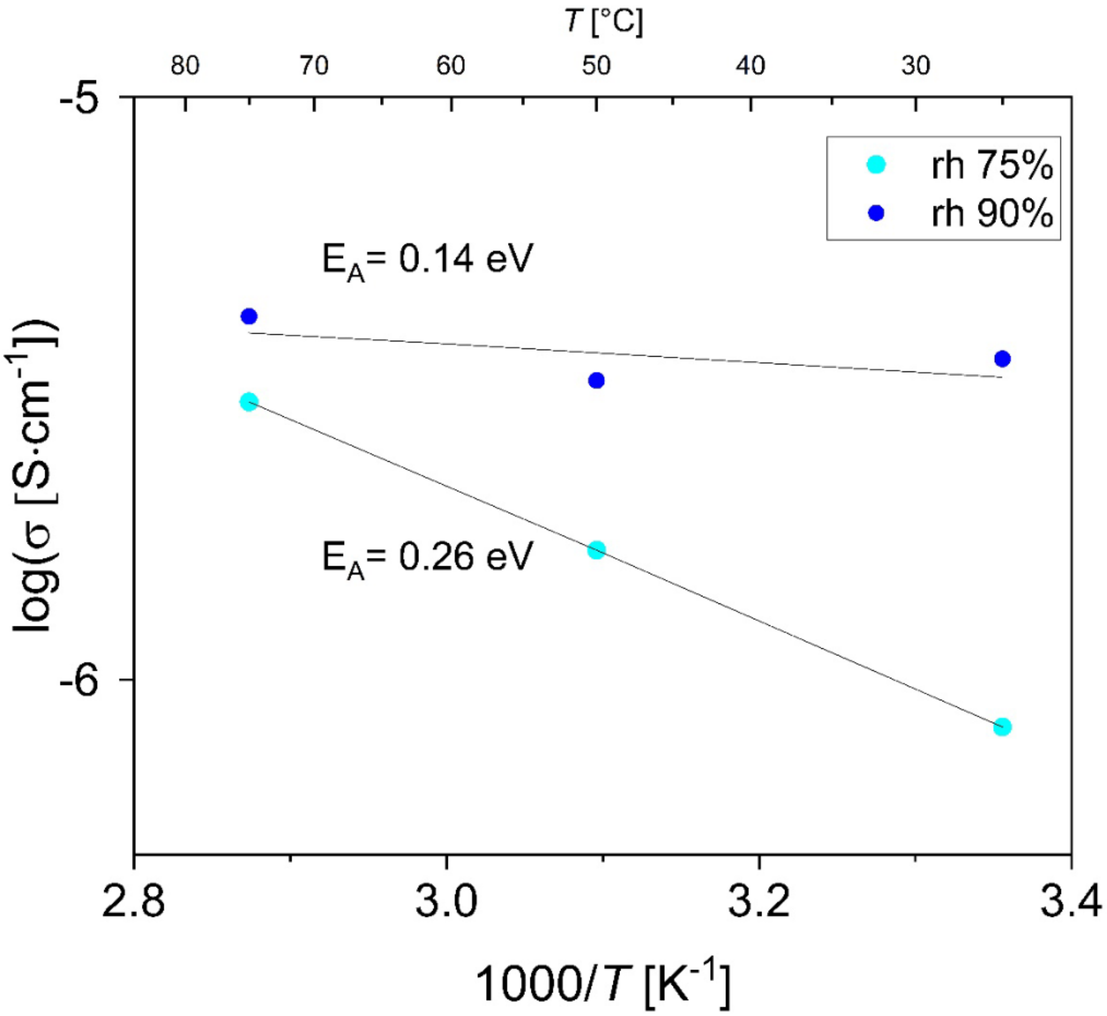

Figure B3. *Proton conductivity of GTUB-5.*

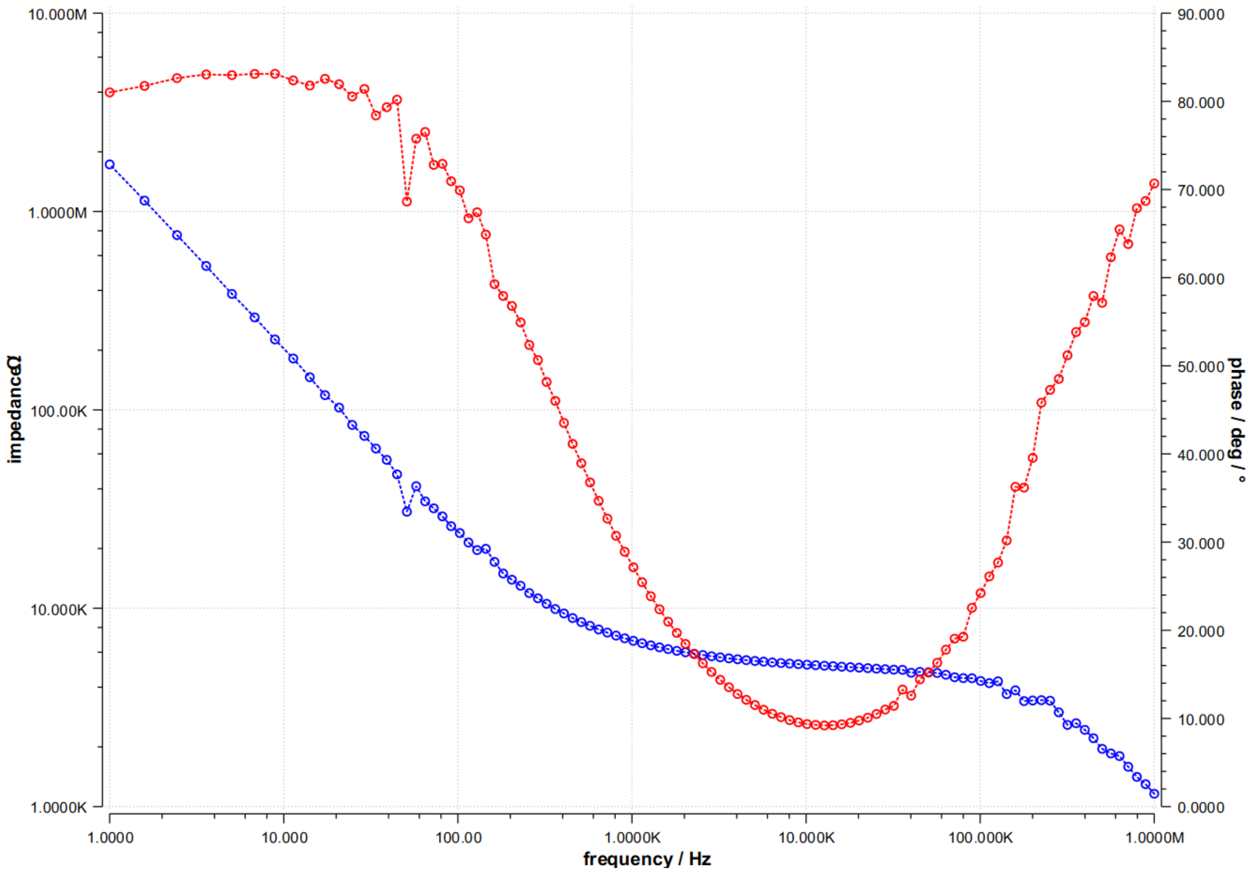

Figure B4. *Bode plot of GTUB-5 at 75°C and 90°C %rh.*

Table B5*. Experimental and DFT-calculated bond distances for the various M-GTUB-5 systems (M=metal ion residing in the porphyrin core). All distances are in Å and standard deviations are in brackets.*

	Ni-GTUB-5	**Cu-GTUB-5**	**Zn-GTUB-5**	**Pd-GTUB-5**
		Experiment		
M-N	2.00 (0.01)	2.00 (0.00)	2.06 (0.03)	2.02 (0.00)
O-H	0.82 (0.00)	0.84 (0.00)	0.84 (0.00)	0.84 (0.00)
P-O	1.49 (0.07)	1.51 (0.03)	1.51 (0.03)	1.52 (0.01)
P-C	1.79 (0.03)	1.78 (0.03)	1.80 (0.00)	1.79 (0.02)
C-C	1.40 (0.05)	1.40 (0.04)	1.40 (0.05)	1.40 (0.04)
C-H	0.95 (0.01)	0.96 (0.01)	0.96 (0.01)	0.96 (0.02)
N-C	1.44 (0.05)	1.35 (0.08)	1.38 (0.08)	1.41 (0.16)

N-H	0.89 (0.00)	0.91 (0.00)	0.91 (0.00)	0.91 (0.00)
		DFT		
M-N	1.96 (0.00)	2.02 (0.01)	2.05 (0.02)	2.04 (0.01)
O-H	1.05 (0.02)	1.11 (0.10)	1.08 (0.04)	1.06 (0.02)
P-O	1.55 (0.03)	1.55 (0.03)	1.55 (0.02)	1.56 (0.03)
P-C	1.81 (0.01)	1.80 (0.00)	1.80 (0.00)	1.80 (0.00)
C-C	1.41 (0.03)	1.41 (0.03)	1.41 (0.03)	1.41 (0.03)
C-H	1.09 (0.01)	1.09 (0.00)	1.09 (0.00)	1.09 (0.00)
N-C	1.46 (0.04)	1.45 (0.05)	1.45 (0.05)	1.45 (0.06)
N-H	1.06 (0.01)	1.06 (0.00)	1.06 (0.00)	1.05 (0.00)

Table B6. *Experimental and DFT-calculated monoclinic lattice vectors, angles, and unit cell volumes of the M-GTUB-5 systems. Lattice vectors are in Å, angles are in degrees, and volumes are in* Å^3*. The DFT-calculated lattice vectors and volumes are in shown in brackets.*

	Ni-GTUB-5	Cu-GTUB-5	Zn-GTUB-5	Pd-GTUB-5
$\vec{a}$	7.251 (6.658)	7.106 (6.881)	7.090 (6.853)	6.990 (6.915)
$\vec{b}$	23.77 (22.32)	22.91 (22.80)	22.98 (22.62)	23.16 (22.93)
$\vec{c}$	23.64 (24.83)	25.87 (25.84)	25.03 (25.90)	24.88 (25.08)
$\angle\beta$	95.3	93.05	94.51	94.71
$\angle\alpha = \angle\gamma$	90.0	90.0	90.0	90.0
Volume	4057 (3675)	4205 (4048)	4066 (4003)	4013 (3962)

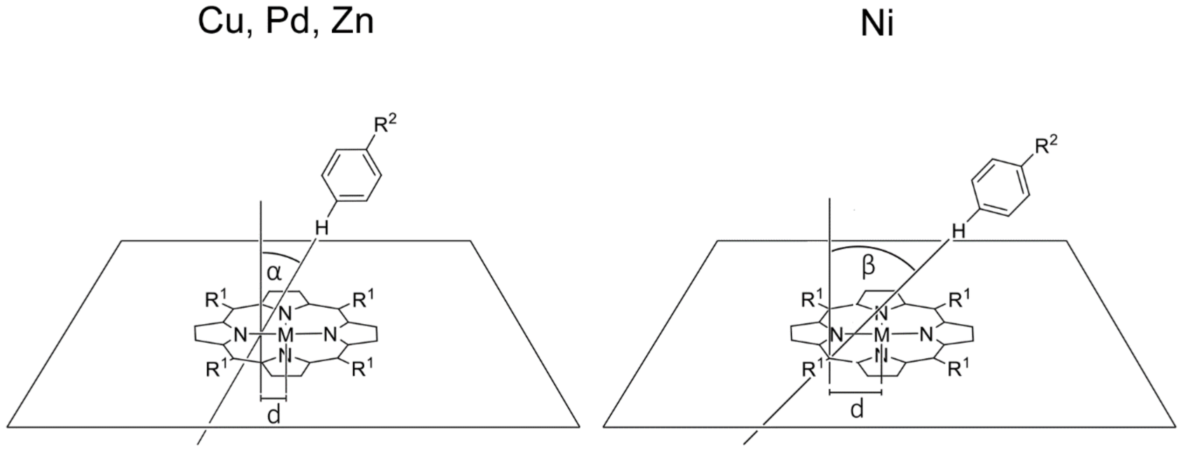

Figure B5. *Schematic representation of interaction distances and angles between M-porphyrin ring and the phenyl phosphonate dianion for Cu-, Pd-, and Zn-GTUB-5 (left panel) and Ni-GTUB-5 (right panel).* R^1 *= p-phenylphosphonic acid,* R^2 *= phosphonate dianion.*

B.1 Surface area and pore characterization via molecular simulation

The textural properties of Cu-, Ni-, Pd- and Zn-GTUB-5 were calculated with the Poreblazer V4.0 software,[260,288] using the crystal structure information (in xyz format) for the M-GTUB-5 systems. Framework atoms were held fixed in their crystallographically determined positions during all calculations.

The specific helium-accessible pore volumes of Cu-, Ni-, Pd-, and Zn-GTUB-5 were calculated using Widom's particle insertion method.[289] Briefly, this calculation involved averaging over 100,000 random insertions of a single helium atom into the framework. Then, the specific pore volume, V_p, was determined by

$$V_p = \frac{1}{m_s} \int e^{-\varphi(r)/kT} dr \qquad \text{B.9}$$

where φ is the helium-solid interaction energy for a single helium atom, dr is a differential volume element, and m_s is the mass of the solid adsorbent in the simulation box, and T = 298 K. The interaction energy between the helium probe and the framework atoms was computed through the Lennard-Jones (LJ) potential:

$$\varphi_{ij} = 4\varepsilon_{ij}\left[\left(\frac{\sigma_{ij}}{r_{ij}}\right)^{12} - \left(\frac{\sigma_{ij}}{r_{ij}}\right)^{6}\right] + \frac{q_i\, q_j}{4\,\varepsilon_0\, r_{ij}} \qquad \text{B.2}$$

where i and j index the interacting atoms, r_{ij} is the distance between atoms i and j, and ε_{ij} and σ_{ij} are the LJ well depth and diameter, respectively. The helium model was taken from Hirschfelder et al.,[290] where σ_{He}= 2.640 Å and ε/k_B-$_{He}$ = 10.9 K. The LJ parameters for Cu-, Ni-, Pd-, and Zn-GTUB-5 atoms were taken from the Universal Force Field (**Table B7**).[240]

Table B7. *LJ parameters for the framework atoms of Cu-, Ni-, Pd-, and Zn-GTUB-5.*

Atom type	**σ (Å)**	**ε/k_B (K)**
H	2.571	22.154
C	3.431	52.8
N	3.261	34.70
O	3.118	30.2
P	3.695	153.37
Ni	2.525	7.54
Cu	3.114	2.51
Zn	2.462	62.38
Pd	2.583	24.154

The limiting pore diameters and maximum pore sizes of Cu-, Ni-, Pd-, and Zn-GTUB-5 were calculated using a point probe. The largest probe that can cross the simulation cell in at least one dimension via a diffusive pathway yields the limiting pore diameter.

The geometric accessible surface areas (SA) of Cu-, Ni-, Pd-, and Zn-GTUB-5 were calculated using the method of Duren et al.[261] The calculations employed a nitrogen probe of 3.314 Å in diameter. A nitrogen probe was chosen because SA is often experimentally derived from N_2 adsorption isotherms.

Table B8. *Results of surface are, pore volume and pore size calculations for M-GTUB-5 series, M = Cu, Ni, Pd, and Zn.*

M-HOF	Cu-GTUB-5	Ni-GTUB-5	Pd-GTUB-5	Zn-GTUB-5
Pore volume calculation				
System mass in g cm^{-3}	50798.272	47570.946	24549.120	25428.640
System density in cm^3 g^{-1}	1.289	1.217	1.269	1.298
Helium accessible volume in cm^3 g^{-1}	0.254	0.207	0.178	0.201
Accessible surface area per volume in m^2 cm^{-3}	259.890	103.380	127.120	260.900
Accessible surface area per mass in m^2 g^{-1}	229.550	84.960	100.160	200.970
Limiting pore diameter and maximum pore size				
Pore limiting diameter in Å	4.570	3.590	3.840	4.040
Maximum pore diameter in Å	9.450	5.420	5.150	5.390
System is percolated in	1D channels	1D channels	1D channels	1D channels

Appendix C: Supplementary Data for Chapter 5 Mechanistic insights into proton conductivities in phosphonate hydrogen-bonded organic frameworks: An ab-initio molecular dynamics study

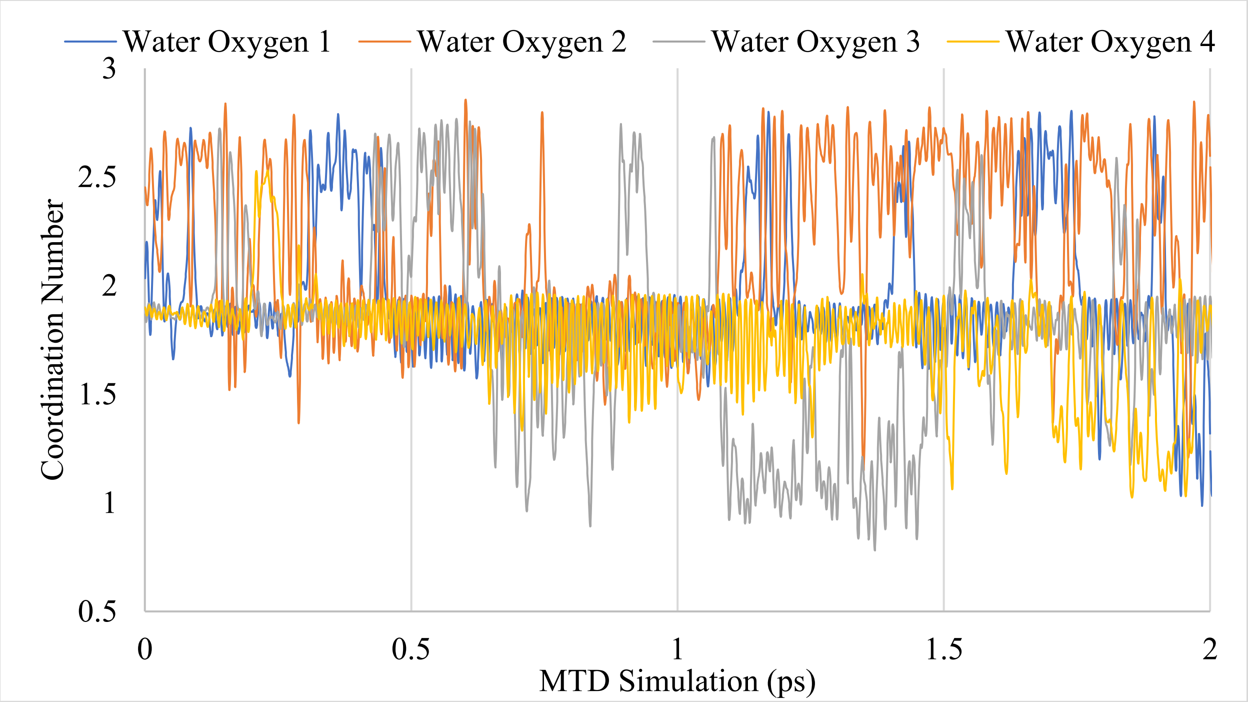

Figure C1. *Oxygen CNs along a W2W-MTD run for UPC-H5a. Grey, blue, orange, and yellow lines correspond to oxygen atoms from waters in the pore.*

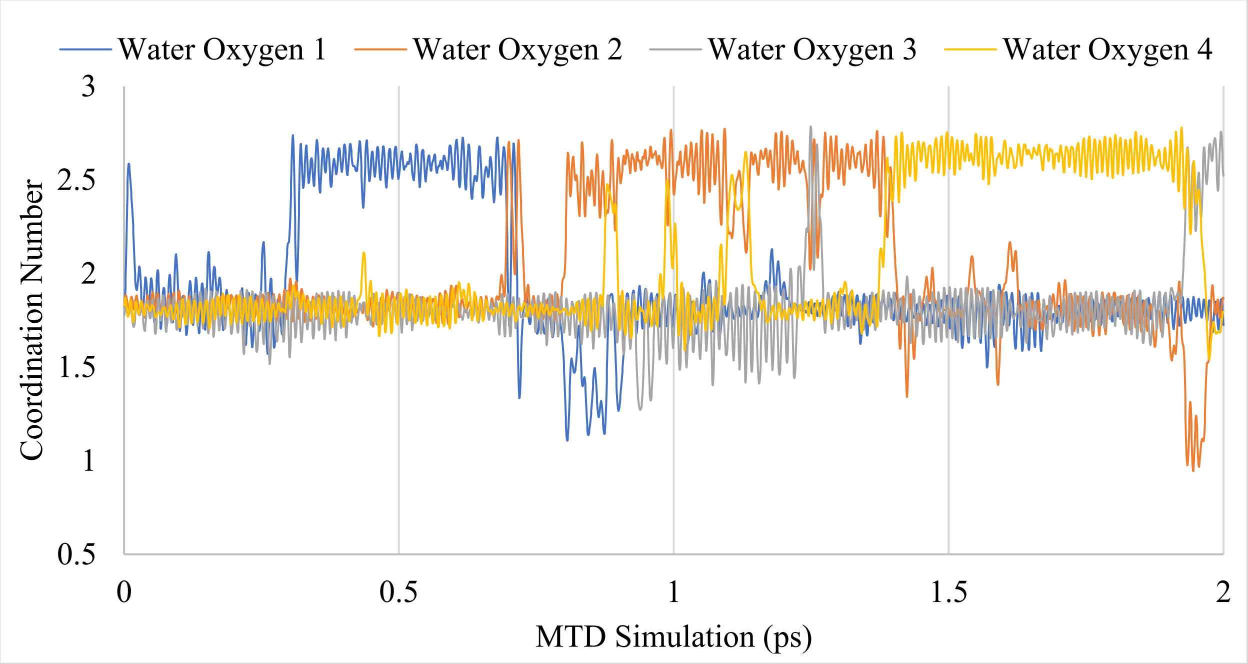

Figure C2. *Oxygen CNs along a W2W-MTD run for GTUB-5. Grey, blue, orange, and yellow lines correspond to oxygen atoms from waters in the pore.*

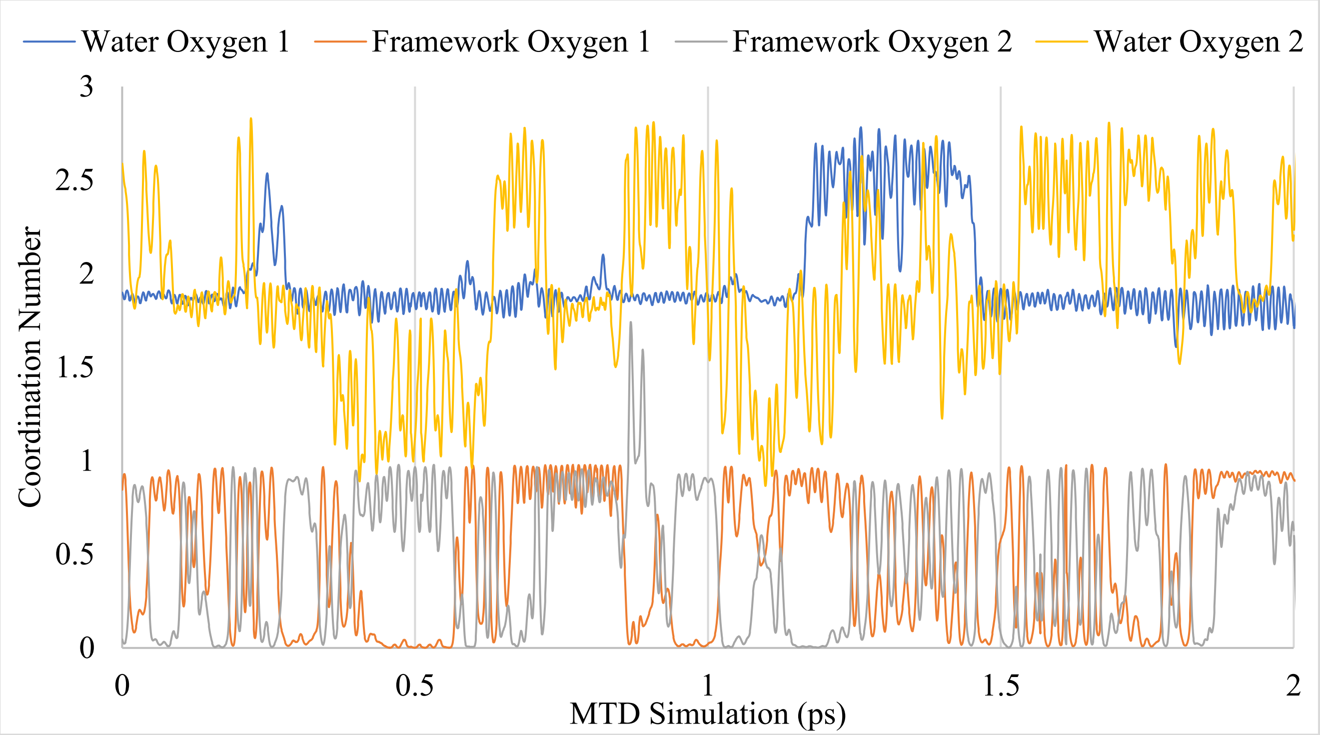

Figure C3. *Oxygen CNs along a W2F-MTD run for UPC-H5a. Yellow and blue lines correspond to oxygen atoms from waters in the pore. Orange and grey lines correspond to oxygen atoms on the phenyl-phosphonate.*

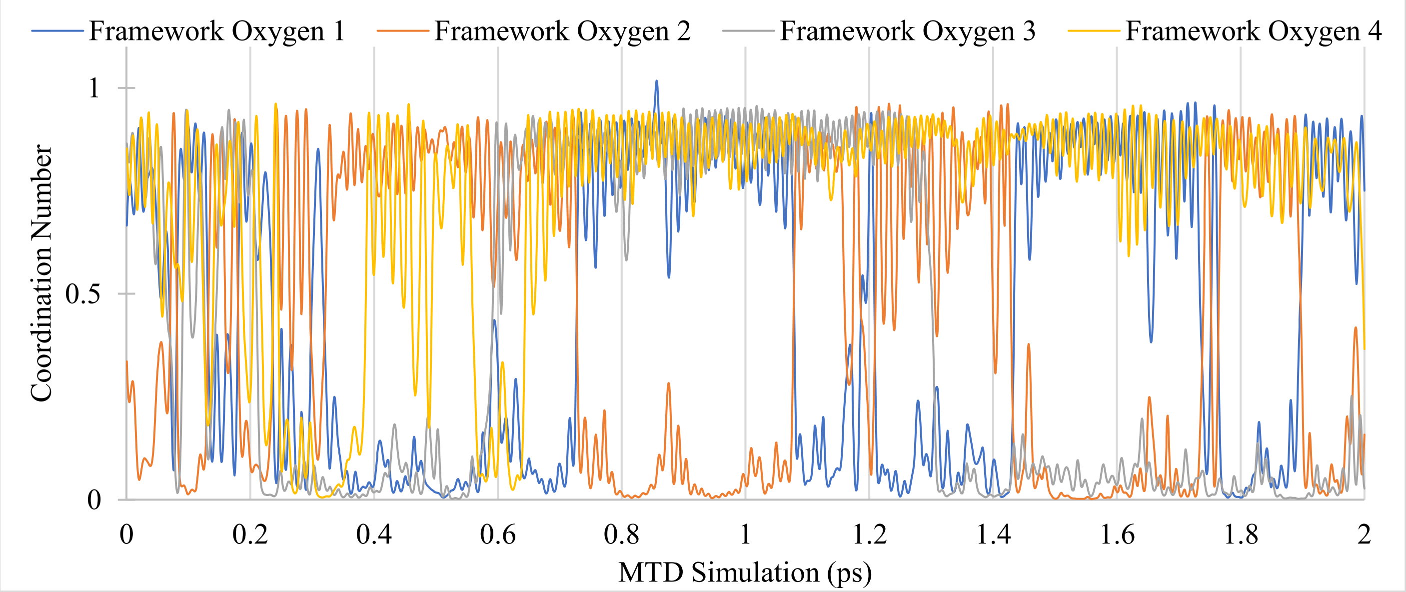

Figure C4. *Oxygen CNs along a F2F-MTD run for GTUB-5. Grey, blue, orange, and yellow lines correspond to oxygen atoms on the phenyl-phosphonate.*

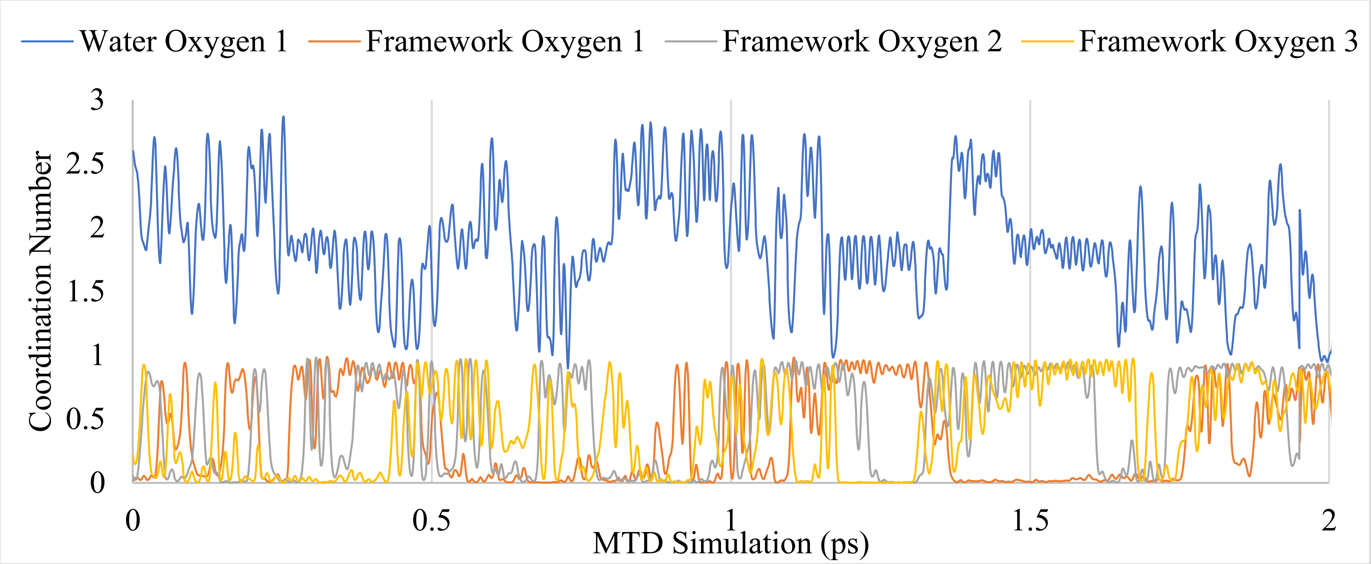

Figure C5. *Oxygen CNs along a F2F-MTD run for UPC-H5a. Blue lines correspond to an oxygen atom from a water in the pore. The orange, yellow and grey lines correspond to oxygen atoms on the phenyl-phosphonates.*

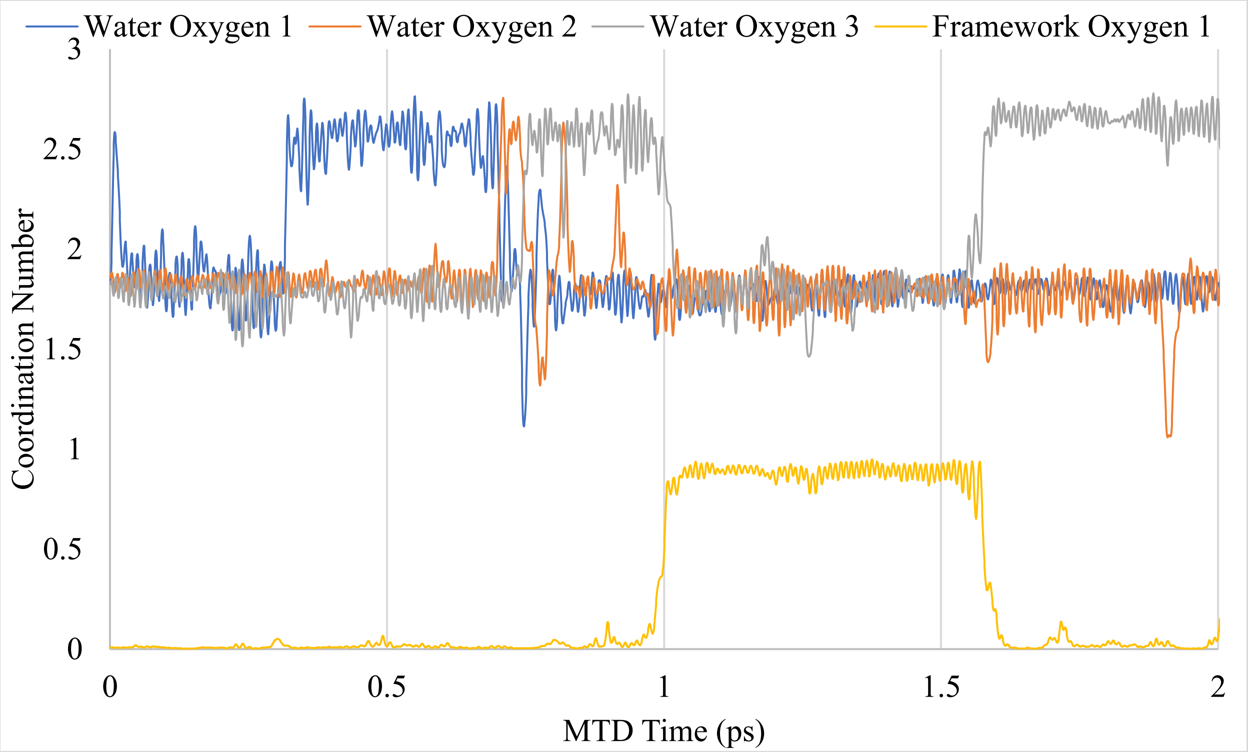

Figure C6. *Oxygen CNs along a WtF-MTD run for GTUB-5. Grey, blue, and orange lines correspond to oxygen atoms from water molecules in the pore, while the yellow line corresponds to an oxygen atom on the phenyl-phosphonate.*

Table C1. *RESP-REPEAT charges of oxygen donor, proton in transit, and oxygen acceptor atoms for the WtW pathway in GTUB-5. These values are from the first three unbiased NVE trajectories, then averaged in the last column. All charges are reported in elementary charge units and brackets indicate standard deviations.*

Atom	**WtW_1**	**WtW_2**	**WtW_3**	**Average**
		Reactant		
O_{donor}	-0.876	-0.773	-0.614	-0.754 (0.132)
H	0.508	0.426	0.499	0.478 (0.045)
$O_{acceptor}$	-0.810	-0.888	-0.881	-0.860 (0.043)
		Transition		
O_{donor}	-0.866	-1.149	-0.645	-0.887 (0.253)
H	0.533	0.684	0.514	0.577 (0.093)
$O_{acceptor}$	-0.878	-0.821	-0.828	-0.842 (0.031)
		Product		
O_{donor}	-0.817	-0.833	-0.848	-0.832 (0.016)
H	0.378	0.549	0.495	0.474 (0.088)
$O_{acceptor}$	-0.657	-0.915	-0.816	-0.796 (0.130)

Table C2. *RESP-REPEAT charges of oxygen donor, proton in transit, and oxygen acceptor atoms for the WtF pathway in GTUB-5. These values are from the first three unbiased NVE trajectories, then averaged in the last column. All charges are reported in elementary charge units and brackets indicate standard deviations.*

Atom	**WtF_1**	**WtF_2**	**WtF_3**	**Average**
		Reactant		
O_{donor}	-0.967	-0.828	-0.642	-0.813 (0.163)
H	0.537	0.360	0.382	0.426 (0.097)
$O_{acceptor}$	-0.855	-0.557	-0.750	-0.721 (0.151)
		Transition		
O_{donor}	-1.102	-0.825	-0.810	-0.912 (0.165)
H	0.581	0.448	0.492	0.507 (0.068)
$O_{acceptor}$	-0.793	-0.699	-0.764	-0.752 (0.048)
		Product		

O_{donor}	-1.042	-0.918	-0.770	-0.910 (0.137)
H	0.552	0.375	0.431	0.453 (0.091)
$O_{acceptor}$	-0.717	-0.584	-0.607	-0.636 (0.071)

Table C3. *RESP-REPEAT charges of oxygen donor, proton in transit, and oxygen acceptor atoms for the FtF pathway in GTUB-5. These values are from the first three unbiased NVE trajectories, then averaged in the last column. All charges are reported in elementary charge units and brackets indicate standard deviations.*

Atom	**FtF$_1$**	**FtF$_2$**	**FtF$_3$**	**Average**
Reactant				
O_{donor}	-0.540	-0.560	-0.694	-0.598 (0.084)
H	0.436	0.415	0.538	0.463 (0.066)
$O_{acceptor}$	-0.673	-0.526	-0.749	-0.649 (0.113)
Transition				
O_{donor}	-0.695	-0.388	-0.716	-0.600 (0.183)
H	0.581	0.343	0.535	0.486 (0.126)
$O_{acceptor}$	-0.889	-0.426	-0.692	-0.669 (0.232)
Product				
O_{donor}	-0.609	-0.697	-0.778	-0.694 (0.085)
H	0.464	0.532	0.499	0.498 (0.034)
$O_{acceptor}$	-0.690	-0.604	-0.565	-0.619 (0.064)

Table C4. *RESP-REPEAT charges of oxygen donor, proton in transit, and oxygen acceptor atoms for the WtW pathway in UPC-H5a. These values are from the first three unbiased NVE trajectories, then averaged in the last column. All charges are reported in elementary charge units and brackets indicate standard deviations.*

Atom	**WtW$_1$**	**WtW$_2$**	**WtW$_3$**	**Average**
Reactant				
O_{donor}	-0.775	-0.915	-0.583	-0.758 (0.167)
H	0.503	0.591	0.440	0.511 (0.076)
$O_{acceptor}$	-0.747	-0.953	-0.823	-0.841 (0.105)
Transition				

O$_{donor}$	-0.791	-0.692	-0.739	-0.741 (0.049)
H	0.421	0.410	0.487	0.439 (0.042)
O$_{acceptor}$	-0.537	-0.667	-0.741	-0.648 (0.104)
Product				
O$_{donor}$	-0.814	-0.796	-1.030	-0.880 (0.130)
H	0.396	0.411	0.554	0.454 (0.088)
O$_{acceptor}$	-0.344	-0.631	-0.834	-0.603 (0.246)

Table C5. *RESP-REPEAT charges of oxygen donor, proton in transit, and oxygen acceptor atoms for the WtF pathway in UPC-H5a. These values are from the first three unbiased NVE trajectories, then averaged in the last column. All charges are reported in elementary charge units and brackets indicate standard deviations.*

Atom	**WtF$_1$**	**WtF$_2$**	**WtF$_3$**	**Average**
Reactant				
O$_{donor}$	-0.766	-1.019	-0.541	-0.776 (0.239)
H	0.462	0.493	0.443	0.466 (0.025)
O$_{acceptor}$	-0.793	-0.599	-0.855	-0.749 (0.134)
Transition				
O$_{donor}$	-0.791	-0.715	-0.796	-0.767 (0.045)
H	0.472	0.391	0.438	0.434 (0.041)
O$_{acceptor}$	-0.862	-0.550	-0.712	-0.708 (0.156)
Product				
O$_{donor}$	-0.591	-0.812	-0.720	-0.708 (0.111)
H	0.458	0.483	0.444	0.462 (0.020)
O$_{acceptor}$	-0.752	-0.580	-0.635	-0.656 (0.088)

Table C6. *RESP-REPEAT charges of oxygen donor, proton in transit, and oxygen acceptor atoms for the FtF pathway in UPC-H5a. These values are from the first three unbiased NVE trajectories, then averaged in the last column. All charges are reported in elementary charge units and brackets indicate standard deviations.*

Atom	**FtF$_1$**	**FtF$_2$**	**FtF$_3$**	**Average**

		Reactant		
O_{donor}	-0.686	-0.300	-0.699	-0.561 (0.227)
H	0.415	0.337	0.458	0.403 (0.062)
$O_{acceptor}$	-0.461	-0.758	-0.725	-0.648 (0.163)
		Transition		
O_{donor}	-0.742	-0.509	-0.746	-0.666 (0.136)
H	0.484	0.425	0.483	0.464 (0.034)
$O_{acceptor}$	-0.643	-0.759	-0.684	-0.695 (0.059)
		Product		
O_{donor}	-0.815	-0.590	-0.742	-0.716 (0.115)
H	0.578	0.430	0.576	0.528 (0.085)
$O_{acceptor}$	-0.704	-0.687	-0.778	-0.723 (0.049)